

# PRINCIPLES OF STRUCTURAL STABILITY OF SP-BONDED SYSTEMS

by

José Carlos Cressoni

Thesis submitted for the degree of

Doctor of Philosophy

and for the

Diploma of Membership

of the

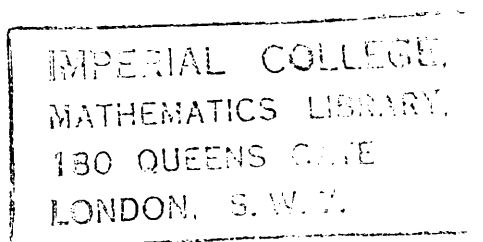
Imperial College of Science, Technology and Medicine

University of London

London

Department of Mathematics

February 1989



## ACKNOWLEDGEMENTS

My sincere gratitude to my supervisor Professor David Pettifor whose constant guidance and encouragement made the whole research project possible.

My thanks to my roommates Andrew Skinner and Roger Davies and also to Leif Goodwin for the friendship and most helpful discussions. It has particularly been a immense pleasure to share these years at Imperial College with friends like Fernando D.Nobre, Luiz C.de Freitas, Fernando A. M.de Oliveira and many others who, in different ways, influenced the completion of this work.

I can not help feeling indebted to the advice service of the Imperial College Computer Centre for the assistance during my first steps in computing.

My sincere thanks to my parents for the unquestionable support, understanding and promptness to help in any case of need.

To my wife Marina and my children Carolina, Franz and André I apologize for the many periods of absence. Most of the time the work came first and I wholeheartedly thank them for their patience, love and understanding. This thesis is dedicated to them.

This work was supported by the Conselho Nacional de Desenvolvimento Científico e Tecnológico – CNPq to whom I wish to express my gratitude.

Except where otherwise acknowledged, the work described in chapters 4, 5 and 6 and part of chapter 2 is original. It is presently being written to be submitted for publication in specialized journals.

# ABSTRACT

During the last decade theoretical solid state physics has undergone rapid advances with the implementation of local density functional (LDF) theory. The advent of fast super-computers made possible the computation of total energies of solids to an accuracy of a few milli Ry which is of the order of structural energy differences. Despite being created more than sixty years ago quantum theory is only now being effective in predicting the relative structural stability of solids.

The LDF *ab-initio* calculations, however powerful, provide little direct information as to the physical mechanisms that are responsible for the bonding in the solid. To this end a simpler yet reliable theory is desired. In this thesis a two-centre orthogonal tight-binding model is used to compare directly the energy between two given structures. The hopping integrals are assumed to be transferable from structure to structure and to vary with the bond-length as in Harrison's  $1/R^2$  model. The comparison of the equilibrium energies of two structures involves taking into account the volume change due to the change in the environment as one goes from one structure to another. This is done with the use of Pettifor's structural energy difference theorem. This model is shown to be able to account for the observed experimental stability trends amongst the sp-bonded elements. It successfully separates between structures as different as a dimer and close packed fcc. The model is also sufficiently simple to allow for a physical interpretation of the predicted trends in terms of local topology. The application to sp-bonded AB compounds is also shown to produce good structural separation amongst the most commonly found AB binary structures.

# Table of Contents

<b>Chapter 1.</b>	<b>Introduction</b>
<b>Chapter 2.</b>	<b>Numerical Methods</b>
2.1	Introduction
2.2	The Local Density of States and the Recursion Method
2.3	The Method of the Moments
2.4	Finite and Infinite Continued Fractions
2.4.1	The Square Root Terminator
2.4.2	The Single Band–Gap Termination
2.5	Conclusions
<b>Chapter 3.</b>	<b>Relevant Energy Expressions</b>
3.1	Introduction
3.2	Band and Bond Energies
3.3	The Tight–Binding Approximation
3.4	The Chemical Pseudopotential Method
3.5	The Total and the Binding Energies
3.6	Conclusions



<b>Chapter 4.</b>	<b>Structural Stability of the sp-Bonded Elements</b>
4.1	Introduction
4.2	The Model
4.3	Structures Considered
4.4	Computational Details
4.4.1	Convergence with the Number of Levels
4.4.2	The $pp\pi/pp\sigma$ ratio
4.4.3	The Second Neighbours in the bcc Lattice
4.5	Results
4.6	Conclusions
<b>Chapter 5.</b>	<b>Interpretation in Terms of the Moments</b>
5.1	Introduction
5.2	Structural Stability and Moments
5.3	Stability of the Close Packed Structures
5.4	Stability amongst the Open Structures
5.4.1	The Single s-Orbital Case
5.4.2	The Pure p Case
5.4.3	The Hybrid sp Case ( $\epsilon_{sp} = 0$ )
5.5	Conclusion

## Chapter 6. The sp-Bonded AB Compounds

- 6.1 Introduction
- 6.2 Setting up the Problem
  - 6.2.1 Structure Types
  - 6.2.2 Parameters Involved
- 6.3 Results for  $h_{pp} \propto h_{\text{bond}}^2$
- 6.4 Results for  $h_{pp} \propto 1/R^5$
- 6.5 Conclusions

## Appendices

- I. Levels, Moments and Notation
- II. Turchi's Termination
- III. Assumptions for the sp Model
- IV. LCAO Solution for the Dimer (Pure s, Pure p and sp)
- V. LCAO Solution for the Dimer (Pure d and sd)
- VI. LCAO Solution for the Linear Chain (Pure cases: s, p and d)
- VII. Experimental Tables
- VIII. Dimer Approximated to a Fixed Number of Moments
- IX. The Double Band Gap
- X. Fourth Moment for Zig-Zag type of Path
- XI. Moments of  $\Delta E_{\text{band}}$  at Constant Band Filling
- XII. DOS for the AB Compounds ( $\epsilon_{sp}^A = \epsilon_{sp}^B = 0$ )
- XIII. DOS for the AB Compounds ( $\epsilon_{sp}^A = \epsilon_{sp}^B = -0.5$ )
- XIV. DOS for the AB Compounds ( $\epsilon_{sp}^A = \epsilon_{sp}^B = -1$ )
- XV. Results for the Transition Metals

## References

## CHAPTER 1: Introduction

A large amount of information on crystal structures has been collected (Villars and Calvert 1985) since the discovery of X-ray diffraction in 1912 by Friedrich, Knipping and Laue. The ordering of this data within the so called structure maps started thirty years ago (Mooser and Pearson 1959) but still is an unfinished matter. The problem is to find an optimum set of coordinates that leads to a good separation scheme among the known structure types (Villars and Calvert op. cit.). Using a combination of s and p radii proposed by Simons and Bloch (1973), Zunger and Cohen (1978, 1979) were able to achieve a good separation among three basic structures (ZnS, NaCl and CsCl) of non-transition AB octet compounds. In a later work Zunger (1980) extended their work to include transition elements in the first attempt to order all the AB structure types.

Other coordinates have been proposed to achieve separation for a given stoichiometry  $A_mB_n$ , namely, the electronegativity difference, the atomic size difference and the average number of electrons per atom (Villars 1983, 1984 and 1985) thus leading to three dimensional structure maps. Despite the large number of two dimensional maps (sixteen altogether, one for each value of the average number of valence electrons) used to separate the stoichiometry AB, the structure of NiAs was not separated. Moreover the scheme does not separate the elements because both the electronegativity difference and the atomic size difference are equal to zero when  $A = B$ . The coordinate left, i.e., the valence, obviously is not enough to characterize uniquely the elements.

A *phenomenological* scale that assigns a unique value to each atomic element was proposed by Pettifor (1986a, 1986b and 1988). This single coordinate

is obtained by running a string through the elements in the periodic table such that it leads to a good separation of the different binary systems in two dimensions. Such a scale is called the Mendeleev number by the author. A single two dimensional map is then shown to be necessary to give a good structural separation of all binary systems with a given stoichiometry  $A_mB_n$ .

In contrast with the phenomenological approach there are the *first principle* calculations performed within the density functional formalism (Hohenberg and Hohn 1964 and Kohn and Sham 1965). This theory implemented with the local density approximation (LDA) in order to handle the exchange and correlation contributions to the total energy, has shown to be able to account for the small differences involved in the calculations of structural energy differences (of the order of a few milli Ry). Since the last decade it has been used in a considerable number of applications not only for elemental systems (see, e.g., Yin and Cohen 1980, 1981 and Chang and Cohen 1985) but also for binary compounds (e.g. Froyen and Cohen 1983, 1984 and Ho et al 1984). The theory seems to be able to cope successfully with metallic, covalent and ionic systems for which the charge density displays such different behaviours, i.e., slowly varying, directional along the bond and whole amount of charge being transferred to selected sites in the structural arrangement. These ab-initio calculations have no arbitrary parameters, needing only the atomic number of the constituent elements and the crystal structure as input. An one-electron Schrödinger equation governs the electronic motion and thus the results can be interpreted within a band framework.

The LDA approach is undoubtedly a very powerful tool for the calculation of the structural properties of solids. It is however time consuming and physical insight is difficult. The most stable arrangement out of a given set of crystal structures can be found but the reason as to the relative stability delivered

by the theory is often hidden from the human mind. On the other hand the phenomenological structure maps can not provide any explanation as to the physical origins of the structural stability regions. Conclusions here are often cause of controversy. For example Zunger (1980) achieved a great success in separating transition element AB compounds using only s and p pseudo-potential radii as coordinates. Since no d pseudo-potential radii were used in the structure maps the conclusion was drawn that d orbitals were not relevant for structural stability. However these orbitals were shown to be necessary in quantum mechanical tight-binding calculations for the prediction of the relative structural stability amongst the pd-bonded AB compounds (Pettifor and Podloucky 1985, 1986).

This thesis is devoted to the study of relative structural stability amongst the sp-bonded elemental systems and AB compounds. To this end, a quantum mechanical tight-binding model of cohesion is employed to compare the binding energies of structures whose coordination range from 1 for the dimers, through 4 for the diamond lattice to 12 for the close packed arrangements. The hopping integrals (Slater and Koster 1954) are chosen to scale as the inverse of the square of the bond length (Harrison 1980) and the binding (or cohesive) energy  $E_b$  is written in accordance to the tight-binding bond model (TBB) of Sutton et al (1988). In this model  $E_b$  is written as a sum of three terms, namely, a bond term  $E_{\text{bond}}$ , a repulsive (sum of pair potentials) term  $E_{\text{rep}}$  and a promotion energy term  $E_{\text{pr}}$  (see also Ducastelle 1970). This can be justified within LDF theory by approximating the ground state charge density by a sum of overlapping atomic charge densities (Harris 1985 and Foulkes 1987).

The usual problem in comparing band energies directly is the determination of the volumes (or the bond lengths) at which the energies of the different arrangements are going to be evaluated. This problem can be

circumvented in the case of the close packed structures like fcc, hcp and bcc. Because of the small change in volume among these arrangements the calculations can be made at fixed volume (Pettifor 1983, MacMahan and Moriarty 1982 and Duthie and Pettifor 1977). However the relative stability of, say, the open tetrahedrally bonded diamond lattice and close packed fcc can not be obtained by comparing their binding energy at fixed volume because there may be large changes in volume between them.

In this work the changes in volume are taken into account via the use of the structural energy difference theorem (Pettifor 1986b). According to this theorem the energy difference between two structures in equilibrium is given, to first order in  $\Delta E_b/E_b$ , by the difference in their bond energies provided that the volumes (or the bond lengths) have been prepared to show the same repulsive energy, i.e.,  $\Delta E_{rep} = 0$ . The binding energy difference is then given by the difference in the promotion plus bond energies for any two structures. In chapter 4 it is shown that this can be written as a difference in the band energy provided that the atomic s and p energy levels are kept fixed as one goes from one structure to another.

This is the model that shall be used in the study of the sp-bonded systems referred to above. Special attention is paid to the elements for which the moments  $\mu_n$  of the local density of states (Ducastelle and Cyrot-Lackmann 1970, 1971) are used in the interpretation of the results. The  $\mu_n$  can be written as a sum of all possible lattice paths of length  $n$  that start and finish at the site of interest, i.e.,  $\mu_n = \langle i | H^n | i \rangle$  where  $i$  labels the site assuming only one orbital per site (Cyrot-Lackmann 1967). As we shall see, if the repulsive pair potentials vary as the square of the bond integrals, the condition  $\Delta E_{rep} = 0$  is equivalent to  $\Delta \mu_2 = 0$ . Then, as long as the ratio between the hopping integrals are kept

unchanged, the results delivered by the model are fairly general and not dependent upon the particular  $R$  dependence of the hopping or bond integrals. This is shown in appendix III.

The calculation of the band energy and related quantities will be carried out in real space. This is in contrast with reciprocal space calculations upon which traditional electronic structure has been based. These require the use of Bloch's theorem (Ashcroft and Mermin 1976) with infinite lattice periodicity as a basic assumption. All geometric arrangements in this thesis are endowed with translational symmetry but  $k$  space calculations are not suitable for our purposes which will require a direct relation between the band energy and local topology. Due to the infinitely extended nature of the Bloch functions, the  $k$  space calculation of, say, the second moment of the local DOS involves summing over all atoms in the solid, or, in other words, over all points in the first Brillouin zone (Heine 1980). In real space this can easily be performed analytically.

The real space method used for the computation of the local densities of states in this thesis is the recursion method of Haydock et al (1972, 1975). This method generates an infinite continued fraction which is terminated after a certain number of levels. Both the method and the termination of the continued fraction used here are discussed in chapter 2. In chapter 3 the energies involved in the relative structural stability studies undertaken in this work are discussed along with the basics of the tight-binding method. The investigation on the structural trends amongst the  $sp$ -bonded elements is the subject of chapter 4. A total of ten structures is considered with a large range of coordination. In chapter 5 a physical explanation will be provided for the trends obtained in chapter 4. To this end the moments of the local density of states are used because of the immediate connection with local topology provided by these quantities. The  $sp$ -bonded AB

binary compounds are considered in chapter 6. A straightforward extension of the model used for the elements is then employed. The theoretical predictions are compared with the experimental trends which are summarized in the structural maps drawn with the use of Pettifor's Mendeleev number (op.cit.). The model is shown to be capable of providing results which are in qualitative agreement with the observed experimental trends for these compounds. Some calculations are also performed for the transition metal elements which are presented in appendix XV.



## CHAPTER 2: Numerical Methods

This chapter presents the numerical techniques used throughout the rest of this work. Attention is focused on those aspects of the subject which are felt to be important for the development of subsequent chapters. The recursion method and the moments method are briefly reviewed along with two basic termination procedures for the reconstruction of the density of states from the calculated recursion coefficients. These are the constant and the Turchi, Duscastelle and Trégliat's (TDT) terminations (Turchi et al 1982). The constant or square root termination is appropriate to connected bands whereas the TDT termination is applicable when band gaps are present in the spectrum. In both cases the knowledge of the band edges (and gap edges, if applicable) is required. In this work such parameters are determined using the optimization procedures developed by Beer and Pettifor (Beer and Pettifor 1984, Beer 1985). The optimization procedure works well for the connected spectrum but its extension to the treatment of a single band gap presents a series of difficulties. We show that such complications can be smoothed out to a reasonable extent by ensuring that the recursion coefficients are kept within certain upper and lower bounds defined by the band and gap edges.

## §2.1 Introduction

The recursion method (Haydock et al 1972, 1975, 1980, Heine 1980) is a numerical technique generally used for calculating densities of states (DOS) projected on a chosen starting state, with the Hamiltonian  $\mathcal{H}$  being expressed in terms of a local orbital basis set. No assumptions about symmetry are required which makes the method useful not only in the description of crystalline materials but also in situations when there is little or no periodicity available. One must specify an initial-state vector  $|\alpha\rangle$  on whose projection the DOS is to be calculated. By means of a three-term recurrence relation the recursion method then sets up a new basis in terms of which the Hamiltonian has a tridiagonal representation  $H_{td}$ . The matrix elements of  $H_{td}$  are the so called recursion coefficients. Provided that  $|\alpha\rangle$  remains the first orbital in the new basis (say  $|u_0\rangle$ ), then via the use of the recurrence relation, extended orbitals ( $|u_1\rangle, |u_2\rangle, \dots$ ) are generated which spread out (over the 1st, 2nd,  $\dots$  shells) further and further away from  $|u_0\rangle$ . Given  $H_{td}$  it is easy to construct  $G_{00}(E)$ , the diagonal matrix element of the Green's function - formally the Green's function is defined as the operator  $(E - \mathcal{H})^{-1}$  - whose imaginary part gives the projected DOS. In terms of the recursion coefficients  $G_{00}(E)$  is then expressed as a continued fraction which, for an infinite system, has an infinite number of levels resulting from the fact that the tridiagonal basis set have an infinite number of elements. The knowledge of an extra level in the continued fraction requires the addition of an extra level in the cluster, which becomes more and more expensive, computationally speaking, as higher and higher levels are involved. In a realistic calculation one is then limited by the finite size of the cluster. Typically a few thousands atoms allow about 10-20 recursion levels to be computed exactly - but about 5 or 6 levels (Beer 1985) are enough for the convergence of integrated

quantities over the density of states. A much larger number of levels may be needed (Anlage 1986, Woodruff 1987) if one is interested, say, in the fine details of the density of states. Limiting the infinite number of levels to a finite number, forces us to approximate the unknown infinite tail of the continued fraction. The simplest approach seems to consist in reproducing the asymptotic behaviour of that tail by an analytic expression - a terminator - which is introduced at the last known level in the continued fraction. The knowledge of the terminator together with its parameters completes the picture and allows the computation of the DOS.

In the next section we give a brief description on the recursion method for the computation of projected local densities of states (DOS). Much has already been said about this method (e.g. Pettifor and Weaire 1985), but a short review here is necessary as it is needed in other parts of this work. The interested reader should refer to Heine (1980) and Haydock (1980) for a more detailed and comprehensive review of the subject. The moments method is presented in section 2.3. The problem of approximating the infinite tail of the continued fraction is the subject of section 2.4. Here both the square root (SQ) or constant termination, appropriate for the description of a connected spectra, and the Turchi, Ducastelle and Tréglià (TDT) terminator, appropriate for dealing with the presence of gaps in the DOS, are discussed. In section 2.5 we conclude.

## §2.2 The Local Density of States and the Recursion Method

The starting point is the time independent Schrödinger equation

$$\mathcal{H} \psi_n = E_n \psi_n \quad (2.1)$$

in which  $\mathcal{H}$  is the Hamiltonian,  $\psi_n$  is a member of a complete set of orthonormal eigenfunctions  $\{\psi_n\}$  with corresponding eigenvalues  $\{E_n\}$ . In the coordinate representation (e.g. Merzbacher 1970) the eigenstate  $\psi_n \equiv |n\rangle$  can be expanded as  $\int |\mathbf{x}\rangle d\mathbf{x} \langle \mathbf{x}|n\rangle$  and we write  $\psi_n(\mathbf{x}) = \langle \mathbf{x}|n\rangle$ . Much of the information about the system is provided by the local density of states (LDOS or DOS for short)

$$n(\mathbf{E}, \mathbf{x}) = \sum_n |\psi_n(\mathbf{x})|^2 \delta(\mathbf{E} - E_n) \quad (2.2)$$

introduced by Friedel to study electronic structure in the absence of perfect periodicity (Friedel 1954). A given spin direction must be understood. Since we will always be working with spin degenerate states  $n(\mathbf{E}, \mathbf{x})$  must be multiplied by 2 at the end of the calculations. This expression involves the knowledge of the extended eigenstates of the Hamiltonian. One can avoid having to solve for the eigenfunctions of the Schrödinger equation by writing  $n(\mathbf{E}, \mathbf{x})$  in terms of the Green function. If one writes the delta function as (Kittel 1985)

$$\delta(\mathbf{E} - z) = -\frac{1}{\pi} \lim_{\epsilon \rightarrow 0} \mathcal{Jm} \frac{1}{\mathbf{E} - z + i\epsilon} \quad (2.3)$$

the DOS can be written as

$$n(E, \mathbf{x}) = -\frac{1}{\pi} \mathcal{I}m \sum_n \langle \mathbf{x} | n \rangle \frac{1}{E - E_n + i\epsilon} \langle n | \mathbf{x} \rangle. \quad (2.4)$$

where the  $\lim \epsilon \rightarrow 0^+$  is assumed. Since the operator in an eigenvalue equation like  $\mathcal{H}|n\rangle = E_n|n\rangle$  can be written as

$$\mathcal{H} = \sum_n |n\rangle E_n \langle n| \quad (2.5)$$

the DOS can be finally put in its usual form

$$n(E, \mathbf{x}) = -\frac{1}{\pi} \mathcal{I}m \langle \mathbf{x} | \frac{1}{E - \mathcal{H} + i\epsilon} | \mathbf{x} \rangle \quad (2.6)$$

$$= -\frac{1}{\pi} \mathcal{I}m G(\mathbf{x}, \mathbf{x}, E + i\epsilon) \quad (2.7)$$

The Green function on the right hand side of this equation is generally expressed as  $G(\mathbf{x}, \mathbf{x}', E) = \langle \mathbf{x} | (E - \mathcal{H})^{-1} | \mathbf{x}' \rangle$  (Haydock et al 1972).

In this work we will be dealing exclusively with a tight-binding Hamiltonian. One considers a localized (atomic-like) set of basis functions  $\varphi_{i\alpha}(\mathbf{x}) = \langle \mathbf{x} | i\alpha \rangle$  centred on sites  $i$  with orbital index  $\alpha$ . The eigenstates  $\psi_n(\mathbf{x})$  are then expanded in terms of a linear combination of atomic-like orbitals (LCAO), i.e.,

$$\psi_n(\mathbf{x}) = \sum_{i\alpha} a_{n,i\alpha} \varphi_{i\alpha}(\mathbf{x}) \quad (2.8)$$

or simply

$$|n\rangle = \sum_{i\alpha} |i\alpha\rangle \langle i\alpha|n\rangle. \quad (2.9)$$

Inserting  $\psi_n(\mathbf{x})$  back into the Schrödinger equation and integrating over  $\mathbf{x}$  after multiplying by  $\varphi_{j\beta}^*(\mathbf{x})$  one has

$$\sum_{i\alpha} [H_{j\beta, i\alpha} - E_n S_{j\beta, i\alpha}] a_{n, i\alpha} = 0 \quad (2.10a)$$

or simply

$$(H - E_n S) a_n = 0 \quad (2.10b)$$

The Hamiltonian is now given as a matrix whose elements are the on site energies and hopping integrals  $H_{j\beta, i\alpha} = \langle j\beta | H | i\alpha \rangle$  (Slater and Koster 1954)

$$\langle j\beta | H | i\alpha \rangle = \int \langle j\beta | \mathbf{x} \rangle H \langle \mathbf{x} | i\alpha \rangle d\mathbf{x} \quad (2.11)$$

The entries in the column vector  $a_n$  are the amplitudes of the eigenfunctions  $\psi_n(\mathbf{x})$  on the  $i\alpha$  basis, namely,  $a_{n, i\alpha}$ . The overlap matrix elements  $S_{j\beta, i\alpha} = \langle j\beta | S | i\alpha \rangle$  are given by

$$\langle j\beta | S | i\alpha \rangle = \int \langle j\beta | \mathbf{x} \rangle \langle \mathbf{x} | i\alpha \rangle d\mathbf{x} \quad (2.12)$$

and they appear because  $i\alpha$  is not, in general an orthogonal basis. Nevertheless we shall always assume it to be so. In fact we will assume that  $\langle j\beta | S | i\alpha \rangle = \delta_{ij} \delta_{\alpha\beta}$ , which becomes the first approximation in our model. Should we carry on with the assumption of nonorthogonality, then the overlap matrix would have to be included in the definition of the Green's function (Williams et al 1982; see also Bullett 1975, 1980). The recursion method can properly take nonorthogonality into

account as in Haydock (1980).

In terms of the local basis,  $n(E, \mathbf{x})$  reads

$$n(E, \mathbf{x}) = \sum_{n, j\beta, i\alpha} \delta(E - E_n) a_{n, j\beta}^* a_{n, i\alpha} \varphi_{j\beta}^*(\mathbf{x}) \varphi_{i\alpha}(\mathbf{x}) \quad (2.13)$$

and therefore, assuming orthonormality, the total DOS  $n(E) = \int n(E, \mathbf{x}) d\mathbf{x}$  is

$$n(E) = \sum_n \sum_{i\alpha} |a_{n, i\alpha}|^2 \delta(E - E_n) \quad (2.14)$$

$$= \sum_n n_{i\alpha}(E) \quad (2.15)$$

The right hand side of this expression defines the local density of states  $n_{i\alpha}$  in terms of the local basis  $i\alpha$ . Following the same lines as before and using  $a_{n, i\alpha} = \langle i\alpha | n \rangle$  we have

$$\begin{aligned} n_{i\alpha}(E) &= -\frac{1}{\pi} \mathcal{I}m \sum_n \langle i\alpha | n \rangle \frac{1}{E - E_n + i\epsilon} \langle n | i\alpha \rangle \\ &= -\frac{1}{\pi} \mathcal{I}m \langle i\alpha | \frac{1}{E - \mathcal{H} + i\epsilon} | i\alpha \rangle \end{aligned} \quad (2.16)$$

where the last equality follows from (2.5). Therefore

$$n_{i\alpha}(E) = -\frac{1}{\pi} \mathcal{I}m G_{i\alpha, i\alpha}(E^+) \quad (2.17)$$

where by  $E^+$  here is understood  $E + i\epsilon$  and the limit  $\epsilon \rightarrow 0$  is implied. Unless confusion may arise this limit will be understood but not explicitly written in the

relevant equations involving the Green function. We shall also drop the plus sign in the argument. We then see that only the diagonal matrix element of  $(E - H)^{-1}$  corresponding to  $|\alpha\rangle$  is required for the calculation of the density of states.

The diagonal Green's function matrix element  $G_{i\alpha, i\alpha}(E) = \langle i\alpha | (E - H)^{-1} | i\alpha \rangle$ , necessary for the calculation of the DOS, will be frequently called  $G_{i\alpha}(E)$  for short. The recursion method (Haydock et al 1972, 1975, Haydock 1980) is a technique developed for the computation of this quantity. It is ideally suited for the calculation of Green's function matrix elements between localized states close to each other in real space, as will become clear below. The basic idea is to construct an orthonormal basis set,  $\{ |u_n\rangle \}$ ,  $n = 0, 1, 2, \dots$ , which is built up in an ordered fashion so that the Hamiltonian becomes tridiagonal. For the local density of states projected on the localized orbital  $|\alpha\rangle$  one takes the first vector in the new basis,  $|u_0\rangle$ , such that  $|u_0\rangle = |\alpha\rangle$ . The Green's function element in (2.16) is then

$$G_{00}(E) = \langle u_0 | (E - H)^{-1} | u_0 \rangle \quad (2.18)$$

and we shall call  $n_0(E)$  the corresponding local DOS. The other elements of the tridiagonal basis are obtained by describing the operation of the Hamiltonian on  $|u_n\rangle$  via a three term recurrence relation, namely

$$H|u_n\rangle = a_n|u_n\rangle + b_{n+1}|u_{n+1}\rangle + b_n|u_{n-1}\rangle \quad (2.19)$$

where  $\{a_0, a_1, \dots\}$  and  $\{b_0, b_1, \dots\}$  are numerical constants. The recurrence is then initialized by defining  $|u_{-1}\rangle = 0$  and  $b_0^2 = \langle u_0 | u_0 \rangle$ . From orthonormality one gets  $a_0 = \langle u_0 | H | u_0 \rangle$ . Therefore  $b_1 |u_1\rangle = (H - a_0) |u_0\rangle$  and use of the normalization condition,  $\langle u_1 | u_1 \rangle = 1$ , gives  $b_1^2 = \langle u_0 | (H - a_0)^\dagger (H - a_0) | u_0 \rangle$ , where  $(\dagger)$  indicates adjoint operation. In this context in which the linear atomic



basis is assumed orthogonal,  $H$  is self-adjoint and the adjoint operation is unnecessary. It would be necessary however if orthogonality had not been assumed from the outset, in which case the overlap matrix would also have to be included (Haydock, 1980). Taking  $b_1$  as the positive square root of  $b_1^2$  one finally gets the second vector in the new set, i.e.,

$$|u_1\rangle = [(H - a_0)/b_1]|u_0\rangle. \quad (2.20)$$

The recurrence then proceeds by making use of the recurrence relation for  $n = 1$ . The other coefficients are obtained by orthogonalising  $|u_{n+1}\rangle$  with respect to  $|u_n\rangle$  and  $|u_{n-1}\rangle$ . Adding the normalization condition  $\langle u_n|u_n\rangle = 1$ , one gets

$$a_n = \langle u_n|H|u_n\rangle \quad (2.21a)$$

and

$$b_{n+1} = \langle u_{n+1}|H|u_n\rangle \quad (2.21b)$$

Therefore  $|u_{n+1}\rangle$  is orthogonal to  $|u_n\rangle$  and  $|u_{n-1}\rangle$  by construction. Moreover, it can be shown that it is also orthogonal to all  $|u_m\rangle$ ,  $m = 0, 1 \dots n-1$  (Haydock 1980). The matrix representation of the Hamiltonian in the new basis is therefore a tridiagonal matrix (or Jacobi or J matrix)

$$H_{td} = \begin{bmatrix} a_0 & b_1 & 0 & 0 & \dots \\ b_1 & a_1 & b_2 & 0 & \\ 0 & b_2 & a_2 & b_3 & \\ 0 & 0 & b_3 & a_3 & \\ \vdots & & & & \ddots \\ \vdots & & & & & \ddots \\ \vdots & & & & & & \ddots \end{bmatrix}. \quad (2.22)$$

Before we go back to the calculation of the density of states let's say a few words

about the simple physical picture we have been led to by the change of basis. The Hamiltonian matrix above is easily seen to describe a semi-infinite chain system (the chain model) like the one in figure 2.1. The orbitals (i.e., the tridiagonal basis vectors) sit on the vertices of the chain and the a's and b's parameters represent the on-site energies and intersite couplings respectively. Following Haydock (1980, page 224) the system can be interpreted as having an initial state  $|u_0\rangle$ , other states being reached by hopping through the closest neighbouring sites. In this way  $|u_n\rangle$  influences the central site more than  $|u_{n+1}\rangle$ , and this more than  $|u_{n+2}\rangle$ , and so on. This interpretation fits nicely within the concept of a local environment (Heine 1980) in which distant parts of the physical system contribute to local phenomena less than the nearer ones.

The Green function matrix element relevant to the DOS is the first element of the matrix  $(EI - H_{td})^{-1}$ . Using standard matrix algebra it can be expanded in terms of a continued fraction (Haydock et al 1975), i.e.,

$$G_{00}(E) = \frac{b_0^2}{E - a_0 - \frac{b_1^2}{E - a_1 - \dots}} \quad (2.23)$$

The leading numerator in this expression (i.e.,  $b_0^2$ ) gives the area under the curve of the DOS, representing the total number of electrons associated with the orbital  $|u_0\rangle$  as shall be seen below. Notice that  $b_0$  is dimensionless whilst the other parameters have the dimension of energy.

We have seen that  $|u_1\rangle$  depends essentially on the action of the Hamiltonian over  $|u_0\rangle$ . If this orbital is localized on, say, a central site of a given

cluster of atoms (see figure 2.1), and connected to its near neighbour environment via the Hamiltonian, then  $|u_1\rangle$  is an orbital that spreads over these neighbours. Further iterations will generate orbitals reaching parts of the cluster more and more distant from the central atom. Since the local density of states on the central site is expected to depend less and less on the higher order iterations, the deep levels in the continued fraction are not expected to be important in the determination of the DOS. The  $n$ th level is the region of the cluster covered by  $|u_n\rangle$  but not reached by  $|u_{n-1}\rangle$ . The number of atoms in a given level depends both on the cluster and on the Hamiltonian. The atoms in the first level for instance, are the closest neighbours of the central atom if only nearest neighbours hoppings are allowed by  $H$ . But the second neighbours must also be counted if the Hamiltonian includes second neighbours couplings. A formal definition could be : " the  $n$ th level contains the atoms that can be reached by a minimum of  $n$  hops from the origin ". Naturally the "size" of the hop is defined by the Hamiltonian.

We have gone through a thorough definition of these concepts here because they will be important later on for interpreting the sp structural stability trends in terms of the local topology of the structures considered.

The recursion method has been referred to as a technique for the computation of diagonal elements of the Green's function. However one might also require the off-diagonal parts, as for the calculation of bond orders (Kelly 1980 p302) or charge densities (Jones 1985). These can still be calculated within the recursion method in its original form, by starting off with symmetric and antisymmetric combinations of the vectors on the two neighbouring sites of interest. The Green's function element between the two sites can be shown to be proportional to  $G_+(E) - G_-(E)$  where  $G_{\pm}(E)$  are the diagonal elements corresponding to symmetric and antisymmetric combinations (Kelly op.cit, Glanville et al 1988). A matrix recursion algorithm allowing direct calculation of off diagonal Green's functions elements was developed by Jones and Lewis (1984)

which is known as Block Recursion. In this approach the coefficients are given as matrices and the Hamiltonian is made block tridiagonal by the change of basis. As showed latter by Inoue and Ohta (1987), block recursion also corrects an anomaly in the (scalar) recursion method, namely the non-invariance of the Green function (if calculated to a few levels) to cluster rotation. We shall only be interested in the recursion method for calculating densities of states. Since we are not interested in the off diagonal elements of the Green function in this thesis, all we need is the traditional scalar algorithm with clusters accurate to about ten levels. Therefore there is no need to discuss block recursion any further and the interested reader is referred to the above references for further information.

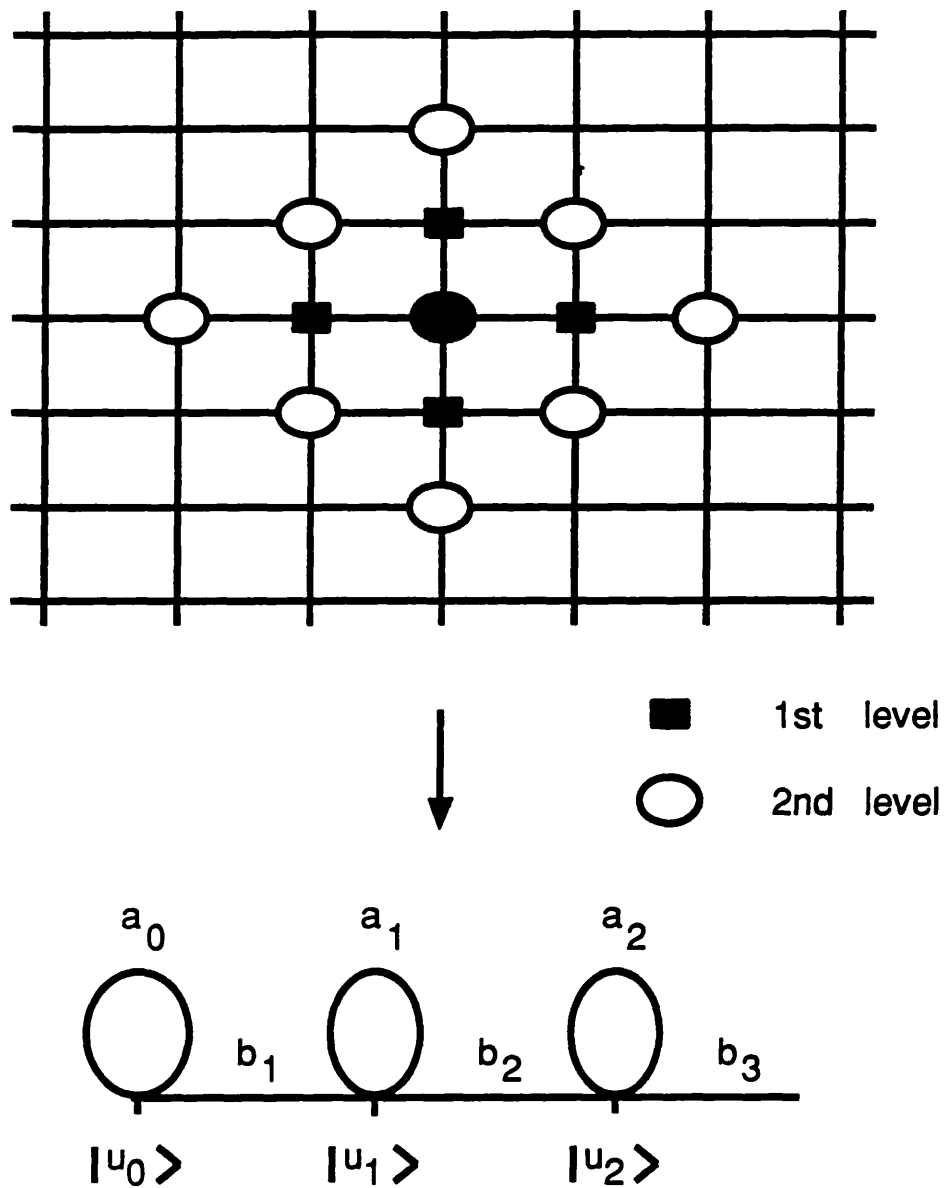


Figure 2.1

Mapping a given structure onto a semi-infinite chain. The central atom is mapped onto the starting atom in the chain, the atoms on the first level onto the 2nd atom in the chain, the atoms on the 2nd level onto the 3rd and so on. Notice the presence of 3rd neighbours among the atoms in the 2nd level.

### §2.3 The Method of the Moments

The problem of finding a bounded and nondecreasing function  $N_0(z)$  in the interval  $(-\infty, +\infty)$  such that

$$\mu_n = \int_{-\infty}^{+\infty} z^n dN_0(z), \quad n = 0, 1, 2 \dots \quad (2.24)$$

for a given set  $\{\mu_n\}$  is called the moments problem (Shohat and Tamarkin 1943, Wall 1948, Jones and Thron 1980). For a given sequence  $\{\mu_n\}$ , a solution to this problem exists if and only if to an infinite continued fraction corresponds a power series expansion in descending powers of  $E$  in which the coefficients are given by  $\mu_n$ , i.e.,

$$G_{00}(E) = \sum_{n=0}^{\infty} \frac{\mu_n}{E^{n+1}}. \quad (2.25)$$

It also turns out (Wall 1948, chapter XVII) that the solutions are such that

$$G_{00}(E) = \int_{-\infty}^{+\infty} \frac{dN_0(z)}{E - z} \quad (2.26)$$

is another form for the continued fraction. One can arrive at this form by considering the following expression for the matrix element of a function  $F(H)$  (Magnus 1985, Paxton 1987),

$$[F(H)]_{mn} = \int_{\Sigma} F(E) P_m(E) P_n(E) dN_0(E) \quad (2.27)$$

where  $\Sigma$  is the set of points on the real axis such that  $N_0(E)$  is an increasing function of  $E$  (the support of  $N_0$ ) and

$$N_0(E) = \int^E n_0(z) dz \quad (2.28)$$

where  $n_0(z)$  is the local density of states. The polynomials  $P_k(E)$  are such that  $|u_k\rangle = P_k(H)|u_0\rangle$ , i.e.,  $P_0(H) = 1$  (the unit matrix),  $P_1(H) = (H-a_0)/b_1$ , etc. The expression above for  $G_{00}$  is obtained by taking  $F(E) = (z-E)^{-1}$  and  $m=n=0$ .

The set of constants  $\{\mu_n\}$  appearing in the moments problem are called moments, after Stieltjes (see, e.g., Shohat and Tamarkin 1943). In this context they are the moments of the local density of states (Ducastelle and Cyrot-Lackmann 1970, 1971) given by

$$\mu_n = \int_{-\infty}^{+\infty} E^n n_0(E) dE \quad (2.29)$$

In the local orbital basis the moments can be expressed in terms of the diagonal matrix elements of powers of the Hamiltonian (Cyrot-Lackmann 1967, Heine 1980 page 80), i.e.,

$$\mu_n^{i\alpha} = \langle i\alpha | H^n | i\alpha \rangle \quad (2.30)$$

for the particular case of the orbital of type  $\alpha$  at site  $R_i$ . If one writes this expression as

$$\mu_n^{i\alpha} = \sum_{i_1 \alpha_1} \sum_{i_2 \alpha_2} \langle i\alpha | H | i_1 \alpha_1 \rangle \langle i_1 \alpha_1 | H | i_2 \alpha_2 \rangle \langle i_2 \alpha_2 | H \cdots H | i\alpha \rangle \quad (2.31)$$

it can be interpreted as a "sum over all possible paths of length  $n$  starting and finishing at  $|i\alpha\rangle$ ". The moments are therefore made up of paths on the cluster which are essentially hoppings from site to site (notice that on-site hoppings are also allowed). Only closed paths are seen to contribute. If one calls  $|u_0\rangle = |i\alpha\rangle$  as before and drop the superscript  $i\alpha$  in the notation of the moments, one notices that  $\mu_0 = \langle u_0 | u_0 \rangle$ . This gives the area under the curve  $n_0(E)$  and is equal to  $b_0^2$ .

There is more than one way one can obtain the moments from the coefficients  $\{a_n, b_n^2\}$  generated by the recursion method. The continued fraction can be expanded into a power series (Wall 1948 p203, Beer 1985 p22) in which the coefficients of the expansion are given in terms of the  $a$ 's and  $b^2$ 's. Direct comparison with (2.25) then gives  $\mu_n$ . One can also generate  $\{a_n, b_n^2\}$  using the recursion algorithm with  $|u_0\rangle = |i\alpha\rangle$  and then use (2.30) to write

$$\mu_n = [H^n]_{00} \quad (2.32)$$

which is advantageous from the computational point of view. But perhaps the easiest way to get the first few moments in terms of the coefficients is to use the path counting procedure on the chain model. Apart from  $\mu_0$  which is given by the normalization factor  $b_0^2 = \langle u_0 | u_0 \rangle$ , one can easily see that

$$\begin{aligned} \mu_0 &= b_0^2 \\ \mu_1 &= a_0 \\ \mu_2 &= a_0^2 + b_1^2 \\ \mu_3 &= a_0^3 + 2a_0 b_1^2 + a_1 b_1^2 \end{aligned} \quad (2.33)$$



Coefficients can also be calculated from the moments. The conversion procedure involves the determinants of matrices constructed from the  $\{\mu_n\}$  (Gaspard and Lambin 1985). Unfortunately, however, it is numerically ill-conditioned if the number of levels involved is relatively large (Kelly 1980, Blumstein and Wheeler 1973). Multiple precision arithmetics is required to obtain coefficients for  $n$  typically larger than 15 (Gaspard and Lambin 1985). Beer (1985 p23) used a recursive algorithm which allowed the calculation of about 20–25 pairs of coefficients (see also Gordon 1968). The root of the problem rests on the nonlinear character of the relationship between  $\{\mu_n\}$  and  $\{a_n, b_n^2\}$  (cf (2.31) and (2.32)) aggravated by the rapid increase of  $\mu_n$  with  $n$ .

The numerical instability of the transformation  $\{\mu_n\} \rightarrow \{a_n, b_n^2\}$  is the basic difficulty with the method of moments for the calculation of DOS. On the other hand if one tries to bypass the continued fraction stage one also runs into difficulties. The numerical computation of a density of states directly from the moments also requires too much computing accuracy and might also lead to hermiticity problems (Haydock 1980). One should mention that a generalized moments method has been proposed to make the transformation  $\{\mu_n^g\} \rightarrow \{a_n, b_n^2\}$  ( $g \rightarrow$  generalized) well defined. This however has been argued to be equivalent to going back to the recursion method (Haydock 1980 p290). For the generalized moments method see Gaspard and Lambin 1985.

In this work the recursion method will be the sole approach used for the calculation of densities of states. However, for explaining the predicted structural trends, the first few moments of the local DOS will be extensively used.

In the following chapters we will mention the number of exact moments used in the calculations. This is directly related to the size of the cluster used to simulate the bulk crystal. This so because the cluster must be of sufficient size to allow all possible paths contributing to a given  $\mu_n$  to be calculated. Unless stated

otherwise, the 0th moment will always be included in the counting. Appendix I shows how the counting is made besides defining the terminology and notation (which varies from author to author) used hereafter.

Before we leave this section let us mention a simple but very useful exact result, now referred in the literature as Ducastelle and Cyrot-Lackmann's theorem (1971). Let's consider a function  $f_0(x)$  which is non-zero and continuous in almost all the interval  $[a,b]$  with

$$f_0(a) = f_0(b) = 0$$

and its moments being defined by

$$\mu_p = \int_a^b x^p f_0(x) dx$$

If  $\mu_p = 0$  for  $p = 0, 1, \dots, n$ , then  $f_0(x)$  has at least  $n + 1$  zeros in the interval  $[a,b]$ , distinct from the ones at  $a$  and  $b$ . Moreover, if

$$f_q(x) = \int_a^x f_{q-1}(x') dx'$$

then  $f_q(x)$  has at least  $n + 1 - q$  roots distinct from  $a$  and  $b$ . The case of interest to us is  $q = 2$  when  $f_2(x)$  represents the structural energy difference for a given  $f_0(x) = n_1(x) - n_2(x)$ ,  $n_i$  being the density of states of structure  $i$ . If the two structures share the first  $n + 1$  moments (i.e.,  $\mu_p = 0$ ,  $p = 0, 1, \dots, n$ ) then  $f_2(x)$  has at least  $n - 1$  zeros in the interval of allowed energies.

## §2.4 Finite and Infinite Continued Fractions

As described, the recursion method is an exact transformation from the local basis  $\{|i\alpha\rangle\}$  to the ordered basis  $\{|u_n\rangle\}$ . The new basis is infinite for the bulk and so is the tridiagonal Hamiltonian. For real applications however, the size of the cluster that can be handled by the computer is finite and the recursion process has to be stopped at some stage. One is then left with a finite dimensional Jacobi matrix which, in the language of the chain model, corresponds to a finite chain. A *truncated* continued fraction is then generated which can be written as (see appendix I)

$$G_{00}^N(E) = (-1)^N \mathcal{K} \left[ \frac{-b_i^2}{E - a_i} \right] . \quad (2.34)$$

It is important to note that orbitals not including surface atoms are not affected by the finiteness of the cluster. In other words if  $N$  levels are kept in the cluster, then the first  $N+1$  pairs of coefficients (see appendix I) will be unaffected the cluster's surface. Such *bulk coefficients* will be called exact.

Truncating the continued fraction as above leads to a density of states consisting of a discrete set of delta functions. This can be seen by writing the starting vector  $|u_0\rangle$  in terms of the eigenfunctions of the Hamiltonian, i.e.,

$$|u_0\rangle = \sum_n \alpha_n |n\rangle . \quad (2.35)$$

The local density of states can then be written as

$$n_0(E) = \sum_{n=0}^{\infty} |\alpha_n|^2 \delta(E-E_n) \quad (2.36)$$

where the  $E_n$  are the eigenvalues of  $H_{td}$ . An approximate (truncated) DOS can be defined by (Nex 1978)

$$n_0^N(E) = \sum_{n=0}^N |\alpha_n^N|^2 \delta(E-\epsilon_n) \quad (2.37)$$

where  $\epsilon_n$  are the eigenvalues of the truncated  $J$ -matrix. The eigenstates  $|n\rangle$  in the subspace generated by  $H_{td}$  and  $|u_0\rangle$  can then be expanded in terms of the tridiagonal basis where the coefficients of the expansion are the polynomials  $P_m(E_n)$  weighted by a function of  $E_n$ . Using the orthonormality of  $|n\rangle$  and  $|u_n\rangle$ , Nex (1978) showed that the weight on the  $n$ th  $\delta$ -function is given by  $[\sum P_n^2(\epsilon_i)]^{-1}$ , where the sum extends up to  $N$ .

The truncated DOS expression given by (2.37) corresponds to expanding  $G_0^N(E)$  into partial fractions, ie

$$G_{00}^N(E) = \sum_{n=0}^N \frac{w_n}{E - \epsilon_n} \quad (2.38)$$

with coefficients  $w_n = |\alpha_n^N|^2$  and eigenvalues  $\epsilon_n$ . The  $\delta$ -functions appear when one takes the  $\lim \delta \rightarrow 0 (E + i\delta)$ . From the representation of the DOS in terms of a discrete set of  $\delta$ -functions one can write

$$\sum_{i=0}^N (\epsilon_i)^n w_i = \mu_n \quad (2.39)$$

which can be used to calculate  $w_i$  and  $\epsilon_i$  ( $n = 0, 1, \dots, 2N-1$ ). This method however is ill-conditioned for large values of  $N$  (Ducastelle and Cyrot-Lackmann 1973).

The discrete set of  $\delta$ -functions does not describe the bulk density of states which is known to consist of a continuum of states. This can only be achieved by allowing the continued fraction to be extended to infinity. Since this can not be done in practice, one must find a way of smoothing the set of  $\delta$ -functions to a continuum curve. In getting a bulk density of states from a cluster calculation, one relies on the fact that the local DOS does not depend much on sites far from the central site of interest. Therefore the information for the smoothness process is, somehow, included in the cluster coefficients.

A most used smoothing procedure is the one known as the gaussian quadrature (GQ) method (Nex 1978). By deriving rigorous upper and lower bounds for the integrated density  $N_0(E)$ , Nex obtains an expression for  $n_0(E)$  by taking the derivative of  $N_0(E)$ . This method has been criticized by Beer and Pettifor (1984) in that it does not preserve those moments which had been calculated exactly. Beer and Pettifor calculated the structural (band) energy as a function of band-filling, for a fcc d-band using canonical parameters. A skew rectangular band, fitted to the first four fcc moments, was used as reference. According to Ducastelle and Cyrot-Lackmann's theorem the resulting structural energy curve should have at least two zeros distinct from those at the bottom and top of the band. The curves presented by Beer and Pettifor (op. cit.) show that the method fails to achieve this requirement. It has been argued later (Paxton 1987 p3.16) that the reason for this failure was due to the reference skew density which was not computed by gaussian quadrature to the same number of levels as the fcc DOS. If this is done, then the errors are canceled in energy difference calculations. Paxton also presents some curves to back up his arguments together with giving a nice review on the GQ method. However, since we are interested in absolute

convergence we will not use this method here.

An alternative to gaussian quadrature consists in appending a terminator which emulates the unknown infinite tail of the continued fraction. The basic difference is that a form for the asymptotic behaviour of the coefficients is now assumed. This is the method we have used which preserves the exact moments we have calculated and the one we describe next.

#### 2.4.1 The Square Root Terminator

Since the early years of the recursion method it has been recognized that for a single band model (continuous or connected band), e.g., for transition metals the coefficients belonging to the deep levels in the continued fraction converge to constant values  $a_\infty, b_\infty$  (Haydock et al 1975, Beer 1985 fig.2.2.2). If one then assumes that convergence has been achieved after, say,  $N$  calculated levels, one may write

$$G_{00}(E) = \frac{b_0^2}{E - a_0 - \frac{b_1^2}{E - a_1 - \frac{b_2^2}{E - a_2 - \dots - \frac{b_L^2}{E - a_L - t(E)}}}} \quad (2.40)$$

where

$$t(E) = \frac{b_\infty^2}{E - a_\infty - \frac{b_\infty^2}{t(E)}} \quad (2.41a)$$

or

$$t(E) = \frac{b_\infty^2}{E - a_\infty - t(E)} \quad (2.41b)$$

This is a quadratic equation that can be solved analytically for  $t(E)$ , which therefore has a square root form. One rejects the plus solution in order to preserve the analytic character of the Green's function as  $E \rightarrow \infty$ . Thus

$$t(E) = 2^{-1} \left[ E - a_\infty - \sqrt{(E - a_\infty)^2 - 4b_\infty^2} \right] \quad (2.42)$$

or, in a more symmetric way

$$t(E) = 2^{-1} \left[ E - \frac{E_t + E_b}{2} - \sqrt{(E - E_t)(E - E_b)} \right] \quad (2.43)$$

where  $E_t = a_\infty + 2b_\infty$  and  $E_b = a_\infty - 2b_\infty$ . One sees that  $a_\infty$  and  $b_\infty$  are the center and the half-width of the band respectively.

This termination is very convenient because the square root provides the necessary branch cut  $[E_b, E_t]$  on the real axis with branch points  $E_b$  and  $E_t$ . Along the cut the imaginary part of  $t(E)$  is finite leading to a band of states. Outside that interval  $\text{Im } t(E) = 0$  thus confining the DOS to  $[E_b, E_t]$ . Isolated  $\delta$ -functions can occur outside the cut if  $\text{Re } t(E)$  changes sign, which happens when the chosen interval  $[E_b, E_t]$  is too small compared to the real one. Notice

that poles are the only kind of singularities of the Green's function that are spotted by the truncated continued fraction. Branch points (giving rise to cuts corresponding to a band of allowed states) and essential singularities (van Hove's singularities) require bulk coefficients (Haydock et al 1975).

One is now left with the problem of determining  $(a_\infty, b_\infty)$ . If the band edges  $E_b$  and  $E_t$  are not known a priori, a reasonable choice about the limiting values of the coefficients must be made. The two limiting cases are clearly when they are chosen so that the corresponding band width is either too narrow or too wide. In the first case delta functions split off at the edges and in the second spurious oscillations develop in the band (Heine 1984).

Beer and Pettifor (1984) treated  $(a_\infty, b_\infty)$  as adjustable parameters, calculated in a self-consistent way from the knowledge of the (exact) coefficients, which have been calculated from the cluster. The method consists in choosing the minimum bandwidth consistent with no loss of weight from the band, thus imposing that  $G_{00}$  diverges simultaneously at the top and bottom band edges. Therefore the minimum and maximum eigenvalues of the truncated tridiagonal matrix corresponding to  $G_{00}(a_\infty \pm 2b_\infty)$ , must be situated, simultaneously, at the bottom and top of the band respectively.

This optimised square root terminator has been shown (Beer and Pettifor 1984) to give structural energy curves that satisfy Ducastelle and Cyrot-Lackmann's theorem (1971). Preservation of the number of nodes is certainly an essential requirement in relative structural stability studies. It is directly linked to the preservation of the information contained in the moments used to calculate  $a_\infty$  and  $b_\infty$ .

Due to the very nature of the method,  $G_{00}(E)$  diverges at the band extreme resulting in small spikes at the top and bottom of the band. In order to get rid of these one can increase the band width by a small amount, a few percent of the bandwidth. We have been experimenting with 1%, 2% ... 5% and the



results are shown in figures 2.2–2.5. For these figures a simple cubic cluster with one s-orbital per site was used with the diagonal (onsite) energy and hopping integral given by  $\epsilon_s = 0$  and  $ss\sigma = -1$  respectively. Figure 2.2 shows the changes in the density of states with 5 levels computed exactly. Therefore  $5 + 1 = 6$  pairs of exact coefficients are used, i.e.,  $(a_0, b_0^2) \cdots (a_5, b_5^2)$ , which means that  $2 \cdot 6 = 12$  exact moments are kept (see appendix I). Figure 2.3 shows the corresponding changes in the structural energy  $\int E [n(E) - n_{\text{ref}}(E)] dE$  as a function of the band filling. In this expression a reference DOS is used as a background in order to emphasize the energy differences. This corresponds to a skew rectangular density of states with the same first four moments as the simple cubic structure. It is not difficult to show that in this case with  $\mu_1 = \mu_3 = 0$  the reference DOS is rectangular with height  $\mu_0/W$  where  $W = (12 \cdot \mu_2/\mu_0)^{1/2}$  is the bandwidth. Furthermore its corresponding band energy  $E_b = \int E n_{\text{ref}}(E) dE$  is parabolic with respect to the band filling  $N$ , i.e.,  $E_b(N) = \mu_0^{-1} (3 \cdot \mu_2/\mu_0)^{1/2} N(N - \mu_0)$ . With  $\mu_0 = 2$  and  $\mu_2 = 2 \cdot 6 \cdot ss\sigma^2 = 12$  (here we have included spin degeneracy and 6 stands for the number of neighbours in the simple cubic structure) we have 0.24 and 8.49 approximately for the height and the bandwidth respectively and  $E_b(N=1) \simeq -2.12$  for the band energy at half bandfilling. These values should be compared with figures 2.2 and 2.3.

The inset in figure 2.3 shows the curves for the different corrections to the bandwidth in a reduced scale. In this case, in order to emphasize the energy differences even more, the background used was a cubic spline fitted to all the data points (we will see later that the spline will be very useful to separate the structural energy amongst different structures, due to the impossibility to fit a skew DOS for all possible values used for the parameters). A NAG (Numeric Algorithms Group) routine was used for this purpose. The routine fits cubic polynomials between knots and joins them together by imposing continuity of the

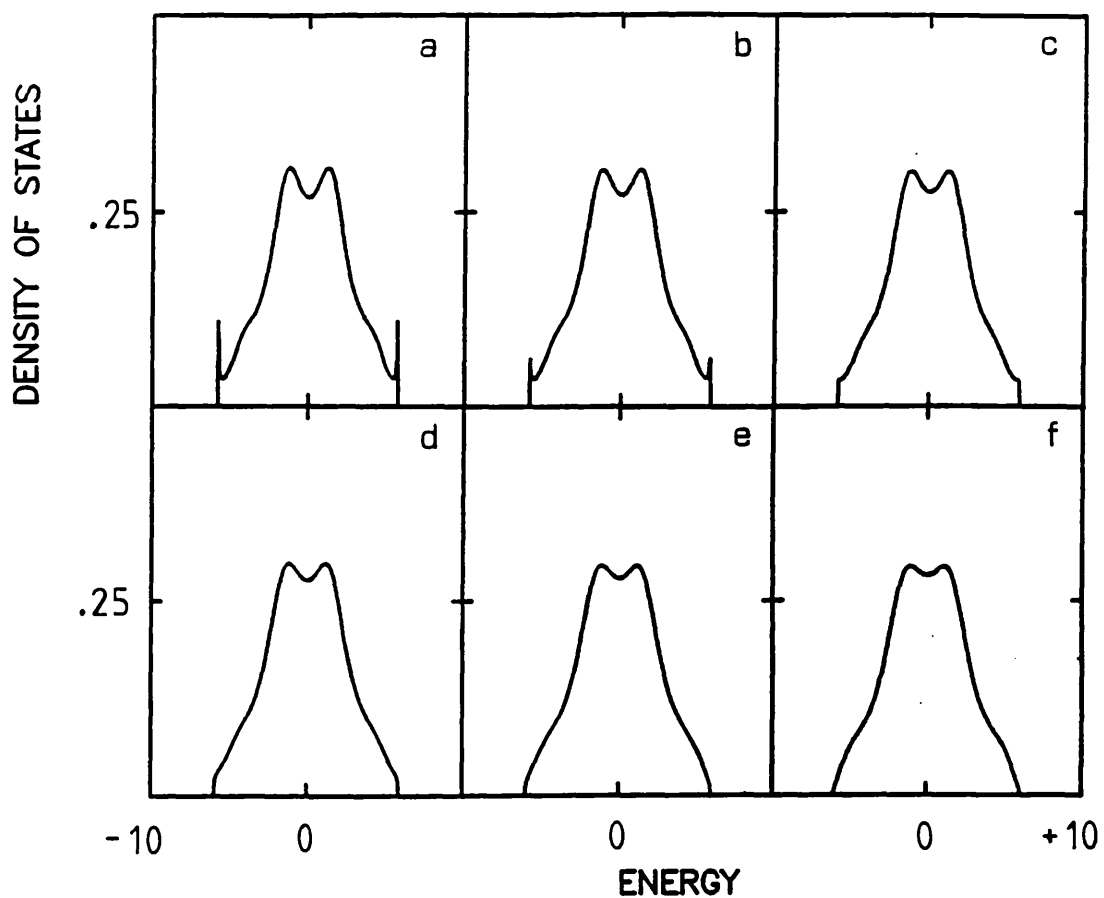


Figure 2.2  
 Simple cubic s-band densities of states ( $\epsilon_s = 0$ ,  $(s\sigma) = -1, 5$  levels) as a function of the band edges. Beer and Pettifor termination was used with a few percent corrections for increasing the band-width. These are: 2.2a (0%), 2.2b (1%), ... 2.2f (5%).

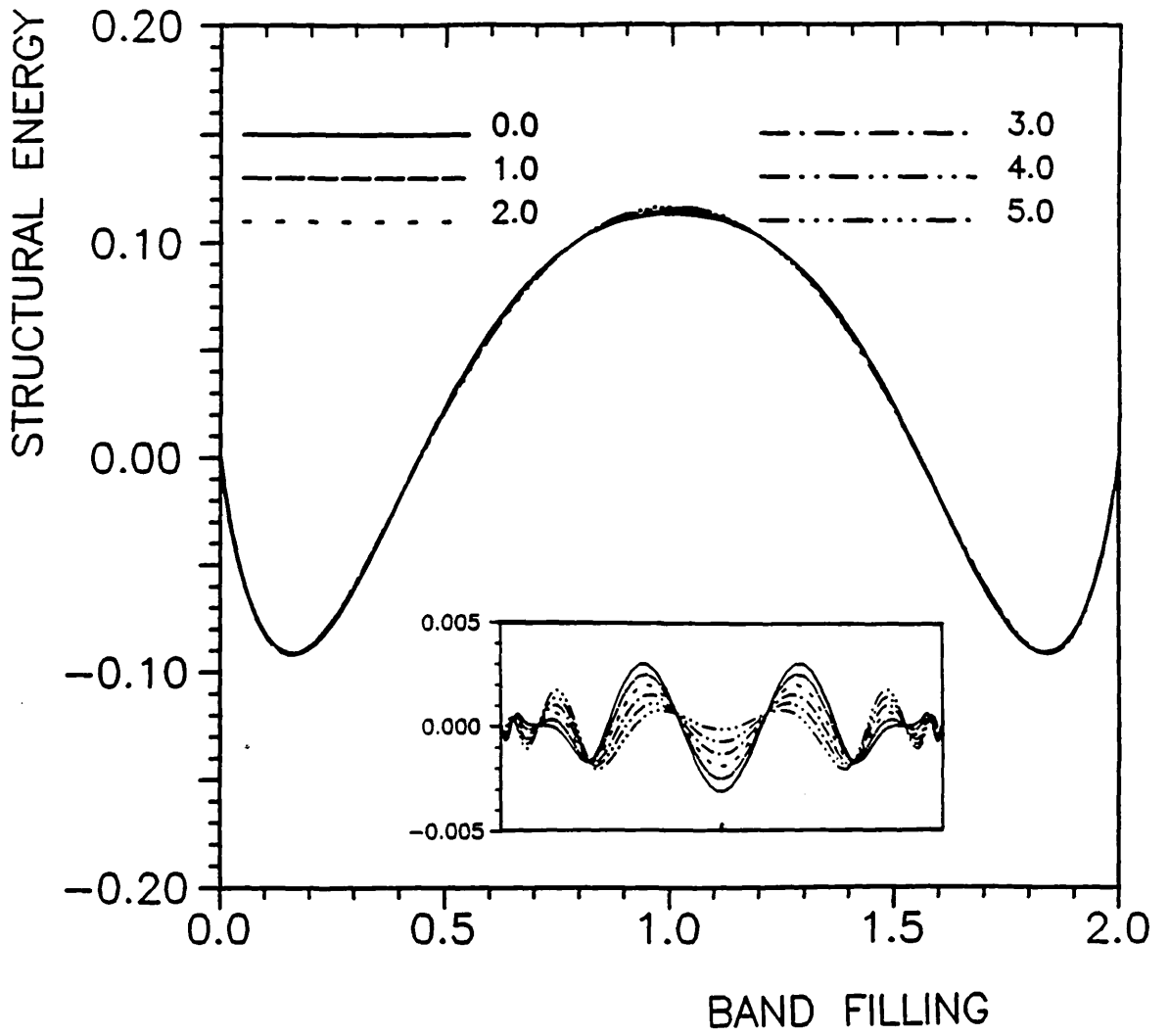


Figure 2.3  
 Structural energy as a function of the band-filling for the DOS  
 in figure 2.2. The inset shows the curves in more detail with an  
 spline chosen as the reference.

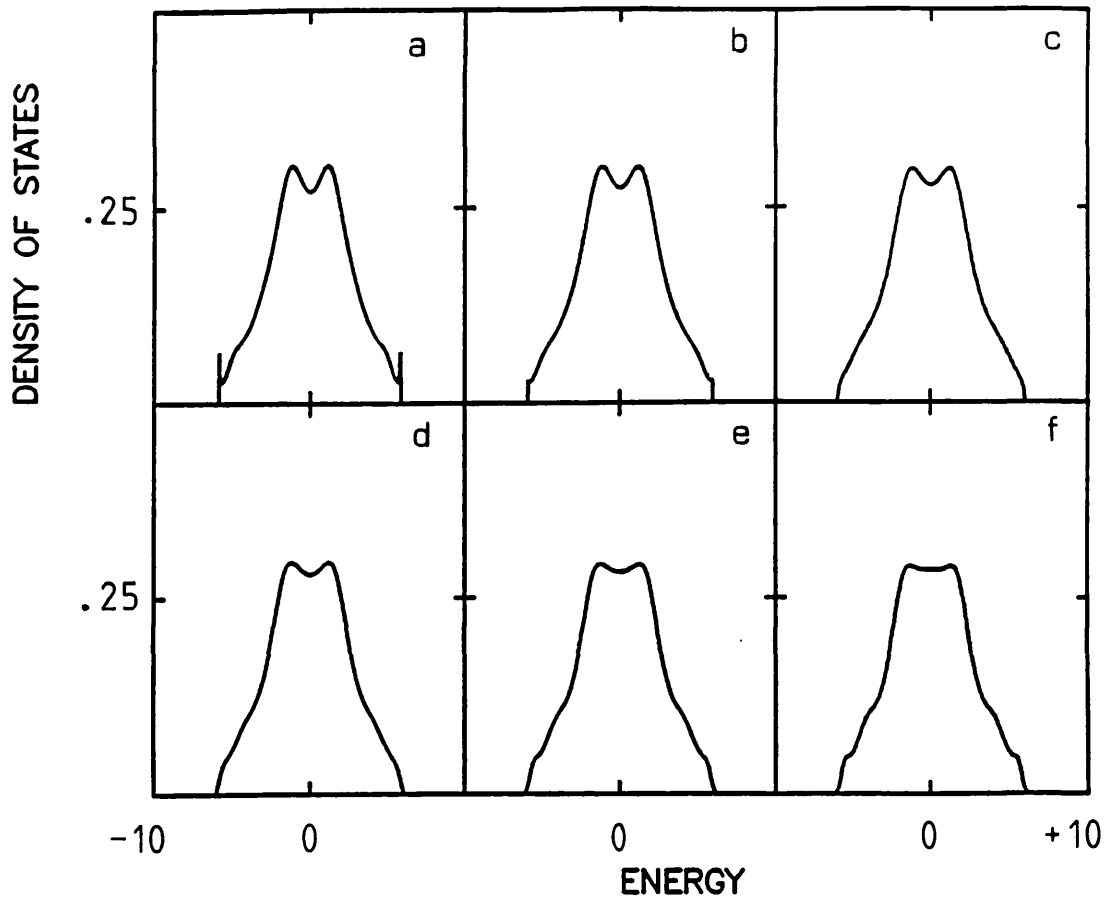


Figure 2.4  
The same as figure 2.2 but keeping 7 levels exact.

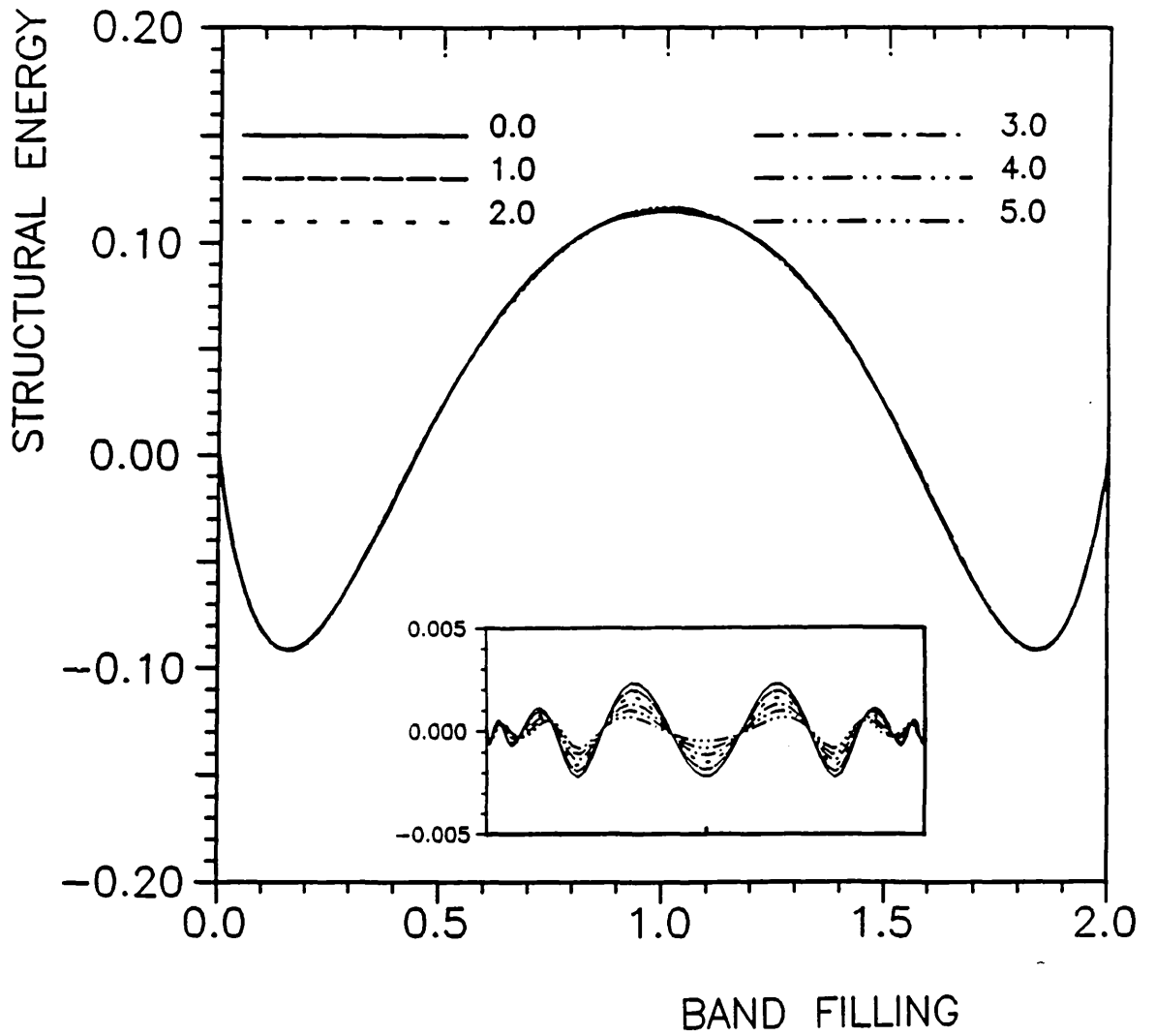


Figure 2.5  
 Structural energy as a function of the band-filling for the DOS  
 in figure 2.4. The inset shows the curves in more details.

function and its first and second derivatives at the joining point (see NAG documentation for details). The knots used for this curve were 0.1, 0.2, 0.4, 0.8, 1.2, 1.6, 1.8, 1.9. Figures 2.4 and 2.5 are just the same as the previous two, but with the number of levels equal to 7.

As we will see in the next chapters, the differences in the structural energies of the different structures studied, are far much greater than the small deviations shown in figures 2.3 and 2.5. One is then free to increase the optimized (Beer and Pettifor) terminated band-width by, at least, as much as 5%. Since 3% is enough to get rid of the spikes at the band edges, we decided to take this for the correction used in this work.

#### 2.4.2 The Single Band-Gap Termination

The square root terminator is not suitable when one is dealing with gaps in the spectrum of energy since it gives rise to a single connected band. In the case of band gaps the coefficients do not have definite limits but rather oscillate with undamped amplitude between two asymptotic limit points (Gaspard and Cyrot-Lackmann 1973). Internal Van Hove singularities in the density of states also cause the recursion coefficients to oscillate but with decaying amplitude, the oscillations decaying with increasing recursion number. As pointed out by Gaspard and Cyrot-Lackmann, the damping and frequency of the oscillations are related to the nature and position of the singularity (see also Hodges 1977). In the presence of several kinds of singularities one must therefore use a suitable procedure for terminating the continued fraction. Sometimes a combination of two may be necessary (Woodruff et al 1987).

The influence of band gaps in the behaviour of the coefficients has been

fully discussed by Turchi et al (1982). Their method is described in some detail in Appendix II where many of the expressions to be used below are derived. Here we shall be mostly interested in pointing out the problems found by Beer (1985) in extending his optimisation procedure from the connected spectrum to a single band gap. A simple prescription which sorts out most of these problems will be given.

Let us first introduce briefly the notation, which will follow that of Turchi et al (op.cit.) as closely as possible. Notice however that the counting index used by Turchi et al for the  $a$ 's, starts from 1 and not from 0 as in this work. Notice also that our sole concern here is the case of a band with a single gap. In this case the band and gap edges shall be represented by  $E_1 < E_2 < E_3 < E_4$  and some useful parameters are

$$\begin{aligned} W &= \frac{1}{2} (E_4 - E_1) & G &= \frac{1}{2} (E_3 - E_2) \\ a &= \frac{1}{2} (E_4 + E_1) & g &= \frac{1}{2} (E_3 + E_2) \end{aligned} \quad (2.44)$$

With the  $n$ th level of recursion within the asymptotic regime, i.e., when the oscillations in the coefficients have settled down, one writes the last level as

$$E - a_{n-1} - g_n(E) \quad (2.45)$$

Two equivalent forms of the terminating function are then given by Turchi et al, which are to be used according to whether the last known pair of coefficients is  $(a_{n-1}, b_n)$  or  $(a_n, b_n)$ . We will always be working with  $(a_n, b_n)$  as the last pair. In this case  $g_n(E)$  can be written as

$$g_n(E) = \frac{2b_n^2 (E + A_1 + a_n)}{E^2 + A_1 E + A_2 + 2b_n^2 + [X(E)]^{\frac{1}{2}}} \quad (2.46)$$

where

$$X(E) = (E - E_1)(E - E_2)(E - E_3)(E - E_4) \quad (2.47a)$$

$$A_1 = -(g + a) \quad (2.47b)$$

$$A_2 = ga - \frac{1}{2}(W^2 + G^2) \quad (2.47c)$$

The asymptotic coefficients are bounded, i.e.,

$$a - G \leq a_n \leq a + G \quad (2.48a)$$

and

$$\frac{W - G}{2} \leq b_n \leq \frac{W + G}{2} \quad (2.48b)$$

and satisfy some recurrence relations that can be obtained from the two forms for the terminating function referred to above (see Appendix II). If the asymptotic limit has been reached then one can use such recurrence relations to obtain the parameters that enter into  $g_n(E)$ . One should then generate the asymptotic coefficients to check whether they match well with the exact ones at the boundary. If, on the other hand, only a few levels are available so that the asymptotic regime has not yet been firmly established, then one needs another procedure to find the parameters. This was provided by Beer (1985) and is a natural extension of the same author's work on the connected band case.

In the single band gap case Beer's method imposes that the Green function diverges (simultaneously) not only at the bottom and top of the band as in the connected case, but also at the gap edges. Beer showed that the Green function at the band and gap edges is given by finite continued fractions, whose associated tridiagonal matrices  $H_G(W)$  and  $H_W(G)$ , respectively, have energy eigenvalues which are responsible for the divergence of the Green function. The



bottom and top of the band are given by the minimum ( $\lambda_{\min}$ ) and maximum ( $\lambda_{\max}$ ) eigenvalues of  $H_W(G)$  when simultaneous divergence is achieved, i.e., when  $\lambda_{\max} = -\lambda_{\min}$ . Similarly the bottom and top of the gap are given by eigen values of  $H_G(W)$  but now one has to give information as to which eigen values are to be used. This is taken from the tridiagonal matrix truncated at the last known level, by counting the number of its eigenvalues in the lower and upper bands. The scheme is carried out in a self-consistent manner between  $H_G(W)$  and  $H_W(G)$ . From an initial guess  $(a_0, W_0, g_0, G_0)$  one determines  $(a_1, W_1)$  from  $H_W(G)$  and  $(g_1, G_1)$  from  $H_G(W)$ . The new set is then used in a second iteration to give  $(a_1, W_1, g_1, G_1)$  until self-consistency is achieved.

Sensible densities of states can then be computed, even when a small number of levels, say  $N = 8$ , is available (Beer op.cit.). Our main interest lies, anyway, on integrated quantities which are known to show little sensitivity to termination parameters (see, for example, Turchi et al 1982, section 5.3).

Beer and Pettifor's procedure for the connected spectrum is fully automatic, thanks mainly to the simple form of the square root terminator at the band edges. Things are more difficult when a gap is present in the density of states, due to the more complicated form of the terminator at the band and gap edges. For example the generalised single band gap procedure requires, as input, initial guesses for the band and gap edges and the knowledge of the number of eigenvalues of the truncated tridiagonal Hamiltonian in each band. All these require prior studies of the coefficients and make the whole procedure non-automatic. But more important and more serious than this is an intrinsic error which arises if the initial positioning of the eigenvalues relative to the true (unknown) gap edges is poor. More specifically the method leads to loss of weights if an eigenvalue of the truncated continued fraction exists inside the gap (see Beer's thesis (1985) section 3.3.2). The weight associated with such states diminishes as the number of levels increases, but we are just interested in working

with a small number of levels. The way out is, then, to restrict ourselves to only those number of levels for which no states exist in the gap. But since the true gap edges are not known a priori, one may not be able to tell for sure from, say, the spectrum of delta functions, whether a state close to one of the gap edges is inside the gap or within the band.

Beer studied the possible effects that incorrect choices would have on the results delivered by his method (Beer (1985) section 3.3.2). In some cases the results were such as to indicate that an incorrect choice had been made. In other cases, however, the results were well acceptable and the error could go on unnoticed. Several times we came across a hardly noticeable negative portion of the density of states which developed in a small region close to one of the calculated gap edges (actually inside the true gap), as a result of such errors (see appendix II for the origin of negative DOS associated with Turchi's termination).

In what follows we make some suggestions as to how to improve the method and avoid the problems mentioned above. We will also show how to bring it closer to full automation. As will be seen, the addition of a simple prescription makes the method a much more reliable tool for the calculation of band and gap edges.

#### 2.4.2.1 Improvements to Beer's Method for a Single Band Gap

Let us list the steps necessary for using Beer's method to evaluate the band and gap edges :

- i) decide whether or not a gap exists;
- ii) estimate band and gap edges (initial guess) and consequently count number of eigenvalues of the truncated tridiagonal Hamiltonian in each

sub-band; and

- iii) compute self-consistent band and gap edges and check them against the initial values for reasonableness of the results.

### Step i)

The decision as to the existence of the gap can be left to the user and in this sense this step is the least important of all three. However it would be interesting if a numeric implementation could be made so that the computing routines could make the decision without the user's intervention. It would certainly save a lot of time, for example, in our case in which one has to deal with a large number of structures, and parameters like the  $sp$ -splitting are varied, which can make the gap appear or disappear from the DOS. Unfortunately we have not been able to arrive to a totally automatic prescription to detect a gap out of a given set of coefficients. In the vast majority of the situations the presence or absence of the gap was sensed succesfully but we came across a few cases in which ~~some doubt was~~ raised. Notice that we have been working with only a few pairs of coefficients, typically about ten levels. With more levels the results were much better as one should expect. We give below a brief description of the methods used, both because it is instructive and it is related to step ii. Several approaches were tried but only the two most releable methods will be described here.

One can tell about the existence of a gap from either the behaviour of the coefficients with the number of levels of recursion or from the square root terminated density of states. The first feature is useless if only a few levels (say less than ten) are available since in this case, in general, the asymptotic regime has not yet settled down. In using the second, one notices that, if a gap exists, the square root termination introduces oscillations in the DOS but 1) leaves band and gap edges reasonably well defined and 2) yields to a very low DOS inside the

gap (Turchi et al 1982). These properties of the square root terminator are good probes in the search for gaps. Furthermore they get more pronounced as more levels are available, because in the limit of an infinite number of levels the DOS must be independent of the termination.

In taking advantage of 1) one must notice that the gap, if present, is situated between two of the eigenvalues of the truncated tridiagonal Hamiltonian. For a given number of levels  $N$ , one then searches for the two eigenvalues between which the square-root terminated DOS is minimum. Since the difference between such two eigenvalues is a good estimate of the gap width  $G(N)$ , one ends up with a procedure that gives  $G(N)$  – or its most probable candidate – as a function of  $N$  (if an eigenvalue exists inside the gap, we will show later that it does not affect the argument). If there is no gap then, as  $N$  increases, there is nothing to prevent other eigenvalues from coming in and slicing up the energy interval where the gap was previously assumed to be. The estimated "gap-width" should then decrease with increasing  $N$ . On the other hand, if the gap does exist then the gap-width should remain practically constant (an eigen value may appear inside the gap for certain values of  $N$  but this state tends to disappear as  $N$  changes). If we then assume that  $G(N)$  depends on  $N$  as

$$G(N) = A \exp(-\lambda N)$$

we should be able to tell whether or not a gap is present in the DOS according to the value of  $\lambda$ . Taking the logarithm of both sides of this expression gives

$$\text{Log } G(N) = \text{Log } A - \lambda N$$

which is a straight line in the plane  $\text{Log } G(N)$  vs  $N$ . In practice  $N = 4, 5, \dots, N_{\text{max}}$ , where  $N_{\text{max}}$  is the number of levels fixed by the user. We

start at  $N = 4$  because the first few levels do not show any regularity at all (see for example Turchi et al, 1972). We now define  $\theta$  by  $\lambda = \tan \theta$ , and according to the arguments above, a low (large) value of  $\theta$  is indicative of the presence (absence) of a gap in the DOS. Generally we found that a low  $\theta$  is around  $2^\circ$  and a large  $\theta$  is around  $12^\circ$ . This method works satisfactorily in most cases but may be misleading in others, for example when the gap is too small. More precisely in some continuous spectra, the decaying in  $G(N)$  may be too slow to give clear evidence of the non-existence of the gap. This seems to be associated mainly with symmetric spectra. Naturally the procedure gets better if the number of levels available is relatively large (say greater than 13).

The second feature, namely that a square root terminated DOS is very low inside the gap, seems to be a more reliable approach. One can exploit this feature more fully by computing the integrated DOS in the intervals between each two neighbouring eigenvalues of the truncated Hamiltonian. It is better to leave out the minimum and maximum eigenvalues in order to avoid picking up a low density at those extrema. We got the best results by integrating over only 50% of each interval, i.e., leaving 25% off each side, thus avoiding including the peaks in the integration (see Turchi et al 1982). Working with an average DOS over this interval (i.e. dividing the result of the integration by the size of the interval and by the total band filling) one gets normalised results, ideally independent of the size of the interval and of the total area under of the DOS curve.

Therefore, to each interval corresponds an average density of states which height we always found to be between 0.1 and 1.0, *except in the gap interval where it was at least one order of magnitude less*. Again one does not claim this to be a totally fool-proof approach for detecting gaps in the DOS and for this reason we do not present more details here. However it made my life much easier, reducing to only a few the cases requiring my direct intervention. Moreover the idea does automate step ii, described in the following.

### Step ii)

If one has decided, by whatever means, that a single gap exists in the DOS then the number of levels in the lower and upper bands must be counted. We see that the previous step already has this information because it detects the gap between two eigenvalues. The initial input guesses for the band edges can then be taken as the minimum and maximum eigenvalues respectively; the gap edges are taken as the two eigenvalues between which the gap was detected. Naturally the procedure does not detect the presence of an eigenvalue inside the gap (it simply finds the interval over which the average DOS is minimum) nor is this its task. If an eigenvalue exists inside the gap for that particular value of  $N_{\max}$ , it will be included to either the upper or the lower band according to where the gap was detected to be. The third step, though, is the one that should tell us that something went wrong and a change in  $N_{\max}$  should then be adequate.

### Step iii)

The computation of the self consistent parameters have already been extensively discussed by Beer (1985). Here we will only be interested in finding out a numerical procedure that analyses the reasonableness of the results. From the reasoning above (see also Beer 1985 section 3.3.2) one only has to worry about the presence of an eigenvalue inside the gap because this is the only source of errors in Beer's procedure.

If the eigenvalue is placed near the center of the gap and is included into, say, the upper (lower) band then the gap will generally jump over one or more eigenvalues into the lower (upper) band (Beer 1985). Since the number of eigenvalues in the lower (upper) band will change from the initial guess, this

situation is easily detected numerically.

On the other hand, if the eigenvalue is close to one of the bands and is included into the band, then, provided that the number of eigenvalues in each band does not change from the input, the gap width delivered by Beer's technique is smaller than the true gap width. This is so because the routines will stretch the gap-edge towards the center of the gap, in order to accommodate an extra eigenvalue in the sub-band. This is the essential problem with the method, because the true gap width being not generally known, makes it difficult to detect the error. In order to study the error Beer carried out some tests by making deliberate incorrect choices for the gap position and analysing the corresponding effects on the results delivered by the computing routines (Beer 1985 p122). His conclusions were that the results should give some indications that an input initial error had been made and an alternative choice should then be tried. This picture is clearly unsatisfactory, particularly if one is attempting to draw structural maps, when a massive number of different values for the parameters of theory must be tried.

The solution for this problem is, however, very simple and straightforward: *if the gap is made too small the bounds in the coefficients (2.48) shall be violated.* This violation can be spotted provided that the number of exact levels is large enough so that the maximum amplitude of oscillation has already been reached by either the a's or the b's. Notice that this condition does not demand that the asymptotic region has been reached, but only that the maximum amplitude of oscillation is reasonably well defined. Therefore typically half the number of coefficients necessary to reach the asymptotic regime is needed here. Actually even less than this may be enough because if a gap eigenvalue (i.e., one that is in the gap) that is close to one of the bands is included in the band, then the gap-width delivered by Beer's routine is sensibly smaller than the true gap-width (Beer 1985 p122). We have noticed that around six levels are enough in most of the situations.

Due to the small gap-width the asymptotic coefficients oscillate with smaller amplitude than the exact coefficients. They almost certainly will not match at the boundary (Turchi et al 1982) which can lead to a negative density of states inside the true gap (see Appendix II).

More quantitatively let us take the asymmetric split rectangular band (figure 2.6) used by Beer (1985) and make intentional errors by including in the band eigenvalues known to be in the gap. The purpose of this exercise is to find out how the method copes with eventual incorrect choices introduced by the user. The proposital errors are the same as Beer's (op.cit. section 3.3.2) and as we will see, in all cases, the bounds shall be violated either for the a's or the b's or both. The coefficients were obtained from the moments by using the determinantal relations described in Shohat and Tamarkin (1943). We then compute the self consistent parameters and check if the bounds are in fact violated. If they are, we calculate, from the computed parameters, the following positive quantities as a measure of the amount of violation of the bounds

$$da_{\pm} = \text{MAX} \left[ \left| a_n - (a \pm G) \right| / (2G) \right] \quad (2.49a)$$

and

$$db_{\pm} = \text{MAX} \left[ \left| b_n^2 - \left[ \frac{W \pm G}{2} \right]^2 \right| / (WG) \right] . \quad (2.49b)$$

Here  $n = 4 \cdots N_{\text{max}}$ , where  $N_{\text{max}}$  is the last known exact coefficient. Notice that the denominators are respectively the amplitude of the oscillation of the a's and b<sup>2</sup>'s, i.e.,



$$2G = (a + G) - (a - G) \quad (2.50a)$$

and

$$WG = \left[ \frac{W + G}{2} \right]^2 - \left[ \frac{W - G}{2} \right]^2 \quad (2.50b)$$

We still have to justify starting the variation of the recursion level from 4 in (2.49). For such we plot in figure 2.7 the phase space representation of the recurrence laws satisfied by the coefficients in the case of the band defined in figure 2.6 (see Appendix II this work and Turchi et al 1982 for details). Here the asymptotic coefficients lie on the continuous curve whereas the calculated ones are represented by other symbols. As expected the higher the recursion level the better the display of asymptotic behaviour from the part of the calculated coefficients. The first few pairs though, are seen not to lie in the asymptotic curve. They have no immediate information about the asymptotic regime and are therefore left out of the analysis. The fifth pair (i.e., the fourth level) is kept and so are all the pairs up to Nmax, the maximum number of exact levels available.

Table 2.1 summarizes the results. Notice that the violation of the bounds generally increases as the number of levels increases. This indicates that Beer's procedure gets more sensitive (the method gets more reliable) to initial input errors as the number of levels increases. Notice also that the bounds have been violated in every case in which a mistake was made, which shows that violation of the bounds is a good indication of bad initial positioning of the eigenvalues. Finally we found that the coefficients are within the bounds for every case for which the correct choice was made (we went up to 19 levels in this analysis).

In practice one can extend the allowed region for the coefficients by a

factor of, say, 1% of its computed value. If a coefficient (from  $N_{\min} = 4$  to  $N_{\max}$ ) is spotted outside this stretched region, the situation will be interpreted as if an eigenvalue exists in the gap. We see that we could set a tolerance of nearly 5% and yet spot the initial mistake.

We would like to stress that the last known pair of coefficients is solely used in the terminating function. They do not make any appearance in the tridiagonal matrix. More specifically from  $N+1$  pairs of exact coefficients available within  $N$  levels of recursion, the  $(N+1)$ th one is to be used in the TDT's terminating function. Only the remaining  $N$  pairs are used to build up the tridiagonal matrix, which is therefore an  $N \times N$  matrix.

Finally, notice that Beer's method places  $\delta$ -functions at the bottom and top of both sub-bands. In other words the method gives the minimum band-width and maximum gap-width consistent with no loss of weight from the band. Just as in the connected case, one can increase (decrease) the band-width (gap-width) in order to get rid of the spikes placed at the edges. However in this case one has to be slightly more careful because the bounds in (2.48) must be respected. Also one must allow for different corrections for each of the two different sub-bands. Let's suppose that the band-width of the lower (upper) sub-band is  $W_1$  ( $W_2$ ) and the gap width is  $G_g$ , the edges being defined by  $E_1 < E_2 < E_3 < E_4$ . We use parameters  $\alpha$  and  $\beta$  for the corrections such that

$$\delta W_1 = 0.01 \cdot \alpha \cdot W_1 \qquad \delta G_1 = 0.01 \cdot \alpha \cdot G_g$$

$$\delta W_2 = 0.01 \cdot \beta \cdot W_2 \qquad \delta G_2 = 0.01 \cdot \beta \cdot G_g$$

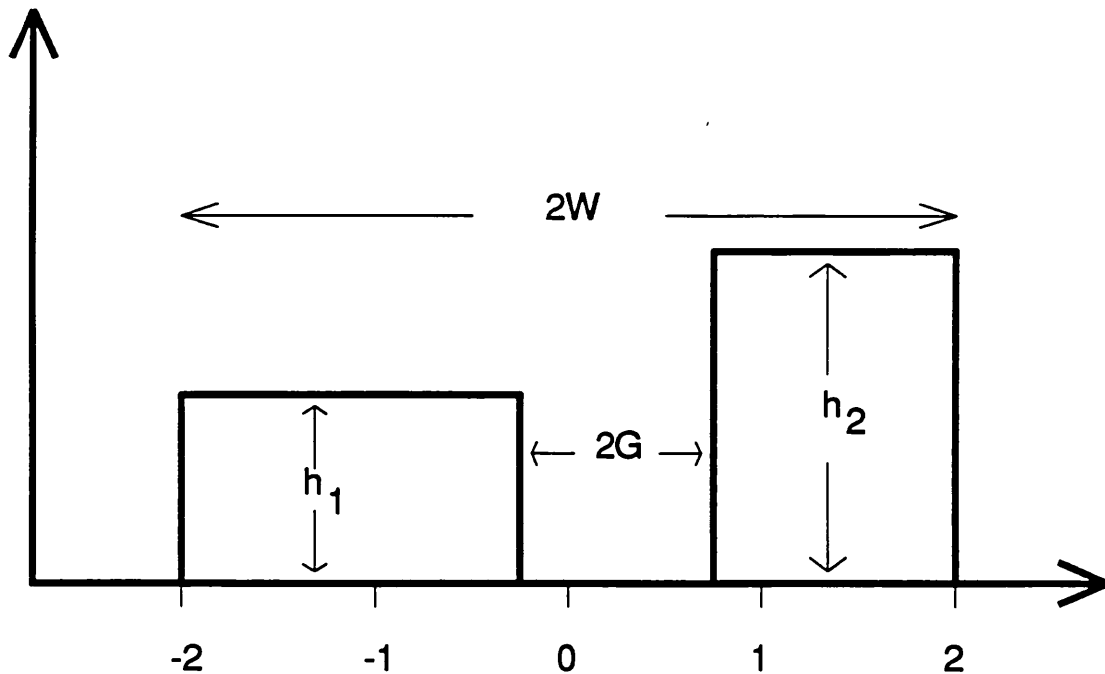


Figure 2.6  
 The asymmetric split rectangular band The parameters are the same used by Beer (1985 p93):

$$\begin{aligned}
 a &= 0 & W &= 2.0 \\
 g &= 0.2 & G &= 0.5 \\
 h_2 &= 1.5 \cdot h_1
 \end{aligned}$$

The total band-filling being equal to 5 gives  $h_1 = 5.0/3.65$ .

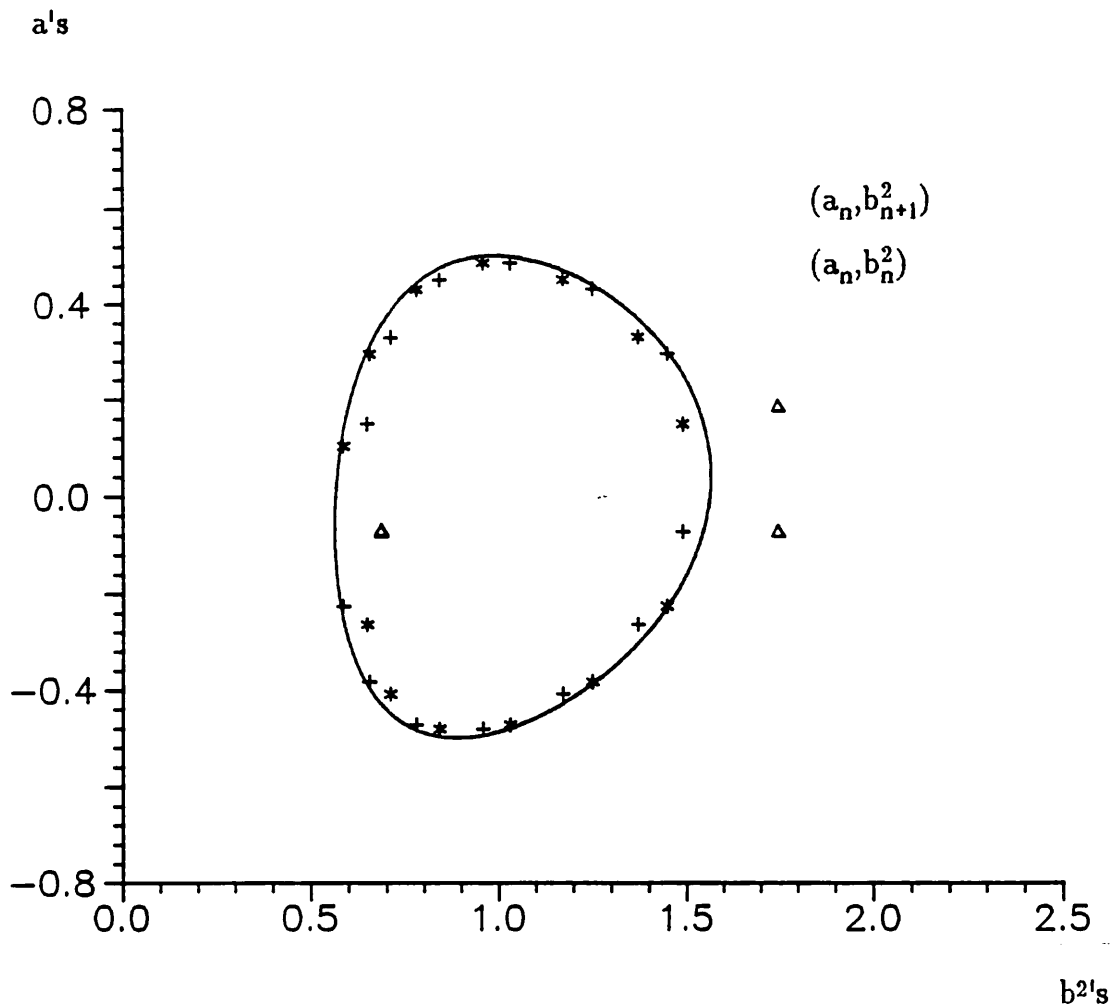


Figure 2.7

Phase space representation of the asymptotic coefficients for the asymmetric split rectangular band of figure 2.6. The asymptotic curve was calculated from the exact band and gap edges. The triangles represent the first few coefficients and the pluses and stars represent the third level and beyond.

No. of levels	Eigen value position	Included into	da <sub>+</sub>	da <sub>-</sub>	db <sub>+</sub>	db <sub>-</sub>
7	-0.28	lower band	0.08	0.02	--	--
10	0.68	upper band	0.05	0.05	--	--
12	0.58	upper band	0.57	0.57	0.30	0.30
14	0.43	upper band	10.4	10.7	9.7	7.6
16	0.23	upper band	1.04	1.07	1.27	0.85
16	0.23	lower band	1.36	1.28	1.60	1.07
18	0.02	upper band	1.50	1.52	1.81	1.30
18	0.02	lower band	4.54	4.40	5.22	3.94

**Table 2.1** Violation of the bounds for the coefficients resultant from proposital incorrect initial positioning of the eigenvalues.

In other words  $\alpha$  corrects for the lower band edges and  $\beta$  corrects for the upper band edges. Finally the changes in the edges are

$$E_1' = E_1 - \delta W_1/2 \qquad E_2' = E_2 + \text{MIN}(\delta W_1, \delta G_1)/2$$

$$E_4' = E_4 + \delta W_2/2 \qquad E_3' = E_3 - \text{MIN}(\delta W_2, \delta G_2)/2 .$$

Figure 2.8 shows how these corrections affect the sp density of states of a cubic diamond structure. Notice how the spikes disappear as the correction increases from 0% (a) to 6% (f) in unity steps. Just as in the connected case the effects of these corrections on the structural energy are negligible, as can be seen from figure 2.9. In this work we shall take  $\alpha = \beta = 3$  which was also the correction factor chosen for the connected band case. Figures 2.8 and 2.9 were obtained from a cubic diamond cluster with nine exact levels and sp-splitting equal to zero. The tight-binding hopping integrals were calculated with respect to  $ss\sigma = -1$ , by using Harrison's ratios (Harrison 1980), which are introduced in chapter 4. The value of  $pp\pi$  was taken as  $-0.33 \cdot pp\sigma$  though, and the reason for this is explained in chapter 4. As we did in the connected case, in figure 2.9a the structural energies were calculated relative to a skew density of states with the same first four moments as the cluster. In figure 2.9b a spline fitted to all the points was used as a background. In this case the knots were chosen at 1, 2, 3, 4, 5, 6 and 7.

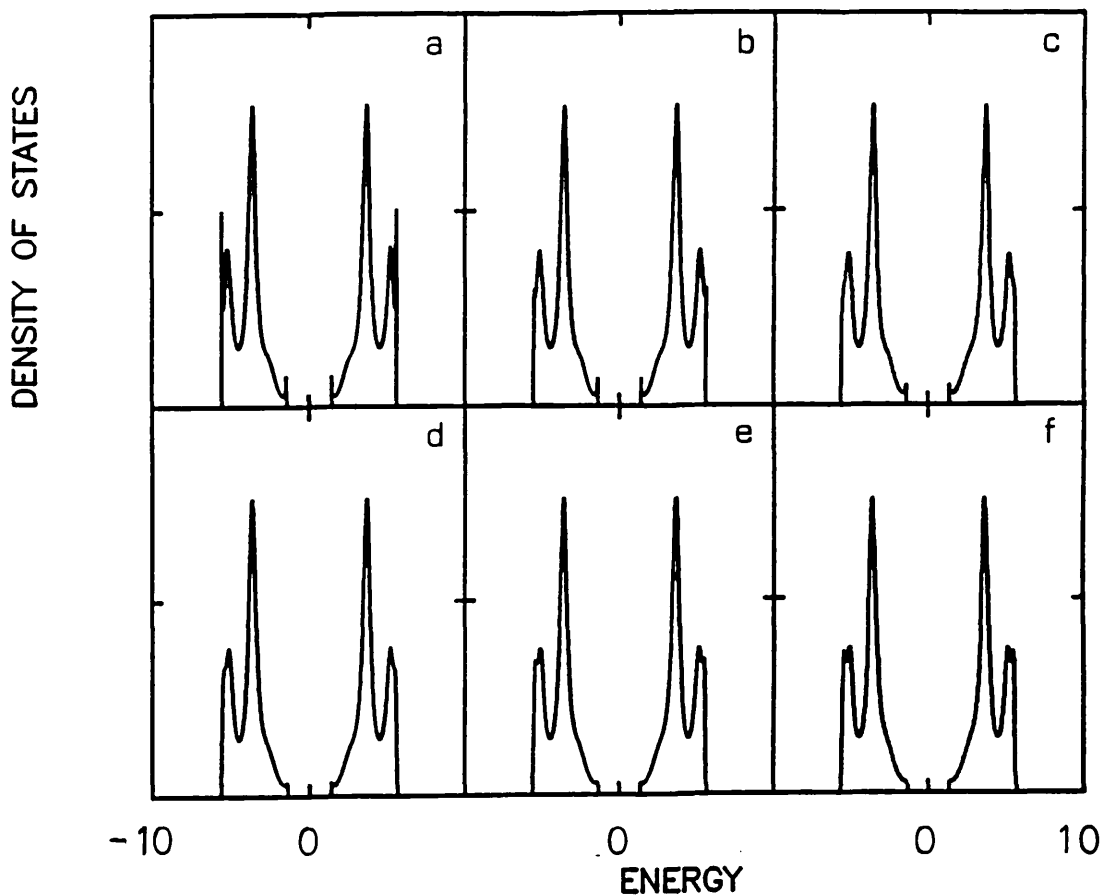
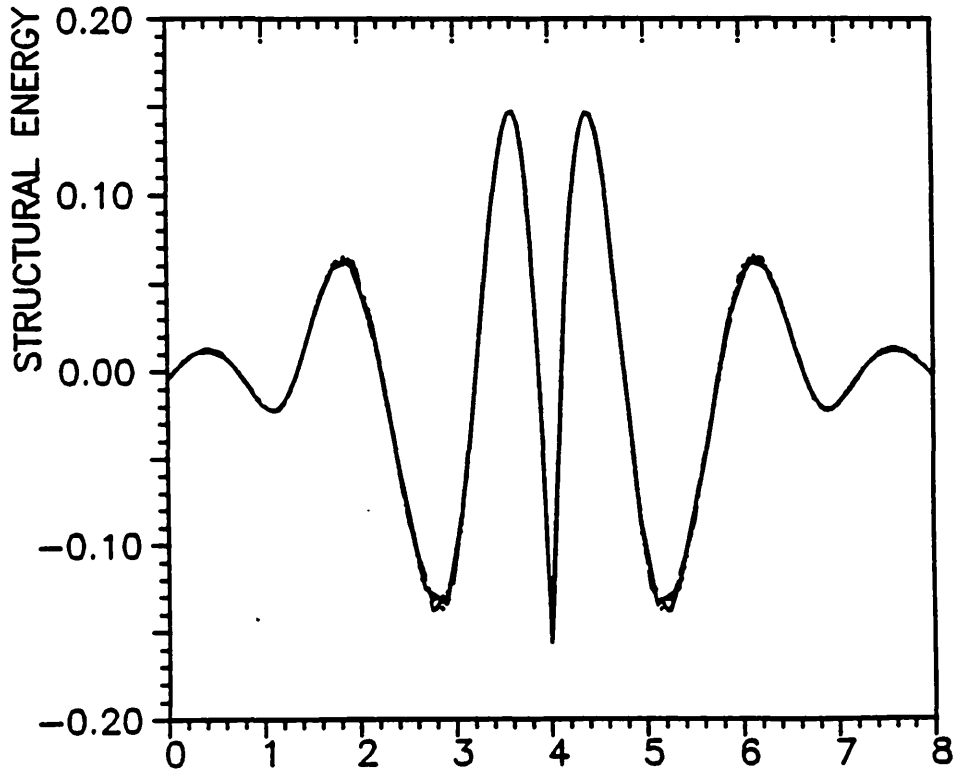
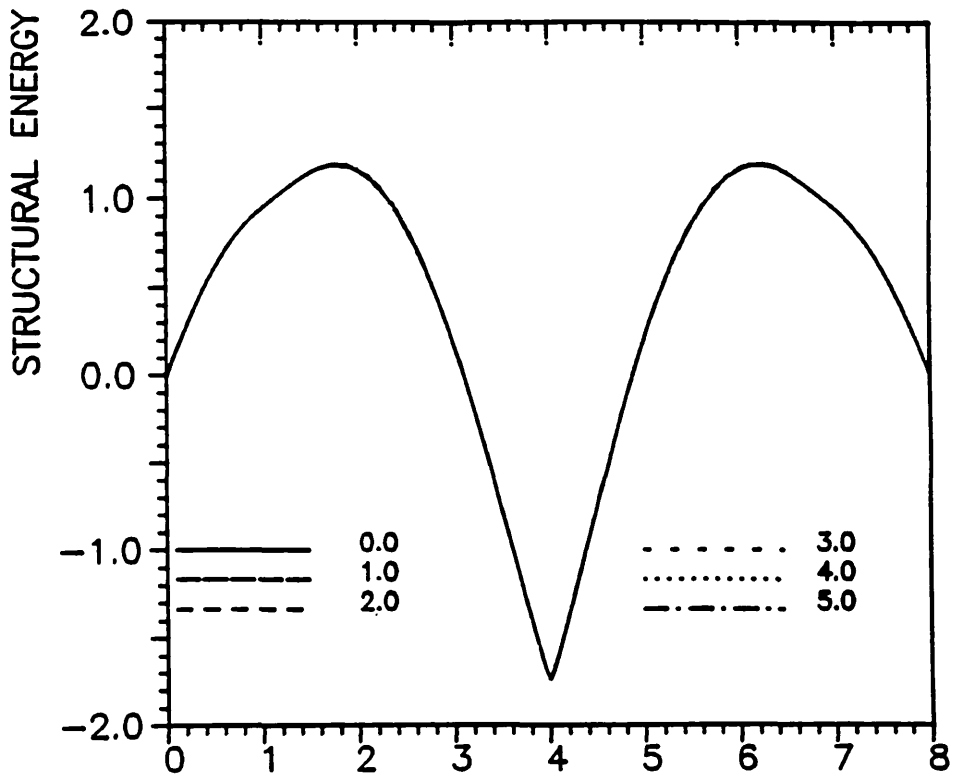


Figure 2.8  
 sp densities of states for a nine levels cubic diamond cluster showing the effect of corrections to the edges. From a to f the corrections are  $\alpha = \beta = 0, 1 \dots 5$ . The sp-splitting was taken equal to zero,  $(ss\sigma) = -1$  and the other hopping integrals fixed using Harrison's ratios, except for  $(pp\pi)$  which was taken as  $-0.33 \cdot (pp\sigma)$ .



**BAND FILLING**

Figure 2.9  
 Structural energies as a function of the band-filling respecting to the densities of states in figure 2.8: a) with a skew density of states as a background; and b) with respect to a spline fitted through all the points. Notice the change of scale in the structural energy axis.



## §2.5 Conclusions

In this chapter we briefly reviewed the recursion method which is the basic tool used for the calculation of the densities of states appearing in various other parts of this work. The moments method was also discussed and its numeric problems pointed out. Setting up the tridiagonal matrix corresponding to a given cluster of atoms was not the end of the story for the bulk and we therefore showed how the asymptotic tail of the continued fraction could be reasonably smoothed out to obtain a continuous band of states. The square root termination was then discussed as appropriate to the connected band case. The more complex single band gap case was also reviewed in connection with Turchi, Ducastelle and Trégliat (1982) terminator. In both cases an optimised technique (Beer 1985) for the calculation of the relevant parameters was discussed. The case when two gaps exist in the spectrum is discussed in appendix IX.

## CHAPTER 3: Relevant Energy Expressions

In this chapter we discuss the energy expressions that shall be used in the subsequent chapters. The tight-binding model is presented and the importance of non-orthogonality contributions to sp systems is stressed. The basics of the chemical pseudopotential approach is also presented and how it can be used to provide a justification for the use of tight-binding in systems with non-localized orbitals.

### §3.1 Introduction

In chapter 2 we presented the recursion method for the computation of the local density of states associated with a given site in the assembly of atoms in the solid state. This quantity can be used for the calculation of the band structure energy (or band energy, or structural energy) of the solid which is an important part of its total energy. In this chapter we show how they are related to each other and also present the different terms contributing to the total energy. A short review on the tight-binding (TB) method for band structure calculation is also included here. The neglect of non-orthogonality contributions in this method can be shown to be justified, in principle, with the use of a suitably chosen basis set which is derived from the Anderson-Bullett scheme (Anderson 1969 and Bullett 1975a, 1975b).

### §3.2 Band and Bond Energies

We have seen in chapter 2 how to express the local density of states  $n(E, \mathbf{x})$  in terms of the Green's function, i.e.,

$$n(\mathbf{x}, E) = \frac{-1}{\pi} \text{Im } G(\mathbf{x}, \mathbf{x}, E) \quad . \quad (3.1)$$

More generally one can define

$$n(\mathbf{x}, \mathbf{x}', E) = \frac{-1}{\pi} \text{Im } G(\mathbf{x}, \mathbf{x}', E) \quad (3.2)$$

which are the matrix elements of the spectral density operator in the  $\mathbf{x}$ -representation (Finnis et al 1988). This quantity when integrated over  $E$  up to the Fermi level gives the elements of the density operator  $\rho$ , i.e. ,

$$\langle \mathbf{x} | \rho | \mathbf{x}' \rangle = \int^{\epsilon_f} n(\mathbf{x}, \mathbf{x}', E) dE \quad (3.3a)$$

$$= \frac{-1}{\pi} \text{Im} \int^{\epsilon_f} G(\mathbf{x}, \mathbf{x}', E) dE \quad . \quad (3.3b)$$

In this representation (the coordinate or  $\mathbf{x}$ -representation) the diagonal element  $\langle \mathbf{x} | \rho | \mathbf{x} \rangle$  is the electronic charge density  $\rho(\mathbf{x})$ . In the representation in which the basis functions are the eigen functions  $|n\rangle$  of the energy operator the density operator is defined as (Kittel 1987, Cohen-Tannoudji et al 1977)

$$\rho = \sum_n |n\rangle p_n \langle n| \quad . \quad (3.4)$$

where the Fermi factor  $p_n$  is the occupancy of the state  $|n\rangle$ . At 0K  $p_n$  is given

by  $\theta(\epsilon_f - \epsilon_n)$  where  $\theta$  is the heaviside or step function, i.e.,  $\theta(x) = 1$  for  $x > 0$ , and zero otherwise. In this case  $p_n$  simply restricts the summation to the occupied states of the system.

The major advantage in using the density operator concept is in the calculation of expectation values of operators in quantum mechanics. For instance given an operator  $\mathcal{O}$  one can calculate its expectation value summed over all occupied states as

$$\langle \mathcal{O} \rangle = \sum_n p_n \langle n | \mathcal{O} | n \rangle$$

which in the  $x$ -representation gives

$$\begin{aligned} \langle \mathcal{O} \rangle &= \sum_n \iint dx dx' p_n \langle n | x' \rangle \langle x' | \mathcal{O} | x \rangle \langle x | n \rangle \\ &= \sum_n \iint dx dx' \langle x | n \rangle p_n \langle n | x' \rangle \langle x' | \mathcal{O} | x \rangle \\ &= \iint dx dx' \langle x | \rho | x' \rangle \langle x' | \mathcal{O} | x \rangle \\ &= \text{Tr} [\rho \mathcal{O}] \end{aligned} \tag{3.5}$$

This form, although derived in the coordinate representation, is actually basis independent because of the invariance of the trace under a change of basis.

We can use the density operator concept to write down an expression for the band energy (also called structural energy) of a material. This is the sum over the occupied states of the eigen values of  $\epsilon_n = \langle n | \mathcal{H} | n \rangle$  of the Hamiltonian, namely,

$$E_{\text{band}} = \sum_n^{\text{occ}} \langle n | \mathcal{H} | n \rangle \quad (3.6a)$$

$$= \sum_n^{\text{occ}} \epsilon_n \quad (3.6b)$$

which in terms of the density operator is given by  $\text{Tr}(\rho \mathcal{H})$ . Notice that this one-electron energy sum is not the total electronic energy of the solid (Heine 1980 p92). The Coulomb repulsion of the ion cores has not been taken into account, the Coulomb energy of the electron charge density has been counted twice and one also has to consider the exchange and correlation energy. Furthermore Schrodinger's equation must be iterated to self consistency so that the eigen vectors give a charge density that is consistent with the effective potential used in the Hamiltonian.

The band energy can be written in terms of the density of states by

$$\begin{aligned} E_{\text{band}} &= \text{Tr} \mathcal{H} \rho \quad (3.7) \\ &= \iint d\mathbf{x} d\mathbf{x}' \langle \mathbf{x} | \mathcal{H} | \mathbf{x}' \rangle \langle \mathbf{x}' | \rho | \mathbf{x} \rangle \\ &= \frac{-1}{\pi} \int^{\epsilon_f} dE \iint d\mathbf{x} d\mathbf{x}' \langle \mathbf{x} | \mathcal{H} | \mathbf{x}' \rangle \text{Im} \langle \mathbf{x}' | G(E) | \mathbf{x} \rangle \\ &= \int^{\epsilon_f} dE \iint d\mathbf{x} d\mathbf{x}' \langle \mathbf{x} | \mathcal{H} | \mathbf{x}' \rangle \langle \mathbf{x}' | n(E) | \mathbf{x} \rangle \end{aligned}$$

where we made use of 2.2. Now since  $\langle \mathbf{x}' | n(E) | \mathbf{x} \rangle = \sum_n \langle \mathbf{x}' | n \rangle \langle n | \mathbf{x} \rangle \delta(E - E_n)$  we can write

$$E_{\text{band}} = \int^{\epsilon_f} dE \iint dx dx' \sum_n \langle x | \mathcal{H} | x' \rangle \langle x' | n \rangle \langle n | x \rangle \delta(E - E_n)$$

and making use of  $\int |x'\rangle \langle x'| = 1$  and  $\mathcal{H}|n\rangle = E_n$  we get

$$E_{\text{band}} = \int^{\epsilon_f} dE \int dx \sum_n E_n \langle x | n \rangle \langle n | x \rangle \delta(E - E_n) .$$

Finally, since  $\sum_n E_n \cdots \delta(E - E_n) = \sum_n E \cdots \delta(E - E_n)$  we have

$$E_{\text{band}} = \int^{\epsilon_f} E dE \int dx n(x, E) \quad (3.8)$$

$$= \int^{\epsilon_f} E n(E) dE \quad (3.9)$$

which writes the band energy in terms of the density of states. A shorter way of deriving (3.8) and (3.9) from (3.7) is by making use of the equation satisfied by the Green's function, namely

$$(E - \mathcal{H})G(\mathbf{x}, \mathbf{x}', E) = \delta(\mathbf{x} - \mathbf{x}') \quad (3.10)$$

which is in accordance with

$$G(\mathbf{x}, \mathbf{x}', E) = \sum_n \frac{\psi_n(\mathbf{x}) \psi_n^*(\mathbf{x}')}{E - E_n} \quad (3.11)$$

from chapter II (see Heine 1980 p17-18). From (3.10) we see that  $\text{Im} \langle x | \mathcal{H} | x' \rangle \langle x' | G(E) | x \rangle = \text{Im} \langle x | E | x' \rangle \langle x' | G(E) | x \rangle$  which could have been used a couple of steps after (3.7) to write  $\text{Im Tr}(\mathcal{H}G) = \text{Im Tr}(EG)$  and make

the connection with the density of states in a more economic way (Finnis et al 1988).

Similar expressions can be written down relevant to the localized basis set  $|i\alpha\rangle$  (orthogonal by assumption) as we did in chapter II. In this case the elements of the spectral density operator, whose diagonal part is the local density of states are

$$\begin{aligned} n_{i\alpha,j\beta}(E) &= \frac{-1}{\pi} \text{Im} \langle i\alpha | \frac{1}{E - \mathcal{H}} | j\beta \rangle \\ &= \frac{-1}{\pi} \text{Im} G_{i\alpha,j\beta}(E) \end{aligned} \quad (3.12)$$

where we remind the reader that the  $\lim_{\epsilon \rightarrow 0} (E+i\epsilon)$  must be taken in the Green's function. As before, when integrated up to the fermi energy,  $n_{i\alpha,j\beta}(E)$  gives the matrix elements of the density operator (Paxton 1987 p2.8) namely

$$\rho_{i\alpha,j\beta} = \int^{\epsilon_f} dE n_{i\alpha,j\beta}(E) \quad (3.13a)$$

$$= \frac{-1}{\pi} \text{Im} \int^{\epsilon_f} dE G_{i\alpha,j\beta}(E) \quad (3.13b)$$

Here  $\rho_{i\alpha,j\beta} \equiv \langle i\alpha | \rho | j\beta \rangle$  which from (3.4) can also be written as

$$\rho_{i\alpha,j\beta} = \sum_n^{\text{occ}} \langle i\alpha | n \rangle \langle n | j\beta \rangle \quad (3.14a)$$

$$= \sum_n^{\text{occ}} a_{n,i\alpha} a_{n,j\beta}^* \quad (3.14b)$$



where we assume that one is working at 0K. The  $a$ 's are the coefficients of the expansion of the eigen states  $|n\rangle$  in the  $|i\alpha\rangle$  basis (see chapter II). In this representation the diagonal element  $\langle i\alpha|\rho|i\alpha\rangle$  is the number of electrons (with both spins) occupying the orbital  $\alpha$  on atom  $i$  and the off diagonal element  $\langle i\alpha|\rho|j\beta\rangle$  represents the order of the bond between the  $\alpha$ -orbital on atom  $i$  and the  $\beta$ -orbital on atom  $j$ . Since the off diagonal Green's function matrix element can be written as a difference between the diagonal Green's function elements corresponding to symmetric and antisymmetric combinations of the orbitals  $|i\alpha\rangle$  and  $|j\beta\rangle$  (chapter II or Kelly 1980),  $\langle i\alpha|\rho|j\beta\rangle$  can be seen to be related to the difference between the occupation of the bonding orbital  $|i\alpha\rangle + |j\beta\rangle$  and the antibonding orbital  $|i\alpha\rangle - |j\beta\rangle$ . It therefore measures the strength of the bond between the two orbitals and is also called partial bond order to contrast with the total bond order (or simply bond order) which is the sum of  $\langle i\alpha|\rho|j\beta\rangle$  over  $\alpha$  and  $\beta$  (Finnis 1987, Coulson 1939).

The band energy is given by  $\text{Tr } \rho \mathcal{H}$  as before, i.e.,

$$E_{\text{band}} = \sum_{i\alpha, j\beta} \rho_{i\alpha, j\beta} \mathcal{H}_{j\beta, i\alpha} \quad (3.15)$$

and like we did in the coordinate representation it can be expressed in terms of the local density of states  $n_{i\alpha}(E) \equiv n_{i\alpha, i\alpha}(E)$ , namely

$$E_{\text{band}} = \sum_{i\alpha} \int_{\epsilon}^{\epsilon_f} E n_{i\alpha}(E) dE \quad (3.16)$$

The off diagonal matrix elements of the Hamiltonian in (3.15) are the tight-binding hopping integrals (Slater and Koster 1954) and the diagonal ones are the on-site energies  $\epsilon_{i\alpha} = H_{i\alpha, i\alpha}$  which can be identified with the atomic energy levels. The hopping integrals are also called bond or transfer or resonance integrals. It is usual to split  $E_{\text{band}}$  into two parts involving the diagonal and off-diagonal elements of  $\mathcal{H}$  in order to identify  $E_{\text{bond}}$ , the covalent bond energy of the solid, i.e.,

$$E_{\text{band}} = \sum_{\substack{i\alpha, j\beta \\ i \neq j}} \rho_{i\alpha, j\beta} \mathcal{H}_{j\beta, i\alpha} + \sum_{i\alpha} \epsilon_{i\alpha} \rho_{i\alpha, i\alpha} \quad (3.17a)$$

$$= \frac{1}{2} \sum_{\substack{i\alpha, j\beta \\ i \neq j}} E_{\text{bond}}^{i\alpha, j\beta} + \sum_{i\alpha} \epsilon_{i\alpha} \rho_{i\alpha, i\alpha} \quad (3.17b)$$

$$= E_{\text{bond}} + \sum_{i\alpha} \epsilon_{i\alpha} \rho_{i\alpha, i\alpha} \quad (3.17c)$$

Here  $E_{\text{bond}}^{i\alpha, j\beta} = 2 \rho_{i\alpha, j\beta} \mathcal{H}_{j\beta, i\alpha}$  is the energy due to the bond between orbitals  $\alpha$  and  $\beta$  on sites  $i$  and  $j$  respectively and the factor  $1/2$  in (3.17b) accounts for the double counting of each bond. Therefore  $E_{\text{bond}}$  is given as a sum of the covalent bond energies of all bonds and we assumed that  $\mathcal{H}_{j\beta, i\alpha} = \epsilon_{i\alpha} \delta_{\alpha\beta}$ , i.e., the only contribution to the on-site energy comes from orbitals of the same type. In terms of the density of states one can write (Allan 1970)

$$E_{\text{bond}} = \sum_{i\alpha} \int^{\epsilon} f(\epsilon - \epsilon_{i\alpha}) n_{i\alpha}(\epsilon) d\epsilon \quad (3.17)$$

which gives the bond energy as a sum over sites as opposed to a sum over bonds. This expression is very useful for the calculation of bond energies since it only involves the knowledge of one matrix element of the Green's function. The corresponding expression from (3.17) on the other hand requires the calculation of all matrix elements of  $G(E)$ . However it gives information on all the individual bonds and plays an important role in the tight binding bond model (TBB) of Sutton et al (1988). Up to now we have omitted any consideration about the electron spin. This can be amended by multiplying these energy expressions (and in fact any sum over states like, say, (3.14)) by a factor of two in order to account for spin degeneracy.

### §3.3 The Tight-Binding Approximation

In this section we shall illustrate the basics of the tight-binding method which is used for the calculation of band energies in the following chapter (e.g., Callaway 1964, 1974). For simplicity we will assume that there is only one atom in the unit cell. The TB approach is ideally suitable when the overlap of atomic wave functions requires corrections to the free atoms system but in such a way that some features of the atomic picture still remains in the solid. One assumes that in the immediate neighbourhood of a lattice site the full crystal Hamiltonian  $\mathcal{H}$  can be approximated by the atomic Hamiltonian  $H_{at}$  and that the atomic wave functions are well localized. Let us write

$$H_{at} u_{\alpha}(\mathbf{r}) = \epsilon_{\alpha}^0 u_{\alpha}(\mathbf{r}) \quad (3.18)$$

for the atomic system where  $u_{\alpha}(\mathbf{r})$  represents an atomic orbital. When the atomic sites are well separated so that the lattice constant is large compared to the range of  $u_{\alpha}(\mathbf{r})$  these orbitals will be a good approximation to the states of the full crystal Hamiltonian  $\mathcal{H}$ . As the atoms are brought closer to each other one can think of  $\mathcal{H}$  as being given by the atomic Hamiltonian plus a small perturbation  $U(\mathbf{r})$  which accounts for the corrections to the atomic potential in order to account for the presence of the other atoms. Thus

$$\mathcal{H} = H_{at} + U(\mathbf{r}) \quad (3.19a)$$

where

$$U(\mathbf{r}) = \sum_{i \neq 0} V(\mathbf{r} - \mathbf{R}_i) \quad (3.19b)$$

and the prime means that  $i = 0$  (which stands for  $R_i = 0$ ) must be excluded from the summation over lattice vectors  $R_i$ . One now constructs linear combinations of the  $u_\alpha(\mathbf{r})$  that preserve Bloch's description, i.e.,

$$\phi_{\alpha\mathbf{k}}(\mathbf{r}) = \frac{1}{\mathcal{N}^2} \sum_i \exp(i\mathbf{k}\cdot\mathbf{R}_i) u_\alpha(\mathbf{r}-\mathbf{R}_i) \quad (3.20)$$

chosen to preserve Bloch's theorem, i.e.,  $\phi_{\alpha\mathbf{k}}(\mathbf{r}+\mathbf{R}) = \exp(i\mathbf{k}\cdot\mathbf{R}) \phi_{\alpha\mathbf{k}}(\mathbf{r})$ , from which the Bloch wave functions are constructed, namely,

$$\psi_{n\mathbf{k}}(\mathbf{r}) = \sum_\beta a_{n\beta}(\mathbf{k}) \phi_{\beta\mathbf{k}}(\mathbf{r}) \quad (3.21)$$

where  $n$  is the band index. Schrödinger's equation

$$\mathcal{H} \psi_{n\mathbf{k}}(\mathbf{r}) = E_n(\mathbf{k}) \psi_{n\mathbf{k}}(\mathbf{r}) \quad (3.22a)$$

can then be multiplied from the left by  $\phi_{\alpha\mathbf{k}}^*(\mathbf{r})$  and integrated over all  $\mathbf{r}$  to give

$$\begin{aligned} \sum_\beta a_{n\beta}(\mathbf{k}) \int \phi_{\alpha\mathbf{k}}^*(\mathbf{r}) \mathcal{H} \phi_{\beta\mathbf{k}}(\mathbf{r}) d\mathbf{r} &= \\ &= E_n(\mathbf{k}) \sum_\beta a_{n\beta}(\mathbf{k}) \int \phi_{\alpha\mathbf{k}}^*(\mathbf{r}) \phi_{\beta\mathbf{k}}(\mathbf{r}) d\mathbf{r} \end{aligned} \quad (3.22b)$$

The matrix elements in this expression can be written in terms of the  $u_\alpha(\mathbf{r})$  using (3.20), i.e.,

$$\int \phi_{\alpha\mathbf{k}}^*(\mathbf{r}) \mathcal{H} \phi_{\beta\mathbf{k}}(\mathbf{r}) d\mathbf{r} = \frac{1}{\mathcal{N}} \sum_{i,p} e^{i\mathbf{k}\cdot(\mathbf{R}_i-\mathbf{R}_p)} \int u_\alpha^*(\mathbf{r}-\mathbf{R}_p) \mathcal{H} u_\beta(\mathbf{r}-\mathbf{R}_i) d\mathbf{r}$$

$$= \sum_j e^{i\mathbf{k}\cdot\mathbf{R}_j} \int u_\alpha^*(\mathbf{r}) \mathcal{H} u_\beta(\mathbf{r}-\mathbf{R}_j) d\mathbf{r} \quad (3.23)$$

where we called  $\mathbf{r}-\mathbf{R}_p = \mathbf{r}'$  and then  $\mathbf{r}-\mathbf{R}_i = \mathbf{r}' - (\mathbf{R}_i - \mathbf{R}_p) = \mathbf{r}' - \mathbf{R}_j$  and used the fact that the Hamiltonian is invariant with respect to a displacement by a lattice vector. Similarly the integral in the right hand side of (3.22b) can be written

$$\begin{aligned} \int \phi_{\alpha\mathbf{k}}^*(\mathbf{r}) \phi_{\beta\mathbf{k}}(\mathbf{r}) d\mathbf{r} &= \sum_j e^{i\mathbf{k}\cdot\mathbf{R}_j} \int u_\alpha^*(\mathbf{r}) u_\beta(\mathbf{r}-\mathbf{R}_j) d\mathbf{r} \\ &= \sum_j e^{i\mathbf{k}\cdot\mathbf{R}_j} S_{\alpha\beta}(\mathbf{R}_j) \end{aligned} \quad (3.24)$$

where  $S_{\alpha\beta}(\mathbf{R}_j)$  represents the overlap integral between the  $\alpha$  orbital at the origin and the  $\beta$  orbital on atom  $j$ . We can now use the explicit form of the Hamiltonian which we assumed to be given by (3.19) in (3.23). This gives

$$\begin{aligned} \int \phi_{\alpha\mathbf{k}}^*(\mathbf{r}) \mathcal{H} \phi_{\beta\mathbf{k}}(\mathbf{r}) d\mathbf{r} &= \\ \sum_j e^{i\mathbf{k}\cdot\mathbf{R}_j} \left[ \epsilon_\alpha^0 S_{\alpha\beta}(\mathbf{R}_j) + \sum_{i \neq 0} \int u_\alpha^*(\mathbf{r}) V(\mathbf{r}-\mathbf{R}_i) u_\beta(\mathbf{r}-\mathbf{R}_j) d\mathbf{r} \right] \end{aligned} \quad (3.25)$$

which can also be written as

$$\int \phi_{\alpha\mathbf{k}}^*(\mathbf{r}) \mathcal{H} \phi_{\beta\mathbf{k}}(\mathbf{r}) d\mathbf{r} = \sum_j e^{i\mathbf{k}\cdot\mathbf{R}_j} \epsilon_\alpha^0 S_{\alpha\beta}(\mathbf{R}_j)$$

$$\begin{aligned}
& + \sum_{i \neq 0} \int u_{\alpha}^*(\mathbf{r}) V(\mathbf{r}-\mathbf{R}_i) u_{\beta}(\mathbf{r}) d\mathbf{r} \quad (j = 0 \text{ term}) \\
& + \sum_{j \neq 0} e^{i\mathbf{k} \cdot \mathbf{R}_j} \int u_{\alpha}^*(\mathbf{r}) V(\mathbf{r}-\mathbf{R}_j) u_{\beta}(\mathbf{r}-\mathbf{R}_j) d\mathbf{r} \quad (i = j \text{ term}) \\
& + \sum_{j \neq 0} e^{i\mathbf{k} \cdot \mathbf{R}_j} \sum_{i \neq 0, j} \int u_{\alpha}^*(\mathbf{r}) V(\mathbf{r}-\mathbf{R}_i) u_{\beta}(\mathbf{r}-\mathbf{R}_j) d\mathbf{r} \quad (3.26)
\end{aligned}$$

The matrix element in the second line represents the effect of the potential of all other sites on the central atom and is called the crystal field term  $K_{\alpha\beta}(\mathbf{R}_i)$ . The term in the third and fourth lines represent the two-centre hopping integral  $H_{\alpha\beta}(\mathbf{R}_j)$  and the three-centre integral  $H_{\alpha\beta}(\mathbf{R}_i, \mathbf{R}_j)$  respectively. Inserting (3.26) and (3.24) back into (3.22b) gives

$$\begin{aligned}
\sum_{\beta} a_{n\beta}(\mathbf{k}) \left( [\epsilon_{\alpha}^0 - E_n(\mathbf{k})] \sum_i e^{i\mathbf{k} \cdot \mathbf{R}_i} S_{\alpha\beta}(\mathbf{R}_i) \right. \\
\left. + \sum_{i \neq 0} K_{\alpha\beta}(\mathbf{R}_i) + \sum_{i \neq 0} e^{i\mathbf{k} \cdot \mathbf{R}_i} H_{\alpha\beta}(\mathbf{R}_i) + \sum_{i \neq 0} e^{i\mathbf{k} \cdot \mathbf{R}_i} \sum_{j \neq 0, i} H_{\alpha\beta}(\mathbf{R}_i, \mathbf{R}_j) \right) = 0
\end{aligned} \quad (3.27)$$

In the TB approximation this expression can be simplified to a large extent. One can start by neglecting three-center terms and assuming that two center terms are negligible if  $R_i$  is larger than the nearest neighbour (nn) distance. The overlap integral can be simplified by assuming that the basis functions are orthogonal and if by crystal symmetry  $K_{\alpha\beta}(\mathbf{R}_i) = K_{\alpha\alpha}(\mathbf{R}_i) \delta_{\alpha\beta}$  we get the secular equation

$$\det \left( \left[ \epsilon_{\alpha}^0 + \sum_{i \neq 0} K_{\alpha\alpha}(\mathbf{R}_i) - E_n(\mathbf{k}) \right] + \sum_{i \neq 0} e^{i\mathbf{k} \cdot \mathbf{R}_i} H_{\alpha\beta}(\mathbf{R}_i) \right) = 0 \quad (3.28)$$

whose eigenvalues  $E_n(\mathbf{k})$  correspond to the bandstructure of the material.

In the case of a single s-band for example, the TB band structure is easily found to be given by

$$E_s(\mathbf{k}) = \epsilon_s + \sum_{i \neq 0} e^{i\mathbf{k} \cdot \mathbf{R}_i} ss\sigma \quad (3.29)$$

in which the  $ss\sigma$  hopping integral is not dependent on the direction of the vector  $\mathbf{R}_i$  but only on its magnitude and  $\epsilon_s$  corresponds to the diagonal energy corrected by the crystal field effects. For the simple cubic lattice it then follows that the bottom ( $\mathbf{k} = (0,0,0)$ , i.e., the center of the Brillouin zone) and the top ( $\mathbf{k} = (\pi/a)(1,1,1)$ , i.e., the zone boundary) of the s-band have the energies  $E_b = \epsilon_s - 6 \cdot |ss\sigma|$  and  $E_t = \epsilon_s + 6 \cdot |ss\sigma|$  respectively. Thus the band width of the simple cubic single s-band within TB is given by  $12 \cdot |ss\sigma|$ . In the next chapter we shall be scaling our energy calculations in terms of this band-width.



### §3.4 The Chemical Pseudopotential Method

The tight-binding approximations are acceptable in the case of fairly localized orbitals like the transition metal systems which are characterized by a well localized d-band. It is more difficult to accept those approximations when the overlap between neighbouring orbitals is appreciable like in the case of sp-bonded systems. The non-orthogonality contributions play a very important part in systems where the atomic orbitals are not well localized. In fact these terms have been shown to be the largest one in total energy calculations for  $H_2$  (Skinner and Pettifor) and sp-bonded materials (Majewski and Vogl 1987). However it is possible, in principle, to include overlap and three-center terms within the TB formalism by working with a basis of chemical pseudopotential orbitals (Anderson 1969, Bullett 1975a 1975b). In the Anderson-Bullett scheme one thinks of the system of  $N$  atoms as being divided into  $N$  atomic subsystems each of which is assigned to a Hamiltonian  $H_a$ . The term subsystem allows room for generalizations but, in particular, they can always be identified with isolated atomic systems. The Hamiltonian of the whole system is then written as

$$H = H_a + \sum_{b \neq a} V_b \quad (3.30)$$

where  $H_a = T + V_a$  is the Hamiltonian of the isolated atom  $A$ ,  $T$  being the kinetic energy. A set of localized orbitals  $\phi_a \equiv |a\rangle$  are defined by Anderson (op.cit.) by

$$\left( T + V_a + \sum_{b \neq a} (V_b - |b\rangle\langle b|V_b) \right) |a\rangle = \epsilon_a |a\rangle \quad (3.31)$$

This represents a set of  $N$  equations which once solved (self-consistently) gives the set  $\phi_a$  which can be used to expand the Hamiltonian eigen functions  $|\psi_n\rangle$  given by the Schrödinger equation

$$H|\psi_n\rangle = E_n |\psi_n\rangle \quad . \quad (3.32)$$

Thus writing

$$|\psi_n\rangle = \sum_a c_{na} |a\rangle \quad (3.33)$$

and inserting this into (3.32) and using (3.31) one gets the secular determinant (Anderson 1969)

$$\det \left( (\epsilon_a - E_n) \delta_{ab} + \langle a | V_a | b \rangle (1 - \delta_{ab}) \right) = 0 \quad . \quad (3.34)$$

From (3.31) we also see that

$$\epsilon_a = \langle a | T + V_a | a \rangle + \sum_{b \neq a} \langle a | V_b | a \rangle + \sum_{b \neq a} \langle a | b \rangle \langle b | V_b | a \rangle \quad . \quad (3.35)$$

Expression (3.34) should be compared with (3.28) obtained by making the TB approximations. The off-diagonal elements in (3.34) are of the two-center type although no approximations were made to achieve this result. The overlapping terms neglected in (3.28) appear in the diagonal elements  $\epsilon_a$  as can be seen from the third term in (3.35). Therefore the chemical pseudopotential method has provided a basis for the justification of the use of TB binding in the study of sp-bonded systems.

### §3.5 The Total and the Binding Energies

In the next chapter we will be studying the relative stability amongst several different crystal structures by comparing their binding energies. Let us then discuss briefly the energies involved in the total energy  $E_{\text{tot}}$  of the solid. It can be written as

$$E_{\text{tot}} = E_{\text{ee}} + E_{\text{ei}} + E_{\text{ii}} \quad (3.36)$$

thus separating the contributions from the electron–electron (ee), electron–ion (ei) and ion–ion (ii) interaction energies. The electron–electron term includes the kinetic energy, the interelectronic Coulomb energy (Hartree term) and the exchange and correlation energy  $E_{\text{xc}}[\rho]$ . More explicitly we have

$$E_{\text{tot}} = E_{\text{kin}} + E_{\text{H}} + E_{\text{xc}} + E_{\text{ei}} + E_{\text{ii}} \quad (3.37)$$

This total energy expression can be written in terms of the band energy  $E_{\text{band}}$ . Within density functional theory (Hohenberg and Kohn 1964, Kohn and Sham 1965)  $E_{\text{band}}$  can be obtained by summing the eigenvalues of the one–electron equation

$$\left( \frac{\hbar^2}{2m} \nabla^2 + V_{\text{KS}}[\rho(\mathbf{r})] \right) \phi_j(\mathbf{r}) = E_j \phi_j(\mathbf{r}) \quad (3.38)$$

over all the occupied states (see (3.6)). In this expression the Kohn–Sham potential has the form

$$V_{\text{KS}}[\rho(\mathbf{r})] = V_{\text{ext}}(\mathbf{r}) + V_{\text{H}}[\rho(\mathbf{r})] + \mu_{\text{xc}}[\rho(\mathbf{r})]$$

$$= V_{\text{ext}}(\mathbf{r}) + e^2 \int d\mathbf{r}' \frac{\rho(\mathbf{r}')}{|\mathbf{r} - \mathbf{r}'|} + \frac{\delta E_{\text{xc}}[\rho]}{\delta \rho(\mathbf{r})} \quad (3.39)$$

where  $V_{\text{ext}}(\mathbf{r})$  represents the external potential produced by the atoms' core (which gives rise to  $E_{\text{ei}}$  in (3.36)) and the other two terms represent the Coulomb and exchange–correlation potentials respectively. Expression (3.38) must be solved self–consistently for the charge density  $\rho(\mathbf{r}) = \sum |\phi_j(\mathbf{r})|^2$  and the unknown xc potentials are usually treated in the local density approximation (LDA)

$$E_{\text{xc}}[\rho] \cong \int d\mathbf{r} \rho(\mathbf{r}) \varepsilon_{\text{xc}}[\rho(\mathbf{r})] \quad (3.40)$$

where  $\varepsilon_{\text{xc}}[\rho(\mathbf{r})]$  is the xc energy per electron of a uniform electron gas of density  $\rho$ . When self–consistency is reached the kinetic energy can be evaluated by

$$E_{\text{kin}} = \sum_j \langle \phi_j | E_j - V_{\text{KS}}[\rho] | \phi_j \rangle \quad (3.41)$$

Inserting this back into (3.37) and using (3.39) gives

$$E_{\text{tot}} = \sum_j E_j - \frac{1}{2} E_{\text{H}} - \int \rho(\mathbf{r}) \mu_{\text{xc}}[\rho(\mathbf{r})] d\mathbf{r} + E_{\text{xc}} + E_{\text{ii}} \quad (3.42)$$

where  $\sum E_j = E_{\text{band}}$ . For simplicity of notation let us group together the electrostatic and xc terms which we call  $E_{\text{dc}}$  (the double–counting term). Then

$$E_{\text{tot}} = E_{\text{band}} + E_{\text{dc}} + E_{\text{ii}} \quad (3.43)$$

In the Harris–Foulkes (Harris 1985, Foulkes 1987) approximation to density functional theory the Kohn–Sham equation (3.38) is not iterated to

self-consistency but solved only once for the charge density starting with an input charge density  $\rho_f$ . This is given by a superposition of atomic charge densities and an approximate  $\rho_{out}$  to the true self consistent ground state charge density is obtained as a result of a sole iteration. Within the Harris-Foulkes scheme an approximate expression for the total energy of the solid can then be written as

$$E_{tot} = \hat{E}_{band} + \hat{E}_{dc} + E_{ii} \quad (3.44)$$

where  $\hat{E}_{band}$  and  $\hat{E}_{dc}$  are evaluated using  $\rho_{out}$  and  $\rho_f$  respectively. This expression is valid in first order in the charge densities differences  $(\rho_{sc} - \rho_{out})$  and  $(\rho_{sc} - \rho_f)$ . Sutton et al (1988) showed that, if non-orthogonality is neglected, the binding energy (i.e., the total energy minus the energy of the isolated atoms) can be written to first order as

$$E_b = E_{bond} + E_{pr} + \Delta E_{es} + \Delta E_{xc} \quad (3.45)$$

where  $E_{pr}$  is the promotion energy. The last two terms represent the change in the electrostatic and exchange and correlation energies respectively in going from the system of isolated atoms to a solid state system consisting of overlapping atomic charge densities. These can be approximated by a sum of pair potentials. Therefore

$$E_b = E_{bond} + E_{pr} + E_{rep} \quad (3.46)$$

The inclusion of non-orthogonality leads from equation (3.35) to an additional repulsive pairwise contribution, which is very important in sp-bonded systems (see for example Majewski and Vogl (1987), Skinner and Pettifor).

### §3.6 Conclusions

In this chapter we presented the basic constituents of the total energy of the solid. The TB approximation for extended systems was shown to be justifiable, in principle, with the use of a suitably chosen basis set within the Anderson-Bullett chemical pseudopotential approach. An expression for the binding energy was presented which will be basic in the study of relative structural stability that is undertaken in the next section. The binding energy expression was shown to be backed up by a first order approximation within density functional theory. Therefore the grounds are firm for the next step to follow, namely the application of the ideas described so far in a real situation which is taken to be the study of the relative stability of sp-bonded systems.

## CHAPTER 4 : Structural Stability of the sp-Bonded Elements

In this Chapter the relative stability of the most common sp-bonded elemental systems is investigated using a tight-binding model for cohesion. The structures considered range from coordination one for the dimers through coordination four for the diamond lattices to coordination twelve for the close packed fcc and hcp systems. A simple tight-binding model is used to determine the sp-band energy of the different structures. The bond-lengths are "prepared" in accordance with the structural energy difference theorem and Harrison's  $R^{-2}$  scaling model is used to set the relevant hopping integrals. The model shows a good agreement with the observed structural trends across the periodic table.

## §4.1 Introduction

Our main interest in this chapter is to develop a theory that explains the global trends observed in the periodic table for the relative stability of the  $sp$  elements (Wyckoff 1963, Donohue 1974). For example as one departs from the far left side of the table one goes from the close-packed metals like Na and Mg through the four-fold coordinated semiconductors Si and Ge to the group VII elements whose tendency is to form molecular crystals in which the basic entities are molecules (dimers) which are bound together by a covalent bonding. At the bottom of group IV one finds metallic Pb which crystallizes in the fcc structure. It has been shown that this close-packed arrangement for lead is due to relativistic shifts which widen the  $sp$ -splitting and makes Pb metallic (Christensen et al 1986). The solid noble gases at the extreme right of the table crystallize in monatomic fcc lattices (except for He). The very stable closed shells remain so in the solid which is held together by weak van der Waals forces. Therefore these elements will be left out of this discussion. In table 4.1 we list the  $sp$ -bonded elements along with their low temperature structural phase (Donohue 1974).

In attempting to reproduce these trends we will be aiming at developing a model that incorporates both simplicity and predictive power as basic ingredients. Accurate calculations such as those from *ab-initio* local density functional theory (e.g. Yin and Cohen 1980, 1981) rely on heavy computing and do not provide easy physical insight. The use of adjustable parameters within semi empirical calculations on the other hand is also unsatisfactory because different parameters would have to be used for different structures and interpretation of the results would be difficult. We shall rather concentrate on the physics of the



Table 4.1

IA	IIA	IIIB	IVB	VB	VIB	VIIB
H (dim)						
Li (hcp)	Be (hcp)	B (compl)	C (gra)	N (dim)	O (dim)	F (dim)
Na (hcp)	Mg (hcp)	Al (fcc)	Si (dia)	P (compl)	S (chain)	Cl (dim)
K (bcc)	Ca (fcc)	Ga (compl)	Ge (dia)	As (lay)	Se (chain)	Br (dim)
Rb (bcc)	Sr (fcc)	In (tetr)	Sn (dia)	Sb (lay)	Te (chain)	I (dim)
Cs (bcc)	Ba (bcc)	Th (hcp)	Pb (fcc)	Bi (lay)	Po (sc)	As (dim)
Fr (···)	Ra (bcc)					

Table 4.1. The sp-bonded elements and their structural arrangements: dim dimer, hcp hexagonal close packed, bcc body centred cubic, fcc face centred cubic, compl complex, tetr tetragonal, gra graphite, dia diamond, lay, chain and dimers are for structures made up from puckered layers, helical chains and dimers, respectively.

problem and work with a model which is as simple and universal as possible. The tight-binding (TB) bond model (Pettifor 1986, Sutton et al 1988 and chapter 2 this work) will be used with the hopping integrals following Harrison's (1980)  $1/R^2$  decaying law. Our calculations are made within the two centre orthogonal approximation and the TB hopping integrals are assumed to be transferable from one structure to another. Local densities of states are calculated using the real space recursion method (Haydock et al 1972, 1975) reviewed in chapter 3. These TB real space calculations are particularly useful because they make contact with the local atomic environment of each site. This access to the local topology of the lattice is of great importance in our study and will be fully exploited in the next chapter to provide a simple physical understanding of the predicted trends.

## §4.2 The Model

The binding energy  $E_b$  of a system of atoms is defined as the total energy of the system minus the energy of the free atoms, i.e., when infinitely separated. In the tight-binding bond model of Sutton et al (1988)  $E_b$  is given by (3.46) which we rewrite here

$$E_b = E_{\text{bond}} + E_{\text{pr}} + E_{\text{rep}} \quad (4.1)$$

$E_{\text{pr}}$  is the promotion energy, i.e., the change in energy due to the differences in individual orbital occupation when going from the infinitely separated atoms to the solid state system.  $E_{\text{rep}}$  is a repulsive energy difference arising from the change in the electrostatic and exchange-correlation energies as the atoms are brought together to form the final system. Its electrostatic part involves the ion-ion, electron-ion and electron-electron electrostatic energies. Sutton et al showed that the repulsive term can be approximated as a sum of pair potentials (see also Ducastelle 1970).

In the tight-binding bond model the exact ground state charge density is approximated by the sum of overlapping atomic charge densities following Harris (1985) and Foulkes (1987). The Kohn-Sham equations (Kohn and Sham 1965, Hohenberg and Kohn 1964) are not iterated to self-consistency, the Hamiltonian being the result of a single iteration which produces an output charge density  $\rho_{\text{out}}$ . The error involved in this approximation has been shown (Harris op.cit.) to be of second order in the difference  $\rho_{\text{out}} - \rho_f$  where  $\rho_f$  is the superposition of atomic charge densities used as an input. The approximated single particle Hamiltonian  $\tilde{H}$  and the corresponding charge density  $\rho_{\text{out}}(\mathbf{r})$  give the band energy (Sutton et al op.cit.), namely,

$$E_{\text{band}} = \text{Tr } \rho_{\text{out}} \tilde{H} \quad (4.2a)$$

$$= \text{Tr } (\rho_{\text{out}} - \rho_f) \tilde{H} + \text{Tr } \rho_f \tilde{H} \quad (4.2b)$$

In the atomic orbital representation the first term in this equation represents  $E_{\text{bond}} + E_{\text{pr}}$  (Sutton et al 1988) which can be seen by separating the on-site and inter-site contributions to the trace. Therefore

$$E_{\text{bond}} + E_{\text{pr}} = E_{\text{band}} - \text{Tr } \rho_f \tilde{H} \quad (4.3)$$

If we assume that the on site matrix elements of the crystal Hamiltonian are diagonal with respect to the different orbitals, i.e.,  $\tilde{H}_{i\alpha, i\beta} = 0$  for  $\alpha \neq \beta$  the reference energy can be written as

$$\text{Tr } \rho_f \tilde{H} = \sum_{i\alpha} (\rho_f)_{i\alpha, i\alpha} \tilde{\epsilon}_{i\alpha} \quad (4.4)$$

where we stress that the matrix elements of the density are free atomic quantities whereas the energy values are the free atomic diagonal Hamiltonian matrix elements corrected by the crystal field terms in the solid state.

In order to find out the relative stability of two given structures one has to compare their binding energies. This calculation has to be done at the equilibrium volume  $V_{\text{eq}}$  (or equilibrium bond length) of each structure. The immediate difficulty is that different structures crystallize at different and unknown values of  $V_{\text{eq}}$ . The volume changes can be neglected in the case of close-packed elemental metals because there is little volume difference between one

phase and another. Their relative stability can then be correctly predicted by comparing their band energies at fixed volumes (Jones 1937, Pettifor 1983). However there may be large volume changes between two structures like, say, diamond and fcc and therefore their energy difference can not be obtained by comparing  $E_b$  at fixed atomic volume. Notice also that experimental assessment to this quantity is impossible for any structure other than the actual observed equilibrium one. On the other hand the *ab-initio* determination of  $E_b$  versus Volume curves generally involves heavy computing (Yin and Cohen 1980,1981) which would have to be done for every structure and element of interest.

The structural energy difference theorem (Pettifor 1986) allows one to prepare the relative volumes of two given structures at which  $\Delta E_b$  can be computed within an approximation that is exact to first order in  $\Delta E_b/E_b$ . Let us see this. Consider structures 1 and 2 with equilibrium volumes  $V_1$  and  $V_2$  respectively. Then  $\Delta E_b$  is given by

$$\Delta E_b = E_{b2}(V_2) - E_{b1}(V_1) \quad . \quad (4.5)$$

Expanding  $E_{b2}(V)$  around the equilibrium volume  $V_2$  gives

$$\begin{aligned} E_{b2}(V) &= E_{b2}(V_2) + \frac{1}{2} (V - V_2)^2 \left( \frac{d^2 E_{b2}}{dV^2} \right)_{V=V_2} + \dots \\ &\simeq E_{b2}(V_2) + \frac{1}{2} \left[ \frac{V - V_2}{V_2} \right]^2 V_2 \left( V_2 \frac{d^2 E_{b2}}{dV^2} \right)_{V=V_2} \\ &\simeq E_{b2}(V_2) + \frac{1}{2} B_2 V_2 \left[ \frac{V - V_2}{V_2} \right]^2 \end{aligned}$$

where the first derivative is equal to zero when taken at  $V_2$  and  $B_2$  is the bulk modulus of structure 2. Let us call  $\hat{V}_2$  the volume at which structure 2 displays the same repulsive energy as structure 1, i.e.,

$$E_{\text{rep}2}(\hat{V}_2) = E_{\text{rep}1}(V_1) \quad (4.6)$$

Since the expression above for  $E_{b2}(V)$  holds for any value of  $V$  we can evaluate it for  $V = \hat{V}_2$  which gives

$$E_{b2}(V_2) \simeq E_{b2}(\hat{V}_2) - \frac{1}{2} B_2 V_2 \left[ \frac{\hat{V}_2 - V_2}{V_2} \right]^2 \quad (4.7)$$

One can show (Pettifor 1986) that the second term in this expression is of second order in  $\Delta E_b/E_b$ . Therefore from (4.5) and (4.7) we see that the energy difference between two structures in equilibrium is given to first order in  $\Delta E_b/E_b$  by  $(\Delta E_b)_{\Delta E_{\text{rep}}=0}$ .

Using the structural energy difference theorem one can calculate the energy difference between two structures by

$$(\Delta E_b)_{\Delta E_{\text{rep}}=0} = \Delta(E_{\text{bond}} + E_{\text{pr}}) \quad (4.8)$$

which follows from (4.1). From (4.3) we see that this is also equal to  $\Delta(E_{\text{band}} - \text{Tr} \rho_f \tilde{H})$  and using (4.4) we can write

$$\Delta(\text{Tr} \rho_f \tilde{H}) = N_s \left[ \tilde{\epsilon}_s^{(2)} - \tilde{\epsilon}_s^{(1)} \right] + N_p \left[ \tilde{\epsilon}_p^{(2)} - \tilde{\epsilon}_p^{(1)} \right] \quad (4.9)$$

and we see that  $\Delta(\text{Tr} \rho_f \tilde{H}) = 0$  if  $\Delta \tilde{\epsilon}_s = \Delta \tilde{\epsilon}_p = 0$ . This condition means that the change in the atomic energy levels is the same for both environments 1 and 2.

Therefore we can write the difference in the binding energy in (4.8) as

$$\Delta E_b = \Delta(E_{\text{band}})_{\Delta \epsilon_{s,p}=0} \quad (4.10)$$

where we dropped the tilde in the notation for the energy levels.

This tight binding model of cohesion strictly applies to covalent bonded systems only. We will see however that the nearly free electron close packed metals like Na, Mg and Al will also be neatly separated. That the nearly free electron band structure can be described within a localized atomic functions framework can be seen from the work of Singhal and Callaway (1977) on Al.

### §4.3 Structures Considered

As explained before the basic question we seek to answer is what happens when infinitely separated elemental  $sp$  atoms are brought together to form a solid. More specifically our interest resides in determining what kind of structure will be preferred by the atoms or, in other words, which geometric environment will correspond to the minimum of the equilibrium binding energies out of the several structures considered. We focus attention on several possible arrangements corresponding to a wide range of the coordination number  $z$ , this being the number of first neighbours of a given atomic site. The structures considered here, together with their coordination, are the following:

<u>STRUCTURE</u>	<u>COORDINATION</u>
dimer	1
zig-zag chain	2
honey comb	3
cubic diamond	4
hexagonal diamond	4
simple cubic	6
simple hexagonal	8
bcc	8 + 6
fcc	12
hcp	12

Let us discuss the low dimensional structures first. The lowest possible coordinated arrangement is the dimer which is a simple diatomic molecule like,



e.g.,  $H_2$ . The one dimensional representative, namely the zig-zag chain, was chosen to resemble the observed structures for the group VI elements S, Se and Te (Harrison 1980 p93). This is a chain that coils up along the [111] direction in a simple cubic structure, e.g., starting in the [100] direction along a cube edge, then going along [010], then in the [001] and then restarting again in the [100] direction, and so on (figure 4.1). The actual observed structure is a collection of interacting distorted zig-zag chains with a bond angle of  $105^\circ$  each. The inter chain interaction is small though non-negligible. Here we will only take into account the intra chain bonding with the bond angle equal to  $90^\circ$ . The three fold coordinated honey comb lattice is the familiar non Bravais planar structure (e.g. Ashcroft and Mermin 1976) that fills up the plane with hexagons. The three dimensional structure of graphite is made up of carbon atoms in this two dimensional structure with the distance between successive planes (these are stacked one above the other and displaced laterally) being more than twice the nearest neighbour distance in the plane (Harrison op.cit. p90).

Now we come to the three dimensional arrangements. Figures will be shown in the more general case of the AB binary compounds in chapter 6. Let us start with the close packed structures. It is interesting to note that the densest possible *periodic* sphere packing in three dimensions corresponds to the 12-fold coordinated face-centered cubic (fcc) arrangement (Zangwill and Bruinsma 1987). This structure along with the hexagonal close-packed (hcp) – which fills up space equally efficiently – and the body-centered cubic (bcc) structures is the crystalline arrangement preferred by nearly 75% of the elements of the periodic table at room temperature and atmospheric pressure. The fcc bravais lattice can be seen as a stacking sequence of identical spheres in which the different layers correspond to planar close packed triangular lattices arranged in a  $\dots ABCABCABC\dots$

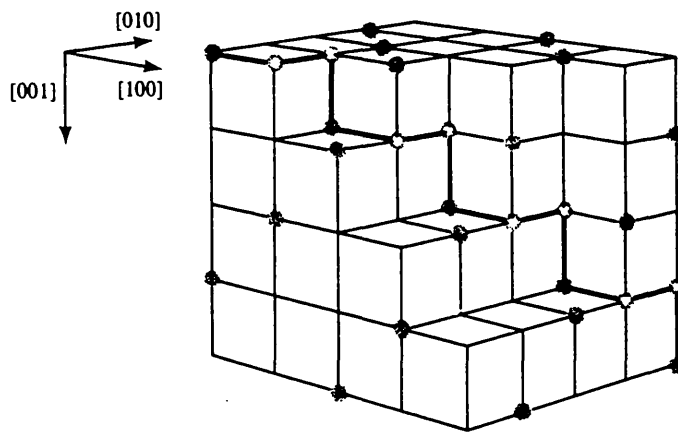


Figure 4.1

The zig-zag chain considered in the text (after Harrison 1980 p93). The chain coils up along a  $[111]$  direction as shown in the figure. The actual structure of Se is a distorted variant of this one with bond angles equal to 105 degrees and intrachain atom distances being larger than interchain distances.

fashion as explained in most text books. Each atom has therefore six neighbours in the plane plus three in the plane above and other three in the plane below. The non-Bravais hcp structure is generated in much the same way by the stacking sequence  $\dots ABABAB\dots$ , which add an extra degree of complexity to the arrangement due the absence of the C planes. The  $c/a$  ratio (where  $c/2$  is the distance between consecutive planes) is taken as the ideal one namely  $c/a = (8/3)^{1/2}$ . The bcc bravais lattice is best seen as the simple cubic structure with an atom in the centre of each cube. Although more loosely packed than fcc and hcp, this structure is also normally seen as a close-packed arrangement. It has eight first neighbours each one in the corner of a cube but its six second neighbours are only about 15% away and have usually to be taken into account. The 8-fold simple hexagonal lattice corresponds to the sequence  $\dots AAAA\dots$ . For a given atom there are six near neighbours in the same layer and two in different layers, one above and one below. Finally, the four-fold coordinated cubic (hexagonal) diamond structure is constructed from the fcc (hcp) arrangement by inserting another plane between each two, directly above the one below, at three quarters of the distance between them. Cubic diamond is a special case of the zincblende structure in which the  $\dots ABCABCABC\dots$  sites (i.e., the fcc sites) are occupied by zinc atoms whereas the new layers inserted between the planes are occupied by sulfur atoms. It is much the same thing for hexagonal diamond now with respect to the wurtzite structure. In this case one type of atom occupies the underlying hcp sites whilst a second atom species is inserted between each two of the close-packed planes just as in zincblende. It is not difficult to see that both in cubic and hexagonal diamond each atom lies in the centre of a regular tetrahedron whose base is perpendicular to the z axis (i.e. the c-direction).

#### §4.4 Computational Details

For the calculation of the band energy we employ a TB model in the two centre approximation as described in the section 4.2. The band energy then depends on the TB hopping integrals (Slater and Koster 1954)  $(ss\sigma)$ ,  $(sp\sigma)$ ,  $(pp\sigma)$  and  $(pp\pi)$  which are assumed to obey Harrison's semi-empirical  $1/R^2$  law (see Harrison 1980 and references therein). This behaviour was obtained by fitting band energies obtained from LCAO and free-electron theory. Selected energy differences obtained in these two limits were equated which gave the power law dependence above because the free-electron energy is proportional to  $R^{-2}$ . The corresponding coefficients once adjusted to fit the bands of Silicon and Germanium give the following ratios

$$(ss\sigma):(sp\sigma):(pp\sigma):(pp\pi)::-1.40:1.84:3.24:-0.81 \quad (4.11)$$

which gives  $-0.25$  for the ratio  $(pp\pi)/(pp\sigma)$ . As we shall see later this ratio turns out to be too small to describe correctly the stability trend at the most bonding part of the spectra (i.e., at  $N_{sp} = 1$ ). These ratios are dependent only upon the crystal structure. We shall however, for the sake of the simplicity (or universality) of the model, assume that they are universal and totally transferable parameters.

The "preparation" of the volumes at which the energies are to be compared is implicitly given by the equation  $\Delta E_{rep} = 0$ , as prescribed by the structural energy difference theorem. If the hopping integrals have the same  $R$  dependence through some function  $F(R)$  as given above and if we further assume that the pair potentials  $h_{pp}$  depend on the bond length as  $h_{pp} \sim [F(R)]^2$ , it is easy to show that  $\Delta E_{rep} = 0$  is equivalent to impose that there is no change in

the second moment  $\mu_2$  of the density of states, i.e.,

$$\Delta\mu_2 = 0 \quad . \quad (4.12)$$

A same type of power law dependence for the pair potentials was used by Pettifor and Podloucky (1986) in the study of the pd-bonded AB compounds. This condition for  $\mu_2$  is independent of the particular form of  $F(R)$  if only first neighbours are considered. However if second neighbours are also taken into account (e.g. for the bcc lattice) then the explicit form of  $F(R)$  has to be given. All this is discussed in appendix III.

Given the hopping integrals the band energy can be calculated as a function of the atomic level difference  $\epsilon_{sp} = \epsilon_s - \epsilon_p$  and the total number of valence electrons. The relative energies of the different structures are then compared for different choices of  $\epsilon_{sp}$  as a function of the band filling. The centre of gravity of the bands are fixed to the zero of energy, i.e.,  $\epsilon_s + 3\epsilon_p = 0$ . This condition along with the value of  $\epsilon_s - \epsilon_p$  gives the values of each of the s and p atomic energies. The local density of states is computed using the recursion method in which the continued fraction is terminated with either the square root (continuum spectrum) or Turchi's termination (single band gap). The band edges for the continuum DOS are calculated using Beer and Pettifor (1984) optimized prescription. The single band gap edges are determined using Beer's (1985) generalized procedure with the safety device presented in chapter 2.

A reference structure has to be given from which the volumes (or the bond-lengths) of the other structures are calculated. (This reference for volume calculation should not be confused with the reference for the energy calculation, usually chosen as a skew DOS or a cubic spline) The reference we chose is the simple cubic Bravais lattice. Since we are only interested in relative energy calculations we can fix one of the interatomic matrix elements to a given value, say

$(ss\sigma)_{sc} = -1$ , and calculate the others using Harrison's ratios. The corresponding values of the hopping integrals for the other structures are then determined imposing  $\Delta\mu_2 = 0$  with  $\mu_2$  being given by

$$\mu_2 = \mathcal{Z} \left[ (ss\sigma)^2 + 2(sp\sigma)^2 + (pp\sigma)^2 + 2(pp\pi)^2 \right] \quad (4.13)$$

where  $\mathcal{Z}$  is the coordination. The values of  $\epsilon_{sp}$  will be chosen to scale with the band-width of the simple cubic s band which is given by  $12|(ss\sigma)_{sc}|$ . More specifically

$$\epsilon_{sp} = 12|(ss\sigma)_{sc}| \tan(n\pi/10) \quad (4.14)$$

with  $n = \pm 1, \pm 2, \pm 3, \pm 4$  and  $\pm 5$ . For  $n = \pm 5$  we have  $\epsilon_{sp} = \pm\infty$  meaning that the s and p orbitals are very far apart. Thus the band filling at the bonding part of the spectrum starts either with s-electrons ( $\epsilon_{sp} = -\infty$ ) or with p-electrons ( $\epsilon_{sp} = +\infty$ ).

All energies in this work will be calculated with respect to the value chosen for  $(ss\sigma)$ , namely  $(ss\sigma) = -1$ . We will be only interested in energy differences and therefore the absolute scale is not relevant.

#### 4.4.1 Convergence with the Number of Levels

Let us check for the number of exact levels in the continued fraction necessary to achieve a suitable accuracy for detecting the structural energy differences. We show here the results for the honey-comb ( $\mathcal{Z} = 3$ ), simple cubic

( $z=6$ ) and fcc ( $z=12$ ) lattices but we have checked that similar results hold for all the other structures.

Figure 4.2a shows the structural energy for the case when only one  $s$ -orbital occupies the lattice sites, the atomic level  $\epsilon_s$  made equal to zero. We keep the plots in the same scale for comparison. As we did in chapter 2 a reference DOS consisting of a skew density of states sharing the same first four moments (i.e.,  $\Delta\mu_n = 0$ ,  $n = 0, 1, 2,$  and  $3$ ) as the simple cubic structure was subtracted to make the energy differences more dramatic. A reference chosen in this way incorporates the gross features of the DOS of the real structures and therefore its structural energy versus band filling curve follows closely the parabolic-like behaviour of the real curves thereby emphasizing the differences. Notice that in this scale (which is the one used for reading the relative energy differences) convergence is practically achieved for a cluster with around six exact shells (or levels). This result agrees with Beer (1985) studies for the close packed fcc, bcc and hcp transition metals DOS. Figure 4.2b shows the same plots on a magnified scale. Here a cubic spline fitted to all data points (except the dimer) was chosen as the reference with respect to which the structural energies were calculated (as explained in chapter 3 a spline is chosen as the reference either when a more dramatic separation of the energy curves is needed or when the fitting of a skew DOS is not possible). The corresponding knots (see chapter 2) were chosen as 0.5, 1.0 and 1.5. We notice that as the number of exact levels increases, the structural energy curves oscillate more and more around the curve with 10 exact levels. This is in accordance with Ducastelle and Cyrot-Lackmann theorem (1971 and chapter 3, this work) since increasing the number of levels means increasing the number of exact moments common to the two clusters which increases the number of zeros in

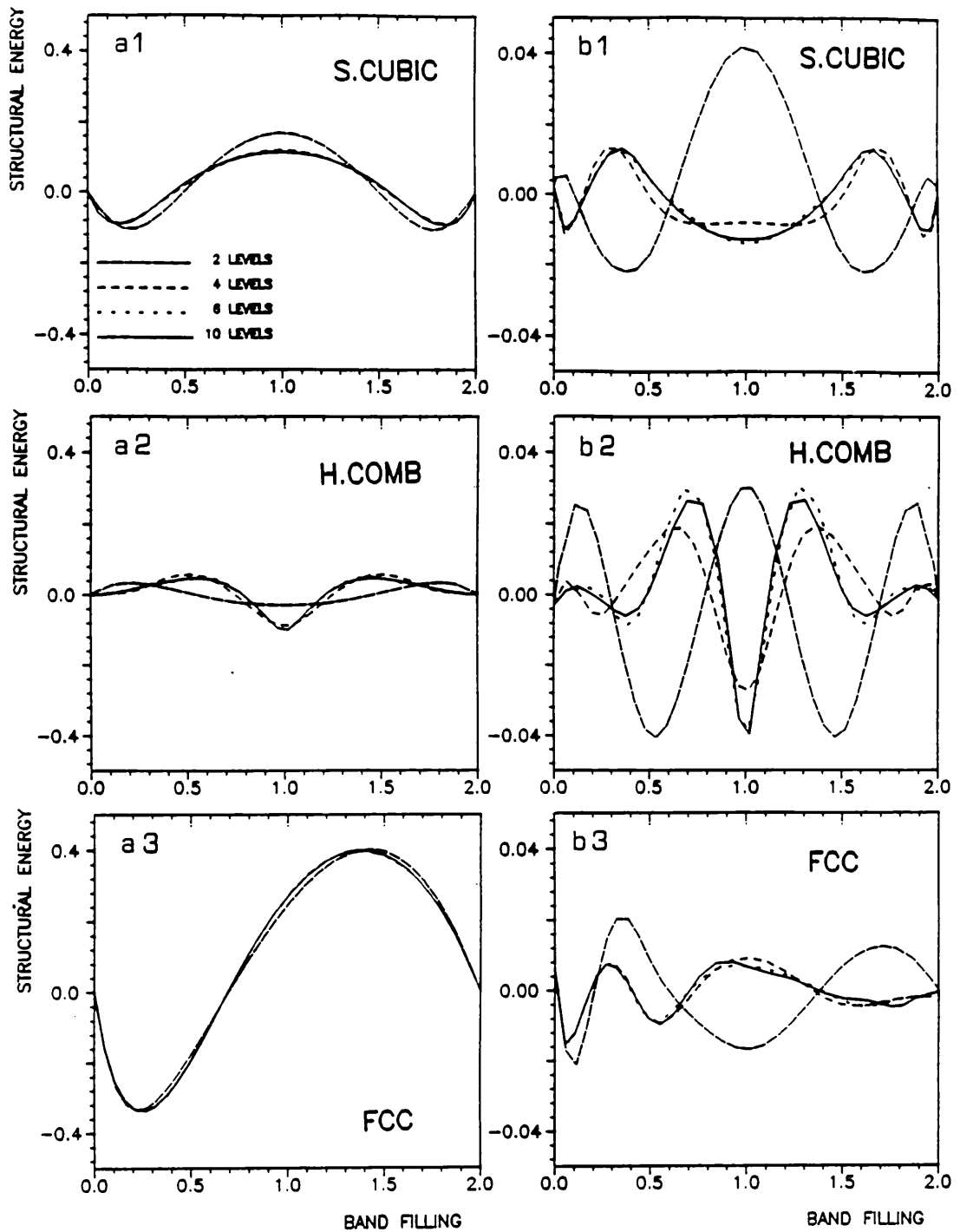


Figure 4.2  
 a) Single s-band ( $\epsilon_s=0$ ) structural energy versus band filling curves showing the convergence with the number of levels. b) The same as a) but in a magnified scale.



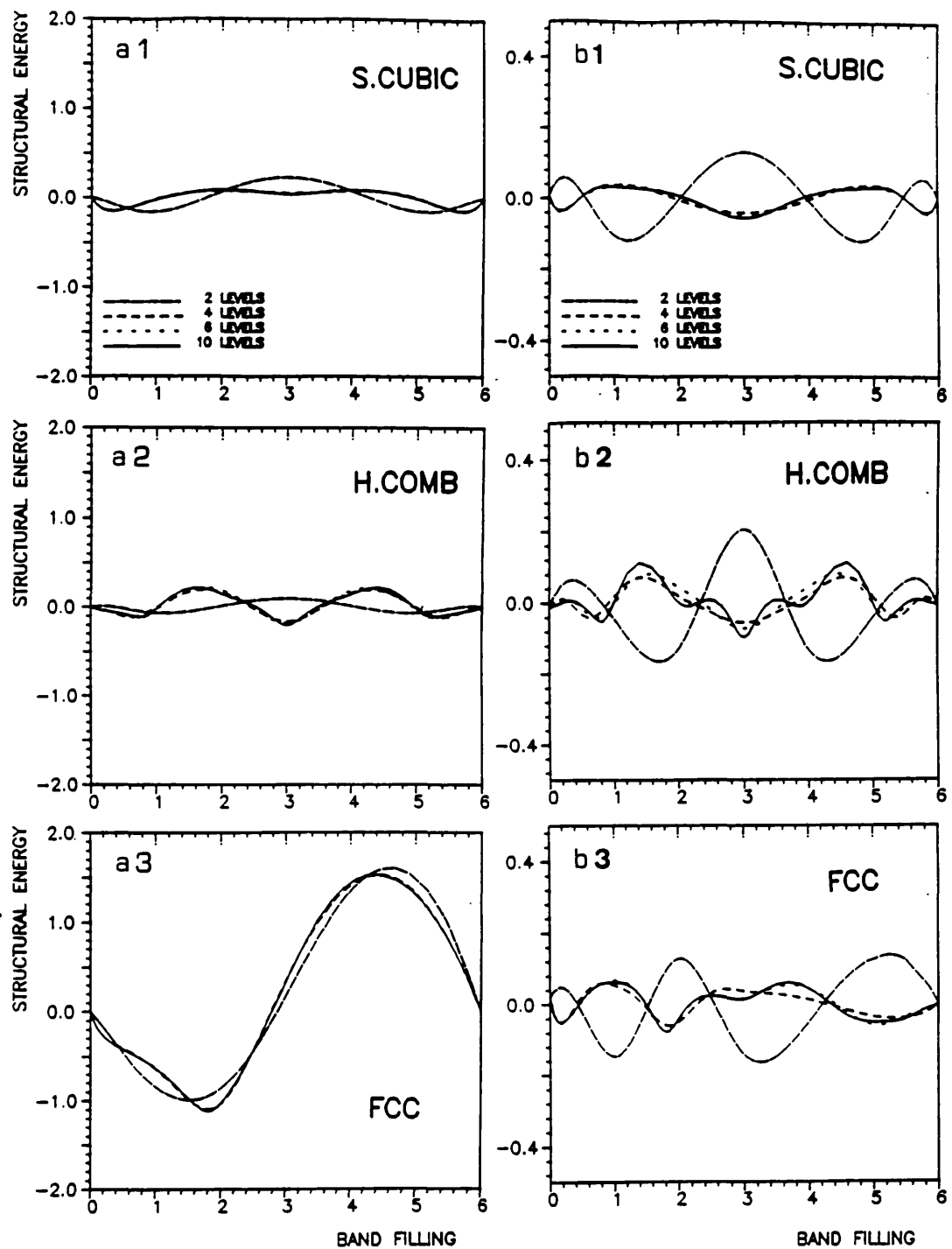


Figure 4.3  
 a) and b): The same as in figure 4.2 but for the pure p case ( $\epsilon_p=0$ ).

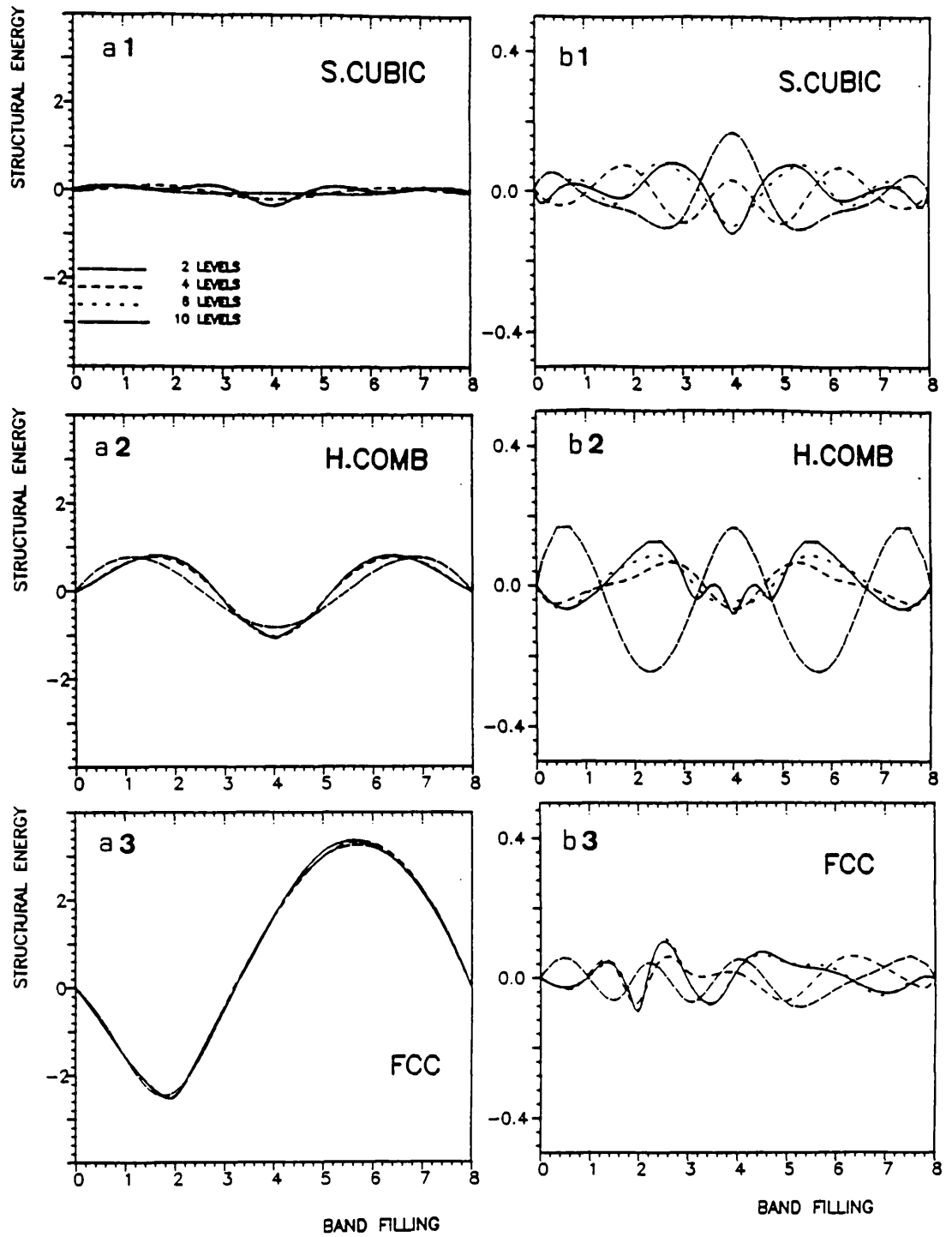


Figure 4.4  
 a) and b): The same as in figure 4.2 but for the sp case ( $\epsilon_{sp}=0$ ).

the difference curve. When eventually the number of shared exact moments goes to infinite the number of zeros in the difference also becomes infinity meaning that the two curves have become identical to each other.

Figure 4.3 shows similar results for the pure p case. The on-site Hamiltonian matrix element, namely the atomic level  $\epsilon_p$ , has been taken equal to zero. Finally in figure 4.4 the corresponding results for the sp case are shown. Here the  $\epsilon_s$  and  $\epsilon_p$  atomic levels were chosen to give a zero sp-splitting, i.e.,  $\epsilon_{sp} = 0$ . The results shown by these curves are essentially the same as for the pure s band. For the actual calculations we shall keep around ten exact levels which, judging by these curves, should be enough to give the correct structural stability separation. In figures 4.3a and 4.4a the reference was a skew DOS as for figure 4.2a. In figures 4.3b and 4.4b a cubic spline was used as reference with the following knots: 1, 2  $\dots$  5 for the pure p case and 1, 2  $\dots$  7 for the  $\epsilon_{sp} = 0$  case.

#### 4.4.2 The $pp\pi/pp\sigma$ ratio

The use of Harrison's adjusted parameters to determine the hopping integrals (as given by (4.11)) does not lead, within our model, to a good separation for the relative stability of the close packed and dimer structures at low values of the band filling. More specifically when the band filling is equal to one the expected result is either the dimer as the most stable structure if the s and p orbitals are very far apart (as for  $H_2$ ) or the close packed structures (as for Li and Na) if a considerable degree of sp hybridization exists. As seen in figure 4.5, the structural energy versus band filling curves using the adjusted parameters,

correctly predict the dimer as the most stable structure when only one s-orbital is present (i.e.,  $\epsilon_{sp} = -\infty$ ). However as the s and p orbitals are hybridized we find that the close packed structures are unable to overcome the dimer stability as shown in figures 4.5 and 4.6. One might argue that this is a failure of the model rather than an indication that Harrison's parameters are unsuitable in this region and for these particular structures. However the correct prediction about the relative stability of two such different structures is a rather difficult question to ask to a simple model that relies on a single set of parameters to separate so many elements and geometric arrangements. Furthermore, rephrasing Harrison (1980 p46), in the choice of the set of parameters " a trade-off must be made between simplicity (or universality) of the choice and accuracy of the predictions ( $\dots$ ) ". Notice that Harrison's parameters have been adjusted to fit the energy bands of silicon and germanium and therefore some bias towards tetrahedral structures should be expected.

In trying to get the correct trend when  $N = 1$ , we notice that we can increase the stability of all structures in the bonding part of the spectrum if we increase the ratio  $|(pp\pi)/(pp\sigma)|$  (i.e., the  $\pi:\sigma$  ratio) by a small amount. At  $\epsilon_{sp} = 0$ , however, the dimer structural energy at that band filling, is not dependent upon the value of  $(pp\pi)$  (see appendix V). This provides us with a procedure to push down all curves with respect to the dimer in the region around  $N = 1$ . Consulting Table 2-1 p49 of Harrison (1980) we notice that the  $\pi:\sigma$  ratio is given by  $|-1.23/3.70|$ , i.e.,

$$\frac{(pp\pi)}{(pp\sigma)} \approx -0.33 \quad (4.15)$$

if the simple cubic TB band structure is fitted to the nearly free electron bands. The corresponding value adjusted for silicon and germanium bands is  $-0.25$ . We found that the changes in the relative stability of the other structures is minimum.

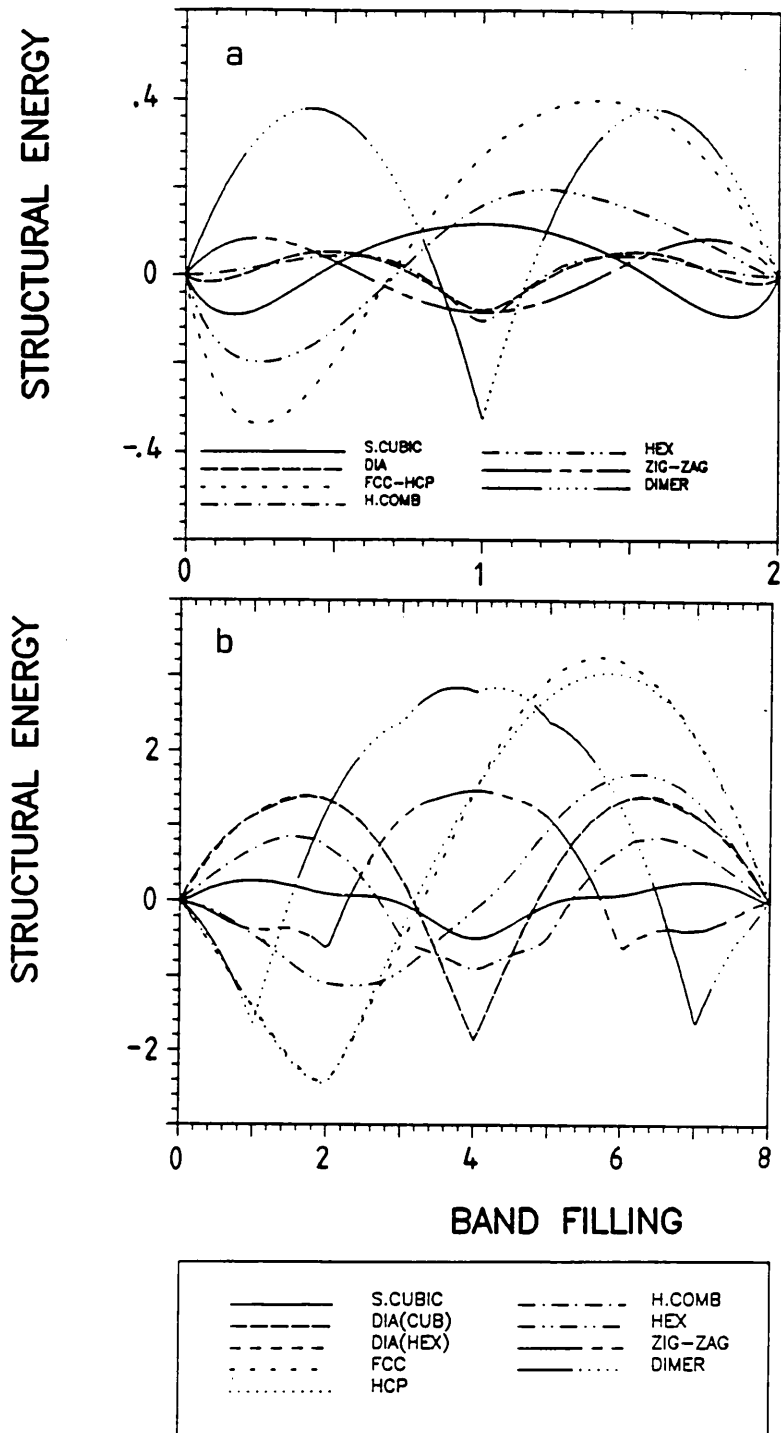


Figure 4.5  
Structural energy versus band filling curves. a) the pure s and b)  $\epsilon_{sp} = 0$  cases. Harrison's parameters have been used and a skew DOS was taken as a reference.

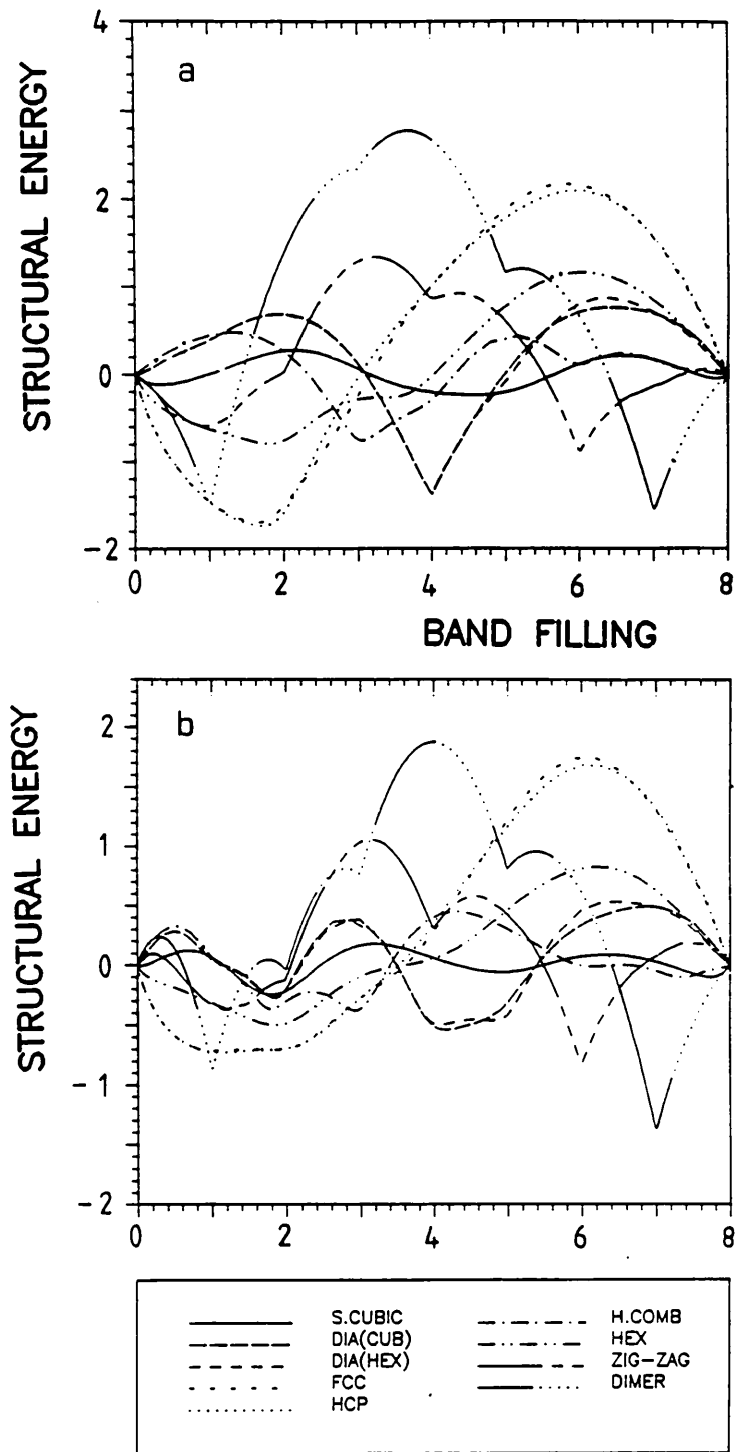


Figure 4.6  
 The same as in figure 4.5, now for a)  $\epsilon_{sp} = -12 \cdot \tan(\pi/10)$ , and  
 b)  $\epsilon_{sp} = -12 \cdot \tan(2\pi/10)$ .

Therefore the bonding integrals will be calculated using Harrison's adjusted values as given in (4.11) except for  $(pp\pi)$  which will be calculated using the ratio above.

#### 4.4.3 The Second Neighbours in the bcc Lattice

In the bcc structure the second to first neighbours ratio is given by  $a/(3^{\frac{1}{2}} \cdot a/2) \simeq 1.15$  where  $a$  is the lattice constant. This ratio is too small (in fcc, for example, the ratio is  $2^{\frac{1}{2}} \simeq 1.41$ ) and considering also that there are six second neighbours in the bcc lattice the importance of these can not be neglected and must be incorporated in the calculations. In trying to keep the theory as simple and general as possible, we will look towards rescaling  $(ss\sigma)$  for the more distant neighbours but keeping the other parameters ratios with respect to  $(ss\sigma)$  the same as for the first neighbours. Figures 4.7a and 4.7b show the behaviour of the bcc structural stability curve for various choices of  $(ss\sigma)_2/(ss\sigma)_1$ , where 2 (1) stands for second (first) neighbours. The single s-orbital case is shown in figure 4.7a and the  $\epsilon_{sp} = 0$  case in figure 4.7b, the fcc structural energy curve being also shown. The first nonzero ratio is 0.33 which corresponds to Andersen's (1984) first principles value for this quantity in the bcc lattice. We go up to  $(ss\sigma)_2/(ss\sigma)_1 = 0.75$  which is the ratio given by a power law of the  $R^{-2}$  type. The low temperature structures expected at the low values of the band filling are close packed of the fcc and hcp type and we see that Andersen's ratio fulfill this requirement. We will therefore keep the second neighbours in the bcc structure and the corresponding tight-binding parameters will be calculated in the same as for the first neighbours but with respect to  $(ss\sigma)_2 = 0.33 \cdot (ss\sigma)_1$ .

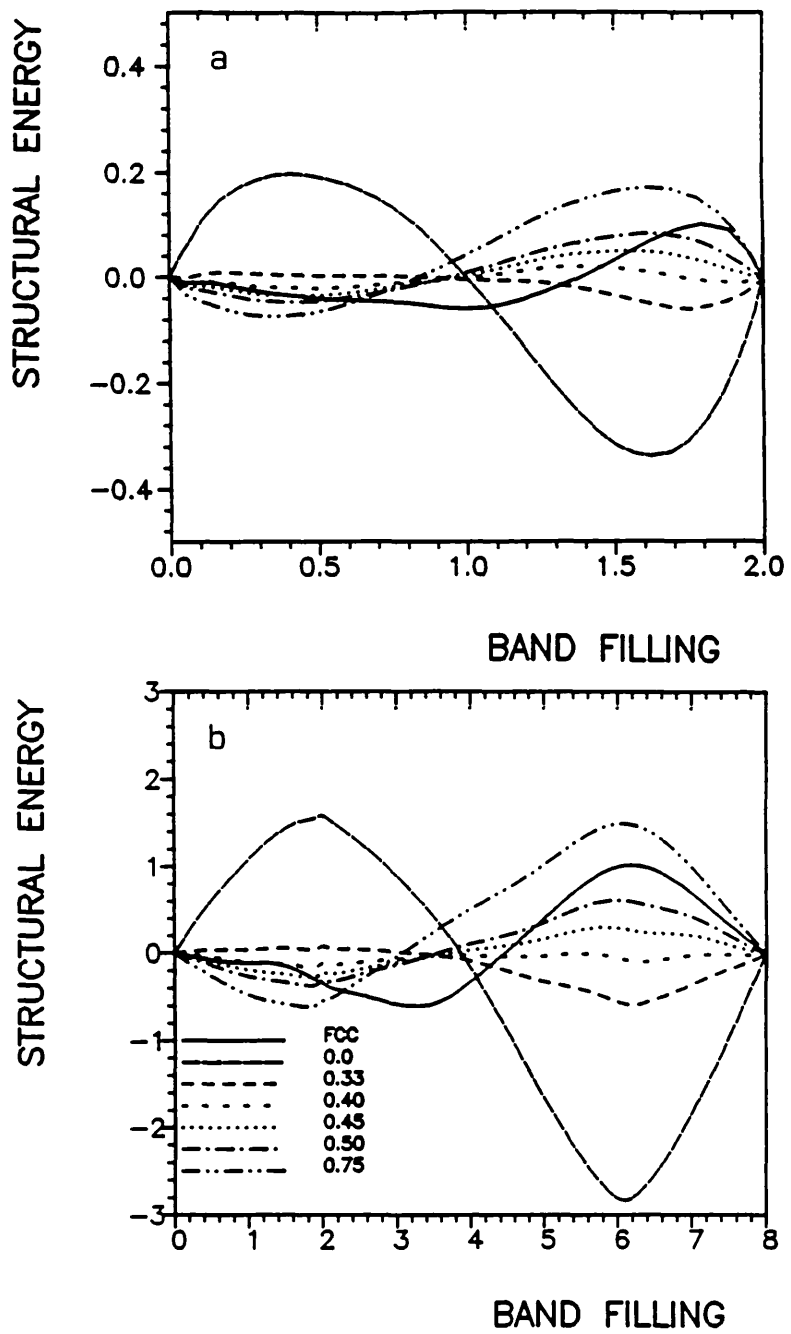
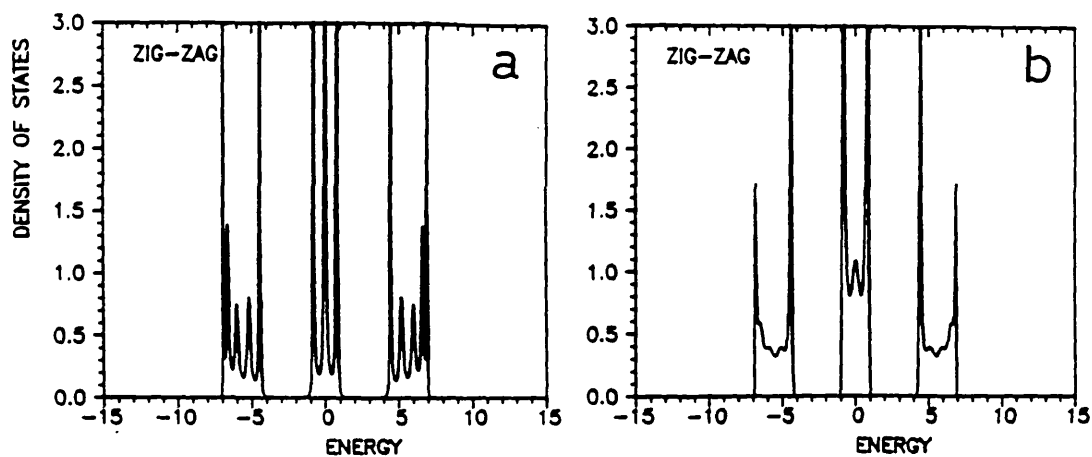


Figure 4.7  
 Relevance of the second neighbours in the BCC lattice. a) single s-band case and b)  $\epsilon_{sp} = 0$  case.



## §4.5 Results

For the final results shown in this section the number of exact levels kept in the continued fraction is not fixed because the calculation of the band and gap edges for any number of levels may not be possible in Beer's method as explained in chapter 2. This is so because an eigen value of the truncated Hamiltonian may exist inside the gap which requires increasing (or decreasing) the number of levels used in the calculations. Whenever possible the computation is carried out with eighteen exact moments (nine levels) which, as indicated in figures 4.2–4.4, is enough to predict the correct relative structural stability behaviour amongst the different structures. Two exceptions are the dimer and the zig-zag chain. The dimer results are exact (see appendix IV) in all cases whereas the zig-zag chain is calculated exactly for the pure s case only (see appendix VI). For the other cases the zig-zag chain has two (sometimes three) gaps in the DOS which consists of very narrow sub-bands. The determination of the band and gap edges in these cases is difficult as discussed in the previous chapter. We therefore show a plot for the zig-zag DOS only in the pure p and  $\epsilon_{sp} = 0$  cases, where the edges were simply read from the square root terminated DOS. Twenty two exact moments (eleven levels) are kept in the continued fraction which is terminated with Turchi Ducastelle and Trégliia (1982) termination as suitable for a double band gap (see previous chapter). However the zig-zag chain integrated quantities were computed using the optimized square root terminator of Beer and Pettifor (1984) while keeping twenty eight exact moments (fourteen levels) in the continued fraction. Although this treats the double band gap DOS as a continuum spectrum, it is well known that the integrated quantities converge much faster than the DOS itself. As we show in figure 4.8 (see Turchi et al (op.cit.) for the



Square root termination

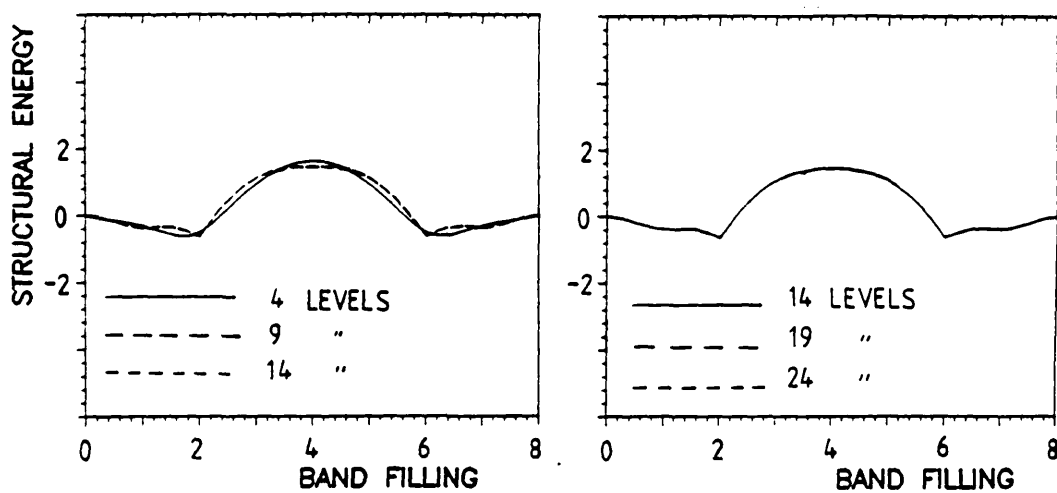


Figure 4.8

Local densities of states and structural energies for the  $\epsilon_{sp} = 0$  zig-zag chain. The DOS were terminated with 15 exact levels of recursion with the square root (a) and Turchi's terminators (b). In the latter case the edges chosen were: -6.9, -4.1, -1.0, 1.0, 4.1 and 6.9.

single band gap) the structural energy has already converged with about nine exact levels of recursion. In this figure the  $\pi:\sigma$  ratio is  $(pp\pi)/(pp\sigma) = -0.25$  and the structural energies are drawn with respect to a skew DOS as explained in section 4.4.1.

Figure 4.9 shows the local densities of states for the single s-orbital case. As explained before, the energy scale is taken with reference to the value of  $ss\sigma$  chosen to be equal to  $-1$ . The absolute scale is not important because only relative energies are used here. The integrated densities of states are also shown (except for the dimer) but in a different scale, the vertical axis needing to be multiplied by five. The dimer energy levels were taken from the exact solution shown in appendix IV and then drawn by the computer by adding a small imaginary part ( $E_i=0.01$ ) to the energy in order to broaden the  $\delta$ -functions. The scale in the vertical axis is dependent on  $E_i$  and on the weight of the  $\delta$ -function (i.e., the number of spin degenerate states that can be accommodated in each level) which is equal to one. The zig-zag chain DOS is the same as the pure s linear chain DOS due to the bond-angle independence of the s-orbitals. For the other structures the number of exact moments retained in the continued fraction was eighteen as explained above and the band widths were corrected by a factor of 3% (see previous chapter). It is interesting to notice that for the bond angle independent pure s case the fcc and the dia(c) structures are identical to their hexagonal analog hcp and dia(h) structures respectively (Burdett and Lee 1985b).

In figure 4.10 the pure p DOS are shown for all ten structures which now assume their individual identity due to the bond angle dependence of the p-orbitals. The remarks here are essentially the same as for figure 4.9 except that the zig-zag chain DOS is now computed within eleven exact recursion levels and terminated using Turchi's termination (see chapter 2). The (exact) dimer levels now show also the doubly degenerate  $\pi$ -states and a gap starts to form at the

middle of the band in the tetrahedral structures. Notice that the fcc and hcp densities of states are very similar which should be expected because their structures are much alike. Also, the bcc DOS follows hcp very closely but lacking the antibonding peaks at the top of the spectrum.

The sp hybridized DOS for different values of the sp-splitting  $\epsilon_{sp}$  are shown in figures 4.11 to 4.15. The corresponding values of  $\epsilon_{sp}$  are  $\epsilon_{sp} = -12|(ss\sigma)| \cdot \tan(n_i\pi/10)$ , with  $n_i = 0, 1, 2, 3$  and  $4$  respectively. Let us list the values of the nondimensional quantity represented by the sp-splitting divided by the simple cubic band-width for the different values of  $n_i$ .

$n_i$	$\frac{\epsilon_{sp}}{12 (ss\sigma) }$
0	0
1	-0.32
2	-0.73
3	-1.38
4	-3.08
5	$-\infty$

See table 4.2 for the parameters used in figures 4.14 and 4.15. The alpha and beta entries were discussed in the previous chapter.

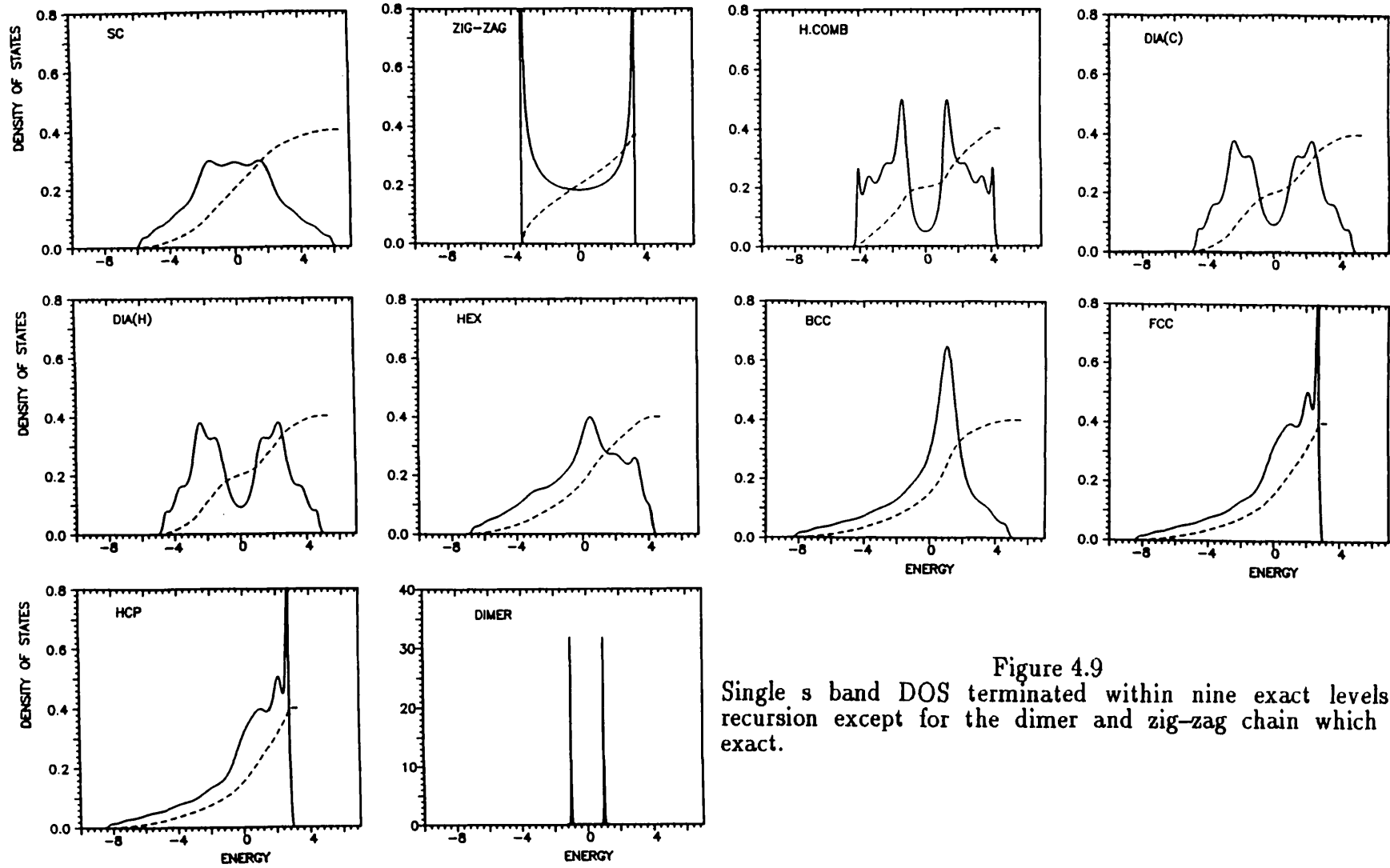


Figure 4.9  
Single s band DOS terminated within nine exact levels of recursion except for the dimer and zig-zag chain which are exact.

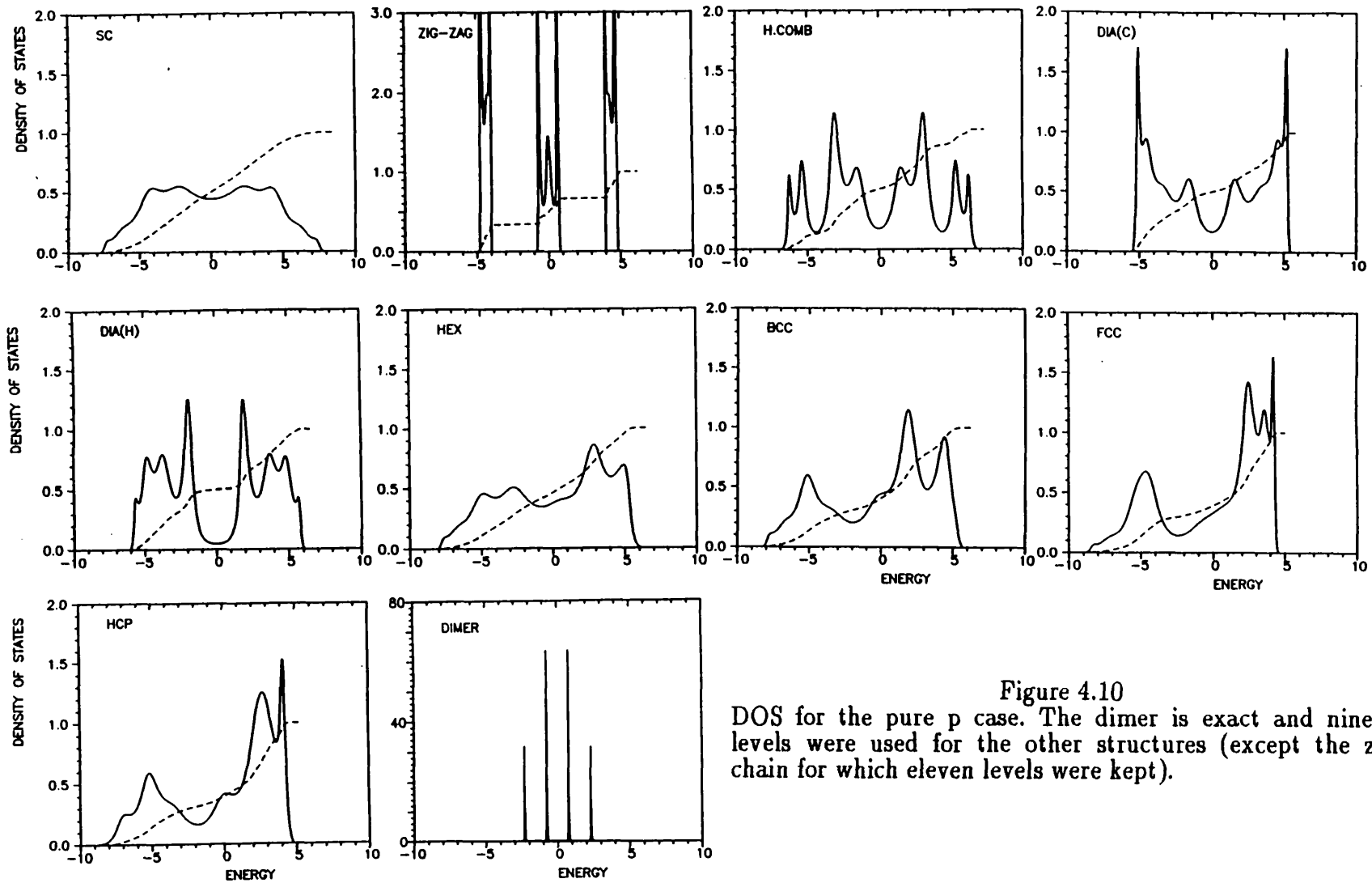


Figure 4.10  
 DOS for the pure p case. The dimer is exact and nine exact levels were used for the other structures (except the zig-zag chain for which eleven levels were kept).

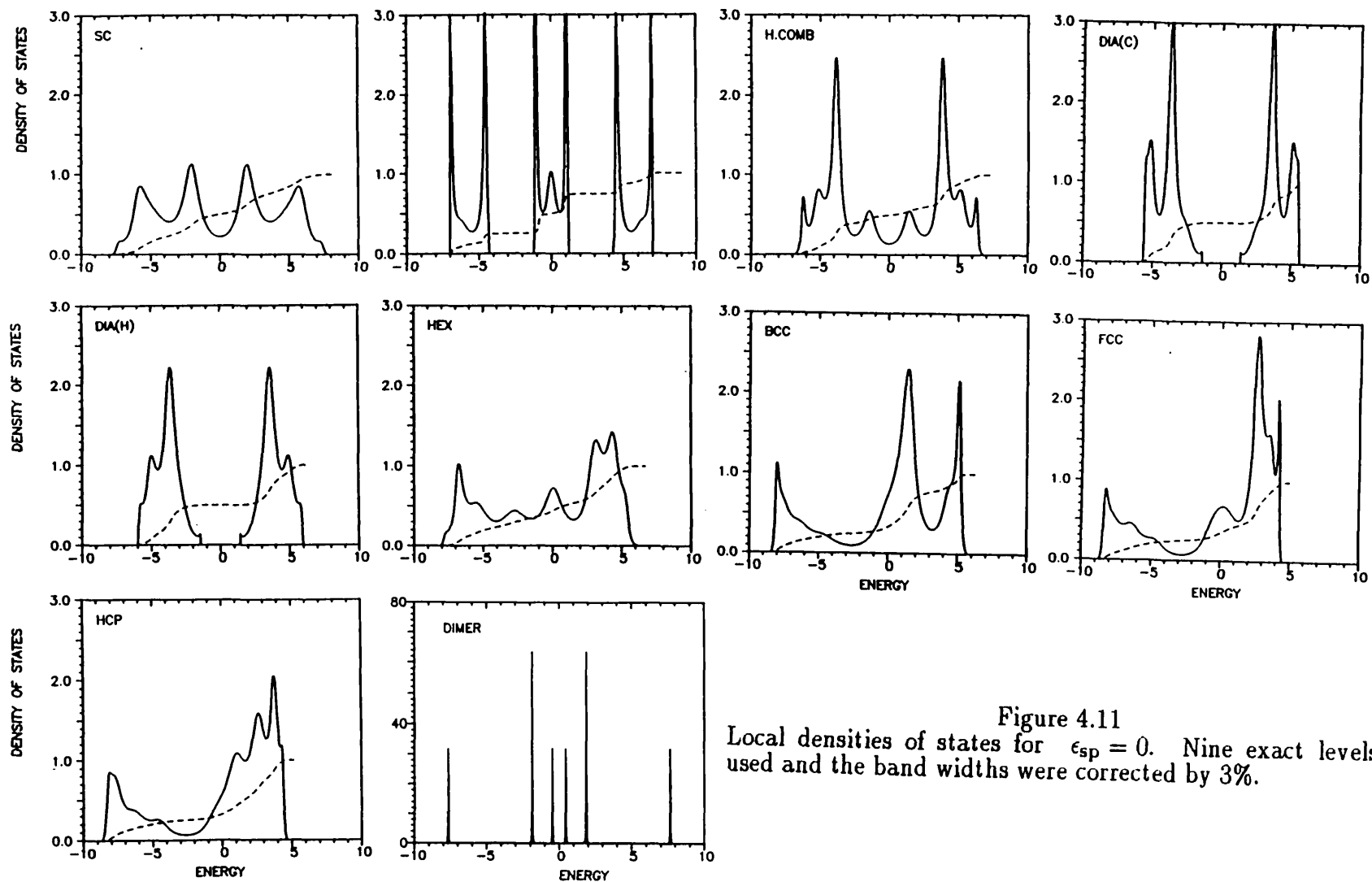


Figure 4.11  
Local densities of states for  $\epsilon_{sp} = 0$ . Nine exact levels were used and the band widths were corrected by 3%.

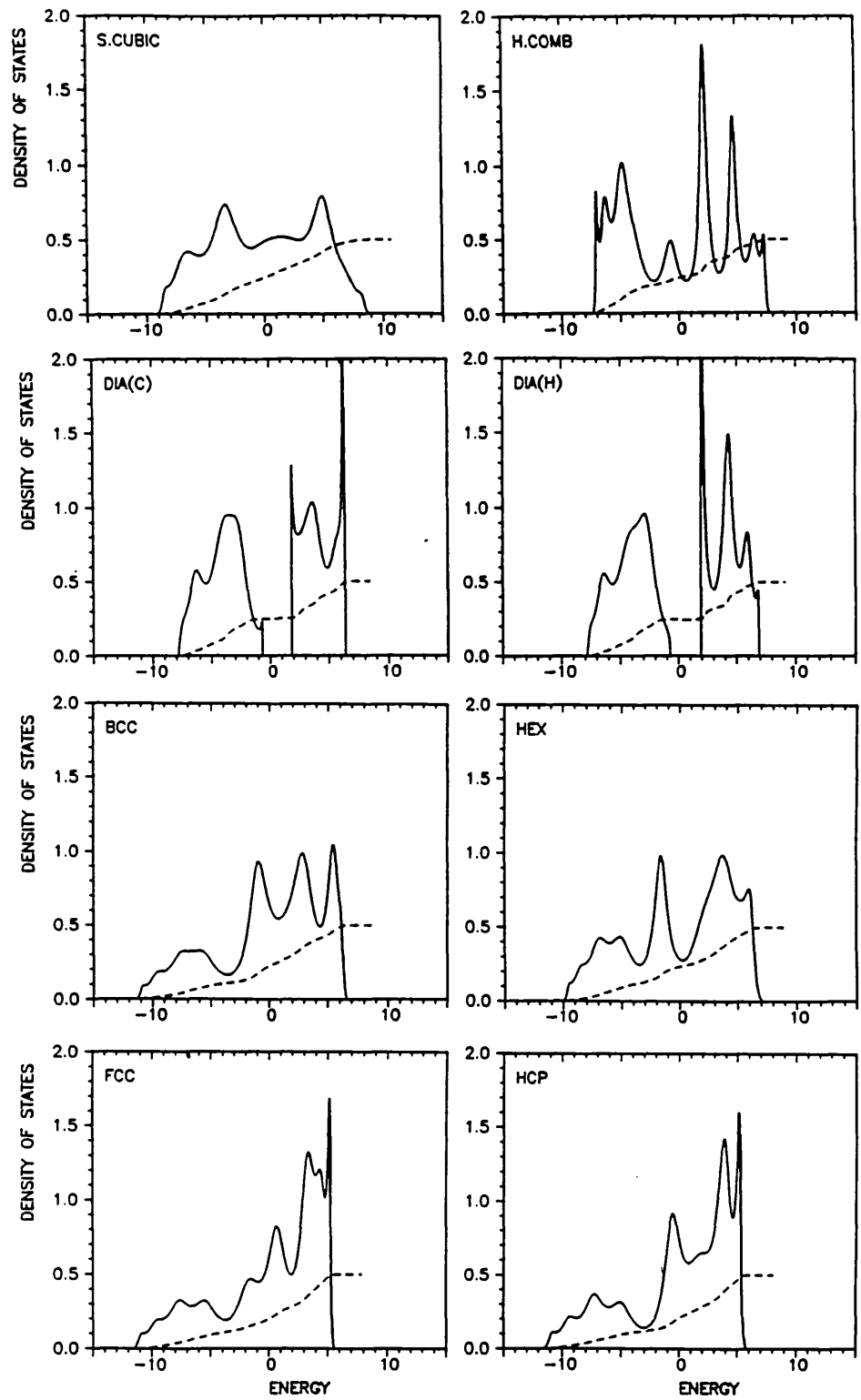


Figure 4.12  
 Local densities of states for  $\epsilon_{sp} = -12 \cdot \tan(\pi/10)$ . Eight exact levels kept for dia(c) and dia(h) lattices and nine for the others. Band widths corrected by 3%.



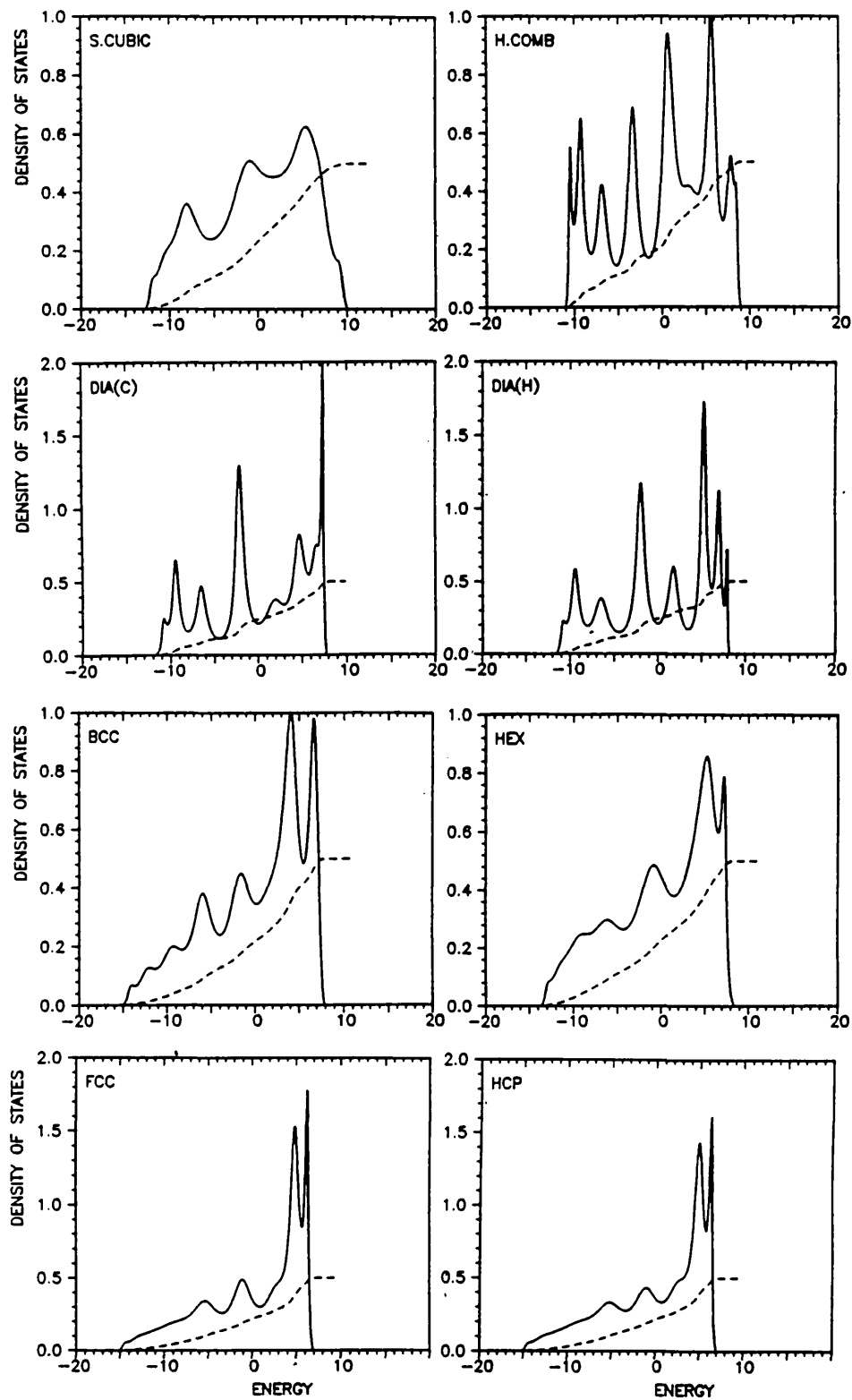


Figure 4.13  
 Local densities of states for  $\epsilon_{sp} = -12 \cdot \tan(2\pi/10)$ . Nine exact levels kept for all structures and band widths corrected by 3%.

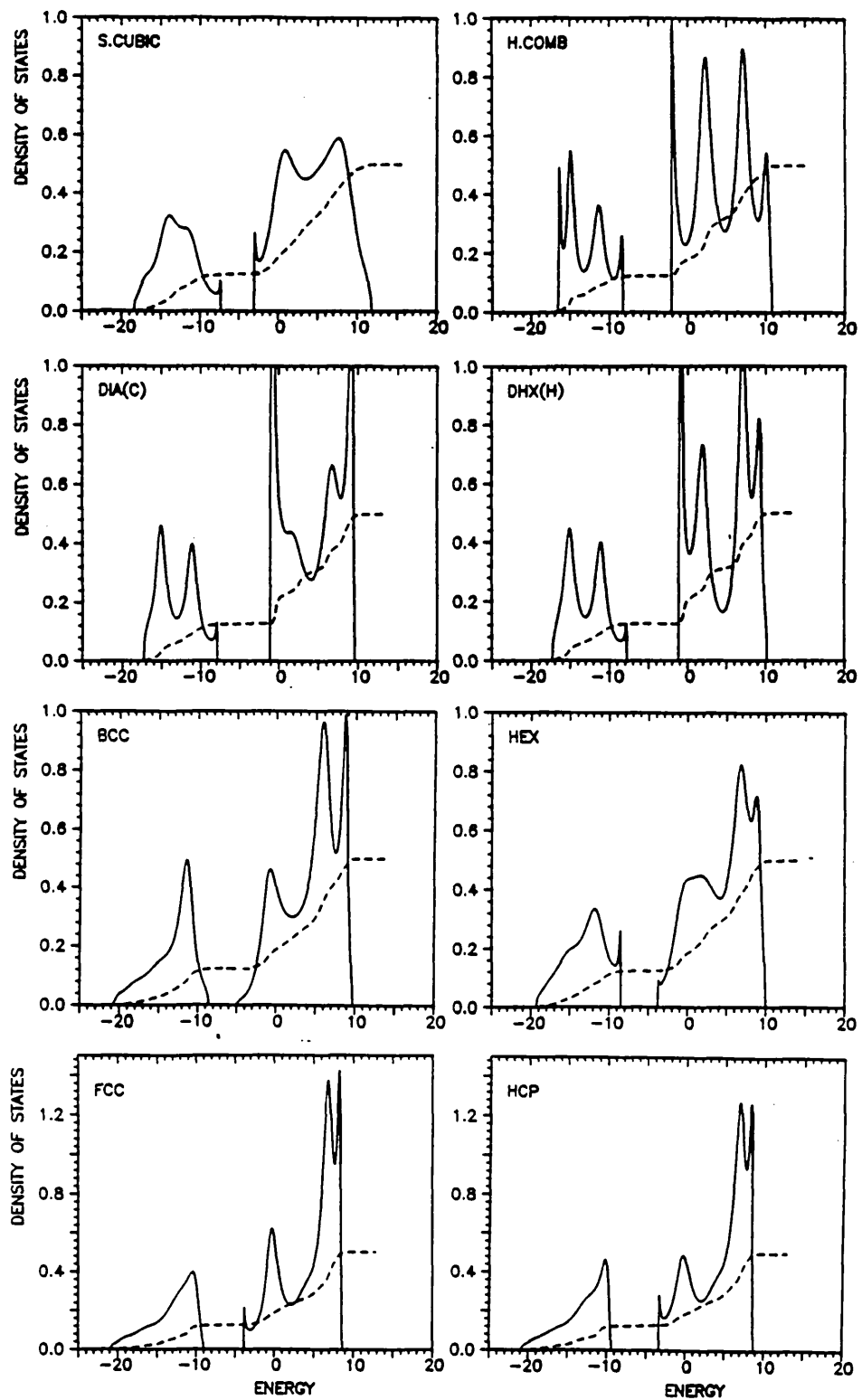


Figure 4.14  
 Local densities of states for  $\epsilon_{sp} = -12 \cdot \tan(3\pi/10)$ . See table 4.2 for band-width corrections and number of levels.

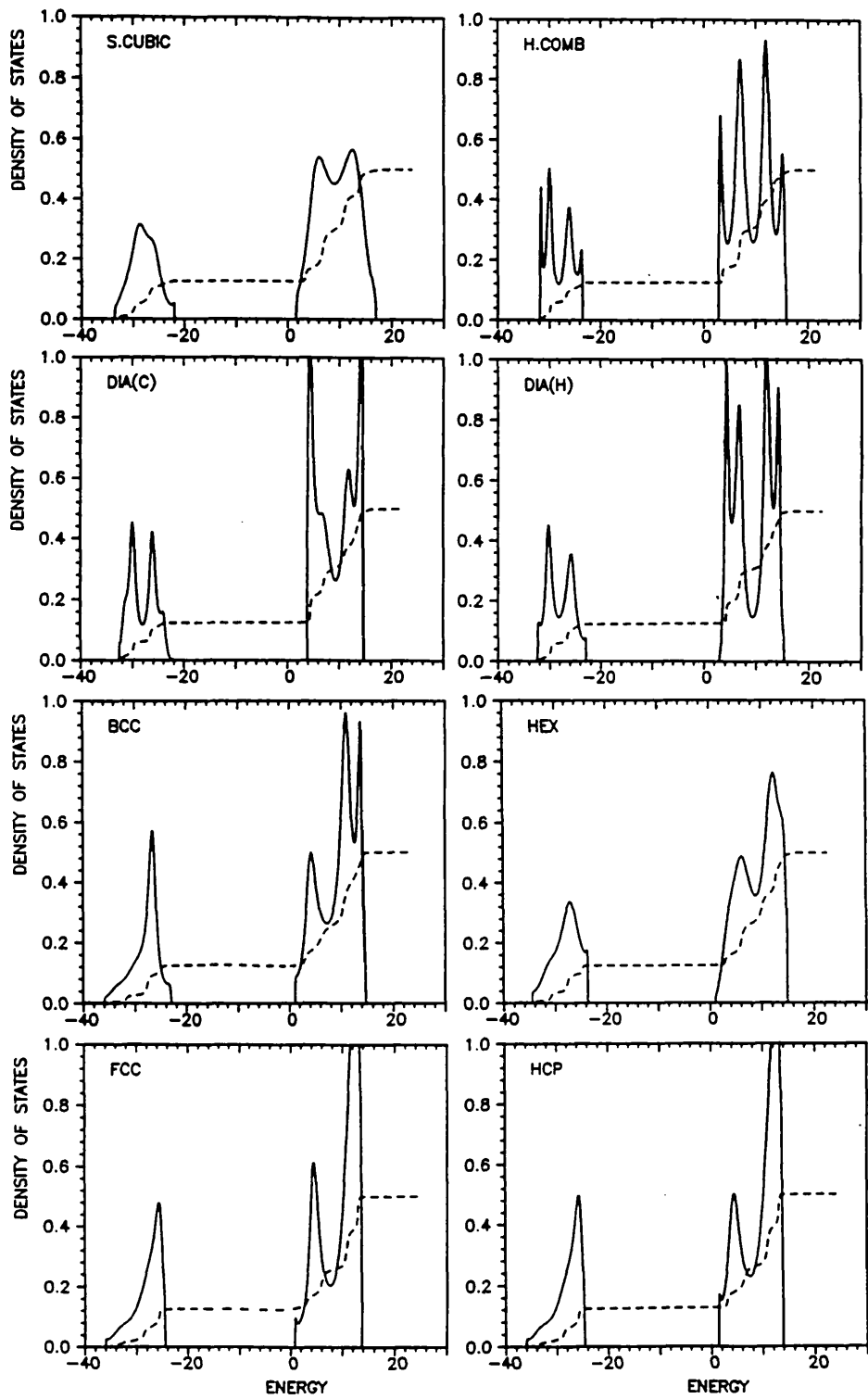


Figure 4.15  
 Local densities of states for  $\epsilon_{sp} = -12 \cdot \tan(4\pi/10)$ . See table 4.2 for band-width corrections and number of levels.

Table 4.2

	$n_i = 3$			$n_i = 4$		
	levels	alpha	beta	levels	alpha	beta
s.cubic	8	3.0	3.0	8	3.0	3.0
h.comb	8	3.0	3.0	8	3.0	3.0
dia(c)	8	3.0	3.0	9	1.5	3.0
dia(h)	8	3.0	3.0	8	3.0	3.0
hex	8	3.0	3.0	8	3.0	3.0
bcc	9	3.0	3.0	9	3.0	3.0
fcc	9	2.4	3.0	7	3.0	3.0
hcp	9	2.8	3.0	7	3.0	3.0

Table 4.2 Parameters used for the DOS in figures 4.14 and 4.15.

The structural energy versus band filling curves corresponding to figures 4.9 to 4.15 are shown in figures 4.16–4.18. These energies were drawn with respect to a skew DOS fitted to the first four moments of the simple cubic structure as explained before, except for figure 4.18. In this figure a cubic spline with nine knots namely 1, 2, 2, 2, 3, 4, 5, 6 and 7 was used to define the reference (see previous chapter and NAG documentation). The triple 2 (a knot of multiplicity three) is here to impose continuity only in the fitted function (not in its derivatives) at that value of the band filling. This is needed when the data points have a cusp (first derivative not continuous). The reason for changing to a cubic spline is because it is not always possible to fit a skew DOS for large values of the sp splitting. This is so because the corresponding increase in the second and third moments (which control the band-width and the skewness respectively) may not be consistent with the fixed value of the area under the DOS (given by the zeroth moment).

For the drawing of these curves the natural procedure would be to calculate the Fermi energy for a fixed value of the band filling and then proceed to the calculation of the structural (band) energy. However, a less expensive way is to compute the structural energy and the band filling at the values of the energy varied from the bottom to the top of the band. Only two integrations per point are done in this way as opposed to typically a few tens (depending on the accuracy) required for Fermi energy calculations. In this way the computing time can be cut down by a factor as large as twenty per each curve. The price to pay is that if the DOS is rapidly varying in a certain range of energy values only a few points are picked up in that region. This will reduce the effective number of points in the final plot against the band filling which can lead to a misinterpretation of the results. However this can be properly cured by improving the mesh (i.e., diminishing the energy step) if such a region is detected. This can be implemented

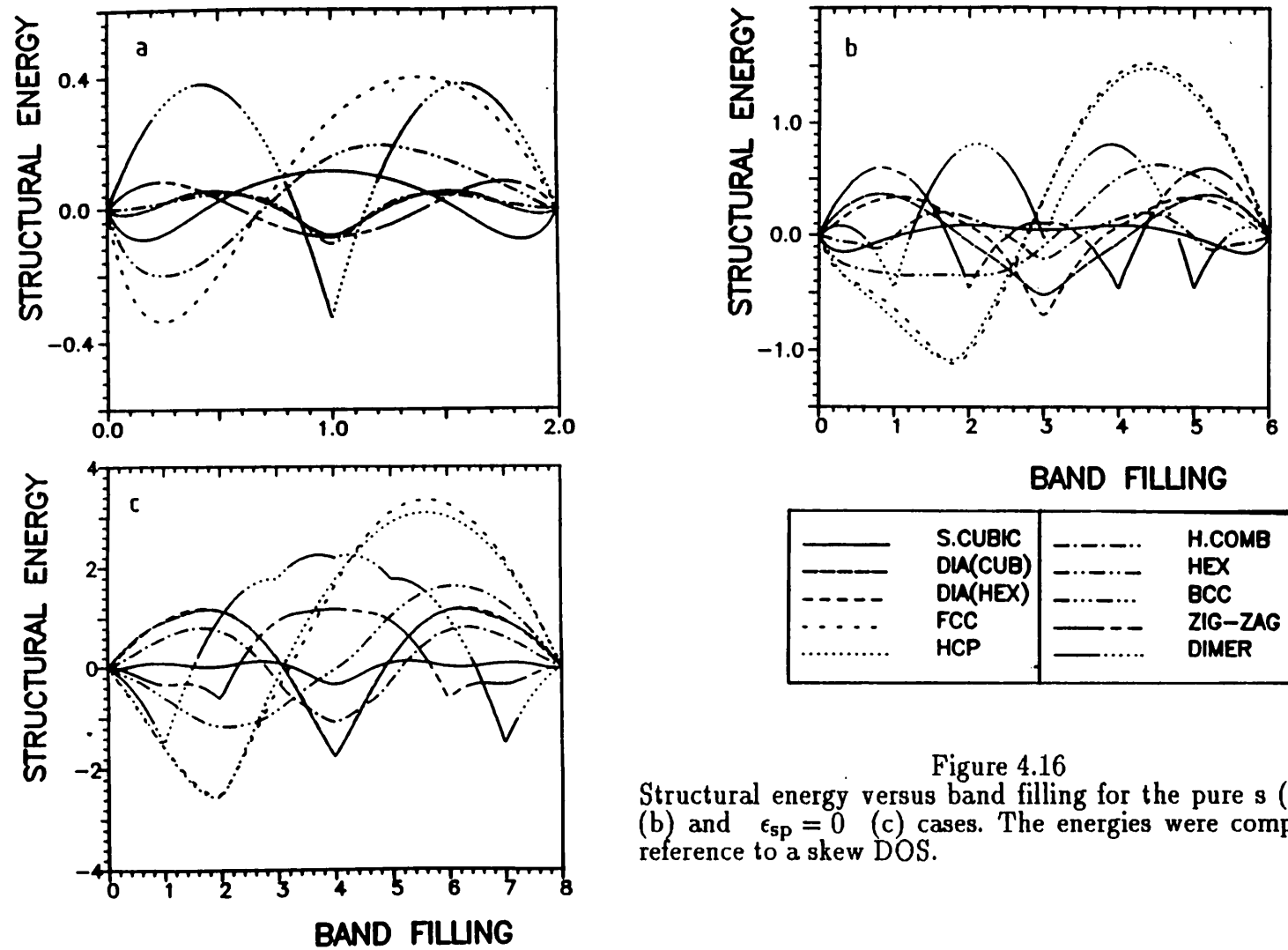


Figure 4.16  
Structural energy versus band filling for the pure s (a), pure p (b) and  $\epsilon_{sp} = 0$  (c) cases. The energies were computed with reference to a skew DOS.

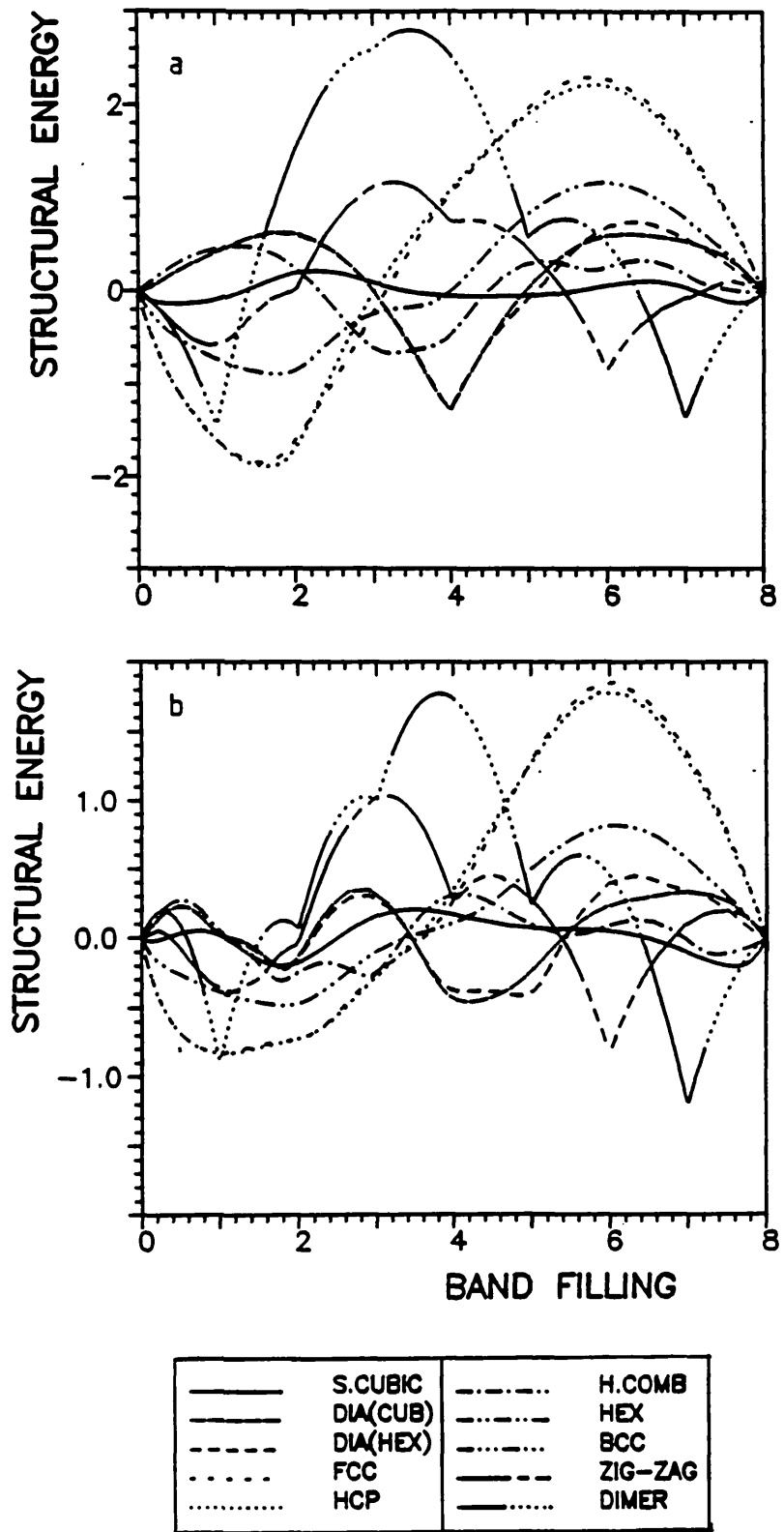


Figure 4.17  
Structural energy versus band filling for  $\epsilon_{sp} = -12 \cdot \tan(n_i \pi / 10)$   
with  $n_i = 1$  (a) and 2 (b). A skew DOS was used as reference.

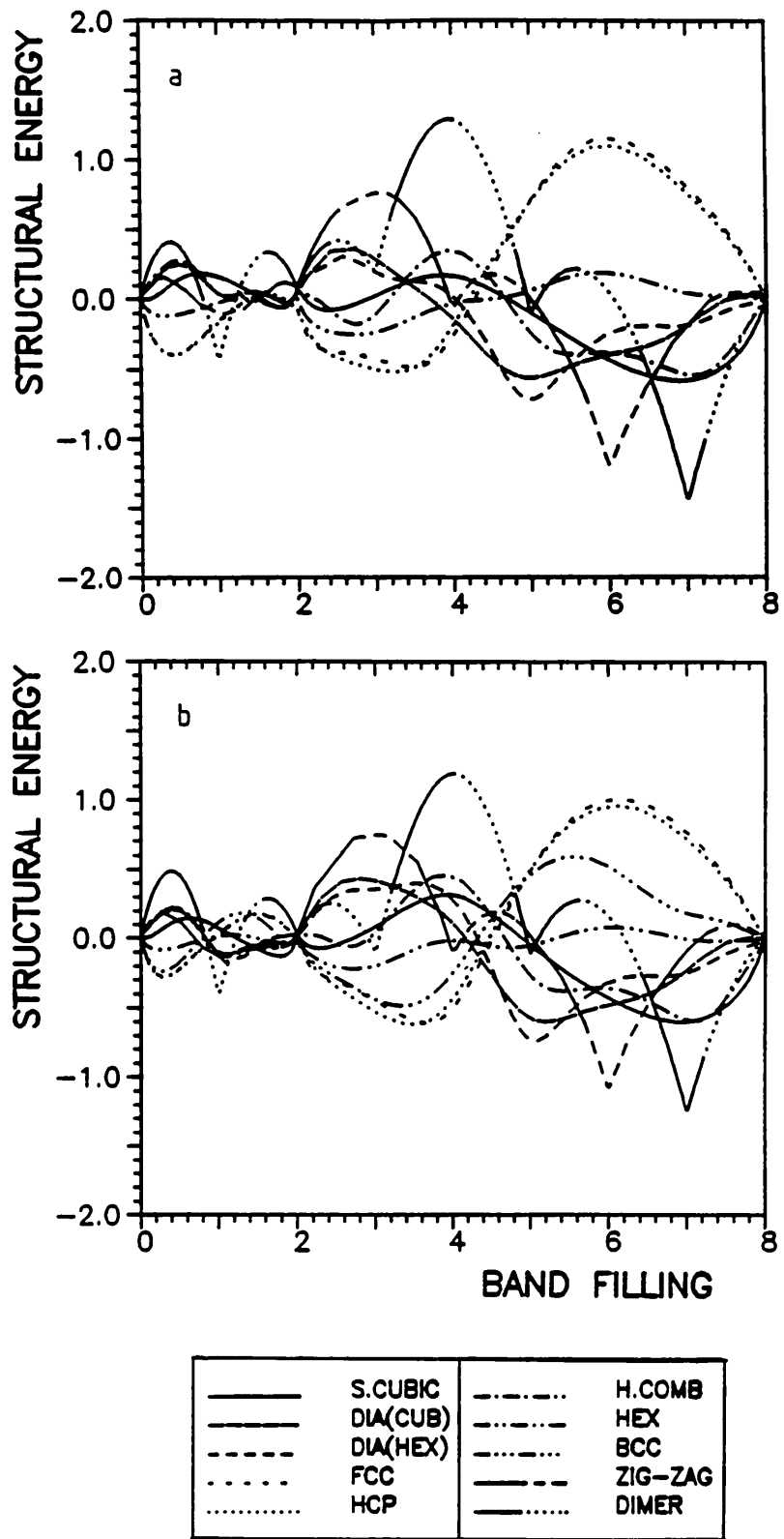


Figure 4.18  
Structural energy versus band filling for  $\epsilon_{sp} = -12 \cdot \tan(n_i \pi / 10)$   
for  $n_i = 3$  (a) and 4 (b). A cubic spline was used as reference.



in the computing routines so that it is automatically taken care of.

For a given value of the band filling we can now read the most stable structure which is the one with the minimum value of the structural energy. Whenever two structures are too close so that separation is difficult to be spotted via these plots, their structure energies can be drawn alone with a reference cubic spline fitted to their data points. In this way the two curves can be usually well separated and the most stable structure identified. If still there is any doubt then Fermi energy calculations are necessary so that the structure energies can be evaluated at the same value of the band filling to allow a numeric separation. This procedure is still much more economic than calculating the Fermi energy for all points.

The final result can be drawn as a structural map shown in figure 4.19 which separates out the different regions of stability derived from figures 4.16–4.18. The vertical axis is a function of the  $sp$ -splitting and the horizontal axis is the band filling which is associated with the different groups of elements in the periodic table. Representing the electronegativity, the vertical axis separates the elements down a given group at fixed band filling. Notice that at the bottom of the scale  $\epsilon_s - \epsilon_p = -\infty$  meaning that the  $s$  and  $p$  orbitals are very far apart. In figure 4.20 the corresponding experimental map is drawn. The data used for the drawing of this map is given in appendix VII.

We see that the most important structural trends are reproduced by the theoretical structural map. The first thing to be noticed is that the close packed regions lie at left hand side as for the Li and Be groups. Hydrogen with its large  $sp$  separation lie below Li and Na and the predicted narrow dimer stability region at band filling equal to one accounts for this fact. We see that hcp Be and Mg are also very well predicted. As for group IIIB the structure of Al is seen to lie on a honey comb region. If it were not for the honey comb structure, fcc aluminum would lie on the border of a large fcc region and a very small island of hexagonal stability

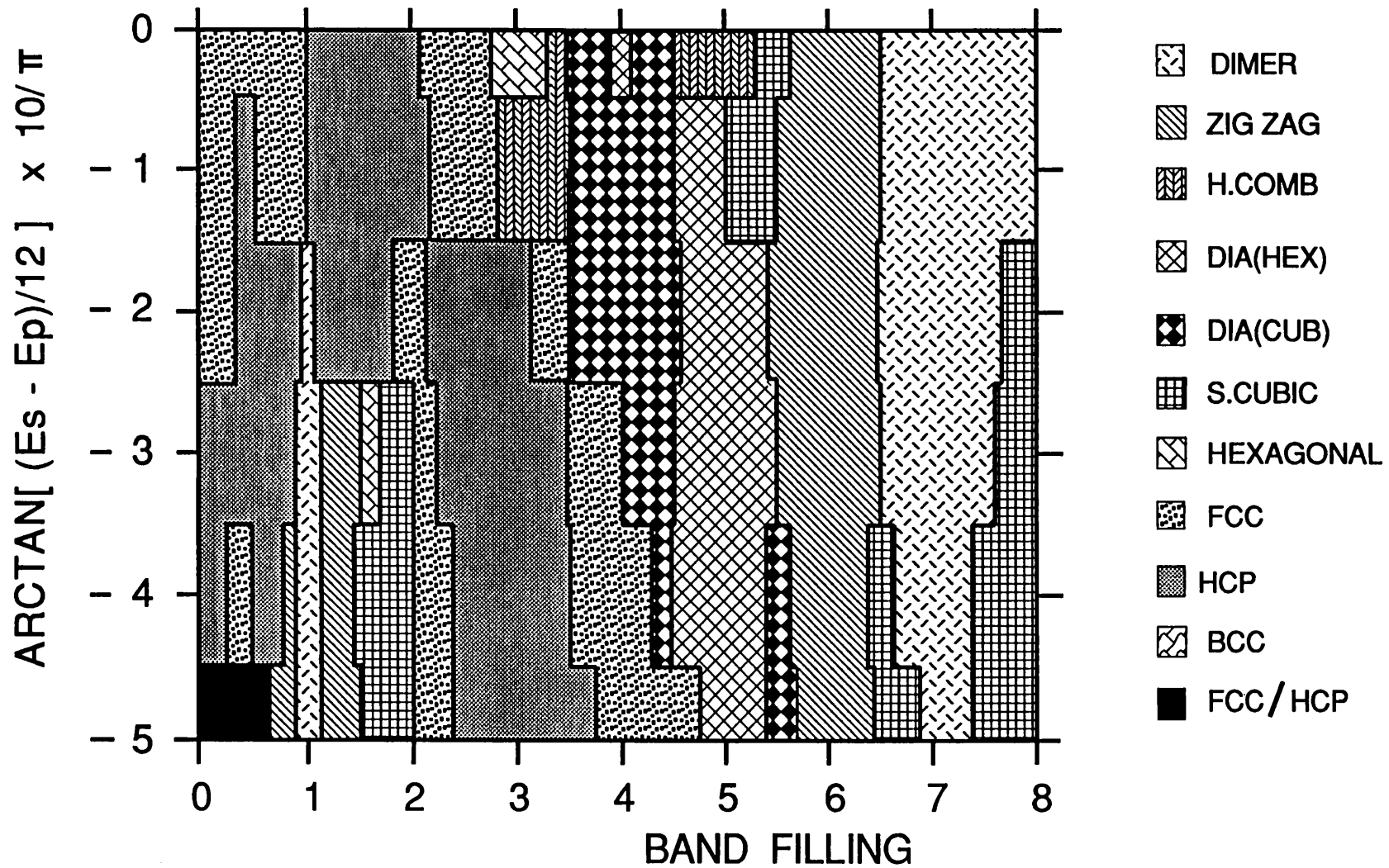


Figure 4.19  
Theoretical structural map for the sp elements.

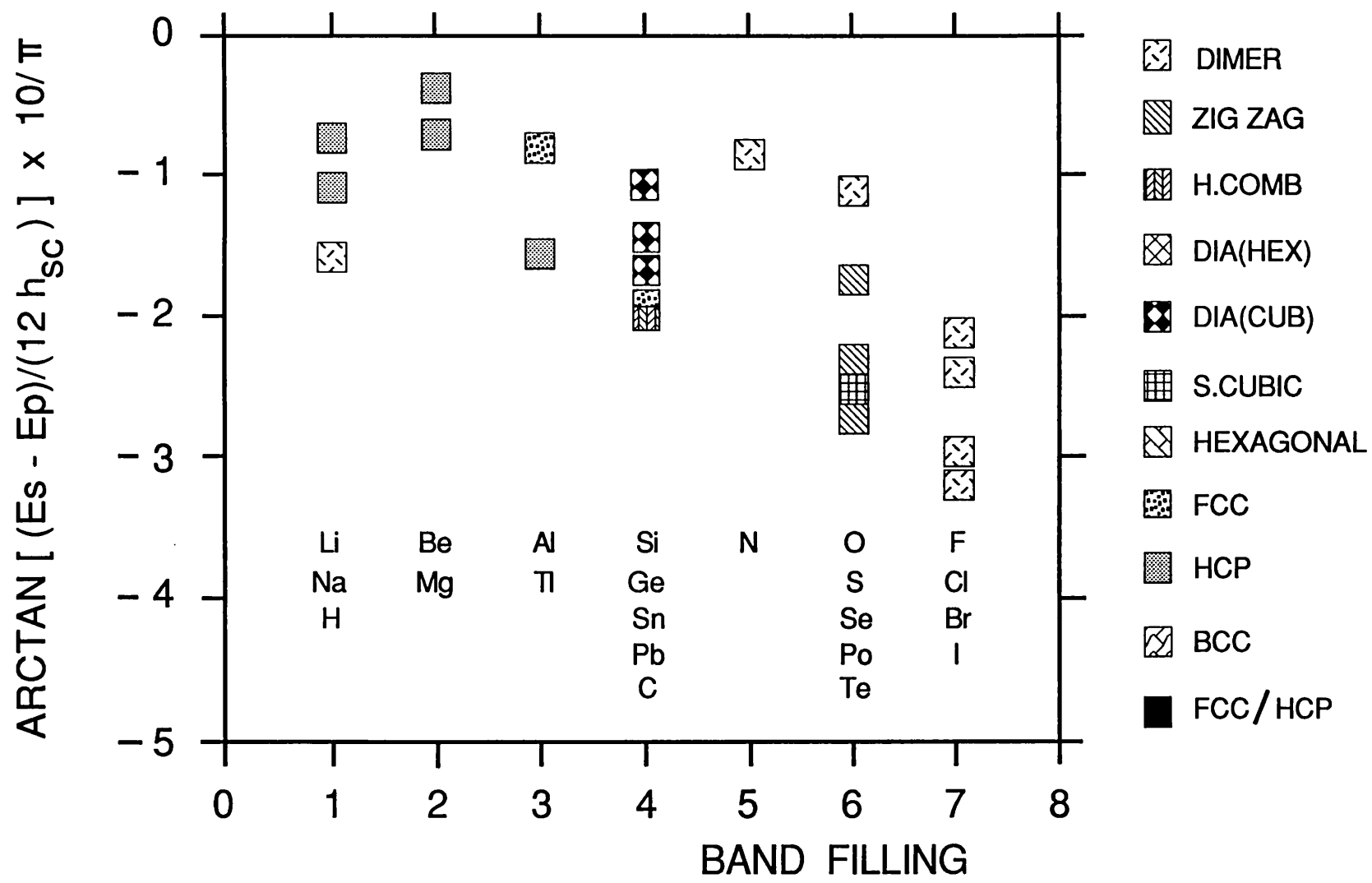


Figure 4.20  
Experimental structural map for the sp elements.

(see structural stability curves for  $n_i = -1$ ) which would be very acceptable. We can attempt to an explanation by noticing that there may be large differences in volume between the two dimensional honey comb (coordination equal to three) and close packed fcc (coordination equal to twelve) lattices which could be only poorly accounted for by the structural energy difference theorem. However hcp thallium is seen to be correctly situated within the theoretical map. Carrying on to the right hand side of the map we leave the close packed regions and ingress into the tetrahedral regions of the group IVB elements. These are very nicely situated in a cubic diamond domain giving an excellent agreement with their observed structures. The fcc arrangement lead however is not predicted correctly. Nevertheless the model reproduces the right trend: going down the structural map at band filling equal to four we find the expected fcc structure. As for the dimer structures represented by nitrogen and oxygen we do not find a good agreement with experiment. Group VIB elements sulfur, selenium and tellurium are represented in our model by zig-zag chains and we see that the agreement with experiment is excellent. Polonium assumes a simple cubic crystalline form which is not predicted correctly but notice that the simple cubic structure comes second in stability (after the zig-zag chain) in that region (see structural energy curves). Finally the halogens represented by dimers are also predicted correctly by the model.

In figure 4.21 we show the structural map with the sp splitting  $\epsilon_{sp}$  extended up to  $+\infty$ . The structural energy versus band filling curves and the corresponding densities of states are shown in figures 4.22-23 and 4.24-4.27 respectively. The  $\epsilon_{sp} > 0$  region is unphysical because the atomic s orbital always lies below the p orbital. However one thing we learn from this map is that the essential trends (say close packed, four-fold coordinated and low dimensional structures as we go from the left to the right in the structural map) are not strictly dependent on the sign of  $\epsilon_{sp}$ .

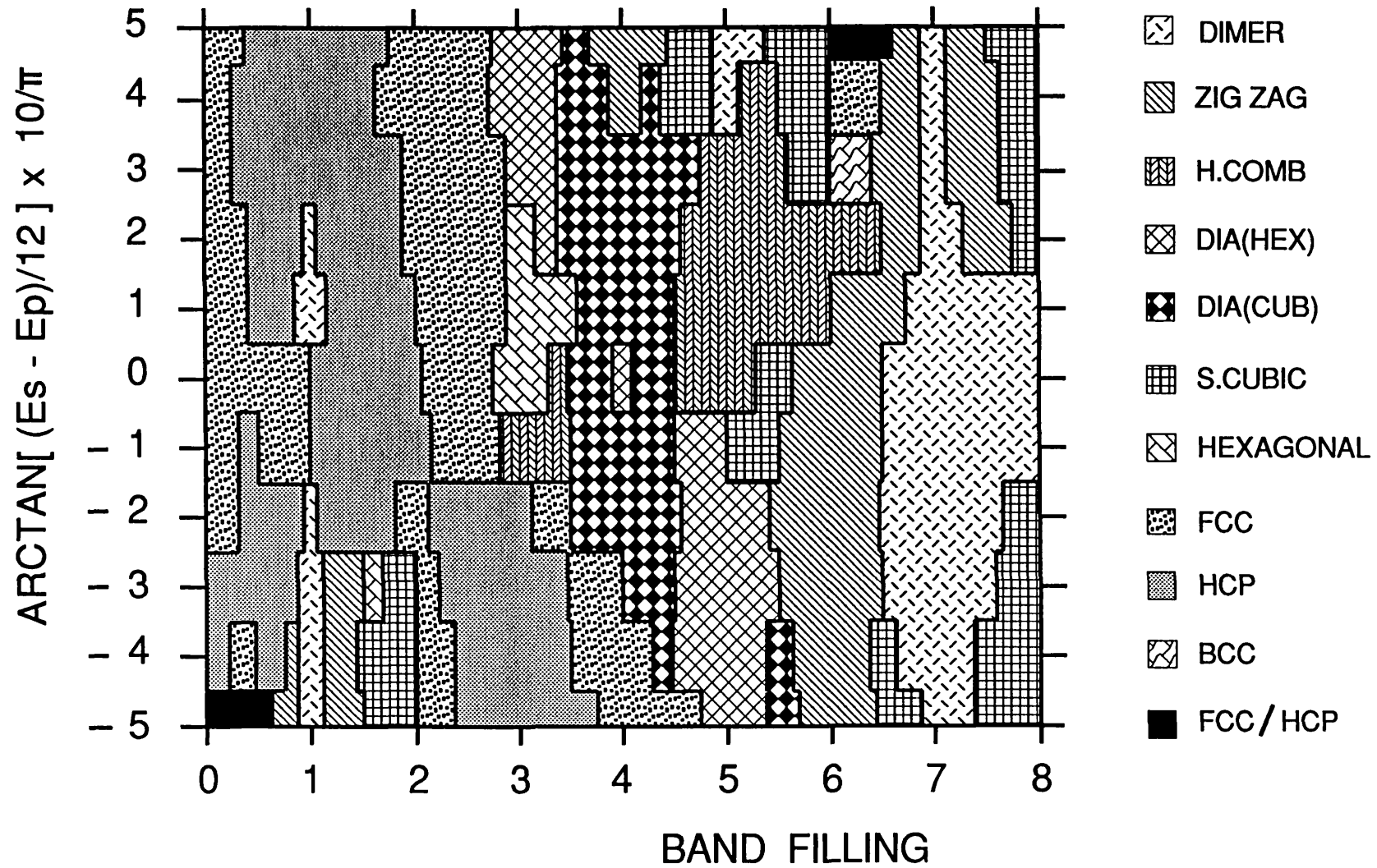


Figure 4.21  
Theoretical structural map including the  $\epsilon_{sp} = > 0$  region.

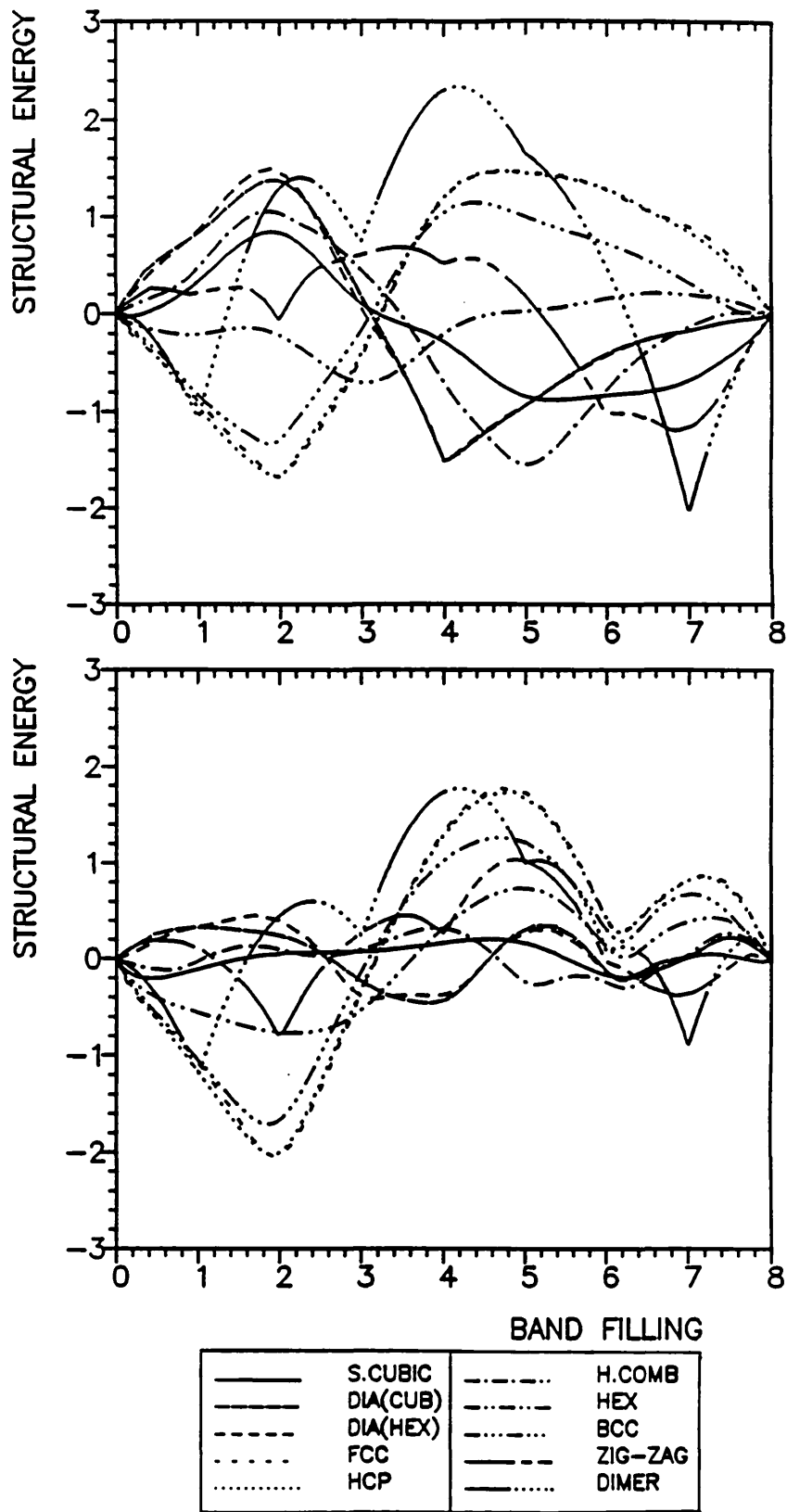


Figure 4.22  
 Structural energy versus band filling curves for the cases  $\epsilon_{sp} = 12 \cdot \tan(n_i \pi / 10)$  with  $n_i = 1$  (top) and 2 (bottom). A skew DOS was used as reference.

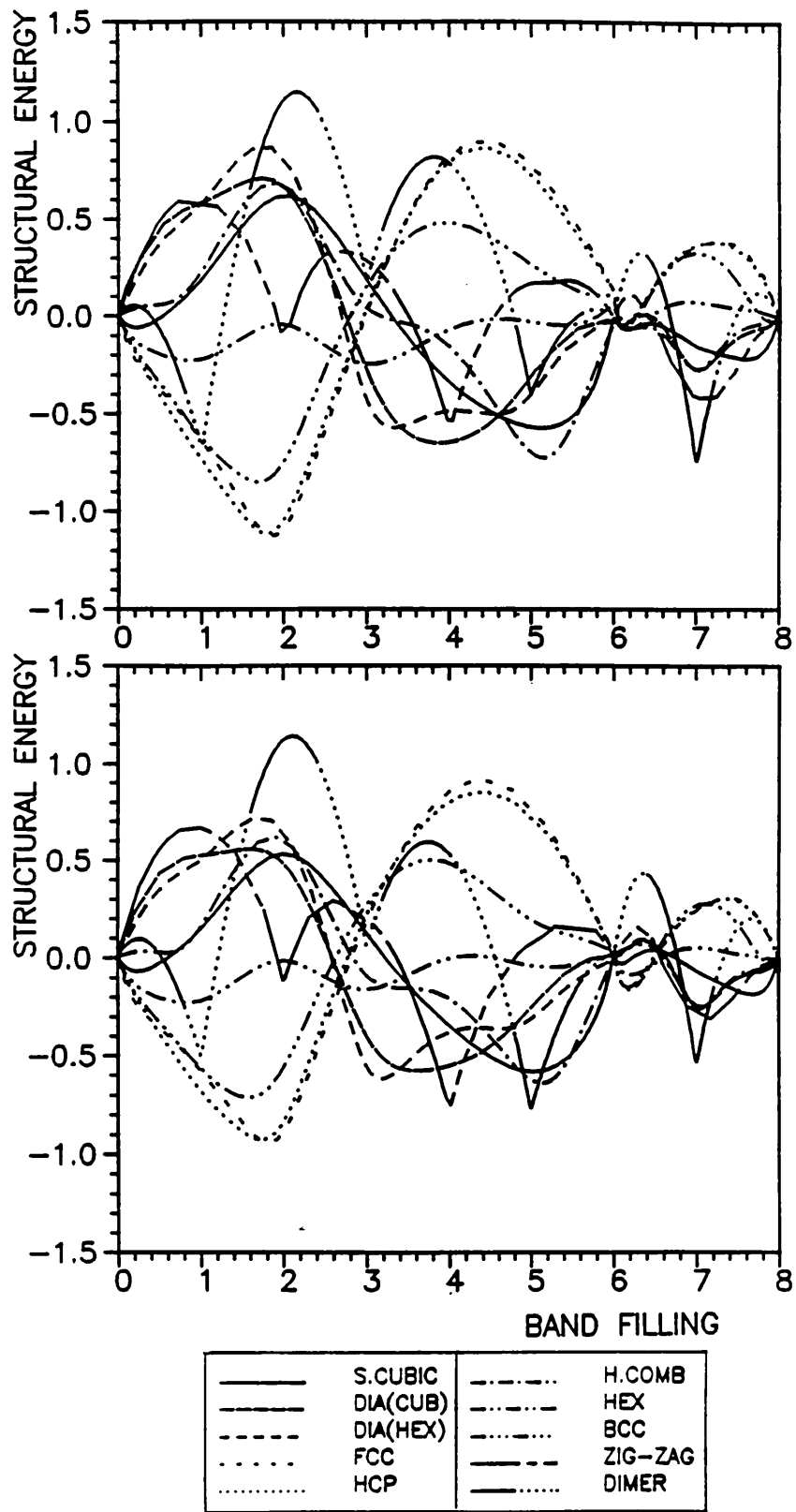


Figure 4.23  
 Structural energy versus band filling curves for the cases  $\epsilon_{sp} = 12 \cdot \tan(n_i \pi / 10)$  with  $n_i = 3$  (top) and 4 (bottom). A cubic spline was used as reference with knots equal to 1, 2, 3, 4, 5, 6, 6, 6, and 7.

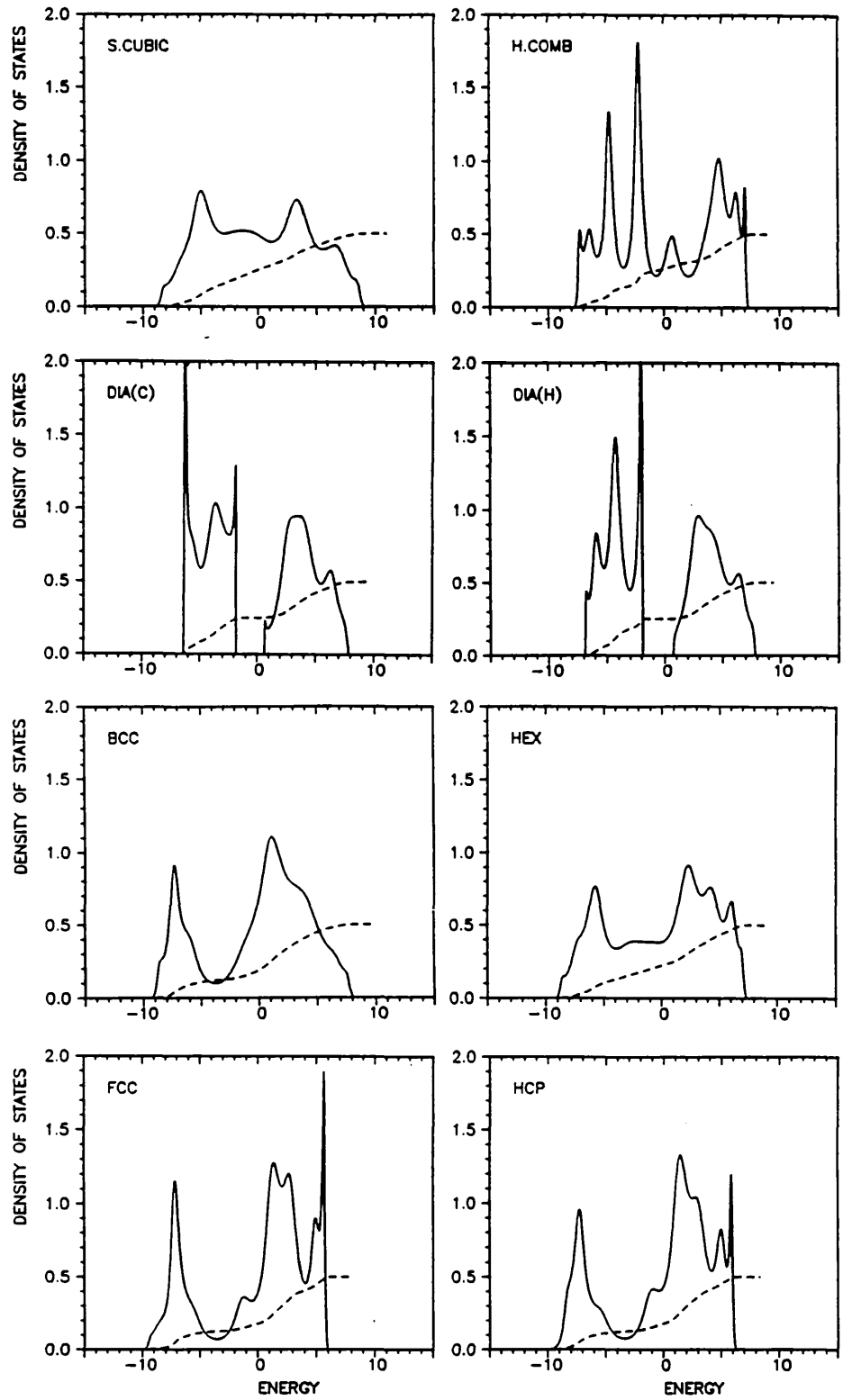


Figure 4.24  
 Densities of states for  $\epsilon_{sp} = 12 \cdot \tan(\pi/10)$ .



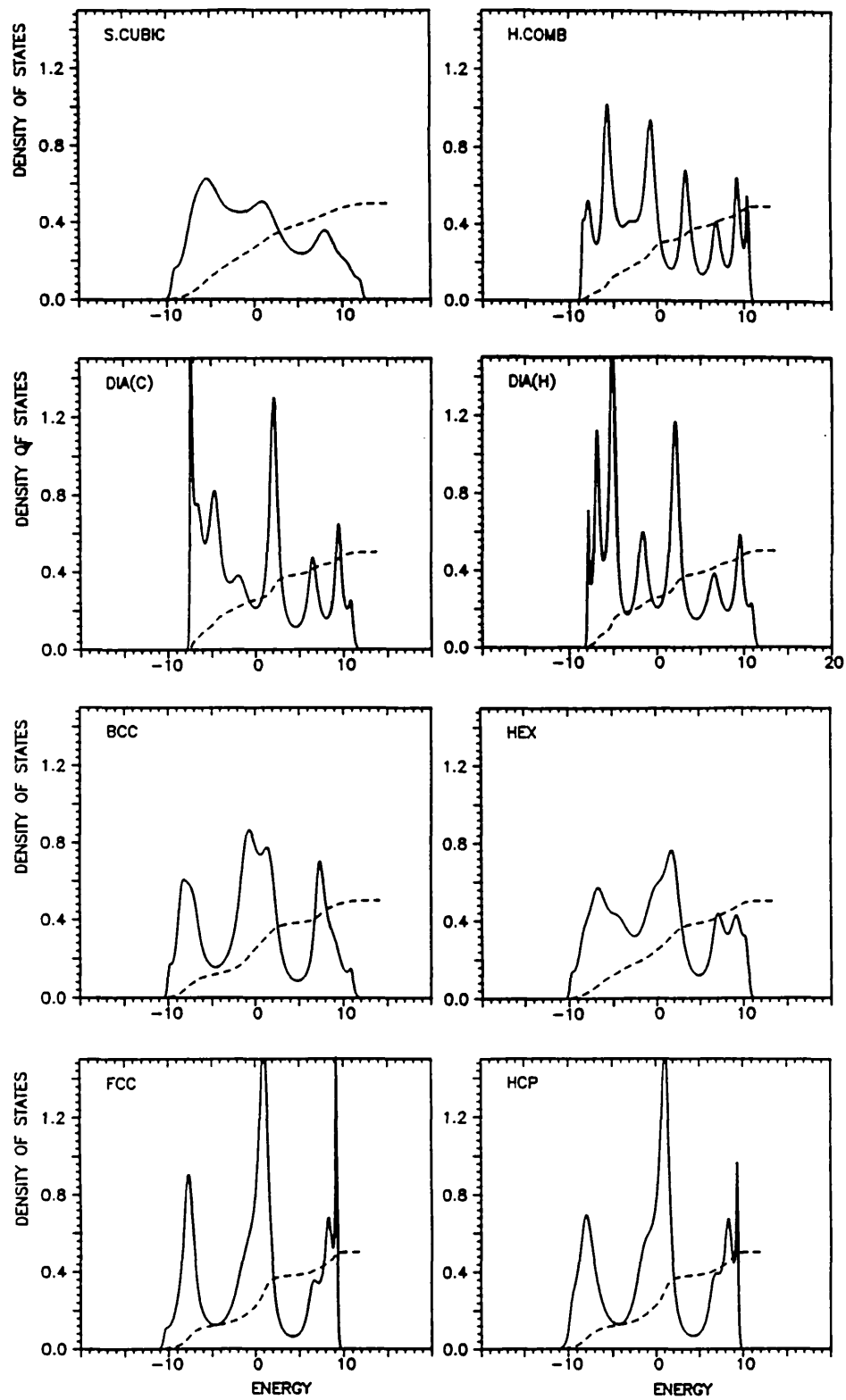


Figure 4.25  
Densities of states for  $\epsilon_{sp} = 12 \cdot \tan(2\pi/10)$ .

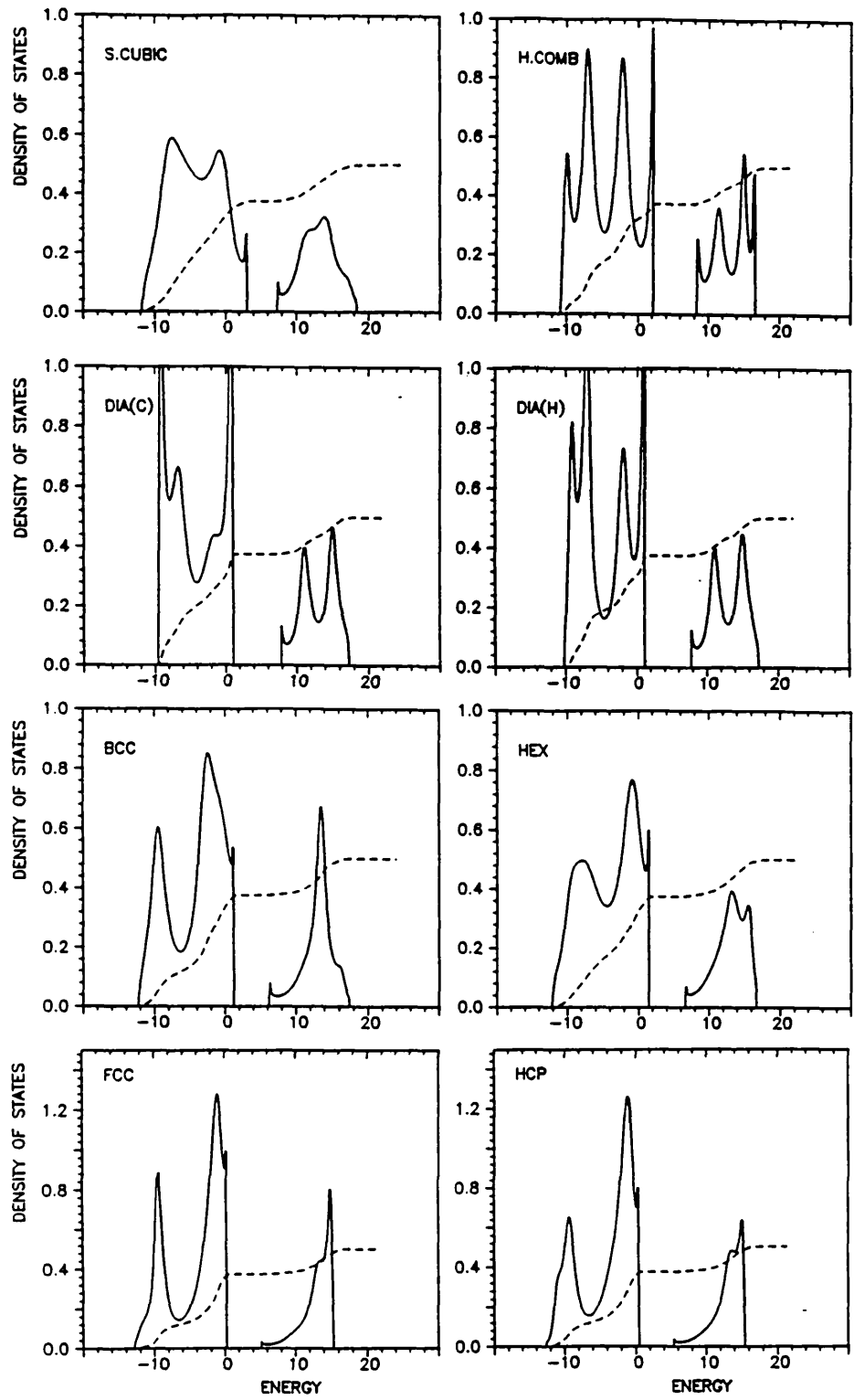


Figure 4.26  
 Densities of states for  $\epsilon_{sp} = 12 \cdot \tan(3\pi/10)$ .

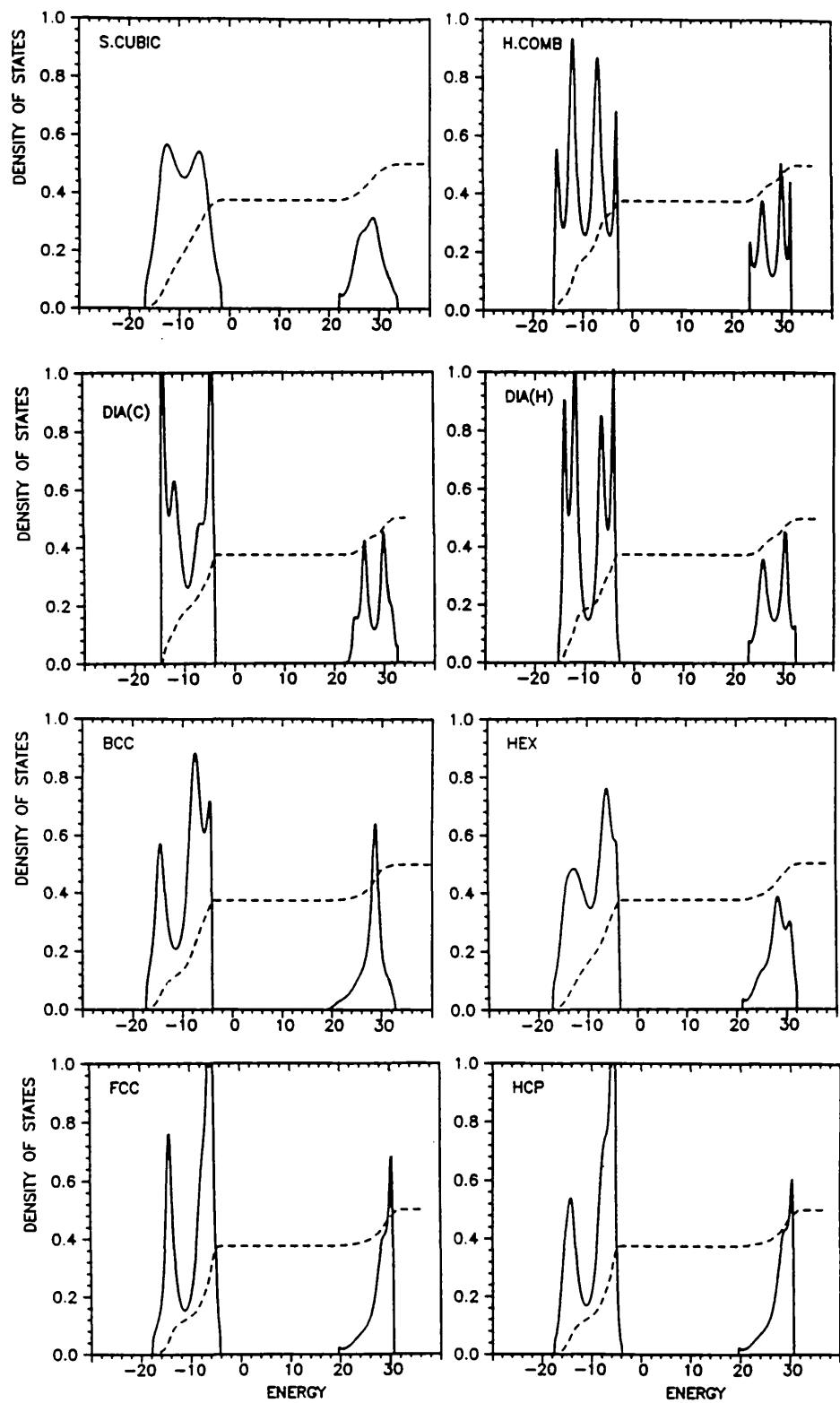


Figure 4.27  
 Densities of states for  $\epsilon_{sp} = 12 \cdot \tan(4\pi/10)$ .

## §4.6 Conclusions

The predictions made by the model are very good. In fact it is amazing that such a simple theory can account for the relative stability of such different structures like the dimer and the close packed arrangements. The degree of success is very encouraging for us to take one step further towards the description of more complicated materials, namely the AB alloys. First, however, we attempt to a explanation as to the physical origins of the different regions of stability observed in the structural map. This is done in the next chapter.

## CHAPTER 5: Interpretation in Terms of the Moments

In the last chapter a tight binding model was developed which proved to be a reliable tool for the prediction of the structural trends amongst the sp-bonded elements. In this chapter we provide a physical explanation to these theoretical results in terms of the local topology. The interpretation will be given in terms of the moments of the density of states because they provide an immediate contact with the local lattice topology. Only up to five moments are shown to be necessary to reproduce the fundamental trends. We will see that the fourth moment plays a fundamental role in the structural separation amongst the open structures. A physical interpretation is then given in terms of number of paths and the associated weight.

## §5.1 Introduction

The successful prediction of the sp structural trends as derived in the last chapter did not provide an explanation as to the origin of the domains in the structural map. We try to give an answer to this question in this chapter. Only the pure s, pure p and  $\epsilon_{sp} = 0$  cases will be considered here. The main reason for choosing these cases is because the on-site energies are then zero which removes all contributions from self-tracing paths (see chapter 2) and thus simplifies the analysis. These limiting cases (notice that  $\epsilon_{sp} = -\infty$  is given by the pure cases) will be sufficient to give a general feeling as to the important parameters governing structural stability. In order to reach our goal, we use the moments of the local density of states as a main tool. The usefulness of these quantities in studies about structural behaviour has been early recognized by the French school (Ducastelle and Cyrot-Lackmann 1970, 1971) so that the ideas have been around for about twenty years. Since the moments directly probe the lattice geometry, they constitute a sensible and natural starting point for our discussion. As discussed in chapter 2 the recursion method and the moments method are entirely equivalent in the sense that they possess the same information about the system. However, while the former is advantageous from the quantitative point of view the latter has in general a greater qualitative appeal. In fact I often find myself going back to the moments when it comes to the interpretation of results.

Only the basic trends between different coordinations will be discussed here so that we will not attempt to separate very similar structures like the close packed fcc, hcp and bcc or the four-fold coordinated cubic and hexagonal diamond lattices. The reason for this lies upon the fact that the more similar the structures the more the minimum number of moments necessary to achieve a good separation. This would complicate the analysis and simplicity would be lost.

## §5.2 Structural Stability and Moments

Let us determine the minimum number of moments necessary to reproduce the basic structural trends observed amongst the  $sp$  elements. Notice that in our model all the moments up to  $\mu_2$  (inclusive) are kept the same for all structures. We therefore expect the relative stability between two given structures to be primarily dependent on the difference between their 3rd moments. In order to find out how far we have to go from the central site to get the correct relative stability we studied the variation in the structural map (pure  $s$ , pure  $p$  and  $\epsilon_{sp} = 0$  cases only) as a function of the number of exact moments. The structural energy versus band filling curves are shown in figures 5.1–5.2 (pure  $s$ ), 5.3–5.4 (pure  $p$ ) and 5.5–5.6 ( $\epsilon_{sp} = 0$ ) in which all the moments up to  $\mu_n$  are exact with  $n = 3, 4, 5$  and  $6$  (the result for  $n = 18$  was shown in chapter 4). For these figures a reference skew DOS was used which was fixed to the first four moments of the simple cubic structure as described in the previous chapters. The continued fractions were terminated using the optimized Beer and Pettifor's square root terminator determined for the bulk, corresponding to a cluster with eighteen exact moments. The resulting terminating function was then appended to the continued fraction with the right number of coefficients to account for the required number of exact moments. The dimer is an exception because the density of states consists in a set of levels which corresponds to a truncation of the continued fraction. In appendix VII we show how the approximation in terms of number of moments was implemented to the dimer structure.

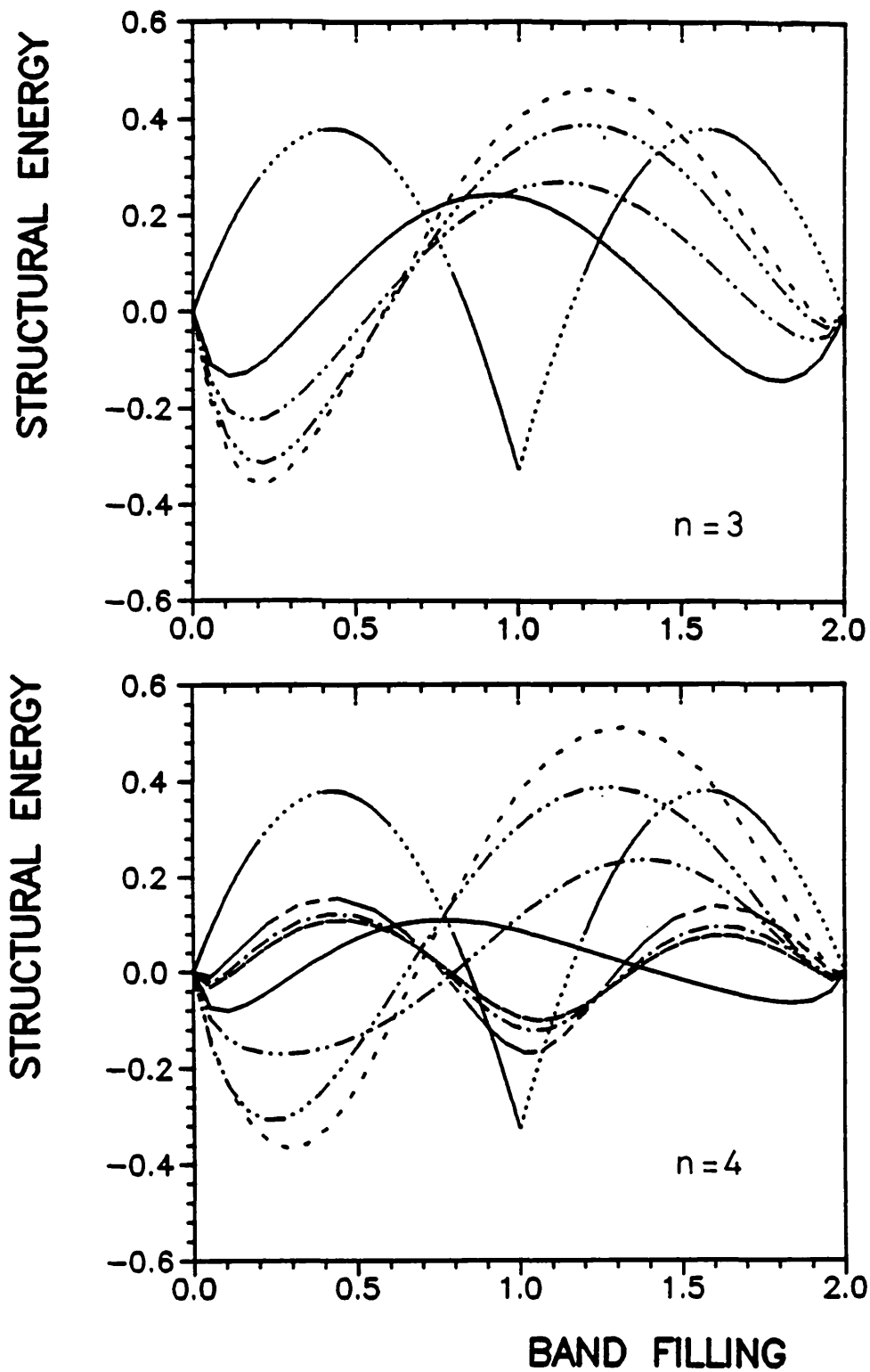


Figure 5.1  
Structural energy versus band filling curves for the pure s case with exact moments up to  $\mu_n$ , with  $n=3$  and  $n=4$ .



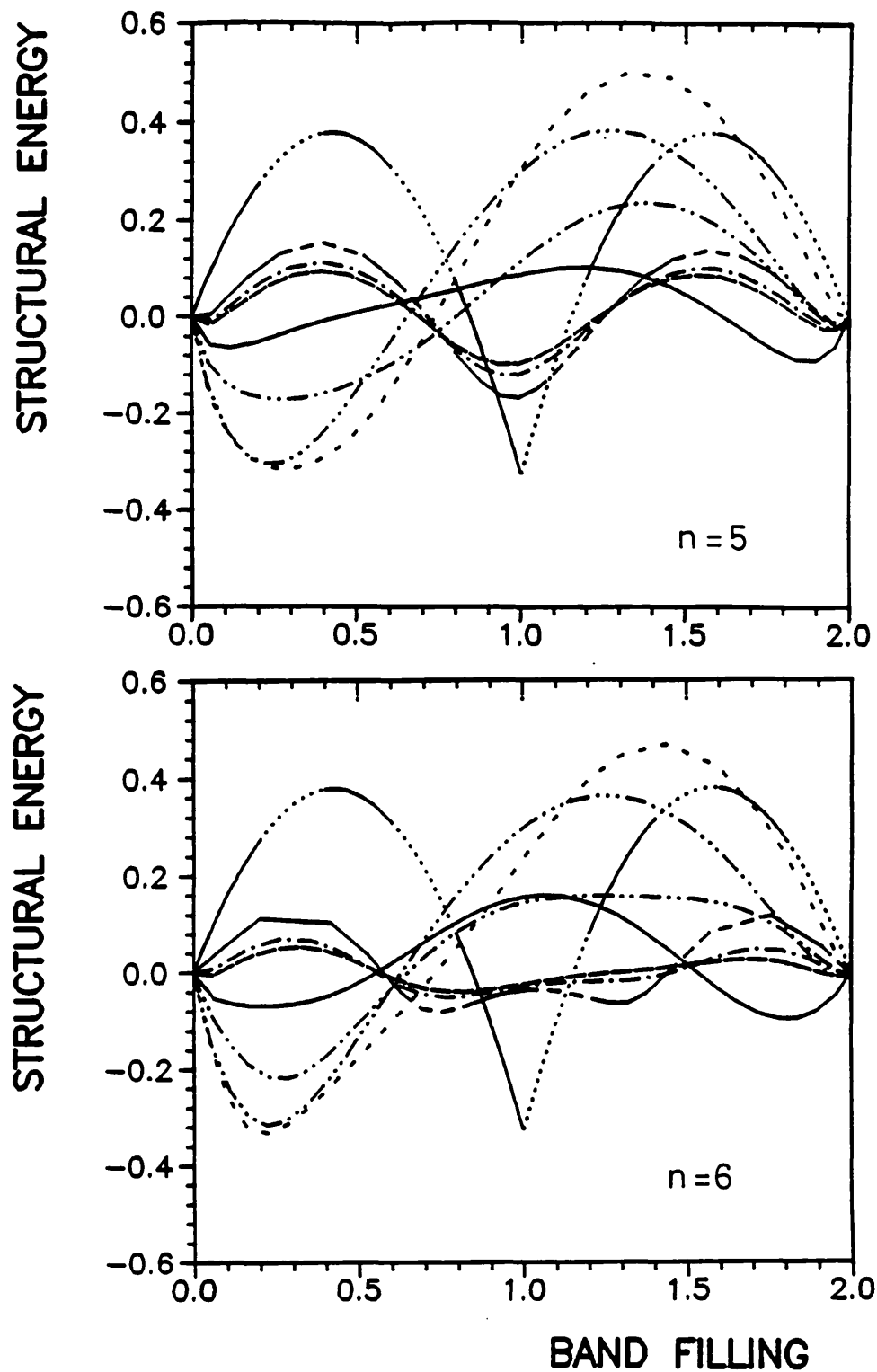


Figure 5.2  
Structural energy versus band filling curves for the pure s case with exact moments up to  $\mu_n$ , with  $n=5$  and  $n=6$ .

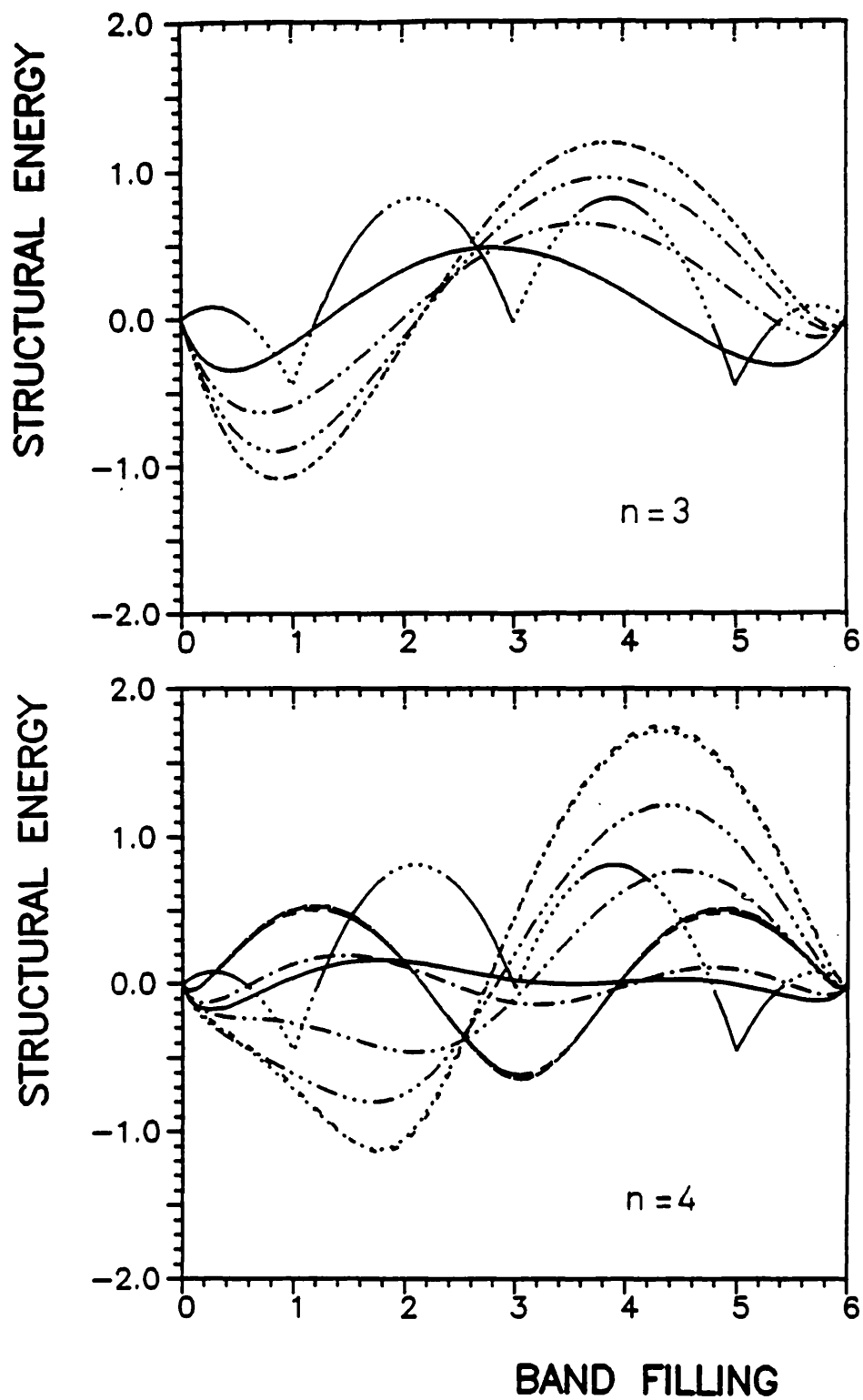


Figure 5.3  
 Structural energy versus band filling curves for the pure p case with exact moments up to  $\mu_n$ , with  $n=3$  and  $n=4$ .

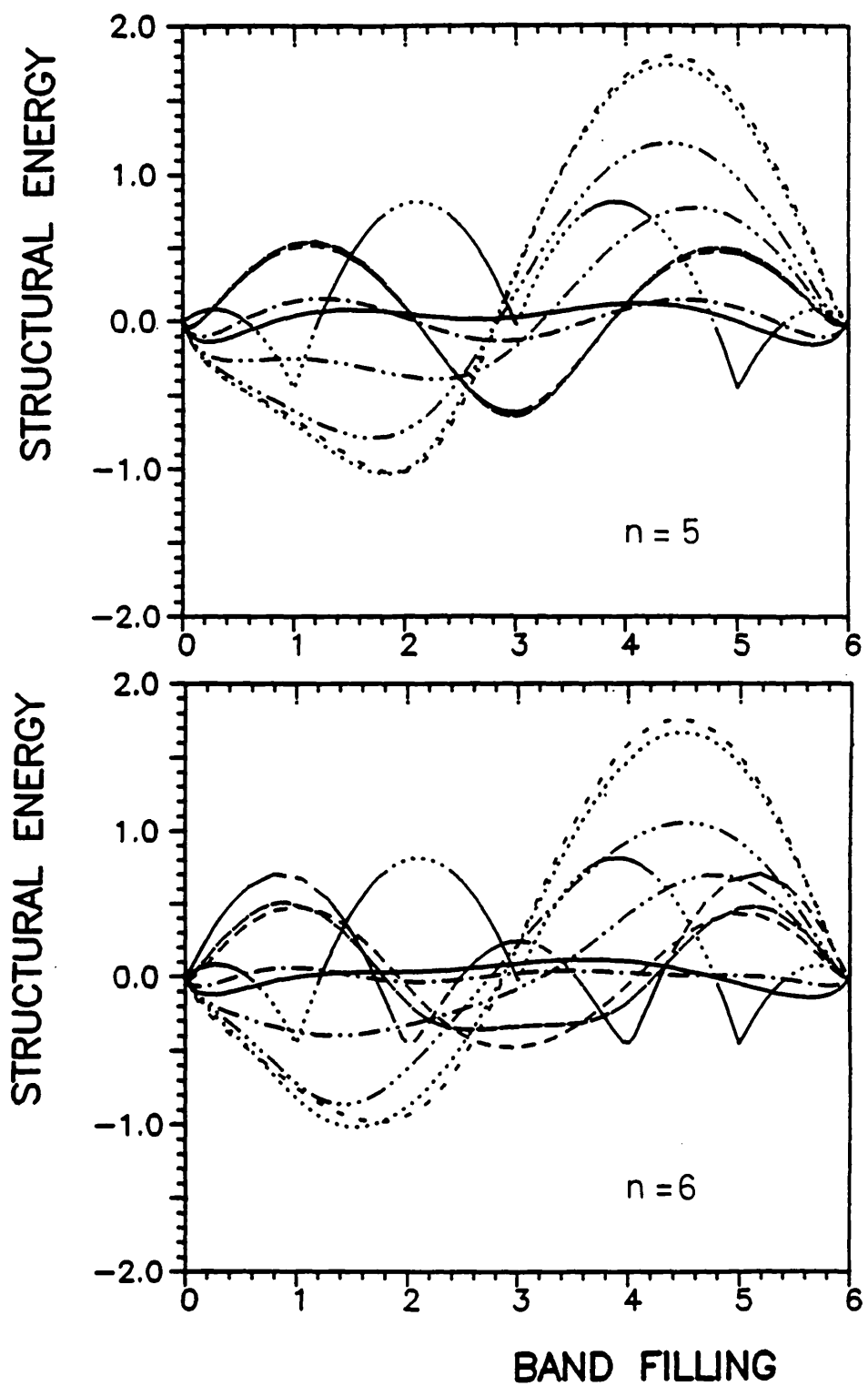


Figure 5.4  
Structural energy versus band filling curves for the pure p case with exact moments up to  $\mu_n$ , with  $n=5$  and  $n=6$ .

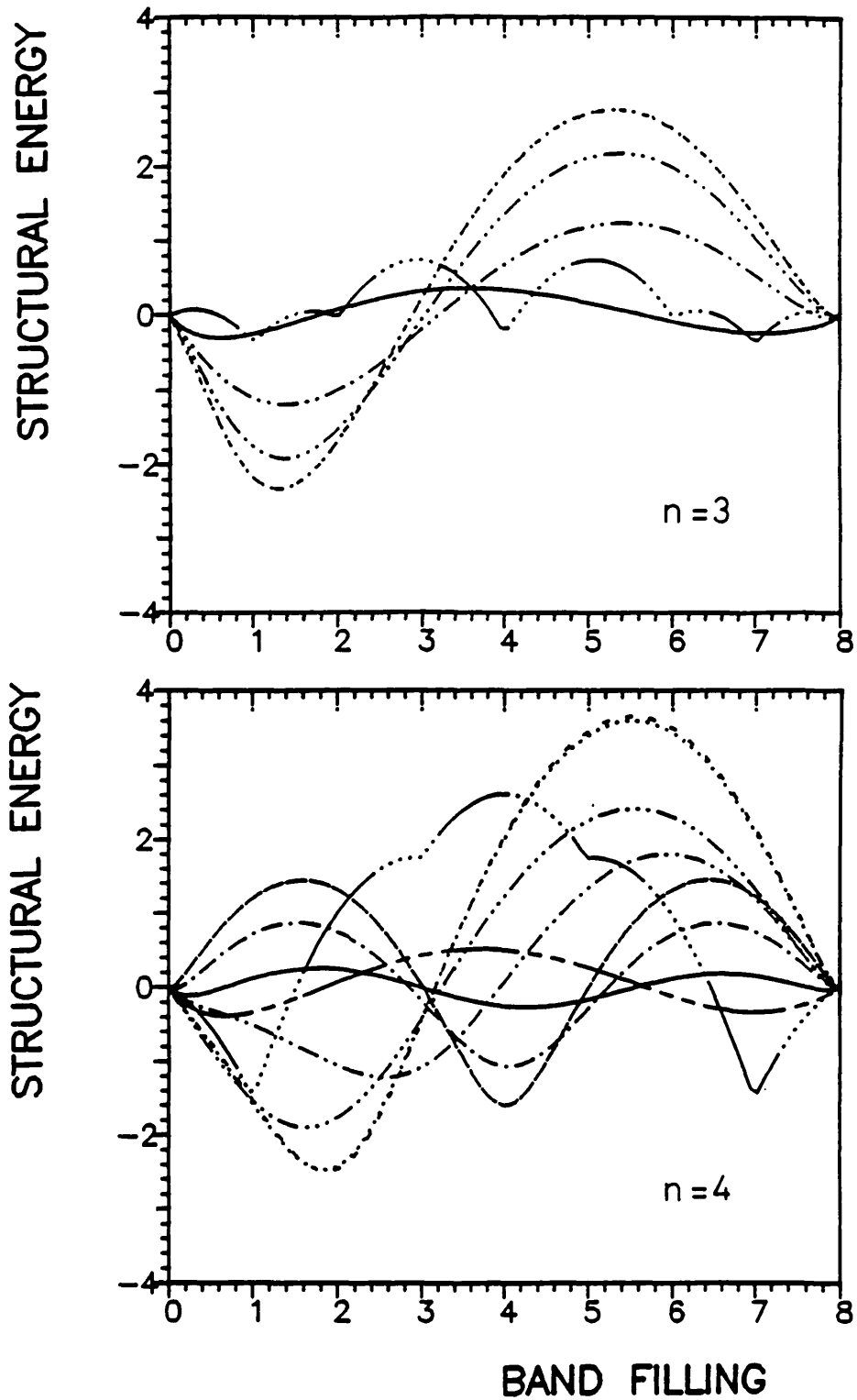


Figure 5.5  
Structural energy versus band filling curves for the  $\epsilon_{sp} = 0$  case with exact moments up to  $\mu_n$ , with  $n=3$  and  $n=4$ .

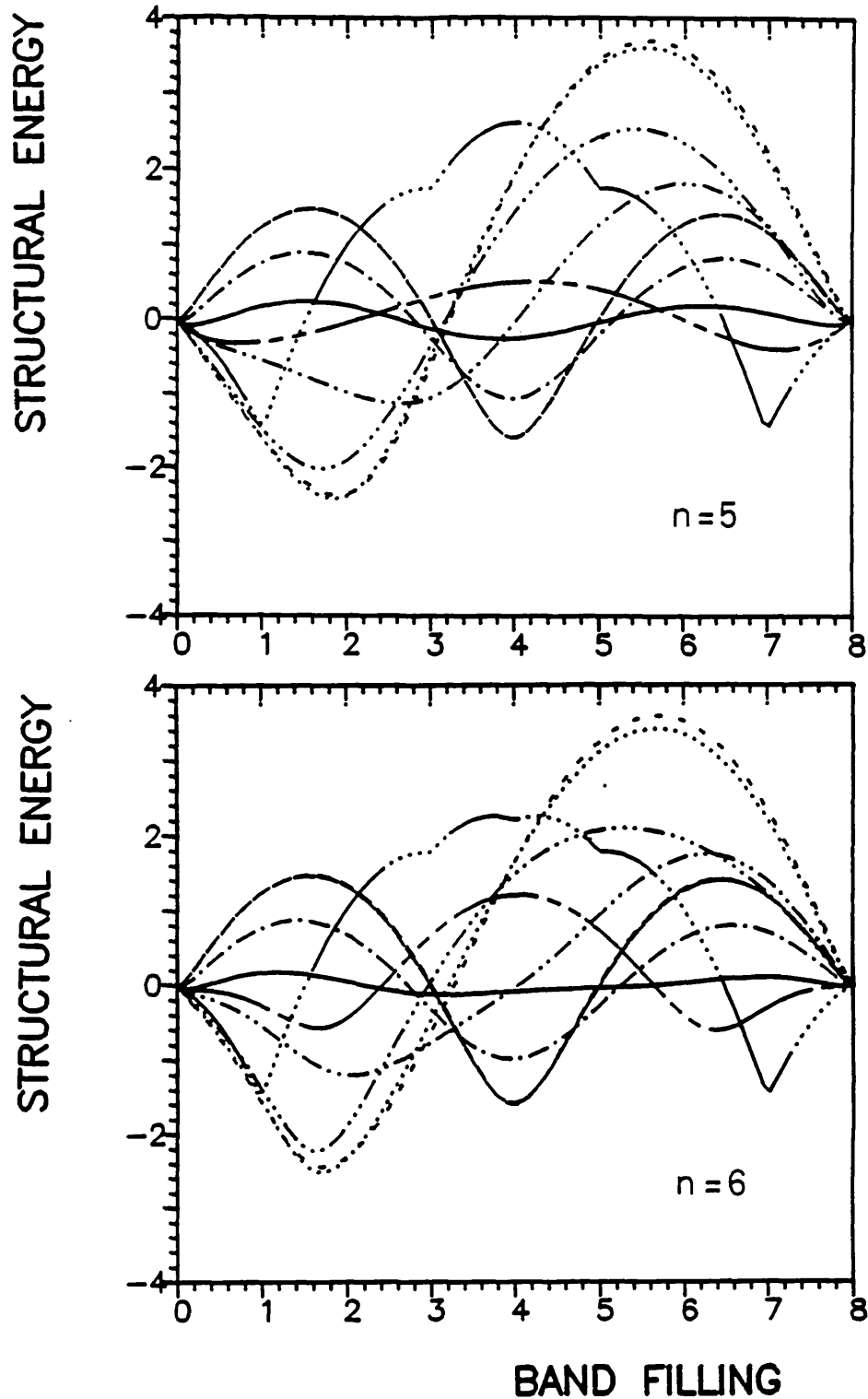


Figure 5.6  
Structural energy versus band filling curves for the  $\epsilon_{sp} = 0$  case with exact moments up to  $\mu_n$ , with  $n=5$  and  $n=6$ .

The convergence of the structural trends with the number of exact moments is summarized in figures 5.7 (pure s), 5.8 (pure p) and 5.9 ( $\epsilon_{sp} = 0$ ). For the pure s case we see that the stability trend from left to right is given by

#### Pure s

n = 18: fcc/hcp  $\rightarrow$  z.zag  $\rightarrow$  dimer  $\rightarrow$  z.zag  $\rightarrow$  s.cub.

n = 4: fcc/hcp  $\rightarrow$  hex  $\rightarrow$  z.zag  $\rightarrow$  dimer  $\rightarrow$  z.zag  $\rightarrow$  dia(c/h)  $\rightarrow$  sc

where dia(c/h) stands for diamond lattice (either cubic or hexagonal), fcc/hcp means either one of these two arrangements and n means that all moments up to  $\mu_n$  are exact. The corresponding pure p and  $\epsilon_{sp} = 0$  trends are, respectively,

#### Pure p

n = 18: fcc  $\rightarrow$  hcp  $\rightarrow$  fcc  $\rightarrow$  dia(h)  $\rightarrow$  dia(c)  $\rightarrow$  z.zag  $\rightarrow$  sc  $\rightarrow$  dimer  $\rightarrow$  sc

n = 4: bcc  $\rightarrow$  hcp  $\rightarrow$  fcc  $\rightarrow$  dia(c/h)  $\rightarrow$  z.zag  $\rightarrow$  h.comb  $\rightarrow$  sc  $\rightarrow$  dimer  $\rightarrow$  sc

and

$$\epsilon_{sp} = 0$$

n = 18: fcc  $\rightarrow$  hcp  $\rightarrow$  fcc  $\rightarrow$  hex  $\rightarrow$  h.comb  $\rightarrow$  dia(c)  $\rightarrow$  dia(h)  $\rightarrow$  dia(c)  $\rightarrow$   
h.comb  $\rightarrow$  sc  $\rightarrow$  z.zag  $\rightarrow$  dimer

n = 4: bcc  $\rightarrow$  hcp  $\rightarrow$  fcc  $\rightarrow$  hex  $\rightarrow$  dia(c/h)  $\rightarrow$  h.comb  $\rightarrow$  sc  $\rightarrow$  z.zag  $\rightarrow$  dimer.

Notice that for integer values of the band filling the correct relative stability of the

bulk can be obtained if all the moments up to  $\mu_4$  are known. The only exception is for the pure p case with band filling equal to four (see figure 5.8). Since however this is a theoretical limiting case which should actually hybridize with an s state, we regard this as a minor drawback (the energy differences are actually very small as can be seen from figure 5.3) and take  $\mu_4$  as the bottom limit above which the systems can be well separated. Naturally, closely similar structures can not be separated with so little information. The close packed fcc and hcp structures for example can only be separated if  $\mu_5$  is also known (see Beer 1985 for transition metals). Also the four fold coordinated cubic and hexagonal diamond lattices are exactly similar up to  $\mu_5$  and require  $\mu_6$  for the separation to occur. Apart from these cases, however, the knowledge of the first five moments (i.e., up to  $\mu_n$ ,  $n = 0, 1, \dots, 4$ ) is enough to provide the basic trends observed in the structural maps discussed in the last chapter.

In order to find the dependence of the structural energy versus band filling curves on the number of exact moments one can derive an expression for the moments of the band energy in terms of the moments of the density of states. One starts with the band (or structural) energy  $E_b(x)$  as a function of the Fermi energy, i.e.,

$$E_b(x) = \int_{-\infty}^x E \rho(E) dE \quad (5.1)$$

where  $\rho(E)$  is the DOS. Notice that in general if  $\int_{-\infty}^{+\infty} t \rho(t) dt = 0$  and  $\rho(t) > 0$  then  $\int_{-\infty}^x t \rho(t) d(t) \leq 0$  for all  $x$ . The proof is trivial for  $x \leq 0$  while

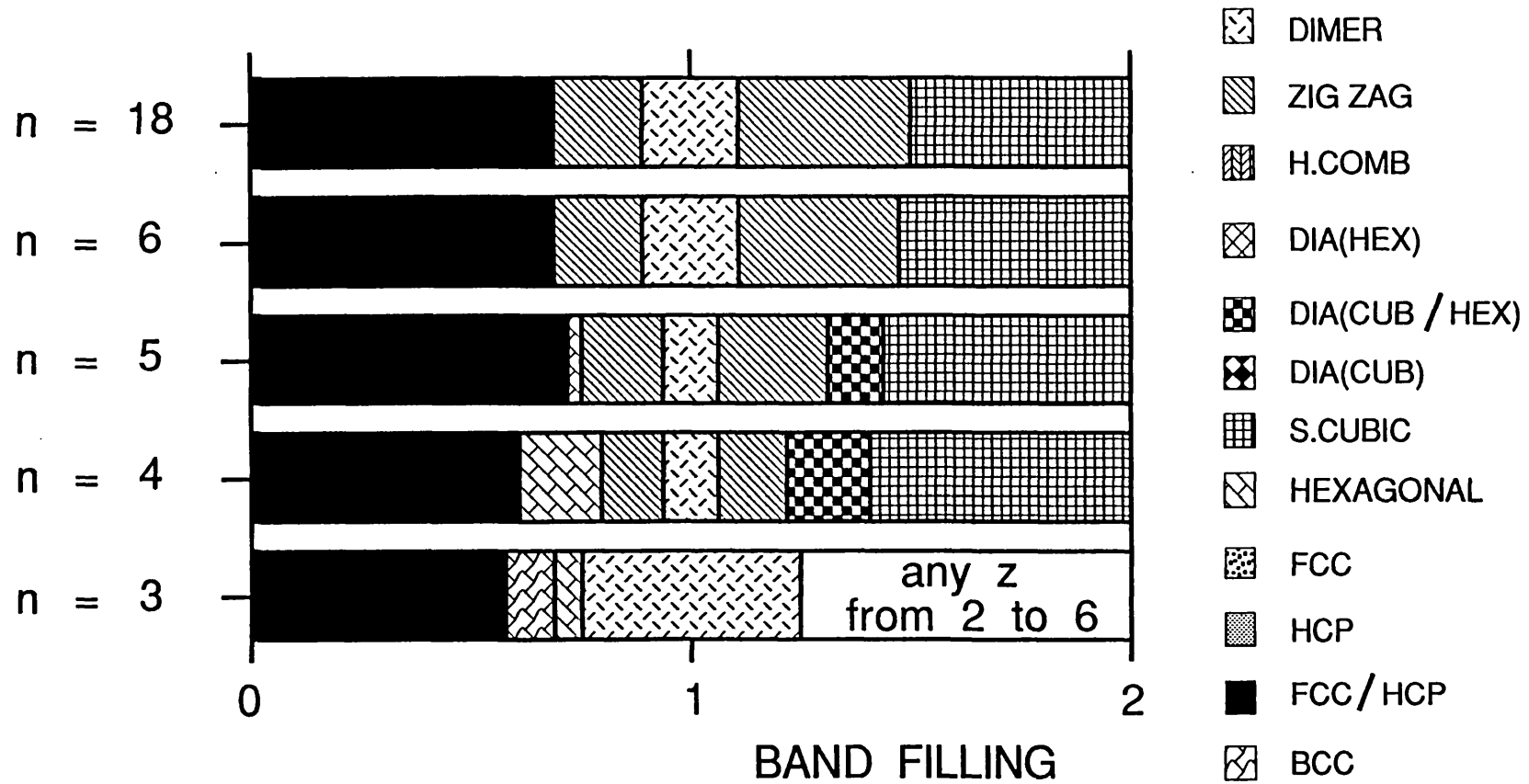


Figure 5.7

Convergence with the number of exact moments for the pure s case. The moments are known up to  $\mu_n$  (inclusive) where  $n$  is indicated in the vertical axis.



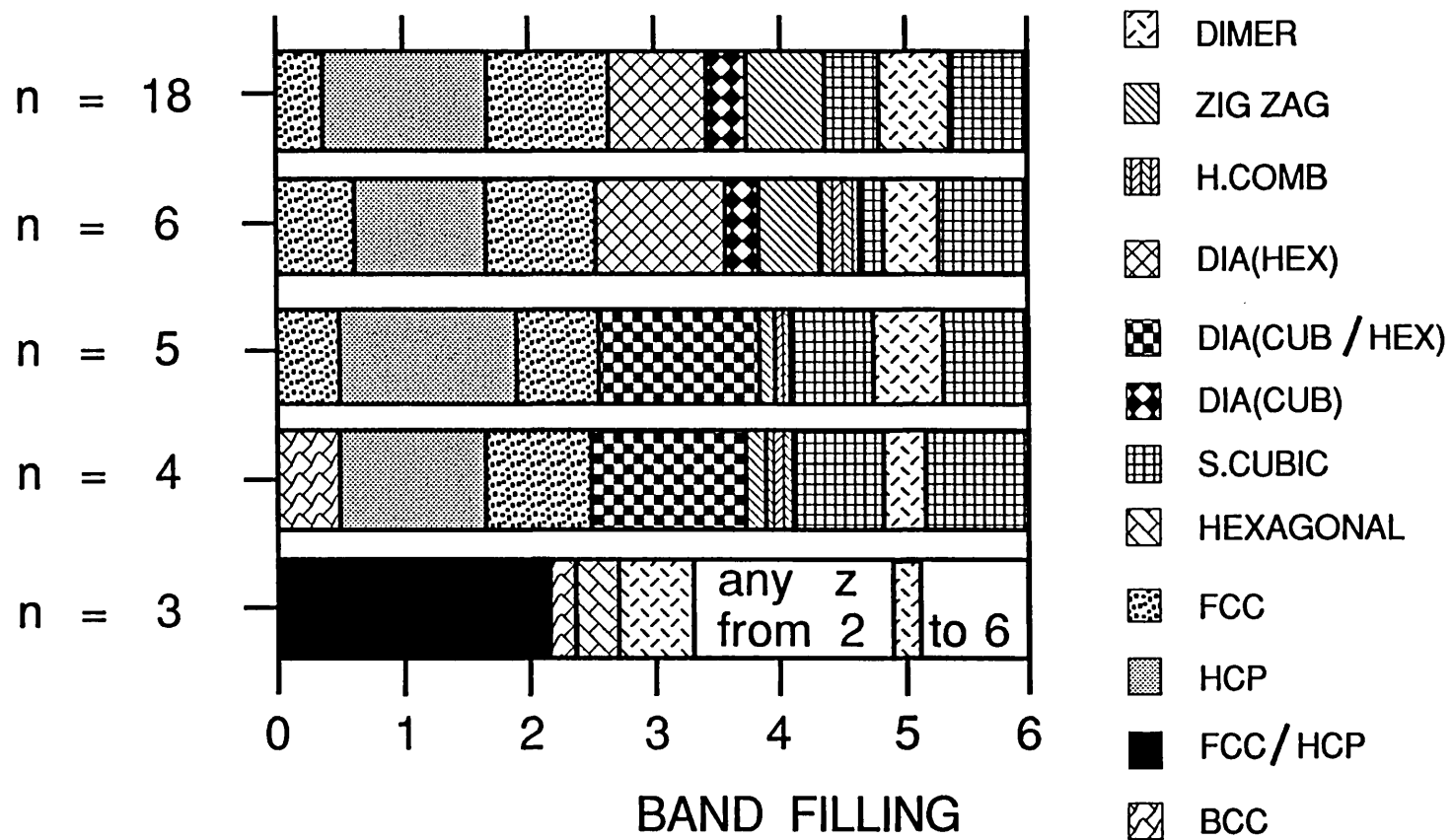


Figure 5.8

Convergence with the number of exact moments for the pure p case. The moments are known up to  $\mu_n$  (inclusive) where  $n$  is indicated in the vertical axis.

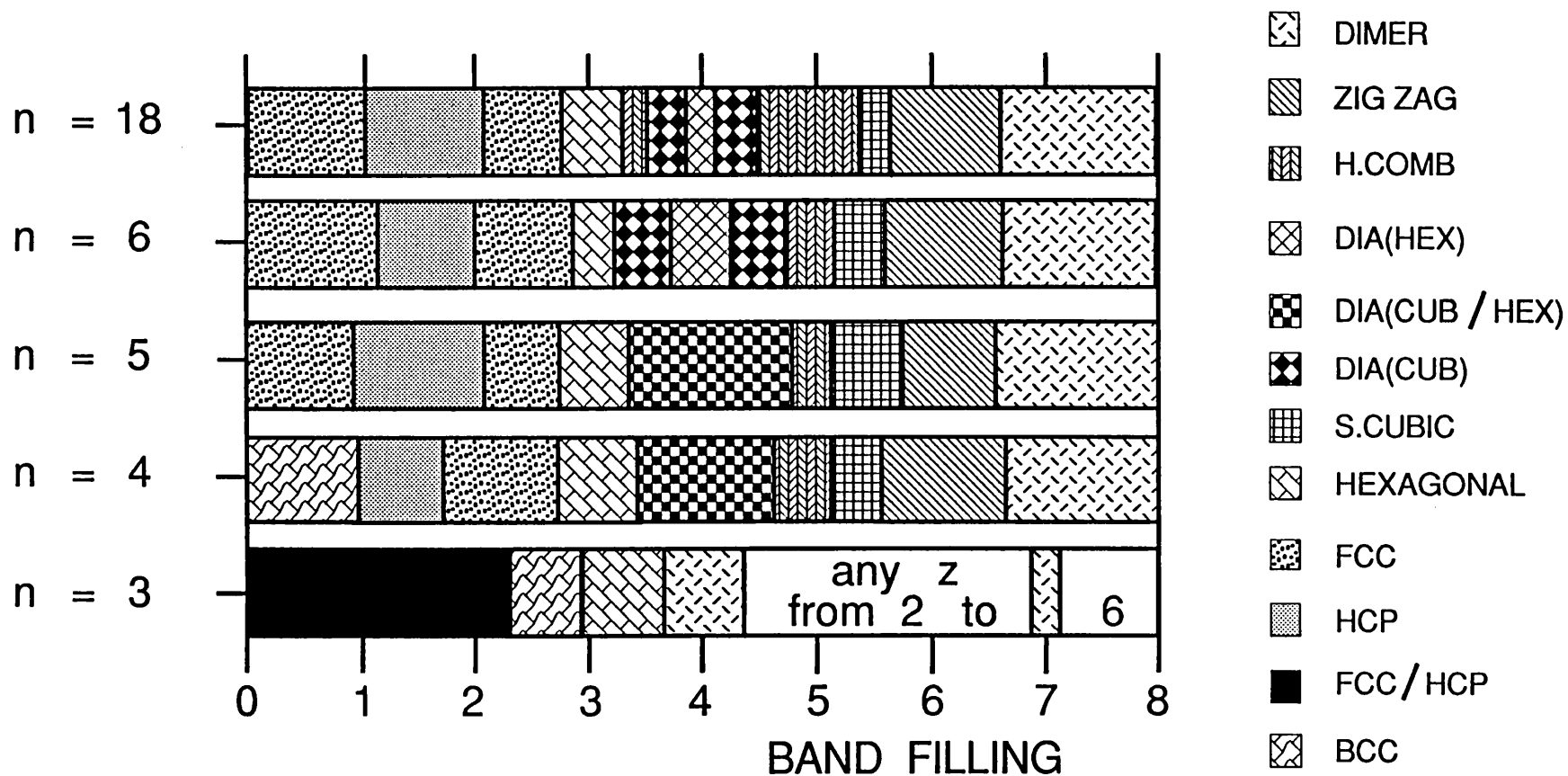


Figure 5.9  
 Convergence with the number of exact moments for the  $\epsilon_{sp} = 0$  case. The moments are known up to  $\mu_n$  (inclusive) where  $n$  is indicated in the vertical axis.

for  $x > 0$  we notice that

$$\begin{aligned} 0 &= \int_{-\infty}^{+\infty} t \rho(t) dt \\ &= \int_{-\infty}^x t \rho(t) dt + \int_x^{+\infty} t \rho(t) dt \end{aligned} .$$

Since  $x > 0$  the second term in the left hand side in this expression is greater than zero and therefore  $\int_{-\infty}^x t \rho(t) dt < 0$  which completes the proof. Therefore provided that the first moment of the density of states (i.e., the center of gravity of the band) is made equal to zero the band energy will always be negative.

The idea now is to work with moments of the band energy rather than with moments of the density of states (Turchi and Ducastelle 1985, Burdett and Lee 1985a, 1985b). For example one can define the moments of  $E_b(x)$ , i.e.,  $\mu_n(E_b)$  by

$$\mu_n(E_b) = \int_{-\infty}^{+\infty} x^n E_b(x) dx \quad (5.2)$$

which can be integrated by parts to give

$$\mu_n(E_b) = \frac{-1}{n+1} \mu_{n+2}(\rho)$$

In the same way that the sequence  $\mu_n(\rho)$  can be used to reconstruct the density of states, the sequence  $\mu_n(E_b)$  can be used to reconstruct the band energy. However we would like to reconstruct the band energy difference  $\Delta E_b$  between two given structures. This difference can be computed either at the same value of the Fermi energy or at the same value of the band filling. In accordance to what we have

been doing so far we shall work with  $\Delta E_b$  at constant band filling. In appendix XI we show how to obtain an expression for  $\Delta E_b(x) = E_{b_2}(x_2) - E_{b_1}(x_1)$  at constant band filling which is valid to first order in the Fermi energy difference  $x_2 - x_1$  (see Turchi and Ducastelle 1985). It is given by (XI.5) and reads

$$\Delta E_b(x) \simeq - \int^x d\epsilon \int^\epsilon \Delta \rho(t) dt$$

where  $x = x_1$  or  $x_2$  for structures 1 and 2. In this case an approximate expression for  $\mu_n(\Delta E_b)$ , similar to the one above for  $\mu_n(E_b)$ , can be written down (see appendix XI and Turchi and Ducastelle op.cit.), namely,

$$\mu_n(\Delta E_b) \simeq \frac{-1}{(n+1)(n+2)} \mu_{n+2}(\Delta \rho) \quad . \quad (5.3)$$

In order to see how the reconstruction of the  $\Delta E_b$  curve works let us consider two structures with densities of states  $\rho_1$  and  $\rho_2$  such that

$$\mu_n(\rho_1) = \mu_n(\rho_2) \quad \text{for } n = 0, 1, \dots, m-1 \quad (5.4)$$

and suppose first that  $m=3$  with  $\mu_3(\rho_1) < \mu_3(\rho_2)$ . From (5.3) we have

$$\mu_0(E_{b_1}) = \mu_0(E_{b_2}) \quad (5.5)$$

which means that the area under the curves  $E_{b_1}(x)$  and  $E_{b_2}(x)$  is the same. However, since  $\mu_3(\rho_1) < \mu_3(\rho_2)$  we see from (5.3) that  $\mu_1(E_{b_1}) > \mu_1(E_{b_2})$  and therefore the center of gravity of the two curves are displaced with respect to each other. Since  $E_{b_1}$  and  $E_{b_2}$  are always negative the relative positions of these curves when the difference  $\mu_3(\Delta \rho)$  is large is as shown schematically in figure

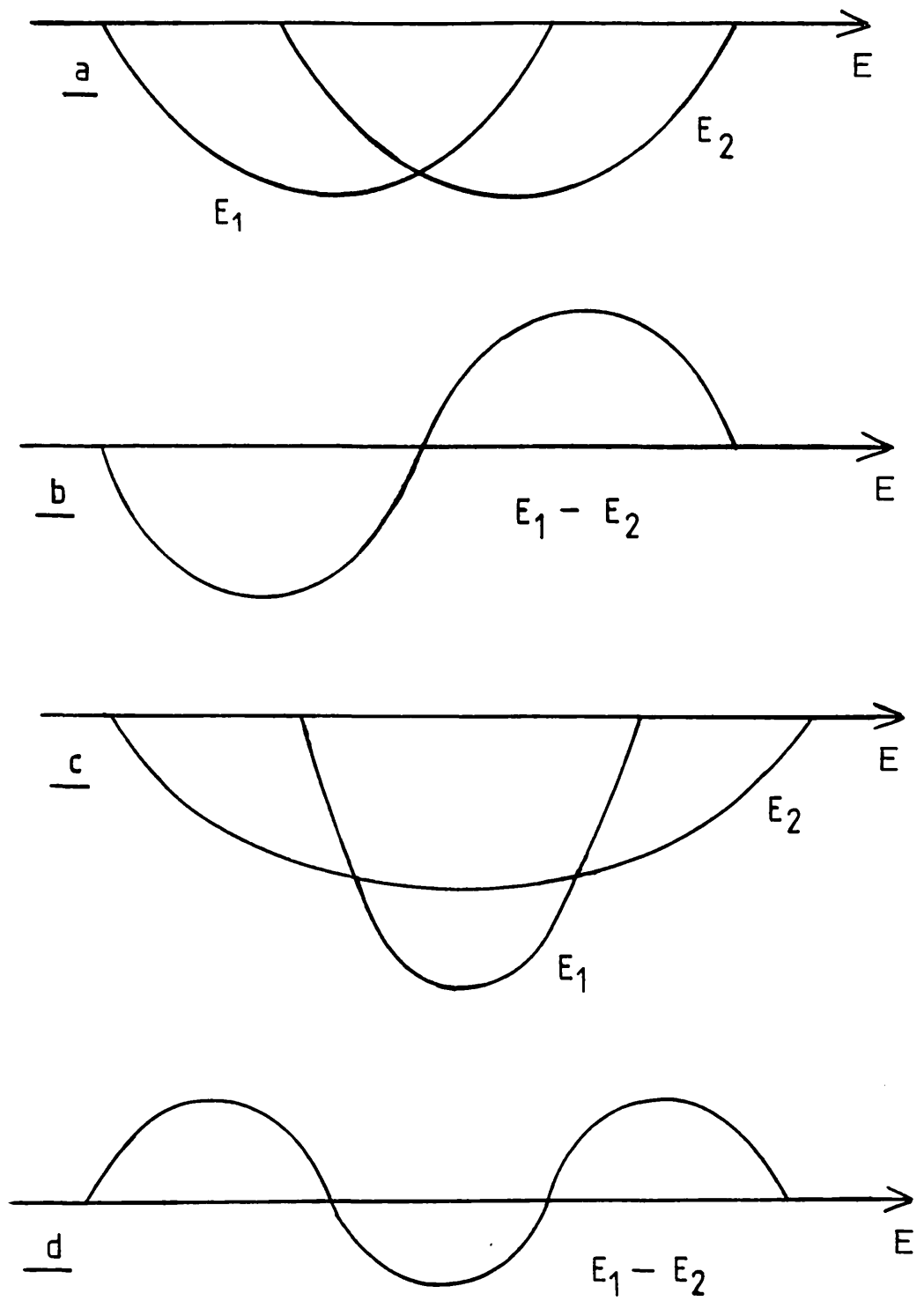


Figure 5.10  
 Band energy as a function of the Fermi energy assuming  $\mu_n(\Delta\rho) = 0$  for  $n = 0, 1, \dots, m-1$ : a) and b)  $m = 3$ ,  $\mu_3(\rho_1) < \mu_3(\rho_2)$ ; c) and d)  $m = 4$ ,  $\mu_4(\rho_1) < \mu_4(\rho_2)$ .

5.10a. Notice that the largest  $\mu_1(E_b)$  goes to the left because the curve is always below the energy axis. The corresponding  $\Delta E_b$  versus Fermi energy curve is shown in figure 5.10b.

Similarly if  $m = 4$  we have  $\mu_n(\rho_1) = \mu_n(\rho_2)$  for  $n = 0, 1, 2$  and  $3$  and the differences between the two structures start in the fourth moment. In this case assuming that  $\mu_4(\rho_1) < \mu_4(\rho_2)$  and that the  $\mu_4(\Delta\rho)$  is large so that the band energy is largely governed by the fourth moment (see Burdett 1985a for details), the curves should look like the ones shown in figures 5.10c and 5.10d.

Notice that the curves in figure 5.10 are given in terms of the Fermi energy rather than the band filling. However since the band filling is a nondecreasing function of the Fermi energy, the  $E_b(N)$  curves are expected to have the same form. Another remark we would like to make is that in drawing these curves only information up to the first nonzero difference in the moments is being used. Therefore the influence of other moments is being implicitly neglected which can be an over simplification if  $\mu_{m+1}(\Delta\rho)$  is important compared with  $\mu_m(\Delta\rho)$ . Burdett and Lee's approach can take this into account in a quantitative way. Here, however, we are not interested in separating too similar structures and therefore the level of detail presented above is enough for our purposes.

In Tables 5.1 to 5.3 we list the values of the first few moments ( $\mu_n$ ,  $n = 0$  to  $6$ ) for the cases we analyze in the next sections, namely the pure s, pure p and  $\epsilon_{sp} = 0$ . The moments are given in a normalized (nondimensional) form which makes them assume values around 1. The number of different paths are also given, on-site paths not contributing since in the three cases considered  $\epsilon_s = \epsilon_p = 0$ .

PURE S				
$(\mu_0 = 2, \mu_1 = 0 \text{ and } \mu_2 = 12)$				
Structures	$\mu_n/(\mu_2)^{n/2}$ (No. of paths)			
	n = 3	n = 4	n = 5	n = 6
Zig-Zag	0 (0)	0.7500 (6)	0 (0)	0.6250 (20)
H.Comb	0 (0)	0.8333 (15)	0 (0)	0.8611 (93)
Dia	0 (0)	0.8750 (28)	0 (0)	1.0000 (256)
S.Cubic	0 (0)	1.2500 (90)	0 (0)	2.1528 (1860)
Hexagonal	-0.3750 (12)	1.3125 (168)	-1.1719 (600)	2.5879 (5300)
fcc	-0.8165 (48)	1.8750 (540)	-3.0619 (4320)	6.1111 (42240)

Table 5.1 – Moments values for the single s orbital case. The moments are listed in a normalized nondimensional form and the number of paths is given in brackets. The first three moments are the same for all structures.

PURE P				
( $\mu_0 = 6, \mu_1 = 0$ and $\mu_2 = 78.2692$ )				
Structures	$\mu_n/(\mu_2)^{n/2}$ (No. of paths)			
	n = 3	n = 4	n = 5	n = 6
Zig-Zag	0 (0)	0.2500 (6)	0 (0)	0.0637 (20)
H.Comb	0 (0)	0.3075 (15)	0 (0)	0.1184 (93)
Dia (cub)	0 (0)	0.2470 (28)	0 (0)	0.06889 (256)
Dia (hex)	0 (0)	0.2470 (28)	0 (0)	0.0725 (256)
S.Cubic	0 (0)	0.3274 (90)	0 (0)	0.1394 (1860)
Hexagonal	-0.1131 (12)	0.3048 (168)	-0.0833 (600)	0.1225 (5300)
fcc	-0.2462 (48)	0.3163 (540)	-0.1584 (4320)	0.1431 (42240)
hcp	-0.2462 (48)	0.3200 (540)	-0.1574 (4320)	0.1416

Table 5.2 – Moments values for the pure p orbital case. The moments are listed in a normalized nondimensional form and the number of paths is given in brackets. The first three moments are the same for all structures.



$\epsilon_{sp} = 0$				
( $\mu_0 = 8, \mu_1 = 0$ and $\mu_2 = 131.7256$ )				
Structures	$\mu_n/(\mu_2)^{n/2}$ (No. of paths)			
	n = 3	n = 4	n = 5	n = 6
Zig-Zag	0 (0)	0.2662 (6)	0 (0)	0.0795 (20)
H.Comb	0 (0)	0.1753 (15)	0 (0)	0.0363 (93)
Dia (cub)	0 (0)	0.1502 (28)	0 (0)	0.0256 (256)
Dia (hex)	0 (0)	0.1502 (28)	0 (0)	0.0258 (256)
S.Cubic	0 (0)	0.2190 (90)	0 (0)	0.05785 (1860)
Hexagonal	-0.2503 (12)	0.2205 (168)	-0.0692 (600)	0.0612 (5300)
fcc	-0.3273 (48)	0.2926 (540)	-0.1633 (4320)	0.1159 (42240)
hcp	-0.3273 (48)	0.2958 (540)	-0.1632 (4320)	0.1163

Table 5.3 – Moments values for the  $\epsilon_{sp} = 0$  case. The moments are listed in a normalized nondimensional form and the number of paths is given in brackets. The first three moments are the same for all structures.

### §5.3 Stability of the Close Packed Structures

The relative structural stability between close packed structures (fcc, hcp and bcc) on one side and the other structures on the other side is expected to depend mainly on the third moment since it is here that the first nonzero moments difference occurs (see tables 5.1 to 5.3). We notice that these close packed structures appear in the structural maps only in the region of low band filling (the region we call the most bonding part of the spectrum). It is not difficult to understand this behaviour in terms of the geometry of the structures involved if we notice that the sole contribution to the third moment comes from triangular paths (on-site paths also contribute but they do not exist when  $\epsilon_s = \epsilon_p = 0$ ). These are absent in the lower coordinated structures (here we mean coordination up to  $z = 6$ , i.e., simple cubic) but they do show up in the close packed environments, where they are more likely to occur. Among the structures considered in this thesis the ones with this kind of path are the fcc, hcp, hexagonal and bcc lattices (actually one has to go to second neighbours in a bcc lattice in order to find triangular paths).

As we have shown in the previous section if the first nonzero moments difference between two structures happens to occur for the third moment the structural energy difference versus band filling curve is expected to have the form given in figure 5.10b. The structure with the minimum value for the third moment is then expected to be more stable at low values of the band filling which is indeed the type of behaviour we find if we look at the curves 4.16–18 shown in the previous chapter. The structures with nonzero  $\mu_3$  are always stabilized at the bonding part of the spectrum. We therefore conclude that the structural stability of the close packed structures for low values of the band filling is essentially due to the presence of triangular paths in these lattices.

These arguments can also be used to give a qualitative explanation for the behaviour of second neighbours hoppings in bcc as shown in figure 4.7. We see that if we totally neglect the presence of second neighbours the result is the long dashed curve which is less stable than all the others in the low band filling region. This is so because triangular paths are suppressed in the bcc lattice if second neighbours hoppings are not allowed. However as these couplings are turned on, the lobe in the bonding region is pushed down thus increasing stability. The net result in this case is then: the more important the second neighbours in bcc the greater the importance of triangular paths and therefore the more (less) stable the lattice becomes in the low (high) band filling region. Notice also that Ducastelle and Cyrot-Lackmann theorem (1971) is also obeyed in figure 4.7. The moments  $\mu_n$  are the same for  $n = 0, 1$ , and  $p$ , where  $p = 2$ , and therefore the number of nodes is at least  $p - 1 = 1$ .

## §5.4 Stability amongst the Open Structures

By open structures we mean the ones without triangular paths in the geometric environment. This excludes the hexagonal, fcc, hcp and bcc lattices from the study we undertake in this section (they will be included in the discussion when we feel that they are illuminating for general arguments). Therefore  $\Delta\mu_3 = 0$  and the relative stability is expected to be dependent on  $\mu_4$ . No attempt will be made to separate the four fold coordinated cubic and hexagonal diamond lattices (for which  $\Delta\mu_4 = 0$ ). Unless otherwise stated we shall refer to both these structures as diamond.

Let's keep in mind that if two structures 1 and 2 are such that  $(\mu_n)_1 = (\mu_n)_2$  for  $n = 1, 2$  and 3, and  $(\mu_4)_1 < (\mu_4)_2$ , then in a first approximation the relative structural energy curve will look like figure 5.10d with  $(\mu_4)_1$  being more stable than  $(\mu_4)_2$  for half filled band.

We focus attention in the half filled band region where the dimer is found more stable than the other structures for the case of pure s symmetry whereas diamond is favoured in the case of sp symmetry. If we understand this region the others can also be understood by extrapolation, following the curve in figure 5.10d. From now on when we mention the term stability, unless stated otherwise, we will be referring to the half filled band region of the spectrum.

First of all let us separate out the contributions of the different paths to the 4th moment for a given structure, i.e. ,

$$\mu_4 = \sum_{i=1}^{N_4} n_i h_i \quad (5.6)$$

where,

$h_i$  : weight of  $i$ th type of path;

$n_i$  : no. of paths with weight  $h_i$ ; and

$N_4$  : no. of topologically different paths contributing to  $\mu_4$ .

For a given lattice,  $i$  runs over all topologically different paths contributing to the fourth moment. Notice that  $n_i$  depends on the local topology, one of its parameters being the coordination  $z$ . Also, in our model, all the structures have the same second moment and therefore  $h_i$  is dependent on  $z$  through  $1/z^2$ . This can be easily seen by noticing that for a given structure  $\alpha$  with coordination  $z_\alpha$  the fixing of the same second moment as, say, the simple cubic lattice gives  $z_{sc} \cdot ss\sigma_{sc}^2 = z_\alpha \cdot ss\sigma_\alpha^2$ . Therefore  $ss\sigma_\alpha \propto 1/z_\alpha^{1/2}$  and since the weights defined in (5.6) are with respect to the fourth moment we have  $h_i \propto ss\sigma_\alpha^4$  which gives  $h_i \propto 1/z^2$ .

One can write (5.6) in such a way to emphasize the different contributions to the fourth moment. With the second moment written as  $\mu_2 = z \cdot \bar{h}_1$  where  $\bar{h}_1$  stands for the weight corresponding to a hopping to one of the nearest neighbours in the calculation of  $\mu_2$ , we divide (5.6) by  $\mu_2^2$  which gives

$$\frac{\mu_4}{\mu_2^2} = \frac{1}{z^2} \sum_i n_i \frac{h_i}{\bar{h}_1^2} \quad (5.7)$$

As remarked above the implicit dependence of  $h_i$  on  $z^2$  is carried out through the hopping integrals which are also present in  $\bar{h}_1^2$  with the same powers. Therefore  $h_i/\bar{h}_1^2$  is not dependent on the coordination (and, as a bonus, is nondimensional) which is the factor that rescales the hopping integrals from one

structure to another. This means that, in these units, topologically equivalent paths have the same weight being therefore structure independent, or perhaps more appropriately, volume (or bond length) independent. Therefore they can be used to compare directly between two given structures to find out which factor is responsible for stability: whether it is the weight itself, or a combination of the weight with the number of paths or yet the volume rescaling factor  $1/\xi^2$ . This separation of effects is a direct consequence of the structure energy difference theorem.

The normalized moments in (5.7) can still be used to compare among the different structures because within our model the second moment is the same for all structures, as following from the structure energy difference theorem. Notice that in accordance with this theorem the only assumption for  $\Delta\mu_2 = 0$  is that the repulsive pair potentials are proportional to the square of the hopping integrals, i.e.,  $h_{pp} \propto h_{\text{bond}}^2$  (as long as one does not need the explicit form of  $h_{\text{bond}}$  to fix any hopping integrals ratio like, say, the second neighbours in the bcc lattice) as explained in appendix III. For different forms of  $h_{pp}$ , even though  $\Delta\mu_2 = 0$  does not hold, it is still possible to write an expression similar to (5.7). If, say,  $h_i$  depends on the coordination through  $1/\xi^n$ , then  $\xi^n \cdot h_i$  is not dependent on  $\xi$ . One can then divide both sides of (5.6) by  $\xi^n \cdot h_1$  (which is independent on the coordination) and work with the  $\xi$  independent weights  $h_i/h_1$ . Notice that one could not divide (5.6) by  $h_1$  alone because it is dependent on the coordination and is thus different, in general, for different structures.

For a given lattice, the effective contribution of  $h_i$  depends on the symmetry of the orbitals being considered. For instance all paths contribute equally to the pure s symmetry case whereas this is not true in the case of angular dependent symmetries. We therefore split up the discussion into the pure s, pure p and  $\epsilon_{sp} = 0$  cases. In what follows we will always take the first weight  $h_1$  to represent the contribution of a "dimer-like" path, i.e., corresponding to one step

length hoppings, back and forth, to one of the neighbours. We will also be working with units such that  $h_1 = 1$ . In this case we have

$$\tilde{\mu}_4 = \frac{1}{\xi^2} \sum_{i=1}^{N_4} n_i \tilde{h}_i$$

which can also be written as

$$\tilde{\mu}_4 = \frac{1}{\xi^2} \left[ \xi + \sum_{i=2}^{N_4} n_i \tilde{h}_i \right] \quad (5.8)$$

where

$$\begin{aligned} \tilde{h}_i &= h_i/h_1 \\ \tilde{\mu}_4 &= \mu_4/(\xi^2 h_1) \end{aligned}$$

We shall be referring to  $\tilde{\mu}_4$  and  $\tilde{h}_i$  as renormalized fourth moment and weights respectively.

#### 5.4.1 The Single s-Orbital Case

In this case the weights are independent of the paths, i.e.,  $h_i = h_1$  (thus  $\tilde{h}_i = 1$ ) for all  $i$ , and the discussion is straightforward. From (5.6) we see that the two important parameters in the evaluation of the moments are the total number of paths, say  $n$ , and the strength of the interaction which is represented here by the weights  $h_i$ . As remarked above  $h_i \propto 1/\xi^2$  and therefore, as  $\xi$  increases, the number of paths and the weights represent competing effects acting on the fourth moment: whilst the former attempts to increase the latter attempts to decrease

the value of  $\mu_4$ . Therefore if we were to forget the influence of the number of paths the dimer ( $g = 1$ ) would have the highest moment of all the structures. Actually it happens that this situation is completely reversed by the effect of the number of paths which grows up faster than  $g^2$  as one can see from table 5.4. Thus  $n/g^2$  is an increasing function of  $g$ , as shown in figure 5.11, which accounts for the dimer stability in the half filled band region (see also figure 4.16a) when only one s orbital is present.

#### 5.4.2 The Pure p Case

We will now divide the discussion into two parts. In part *a* we give an overview of the subject while in part *b* we become more specific. We will also be including another structure, namely the two dimensional square lattice (because of its four-fold coordination like in diamond), when useful for the discussion.

*a)* In this case there is no spherical symmetry and the weights are expected to depend on the particular paths. The largest weight is  $h_1$  which is the straight path we are referring to as a dimer-like path (see Turchi and Ducastelle 1985). The other paths diminish in importance as one can see by comparing tables 5.5 and 5.4 which indicates a drop in the fourth moment relatively to the single s case.



Pure s						
Structure	$\xi$	$\xi^2$	No.Paths (n)	$n/\xi^2$	Path contribution	
					Dimer-like ( $=\xi/n$ )	Others
Dimer	1	1	1	1.0	100%	0%
Zig-Zag	2	4	6	1.5	33%	67%
H.Comb	3	9	15	1.67	20%	80%
Dia	4	16	28	1.75	14%	86%
S.Cub	6	36	90	2.5	7%	93%
Hex.	8	64	168	2.63	5%	95%
Fcc	12	144	540	3.75	2%	98%
Hcp	12	144	540	3.75	2%	98%

Table 5.4 Path contribution to the fourth moment in the pure s case. Notice that the dimer-like contribution is given by  $\left[ \frac{\xi h_1 / \xi^2}{n h_1 / \xi^2} \right] = \xi / n$ .

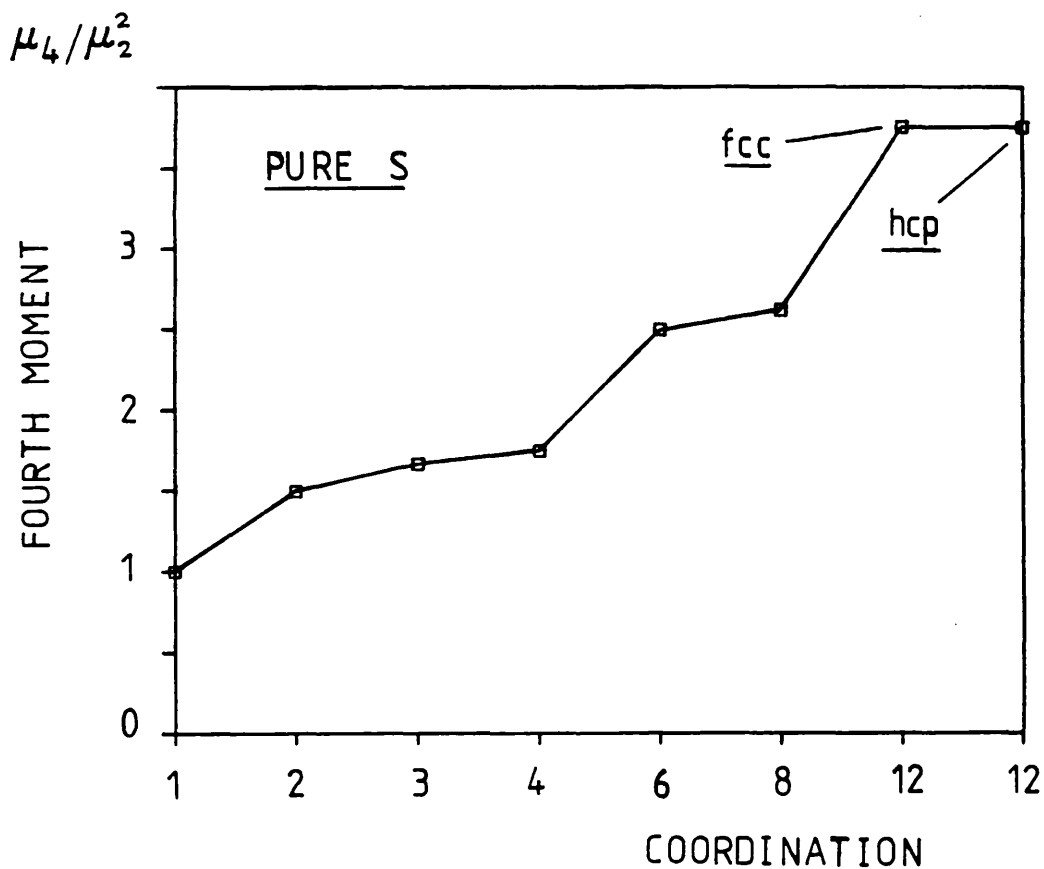


Figure 5.11

Fourth moment (in the nondimensional form  $\mu_4/\mu_2^2$ ) for the structures shown in the horizontal line, in the single s orbital case. The key for the structures is:

Structure	Coordination	Structure	Coordination
dimer	$z = 1$	simple cubic	$z = 6$
zig-zag	$z = 2$	hexagonal	$z = 8$
h.comb	$z = 3$	fcc/hcp	$z = 12$
diamond	$z = 4$		

Figure 5.12 shows  $\tilde{\mu}_4$  versus  $z$  with the two dimensional square lattice included. We see that the number of paths is now unable to overcome the decrease in the fourth moment (caused by the factor  $1/z^2$  as in the single s case but now also due to the uneven distribution of the weights) as  $z$  ranges from the dimer to the higher coordinated structures. We also see from this figure that (apart from the zig-zag chain, the square lattice and the simple cubic structures)  $\tilde{\mu}_4$  decreases monotonically up to  $z = 4$  and then increases, monotonically, in the direction of the more compact structures. This behaviour is due to the fact that for the more compact structures the number of paths is so big that they are able to reverse the situation once again, causing  $\mu_4$  to increase with  $z$  as in the previous case (compare the contribution columns in tables 5.4 and 5.5). For  $z = 6$ , for instance, there is a good "recovery" with the "other paths" reaching a contribution of 82% (it was 93% in the pure s case) and this is why the simple cubic structure is pushed up relatively to the zig-zag chain, the honey comb and the diamond structures. The same type of argument applies to the more compact structures. The dissimilar behaviour of the zig-zag chain, the square lattice and the simple cubic structure with respect to the other structures in figure 5.12 can be understood by noticing that in these cases the p-orbitals lie along the bond lengths. We will come back to this point in part *b* where the contribution of each path will be considered in detail.

b) In this part we attempt to understand the role played by the structure's local topology in the behaviour described in part *a*. General conclusions will be given in the sp case. The units will be as indicated by expression (5.8), which renormalizes  $\mu_4$  in terms of the coordination independent quantity  $z^2 h_4$ .

Pure p				
Structure	$\xi$	No.paths	Path Contribution	
			Dimer-like	Others
Dimer	1	1	100%	0%
Zig-Zag	2	6	69%	31%
H.Comb	3	15	37%	63%
Diamond	4	28	35%	65%
S.Cubic	6	90	18%	82%
Hexagonal	8	168	14%	86%
Fcc	12	540	9%	91%
Hcp	12	540	9%	91%

Table 5.5 Path contribution to the fourth moment in the pure p symmetry case.

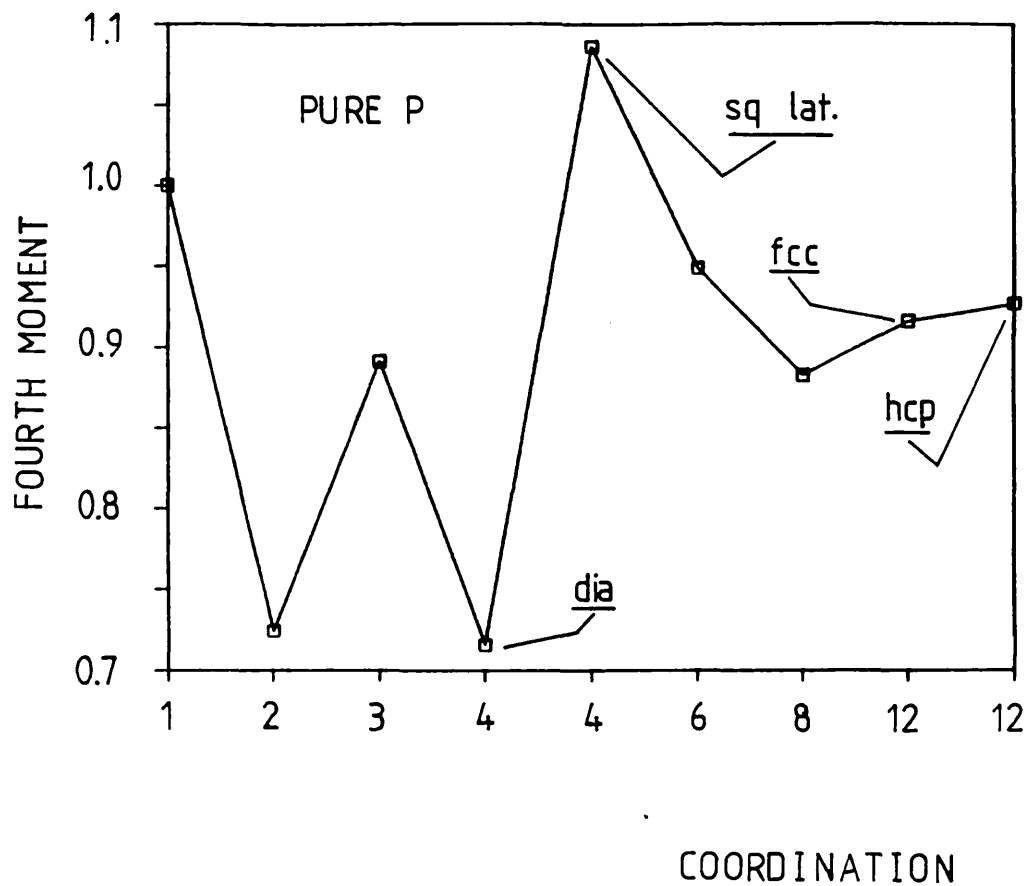




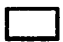

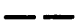

Figure 5.12  
 Fourth moment (the renormalized one) for the structures in the horizontal line for the pure p case. The 2D square lattice is also shown. The key for the structures as a function of the coordination is the same as for figure 5.11.

Table 5.6 summarizes the paths present in the structures under investigation with coordination up to six. We notice that the minimum weight is associated to the path present in the zig-zag chain which also appears in the square lattice and simple cubic structures. On the other hand the maximum weight (other than the one corresponding to the dimer-like path) is associated to straight paths (present in the square lattice and simple cubic structure) and is equal to the dimer-like weight. These points account for the dissimilar behaviour observed for the fourth moment of these structures as pointed out in part *a* and shown in figure 5.12.

In figure 5.13 we are plotting the fourth moment corresponding to planar paths like the ones in the zig-zag chain, as a function of the bond angle ( $\theta$ ) as derived in appendix X. It is not difficult to show (see appendix X) that the weight in this case (let us call it  $h_2$ ) is given by

$$\begin{aligned}
 h_2 &= pp\sigma^2 \left[ l^2 pp\sigma^2 + (1-l^2) pp\pi^2 \right] + \\
 &pp\pi^2 \left[ (1-l^2) pp\sigma^2 + l^2 pp\pi^2 \right] + pp\pi^4
 \end{aligned} \tag{5.9}$$

where  $l = \cos\theta$ . For  $\theta = 0$  this expression gives the weight corresponding to the dimer-like path for the pure p case, i.e.,  $h_1 = pp\sigma^4 + 2 \cdot pp\pi^4$ . We see from figure 5.13 (here it is  $\tilde{h}_2 = h_2/h_1$  that we are plotting) that the weight is minimum for  $\theta = 90$  degrees (the path in the zig-zag chain) and is maximum for  $\theta = 0$  or 180 degrees (the dimer-like and the straight line paths respectively). Notice that the zig-zag chain stability region (as for the structures of S, Se and Te for which the bond angle is 105 degrees - Harrison 1980, p93) that one finds in the structure

Pure p							
Type	Weight	Dimer	Z-zag	H.Comb	Dia	Sq.Lat.	S.Cubic
	0.418	0	0	12	0	0	0
	0.311	0	0	0	24	0	0
	0.224	0	0	0	0	8	24
	0.224	0	4	0	0	16	48
	1.0	0	0	0	0	8	12
	1.0	1	2	3	4	4	6

**Table 5.6** Types of paths and respective weights (p-orbitals) present in the structures with coordinations ranging from 1 to 6. The bond angle  $\theta$  in the diamond path, is given by  $\text{sen}(\theta/2) = (2/3)^{1/2}$ .

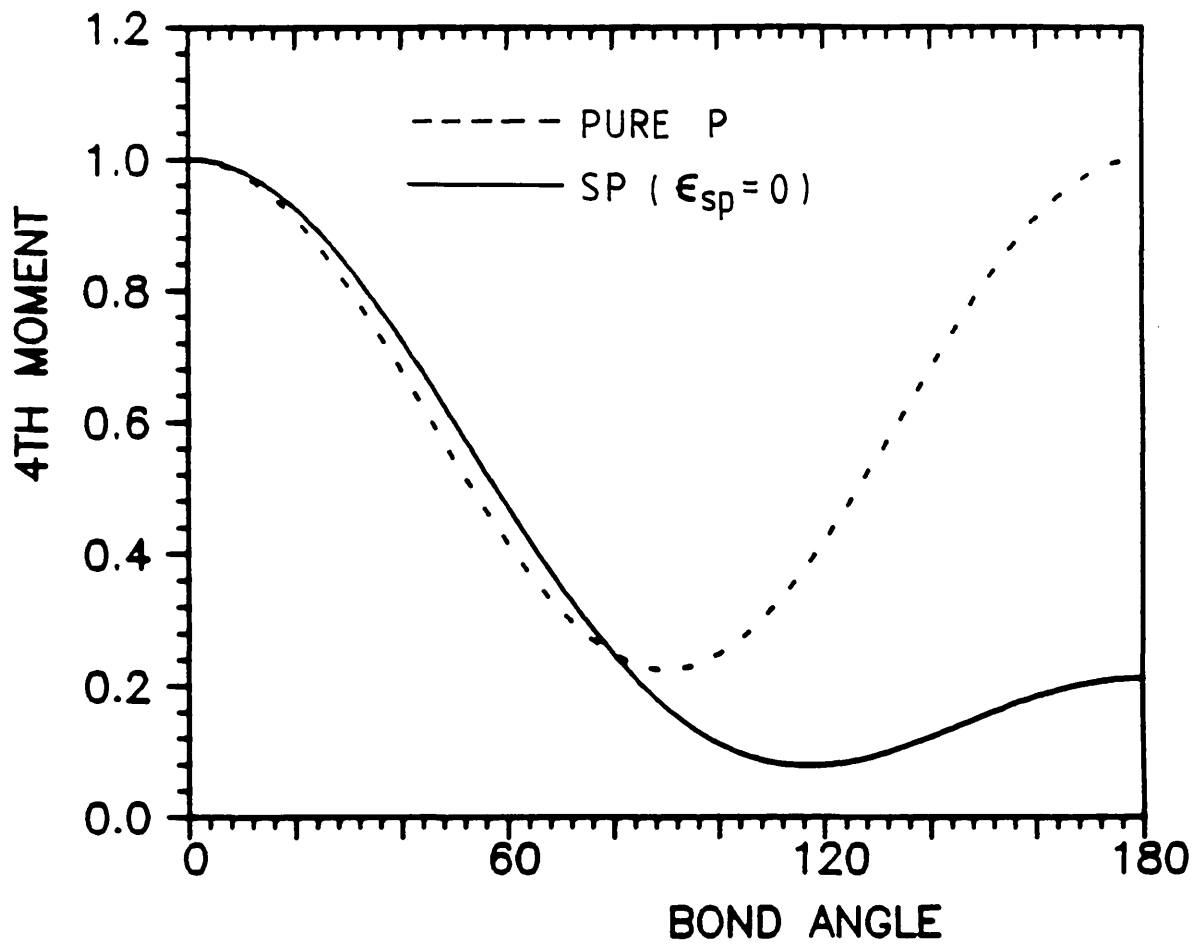


Figure 5.13  
 Renormalized fourth moment versus bond angle  $\theta$  for a planar path like the one in the zig-zag chain (see appendix X). The minimum occurs for  $\theta = 90$  degrees. The dashed (solid) line is for the pure p ( $\epsilon_{sp} = 0$ ) case.



maps (see chapter 4) by going down towards  $\epsilon_{sp} \rightarrow -\infty$ , has much to do with the small weight associated to this path. In fact there is not such a stability region for an ordinary linear chain, as prior studies of the sp stability problem led to.

### 5.4.3 The Hybrid sp Case ( $\epsilon_{sp} = 0$ )

In table 5.7 we are listing the contributions of both the dimer-like and the other paths to the fourth moment for the case of sp-symmetry. We see that there is a sensible drop in the contribution of the other paths for the zig-zag chain, the honey comb lattice and the diamond structures, relatively to the single s orbital case. Notice also the drops in the last two structures relatively to the previous case. These drops cause severe changes in the stability curve  $\tilde{\mu}_4$  versus  $\xi$  which is shown in figure 5.14. We see from this figure that hybridization with an s orbital disfavours the zig-zag chain stability (compare with figure 5.12).

Notice that in our units the weight of dimer-like paths is  $\tilde{h}_1 = 1$  independently of the case (say, pure p or sp) and therefore the relative structural stability between two structures (at half band filling) as one goes from one case to another is only dependent on the "other" paths. From table 5.5 we see that the contribution of other paths in the pure p case was  $31/65 = 0.48$  for the zig-zag chain relatively to the diamond lattice, whereas from table 5.7 the same ratio for the sp case is  $25/34 = 0.74$ . This pushes up the fourth moment of the zig-zag chain relatively to the diamond lattice and therefore reduces the chain stability at half band filling. In table 5.8 we show the different paths contributing to the fourth moment along with the corresponding weights. We see that the second zig-zag chain weight increased considerably relatively to the diamond structure from the pure p to the sp case. In the former the ratio is  $0.224/0.311 = 0.72$  whereas in the

latter it is  $0.167/0.084 = 2.0$ .

We also see from figures 5.12 and 5.14 that the square lattice and simple cubic stabilities are improved from the pure p to the sp case. This is mainly due to the weight associated to straight paths which decrease considerably when the s orbital is included (they were as large as the dimer-like path in the previous case).

These points can be made more clear if we look back to figure 5.13. The solid line represents the weight of a path like the one in the zig-zag chain as a function of the bond angle for the sp ( $\epsilon_{sp} = 0$ ) case. The dashed line is for the pure p case. There are two main differences between these two curves, namely i) that the minimum has been dislocated towards 117 degrees and ii) that a straight path is no longer equal to the dimer-like path as mentioned before. The displacement of the minimum is related to the bond angle observed in the chains for the structures of S, Se and Te. The fact that we obtained 117 degrees for  $\epsilon_{sp} = 0$  and 90 degrees for the pure p case (i.e.,  $\epsilon_{sp} \rightarrow -\infty$ ) is totally consistent with the observed angle of 105 degrees which lies in between those two limiting values. The second of these points is easily understood by noticing that with the presence of a s orbital it does make difference if one goes forth or backwards along the bond.

In figure 5.15a we show a bar graph displaying  $\tilde{h}_i$  versus  $\mathcal{Z}$  ( $\epsilon_{sp} = 0$  and  $h_1$  left out) in order to find out which structure is most favoured by the weight alone. We see from this figure that the non-linear paths of both the honey comb ( $\mathcal{Z} = 3$ ) and diamond ( $\mathcal{Z} = 4$ ) structures are very effective in reducing the weight.

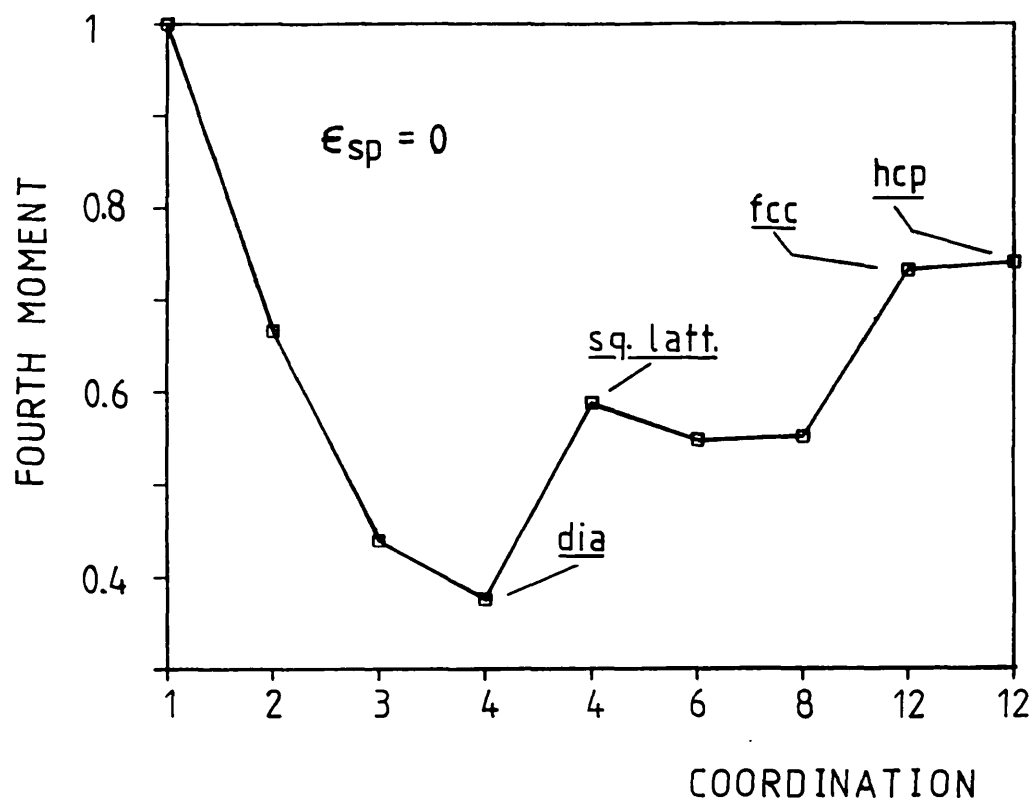


Figure 5.14  
Renormalized fourth moment for the several structures whose coordination are shown in the horizontal axis for the  $sp$  ( $\epsilon_{sp} = 0$ ) case. The key for the structures as a function of the coordination is the same as for figure 5.11.

$\epsilon_{sp} = 0$				
Structure	$\xi$	No.paths	Contribution	
			Dimer-like	Others
Dimer	1	1	100%	0%
Zig-Zag	2	6	75%	25%
H.Comb	3	15	76%	24%
Diamond	4	28	66%	34%
S.Cubic	6	90	30%	70%
Hexagonal	8	168	23%	77%
Fcc	12	540	11%	89%
Hcp	12	540	11%	89%

Table 5.7 Path contribution to the fourth moment in the  $sp$  symmetry case.

Figure 5.15b represents a stacked version of figure 5.15a, now with  $\tilde{n}_i$  included and the weights multiplied by the corresponding number of paths, i.e., we are plotting  $\sum n_i \tilde{n}_i$  versus  $z$  (but not yet multiplied by  $1/z^2$ ). Both figures break down the fourth moment into the contribution of each different path. Since the diamond lattice and the square lattice share the same coordination number, their relative stability will not change with the inclusion of the factor  $1/z^2$ . As expected the coordination is very important in determining the structural stability since otherwise the dimer would be more stable at half band filling.

Figure 5.16a also shows a stacked version of figure 5.15a, this time multiplied by  $1/z^2$  (first weight left out and number of paths not taken into account). We see that both the weight (from figure 5.15a) and the coordination (from this figure) are very much in favour of the diamond structure for stability. Speaking of coordination, the higher the better. But a too large coordination also means an increase in the number of paths, which acts against half band filling sp stability and can just as well be more important than the decrease in  $\mu_4$  caused by the factor  $1/z^2$ . This is what happens to the simple cubic structure, which is unfavoured not only for its large weights (which after divided by  $z^2$  are not at all that big as we see from figure 5.16a) but mainly for its large number of different paths.

In figure 5.16b both the volume rescaling factor and number of paths are present. This is the same as figure 5.14 (except that  $z$  goes up to 12 in figure 5.14) but we are now showing the contribution of each path to the fourth moment.



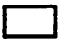

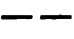

$\epsilon_{sp} = 0$							
Type	Weight	Dimer	Zigzag	H.Comb	Dia	Sq.Lat.	S.Cubic
	0.079	0	0	12	0	0	0
	0.084	0	0	0	24	0	0
	0.134	0	0	0	0	8	24
	0.167	0	4	0	0	16	48
	0.211	0	0	0	0	8	12
	1.0	1	2	3	4	4	6

Table 5.8 Types of paths and respective weights (sp symmetry) present in the structures with coordination ranging from 1 to 6.

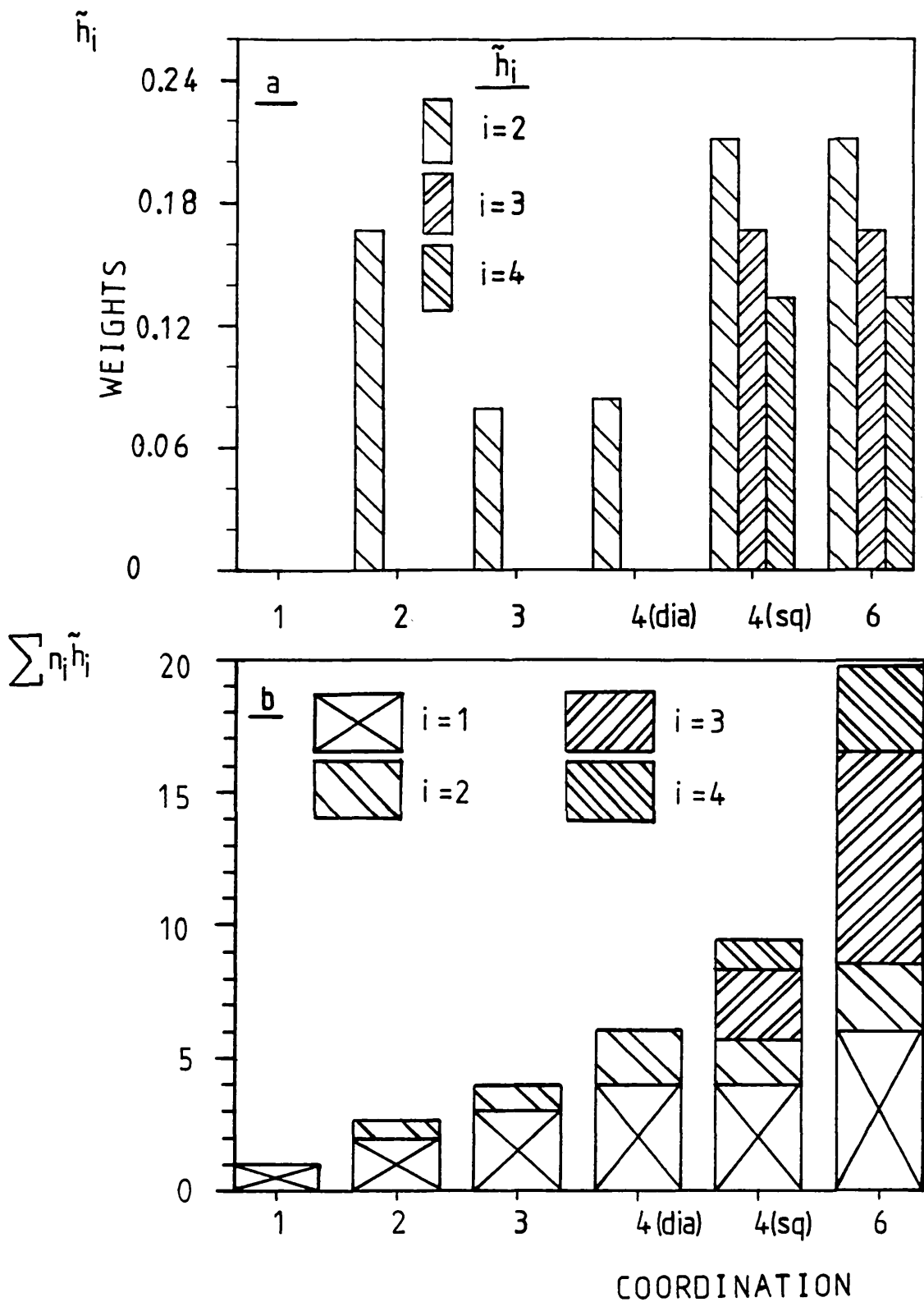


Figure 5.15

a) Renormalized weights for the structures whose coordinations are indicated in the horizontal axis (see figure 5.11 for the key - the square lattice is indicated by sq) for  $\epsilon_{sp} = 0$ . Notice that the third and fourth weights are zero for  $\mathcal{Z} = 2, 3$  and 4 (dia) and that the first weight (equal to unity for all structures) is not shown; b) the same as a) but now multiplying the weights by the corresponding number of paths.

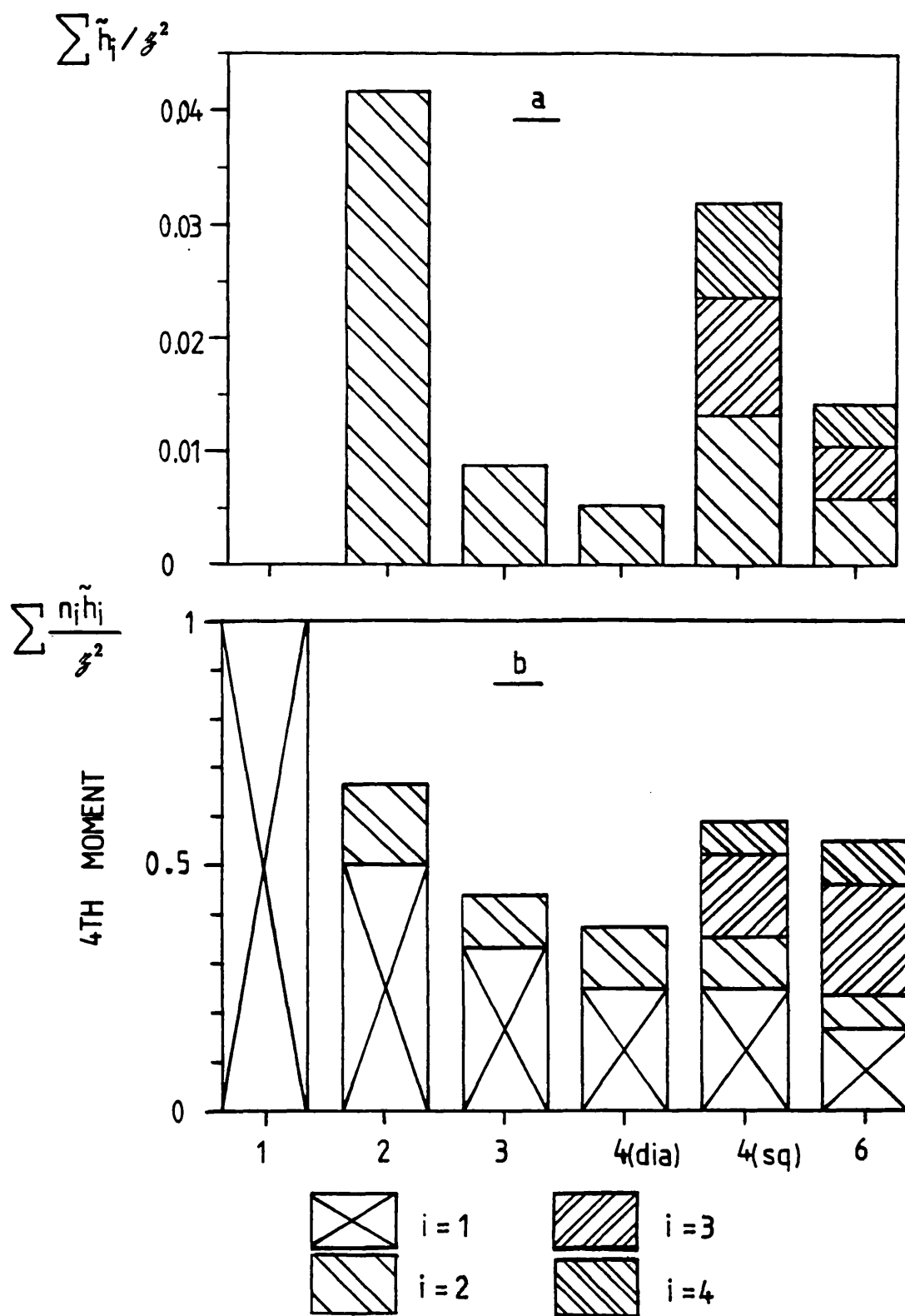


Figure 5.16  
 a) Renormalized weights divided by the square of the coordination ( $\epsilon_{sp} = 0$ ) for the several structures in the horizontal axis; b) renormalized fourth moments broken down into the contributions of the different paths. The key for the structures as a function of the coordination is the same as for figure 5.11 (the square lattice is indicated by sq).



An interesting point that we would like to discuss is the role played by space dimensionality ( $d$ ) in half band filling  $sp$  structural stability. When one tries to increase stability by increasing coordination, one should also keep the corresponding increase in the number of paths down to a minimum. One way to accomplish this is by increasing the dimensionality of the space. This is what is done when one goes from the dimer, which can be thought of as having space dimensionality equal to zero, to the diamond structure with the stability being increased in this process. From this point on, one has already reached  $d = 3$  and the dimension of the space cannot be increased anymore. This accounts for the next lattice in order of increasing coordination, namely the simple cubic structure, being less stable than the diamond structure. Notice that if one tries to "squeeze" a fourfold coordinated structure in two dimensions (see the square lattice in figure 5.16b) the result is a less stable structure if compared to the equally coordinated diamond structure. Obviously the weights should be taken into account in this discussion as one could think of choosing suitable paths with small weights so that these could account for the increase in the number of paths with coordination. Nevertheless this qualitative argument remains valid when one compares structures with the same kind of local topology (so that there are no bias in the choice of the paths) but with different space dimensionalities. We do this in figure 5.17 where the fourth moments of the dimer, the ordinary linear chain, the zig-zag chain, the square lattice and the simple cubic structures are compared. The result is an increase in stability as both the coordination and the dimensionality of the space increase. Notice that the zigzag chain is more stable than the ordinary chain because of its non-linear path, which weights less than the straight paths present in the ordinary linear chain (this structure has four paths of the type  $\bullet\text{---}\bullet\text{---}\bullet$  besides the dimer-like one), which can be seen, for example, from table 5.8.

Figure 5.17b shows a stacked bar version of figure 5.17a, exhibiting the individual contributions of the different paths. Notice that these remarks are only applicable to the  $sp$  case and are also highly dependent on the orbital symmetry. In the pure  $s$  case, for instance, there is no decrease in the fourth moment as both  $\zeta$  and  $d$  increase which is obviously caused by the uniform distribution of the weights (due to the spherical symmetry associated to the  $s$  orbital).

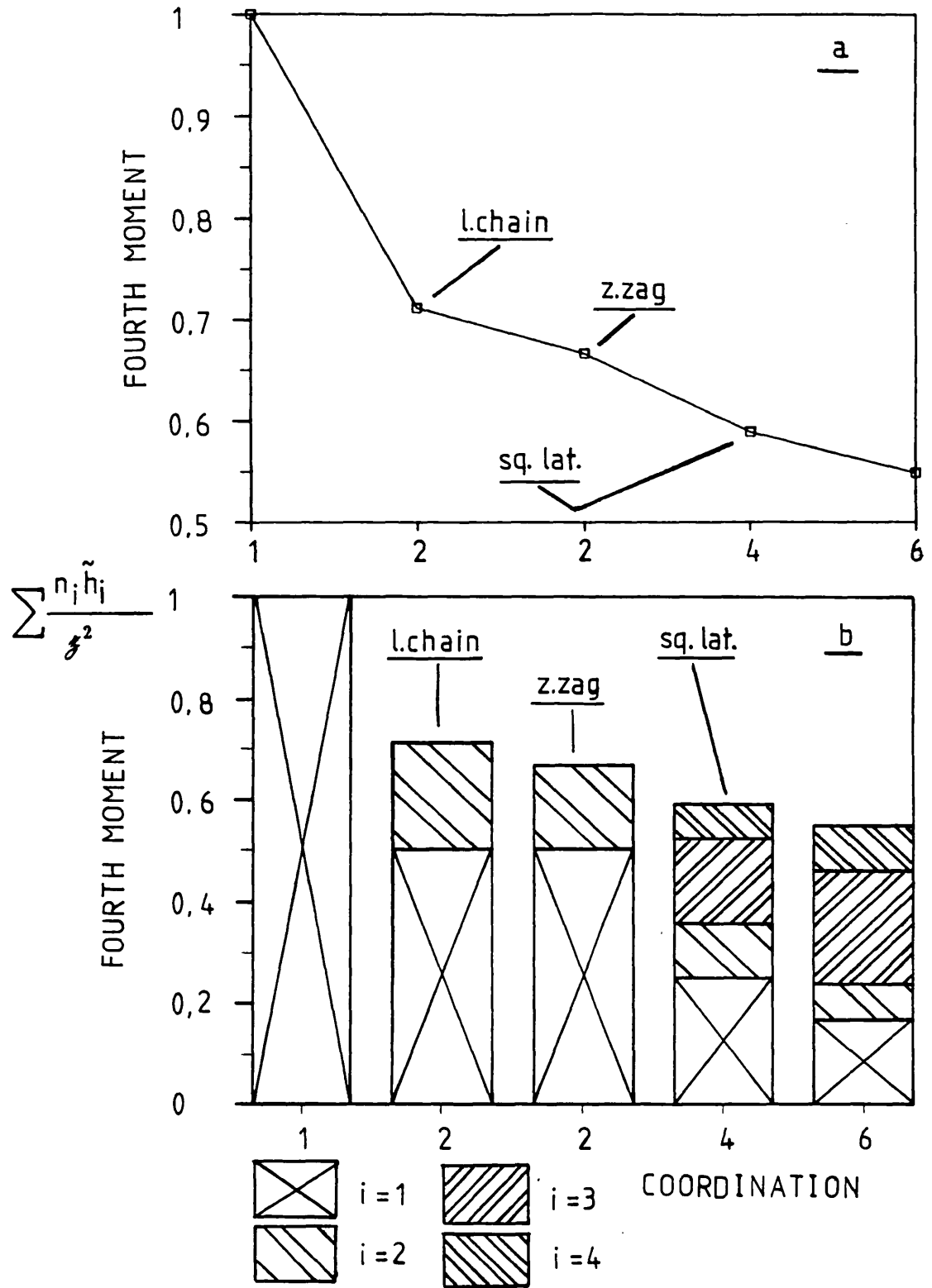


Figure 5.17  
 a) Renormalized fourth moments for the structures indicated in the figure ( $\xi = 1$  is the dimer and  $\xi = 6$  is the simple cubic lattice); b) same as a) but breaking down into the contributions of the different paths.

## §5.5 Conclusions

These concluding remarks are mainly directed towards the  $sp$  case. The predicted relative stability as the  $\epsilon_{sp} = 0$  band is filled up with electrons is

$$fcc \rightarrow hcp \rightarrow fcc \rightarrow hex \rightarrow h.comb \rightarrow dia \rightarrow h.comb \rightarrow sc \rightarrow z.zag \rightarrow dimer .$$

We have shown that the basic characteristics of this trend can be understood in terms of the moments of the local density of states. For example the diamond structure is more stable than the lesser coordinated structures at half band filling for several reasons: it has a relatively small weight, the largest coordination, the same number of topologically different paths (i.e.,  $N_4 = 2$ ) as those structures and its number of paths corresponding to  $\tilde{h}_2$  is not that big. It is also more stable than its equally coordinated counterpart, namely the square lattice, because both the weights and the number of paths (representing several different weights) are larger in this lattice. Finally it is more stable than the simple cubic structure mainly because of the large number of paths present in this structure, which overcomes the decrease in the weights caused by the volume rescaling factor (one increases coordination but the lattice space dimensionality can not be increased anymore).

In conclusion, structural stability results from a combination of several parameters and can not be thought of as being due to only an isolated one. The diamond structure combines a reasonably small number of paths and a small weight, with a reasonably "large" coordination, which seems to be the best recipe towards half band filling  $sp$  stability.

## CHAPTER 6: The sp-Bonded AB Compounds

The tight-binding model developed in the previous chapters is now applied to the study of the sp-bonded AB binary compounds. The extra complication is essentially due to the existence of more than two parameters controlling structural stability which forbids the results to be cast into one single two dimensional structure map. The Mendeleev scale (Pettifor 1988) is used to draw a single two dimensional structure map with which our theoretical results are compared. The model is shown to be able to cope satisfactorily with the basic structural trends observed for the most important binary structures.

## §6.1 Introduction

Up to now we have been dealing exclusively with elemental systems, i.e., systems in which the physical entities occupying the lattice sites were identically the same. In an alloy the lattice is populated by more than one type of atom and our interest here is in the case when the number of different atoms is two, i.e., a binary system, with stoichiometry AB. It has been shown that these systems can be well separated within a two dimensional map with the use of a single phenomenological coordinate (the Mendeleev number  $\mathcal{M}$ ) associated with every atom in the periodic table (Pettifor 1986a, 1986b, 1988). Other stoichiometries have also been well separated with this choice of coordinate system (Pettifor 1988). In table 6.1 we list the sp elements along with their corresponding Mendeleev number. Some elements have been excluded from this table like B, C, N, O and F in the first row because these elements behave in a chemically distinct fashion due to the absence of p electrons in the core. Also Ca, Sr, Ba and Ra in the second column have been left out because hybridization with a d band is important for these elements and can not be neglected.

In the next section we make use of the tight-binding model for cohesion developed in the previous chapters in an attempt to account for the structural trends observed amongst the following AB structure types: NaCl, CsCl, Zincblende, Wurtzite, NiAs and NaTl. These trends are shown in figure 6.5 (this figure is so positioned in the text in order to allow easier comparison with the theoretical ones that will come later) where the Mendeleev number is used to identify each element in the compound. Notice that there is a discontinuity in both

Table 6.1

1A	IIB	IIIB	IVB	VB	VIB	VIIIB
Li (12)	Be (77)					
Na (11)	Mg (73)	Al (80)	Si (85)	P (90)	S (94)	Cl (99)
K (10)	Zn (76)	Ga (81)	Ge (84)	As (89)	Se (93)	Br (98)
Rb (9)	Cd (75)	In (79)	Sn (83)	Sb (88)	Te (92)	I (97)
Cs (8)	Hg (74)	Tl (78)	Pb (82)	Bi (87)	Po (91)	As (96)
Fr (7)						

Table 6.1  $sp$ -bonded elements to be considered in the experimental AB structural map. The Mendeleev number is shown in brackets.

axes (between 12 and 14) because only the sp elements are shown. The map is symmetric with respect to the dashed line that crosses its diagonal. This figure is a simplified version of figure 2 in Pettifor, 1988 (op. cit.) in which 52 AB compounds are shown. We shall see that our model gives good account to the main trends observed in this map.



## §6.2 Setting up the Problem

The presence of an extra kind of atom in the structure introduces an extra set of parameters that need to be considered in the model. The relevant sp parameters are shown schematically in figure 6.1 for the two isolated A and B atoms. We write the center of gravity  $C_g$  of the atomic levels of a given atom as  $C_g = (\epsilon_s + 3\epsilon_p)/4$ , which is related to the first moment by  $C_g = \mu_1/4$ . The relative positions of the energy levels are given by  $\epsilon_{sp}^A = \epsilon_s^A - \epsilon_p^A$ ,  $\epsilon_{sp}^B = \epsilon_s^B - \epsilon_p^B$  and  $\Delta = \mu_1^A - \mu_1^B$ . Here  $\Delta$  is a positive parameter characterizing the difference in the center of gravity between the two bands. As we shall see later the structural trends are not too sensitive to the difference  $\epsilon_{sp}^A - \epsilon_{sp}^B$  which can then be taken as equal to zero. Therefore one is left with two parameters, namely  $\Delta$  and the sp splitting  $\epsilon_{sp}$ . Since we want to study the relative stability of the compounds for every value of the sp band filling our theoretical structure maps will also be given in terms of the number of electrons on each site, i.e.,  $N_A$  and  $N_B$ . These maps are then given in the three-dimensional space defined by  $N_A$ ,  $N_B$  and  $\epsilon_{sp}$  and we will plot two-dimensional cross sections corresponding to particular values of  $\epsilon_{sp}$ . Therefore  $\epsilon_{sp}$  is fixed within a given map and the structural trends can be followed as a function of the number of electrons on each site for the different values of  $\Delta$ .

A natural extension from the elemental case to the binary compounds case consists in comparing the energies of two given structures at fixed values of the on-site energies, i.e.,  $\Delta\epsilon_{s,p}^A = \Delta\epsilon_{s,p}^B = 0$ . Since these diagonal Hamiltonian matrix elements are not determined in such a way to keep local charge neutrality (Sutton et al 1988) there may be charge flow from one site to another. In this case

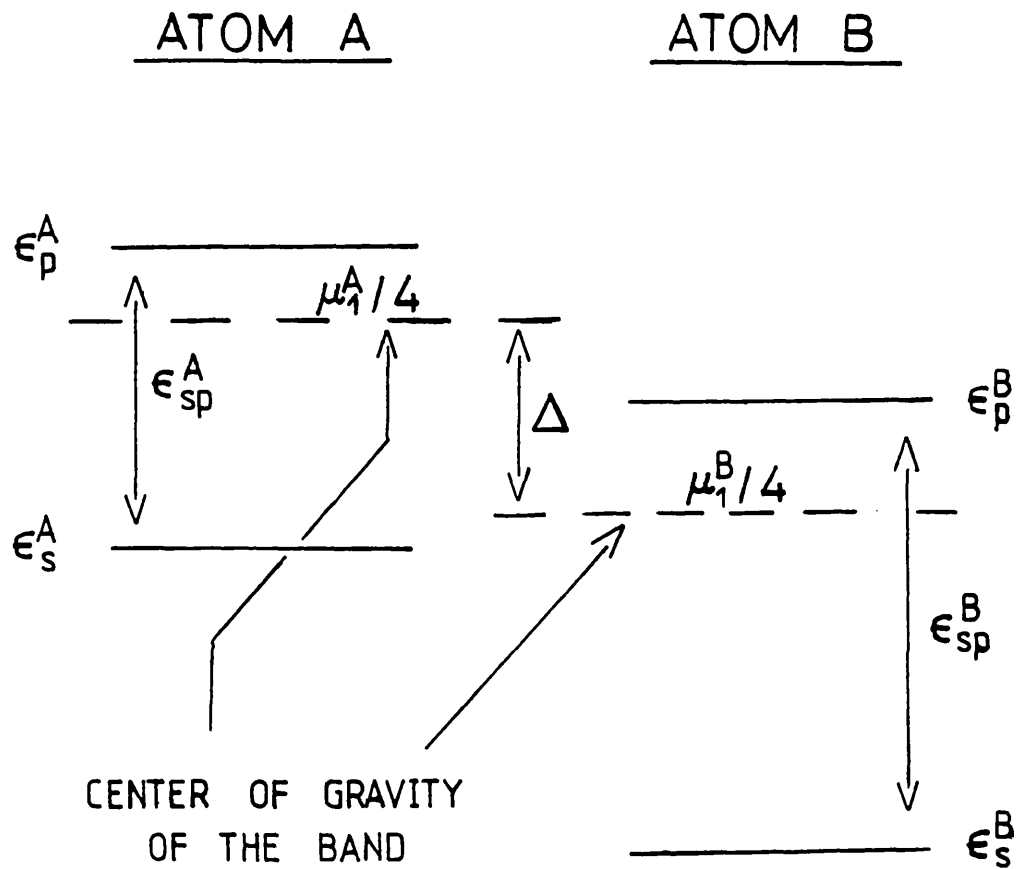


Figure 6.1  
 Relevant parameters for the study of the relative stability of sp binary systems. Only the differences are important here, namely the sp-splitting for each atom and the difference between the center of gravity of the atomic energy levels.

there is a classical charge transfer electrostatic contribution to the binding energy, namely the Madelung energy. This term was found by Majewski and Vogl (1986, 1987) to be important only to the absolute value of the binding energy. Relative phase stability (along with other structural properties) was found not to be governed by the charge transfer energy which played a minor role even in the case of strongly ionic crystals such as NaCl. Moreover the success achieved by Pettifor and Podlucky on the structural separation of the pd-bonded AB compounds (1984, 1986) also had the underlying assumption of local charge neutrality. We therefore neglect the effect of the Madelung term in our relative energy calculations.

The difference in the binding (or cohesive) energy  $E_b$  is thus taken as the difference in the band energy plus a sum of pairwise interactions  $E_{\text{rep}}$ . In accordance with the structural energy difference theorem two given structures are compared at the volumes obtained by fixing  $\Delta E_{\text{rep}} = 0$ . With these considerations  $\Delta E_b$  is given by an expression like (4.10), namely,

$$\Delta E_b = \Delta(E_{\text{band}}) \begin{cases} \Delta \epsilon_{s,p}^B = 0 \\ \Delta \epsilon_{s,p}^A = 0, \end{cases}$$

where  $\Delta E_{\text{rep}} = 0$  is implicit and  $\Delta \epsilon_{s,p}^A = 0$  means  $\epsilon_s^A(2) - \epsilon_s^A(1) = \epsilon_p^A(2) - \epsilon_p^A(1) = 0$  for structures (1) and (2) and similarly for  $\Delta \epsilon_{s,p}^B = 0$ . The difference in energy between the two structures is then characterized by the atomic energy level difference  $\epsilon_{sp}$  (in the case  $\epsilon_{sp}^A = \epsilon_{sp}^B = \epsilon_{sp}$ ), the difference in the center of gravity of the A and B bands  $\Delta$  and the total number of valence electrons per formula unit  $N = N_A + N_B$ . For a given choice of  $\epsilon_{sp}$  and  $\Delta$  the individual site occupancies  $N_A$  and  $N_B$  will be obtained from the TB local densities of states on the A and B sites in the NaCl lattice.

The calculations are carried out in much the same way as we did for the elements. A cluster of the structure of interest is set up in the computer and the recursion method is used to generate a continued fraction which is terminated with either the square root termination technique (connected spectrum) or the Turchi, Ducastelle and Trégliia's (single band gap) terminator. The band edges are determined respectively by Beer and Pettifor's (1984) and Beer (1985) optimization techniques described previously. Once the DOS has been calculated for each of the A and B sites the band energy can be plotted as a function of  $N = N_A + N_B$  and the most stable structure can then be identified for a particular value of  $N$ . In the  $N_A(\text{NaCl})$  versus  $N_B(\text{NaCl})$  plane a point is thus defined which is labelled by the symbol corresponding to the most stable structure at  $N$ .

### 6.2.1 Structure Types

Let us discuss in more detail the AB structure types we consider in this work. General references are Wyckoff 1963, Pearson 1972 and Evans 1966. The structures are all shown in figures 6.2 to 6.4. In the well known NaCl (rocksalt) structure the atoms are arranged in a cubic unit cell which is shown in the top of figure 6.2. Each sodium (chlorine) atom is symmetrically surrounded by six chlorine (sodium) neighbours and all the lattice sites are equivalent in this arrangement. Also shown is the co-ordinating polyhedra with the first neighbours placed at the corners of a regular octahedron.

The CsCl structure shown at the middle of figure 6.2 is also cubic and again there is no privileged position in the lattice. Each Cs (Cl) atom is surrounded by eight Cl (Cs) neighbours disposed at the corners of a cube which

makes the coordination eightfold. If all the atoms were of the same type this would be the bcc arrangement. The second neighbours (not shown in the figure) are only 15% away which is too close to be neglected. Just as we did in the study of the elemental systems these second neighbours will be considered in the recursion calculations with the second to first  $ss\sigma$  ratio taken as  $ss\sigma_2/ss\sigma_1 = 0.33$  (see chapter 4).

Another cubic structure, namely the zincblende arrangement, is shown at the bottom of figure 6.2. It has a fourfold or tetrahedral coordination with each atom being symmetrically surrounded by four neighbours of the other type disposed at the corners of a regular tetrahedron. As implied in the figure the atoms represented by the open circles (say, the Zn atoms) form a cubic fcc arrangement. The cubic zincblende structure is then obtained by placing S atoms (solid circles), along the [111] direction of the cube, directly above each existing Zn atom, a quarter of the cube's edge distance away.

At the top of figure 6.3 the hexagonal unit cell of wurtzite is shown. The  $AB$  layers characteristic of the hexagonal close packed arrangement are indicated along with the distance between alternate layers which is denoted, as usual, by  $c$ . Let us suppose that the open circles represent Zn atoms which form, as indicated in the figure, a hexagonal close packed arrangement. In wurtzite, a layer of sulfur atoms is inserted between each layer of zinc atoms, each sulphur atom being placed directly above each zinc atom in the layer below, at three quarters of the distance between consecutive layers. The  $c/a$  ratio is taken as the ideal one, namely,  $(8/3)^{1/2} \approx 1.63$ . At the bottom of this figure the structure of cubic zincblende is shown again, for comparison with the wurtzite arrangement, this time with the  $z$ -axis along the direction of the diagonal of the cube drawn at the bottom of figure 6.2. There are now three types of layers which form a cubic close packed arrangement, i.e., the fcc structure. Zincblende is formed by inserting

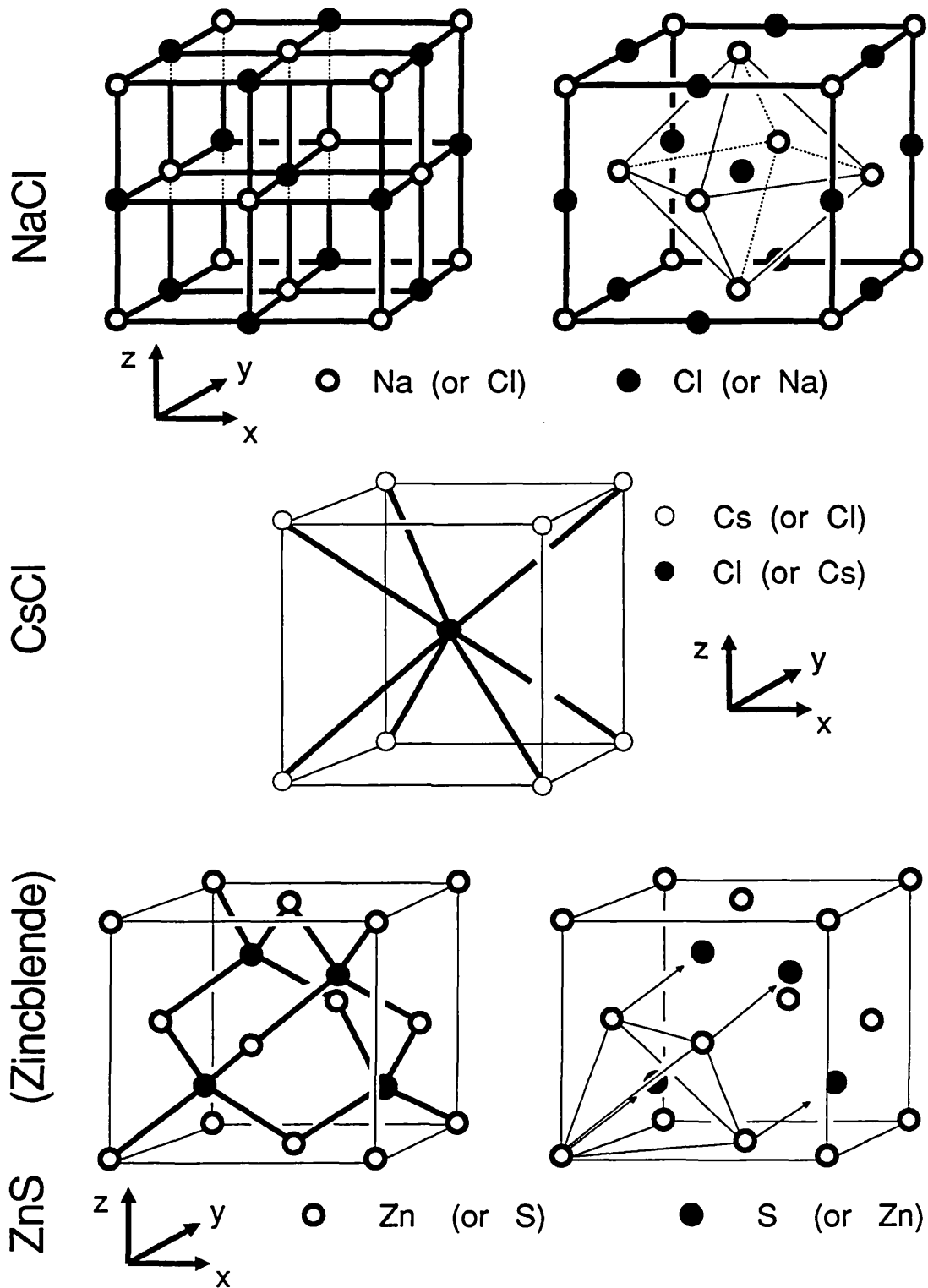
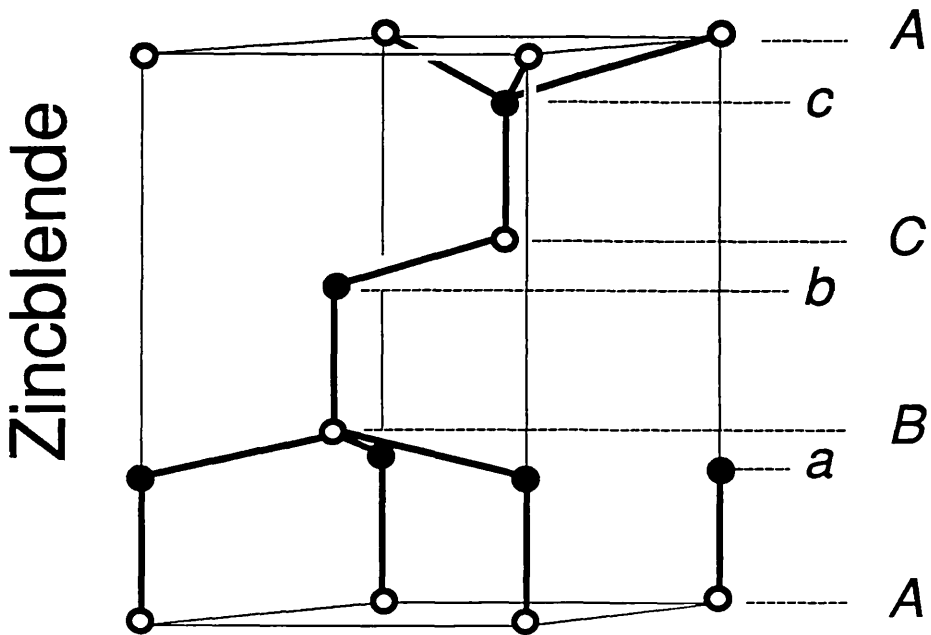
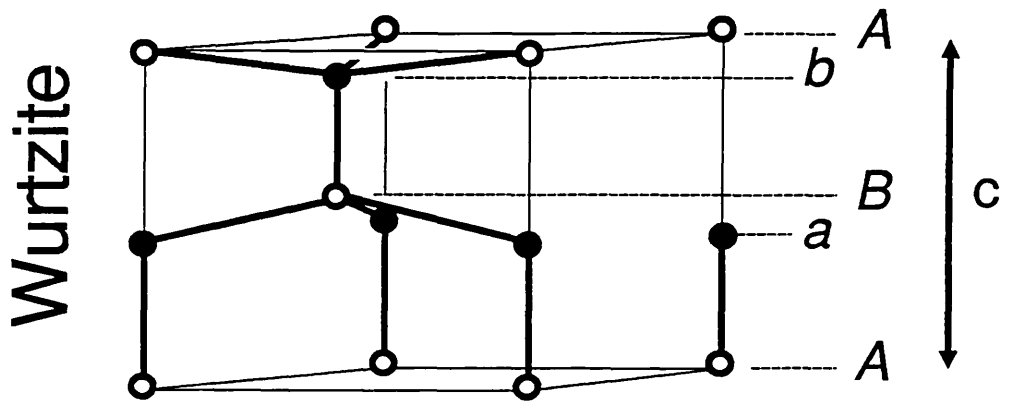


Figure 6.2  
The unit cell of the cubic structures of NaCl (top), CsCl (middle) and zincblende (bottom). The coordination polyhedra is shown for NaCl and zincblende.



For both :

- Zn (or S)
- S (or Zn)

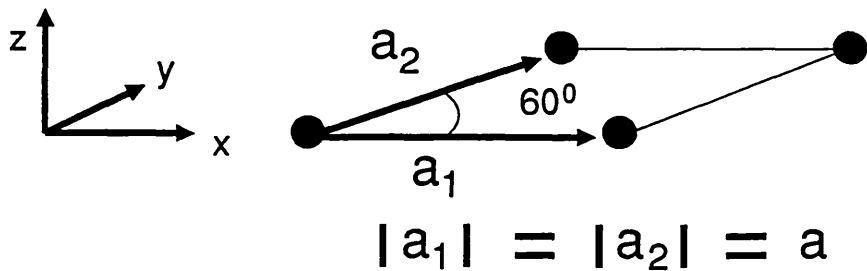


Figure 6.3  
The unit cell of the hexagonal structure of wurtzite (top). Zincblende is also shown along the [111] direction for comparison.

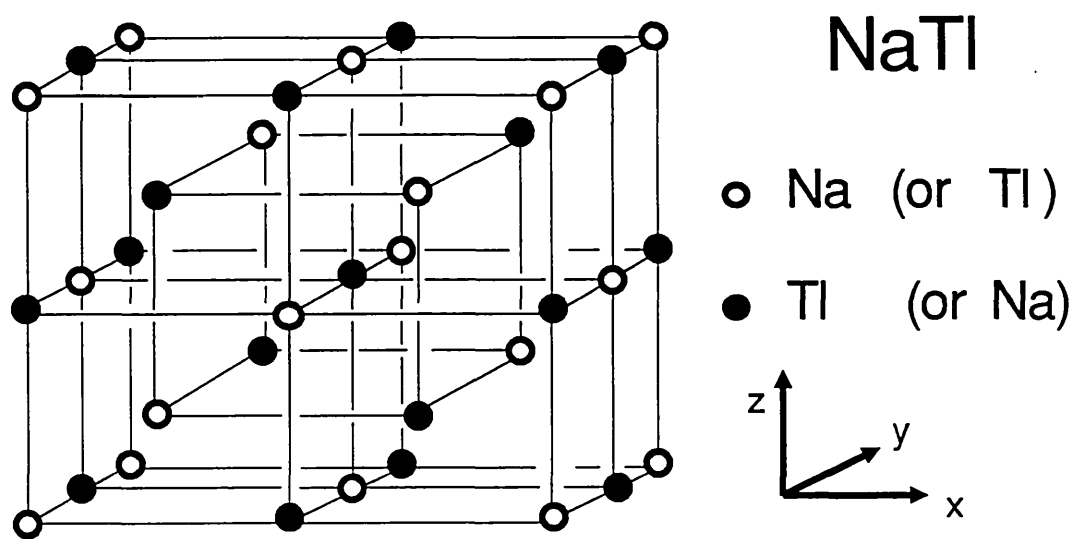
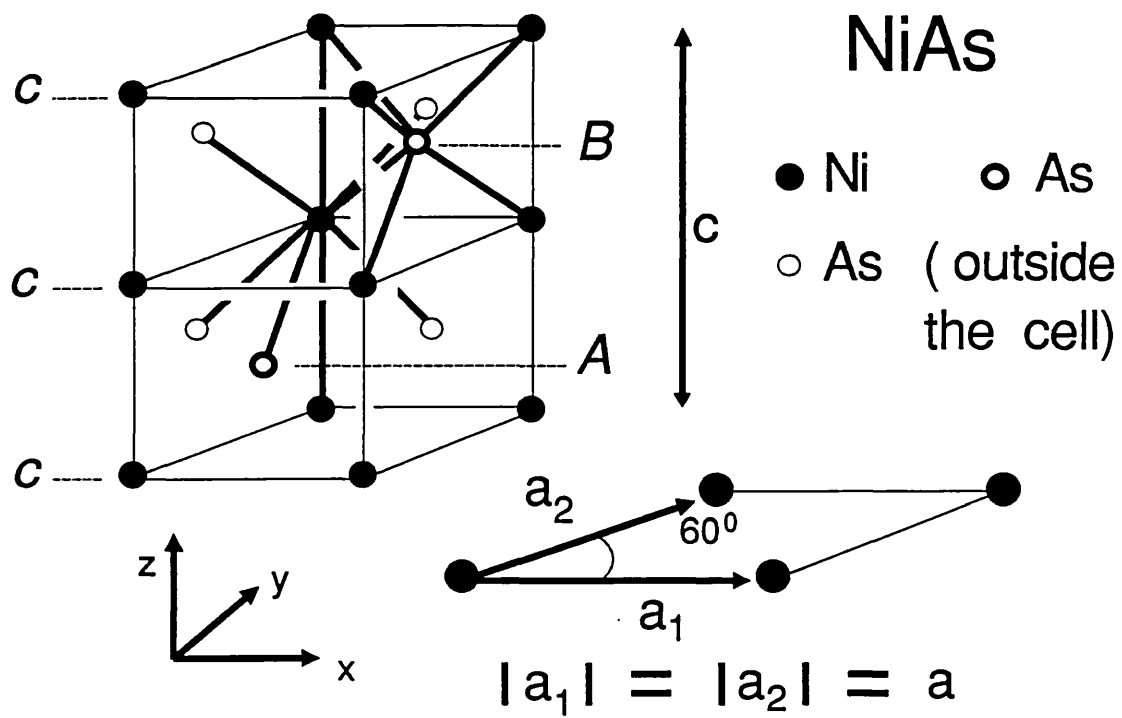
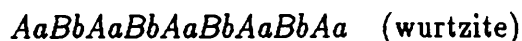


Figure 6.4  
 The hexagonal unit cell of NiAs (top) and the cubic unit cell of NaTl (bottom. Notice that NaTl is reduced to the bcc arrangement if the atoms are all of the same type.



sulfur layers between the existing zinc layers in the same way as explained above for wurtzite. These two structures can therefore be represented as a stacking sequence of hexagonal planes of atoms of the same type, i.e.,

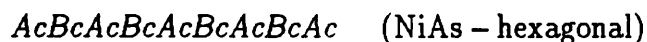


and in this fashion wurtzite can be seen as the hexagonal analog of cubic zincblende.

The structure of NiAs shown at the top of figure 6.4 may be seen as the hexagonal analog of cubic rocksalt (see Froyen and Cohen 1983). Noticing from figure 6.2 (top left) that the structure of NaCl consists of two interpenetrating fcc lattices we can represent this arrangement by a stacking sequence of hexagonal planes, i.e.,



whereas nickel arsenide may be represented by



Unlike all other arrangements considered here, the sites in NiAs are noninterchangeable. The atom in the metallic site (solid circles in figure 6.4 - top) has six neighbours of the opposite type and two of its own type (slightly further away) as indicated in the figure. On the other hand the metalloid site is surrounded by six neighbours equally far apart. In MgPo the metallic site is occupied by magnesium with the  $c/a$  ratio being given by  $0.7077/0.4345 = 1.629$  which justifies our use of the ideal ratio for the nickel arsenide structure. The first neighbour distance (Ni-As) is given by  $a(2)^{1/2}/2$  and the second neighbour distance

(Ni-Ni) is  $a(2/3)^{1/2}$ . This gives a second to first neighbour ratio equal to  $2/3^{1/2} \approx 1.15$  which is exactly the same as for the bcc structure.

Finally at the bottom of figure 6.4 we show the cubic unit cell of NaTl. The atomic positions are interchangeable and we notice that, like the CsCl arrangement, if the atoms were of the same type this structure would be the bcc Bravais lattice.

Therefore there are three structures for which second neighbours have to be considered, namely, CsCl, NiAs and NaTl. The second to first neighbour  $ss\sigma$  ratio taken here is the same as the one used in the study of the sp elements, i.e.,  $ss\sigma_2/ss\sigma_1 = 0.33$ . An interpolation formula has been given by Andersen and Jepsen (1984 – see also Andersen et al 1986) which allows the calculation of the hopping integrals and is dependent on both on the distance and on the Wigner-Seitz radius. Here we keep the simplest possible approach which consists in using the same ratio for all structures (notice that the second to first neighbour distance is the same for all three structures above).

### 6.2.2 Parameters Involved

In the study of the elements we took the simple cubic structure as the reference lattice. Here we take the equivalent to that structure, i.e., the NaCl arrangement, as the reference for the study of the AB compounds. As we did for the elements the value of  $ss\sigma$  for this structure is taken as  $-1$  (the units are not relevant because we are only interested in relative energy calculations) and the ratio of the other hopping integrals with respect to  $ss\sigma$  is also kept the same, i.e.,

Table 6.2

	$\epsilon_s$ (ev)	$\epsilon_p$ (ev)	$\frac{\epsilon_s - \epsilon_p}{12}$	$\frac{\epsilon_s + 3\epsilon_p}{12}$	$\frac{\Delta}{12}$
Zn	-8.40	-3.38	-0.42	-1.55	2.75
S	-20.80	-10.27	-0.88	-4.30	
Mg	-6.86	-2.99	-0.32	-1.32	2.08
Po	-16.21	-8.19	-0.67	-3.40	
Mg	-6.86	-2.99	-0.32	-1.32	0.66
Tl	-9.92	-4.61	-0.44	-1.98	

Table 6.2 Atomic values of the diagonal matrix elements showing values of the sp-splitting and the positive parameter  $\Delta$  for three AB compounds in the structures of wurtzite (ZnS), NiAs (MgPo) and CsCl (MgTl). The data comes from Harrison (1980).

$$\begin{aligned}
sp\sigma &= \frac{1.84}{-1.40} ss\sigma \\
pp\sigma &= \frac{3.24}{-1.40} ss\sigma
\end{aligned} \tag{6.1}$$

and

$$pp\pi = -0.33 pp\sigma \quad .$$

Whenever second neighbours have to be considered the ratio  $ss\sigma_2/ss\sigma_1$  will also be the same as for the elements, i.e., 0.33 as explained above. For a given structure the ratio between the hopping integrals among the second neighbours is taken as the same as the corresponding ratio among the first neighbours, just as we did for the bcc lattice in the elemental case. Therefore the simple model used in the study of the elements is being naturally extended to the study the AB compounds.

Let us find out the range over which the parameters  $\Delta$  and  $\epsilon_{sp}$  are to be varied in order to reproduce the experimental trends. We will be rescaling the experimental quantities by dividing energy values by  $12|ss\sigma_{NaCl}| = 12$ . Let us consider three compounds namely ZnS, MgPo and MgTl which represent the structures of wurtzite (coordination  $Z = 4$ ), nickel arsenide ( $Z = 4, 6$ ) and cesium chloride ( $Z = 12$ ) respectively. From table 6.2 we see that the values of  $-\epsilon_{sp}/12$  and  $\Delta/12$  can be taken as ranging from 0 to 1 and 0 to 5 respectively. From now on when we refer to these parameters we will be meaning their rescaled values unless explicitly stated otherwise.

As explained above the atomic positions in the nickel arsenide structure are not interchangeable. We therefore have to specify to which site will be assigned the atomic entity with, say, the highest center of gravity. In MgPo the metallic (nickel) site is occupied by the magnesium atom whose band is situated above that for polonium (see table 6.2). Accordingly we choose to assign the highest band to the nickel site which is the one with the highest coordination.

### §6.3 Results for $h_{pp} \propto h_{\text{bond}}^2$

In this section we present the results derived for the structural trends assuming that the repulsive pair potentials vary as the square of the bonding energy. As we did for the elements we make use of the structural energy difference theorem to prepare the volumes at which the structures are to be compared. This amounts to fixing the same repulsive energy for all the structures. As summarized in appendix III, when  $h_{pp} \propto h_{\text{bond}}^2$ ,  $\Delta E_{\text{rep}} = 0$  corresponds to comparing the structures at the volumes determined by imposing invariance in their second moments of the local density of states.

The NaTl structure is not being included in this preliminary study. As for NiAs we present the results both with and without the second neighbours. There are only two second neighbours in this structure (as opposed to six in CsCl and NaTl) but their inclusion is important to prevent its stabilization over its cubic analog namely the NaCl structure as will be seen below. Only the results for  $\epsilon_{sp}^A = \epsilon_{sp}^B = 0$  are shown, which is enough to motivate a change in the behaviour of the repulsive energy with bond length. The difference in the center of gravity of the bands for the A and B sites given by  $\Delta$  was taken as 0, 1, 2 and 3. In order to avoid messing up the text with too many curves we show the densities of states in appendix XII where the relevant information about the data used to draw them is also given. The structure maps are shown in figures 6.6 (only first neighbours for NiAs) and 6.7 (second neighbours included in NiAs). The corresponding structural energy versus band filling curves are shown in figures 6.8 and 6.9 respectively.

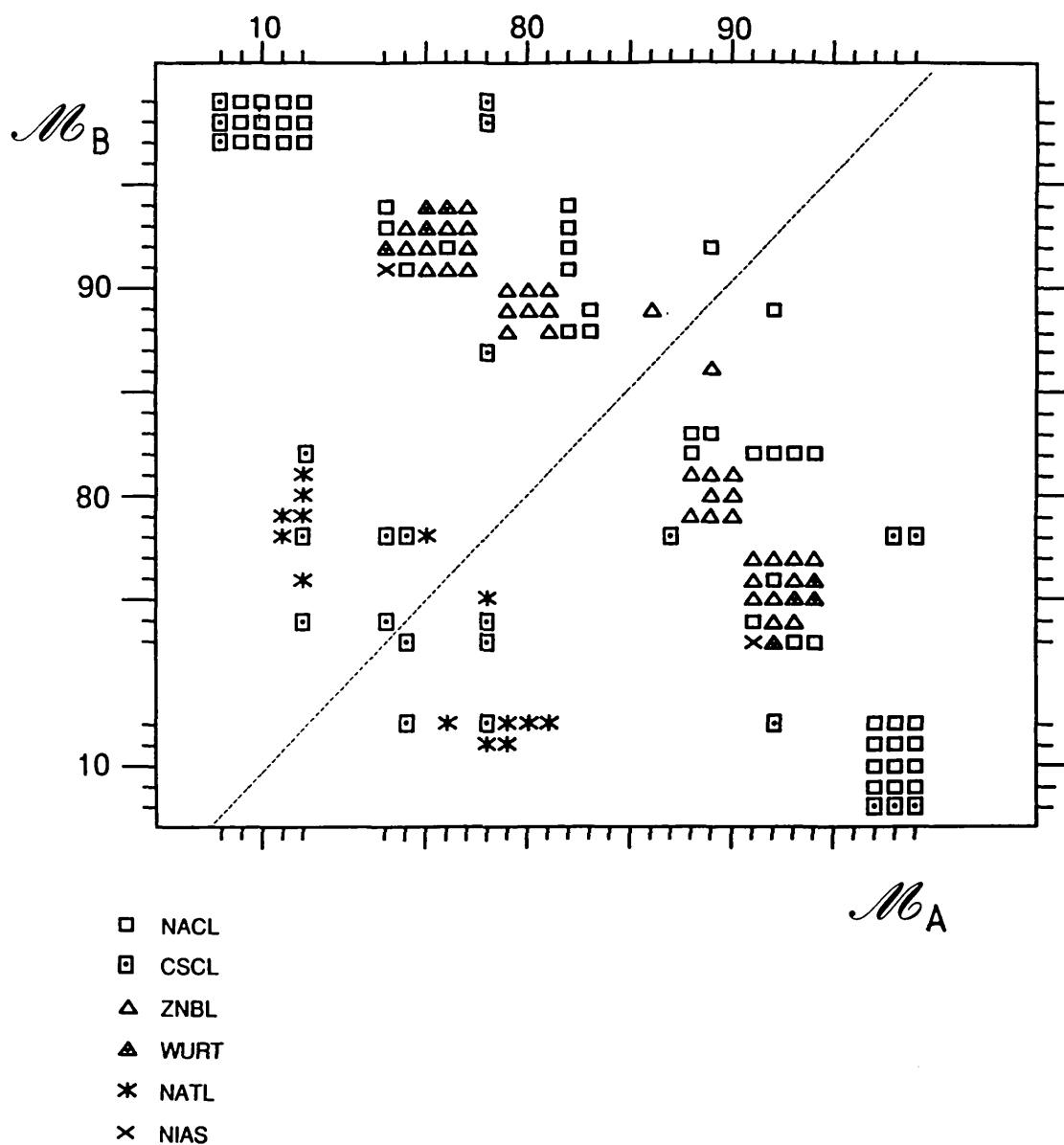


Figure 6.5  
 Experimental AB structure map for the six sp-bonded structures listed in the figure. The Mendeleev number is used in both axis. Notice that there is a discontinuity between 12 and 74.

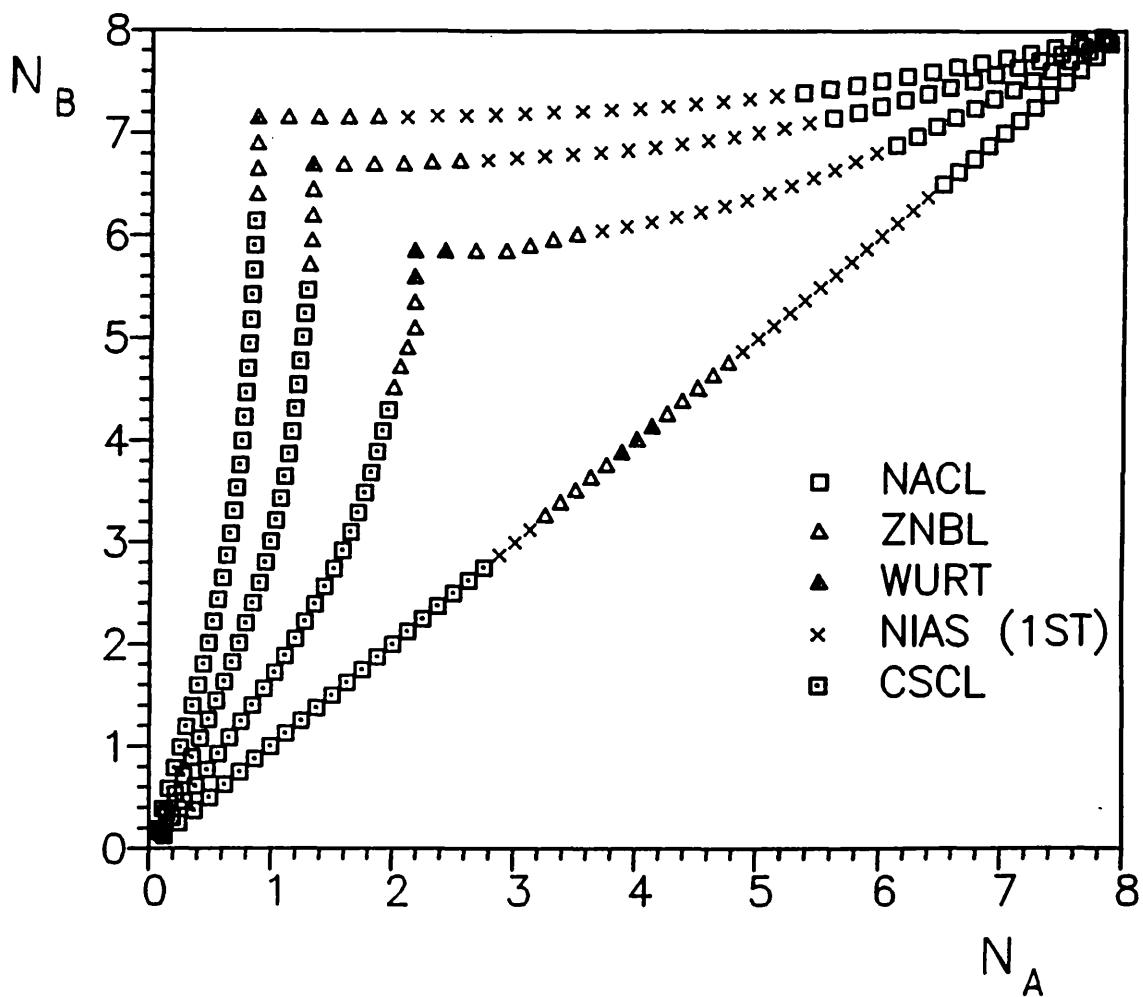


Figure 6.6

Theoretical structure map for  $h_{pp} \propto h_{bond}^2$ . Here  $\epsilon_{sp}^A = \epsilon_{sp}^B = 0$  and, from right to left,  $\Delta = 0, 1, 2$  and  $3$ . Only first neighbours were taken for NiAs. Structure energy versus band filling curves are shown in figure 6.8.

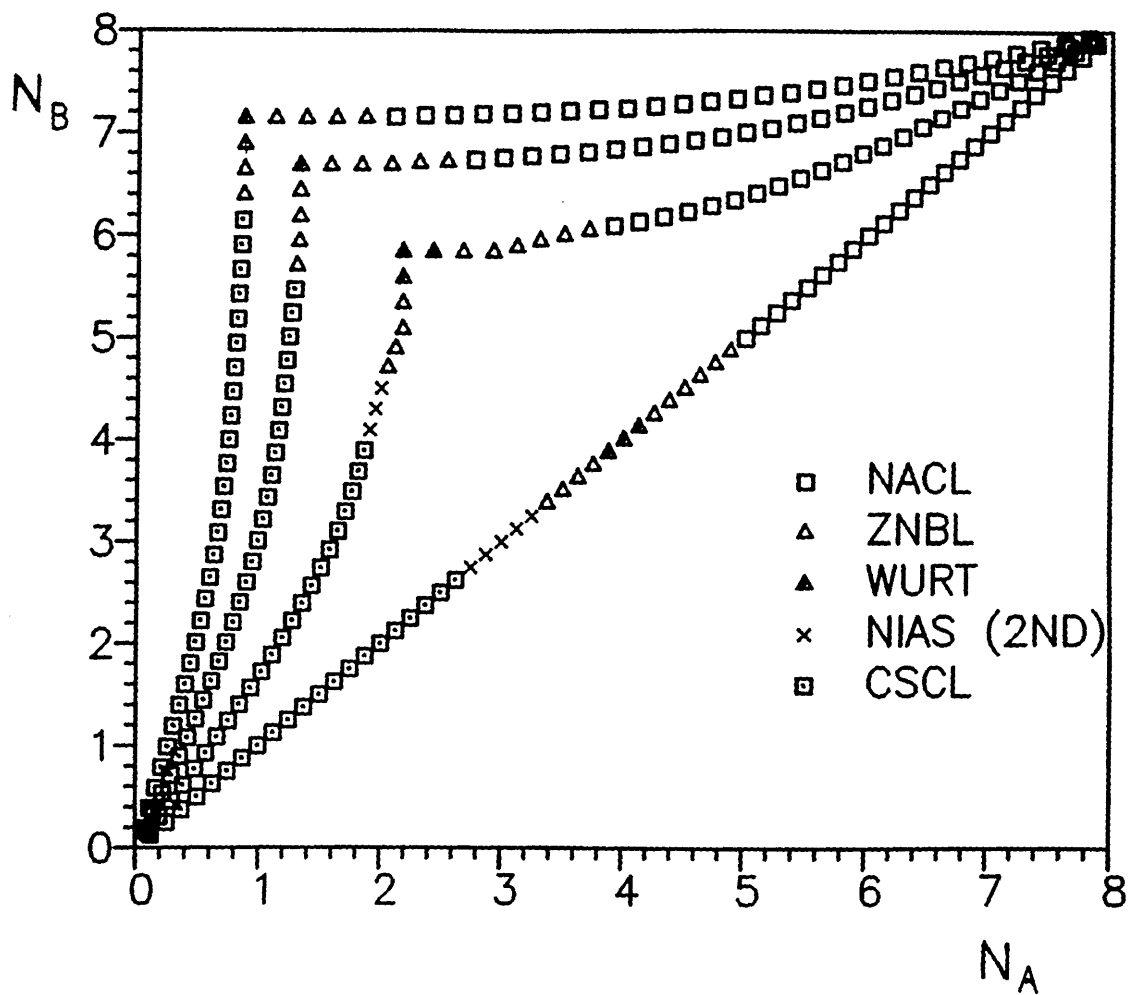


Figure 6.7  
 The same as figure 6.6 but with the second neighbours included for NiAs. Structure energy versus band filling curves are shown in figure 6.9.



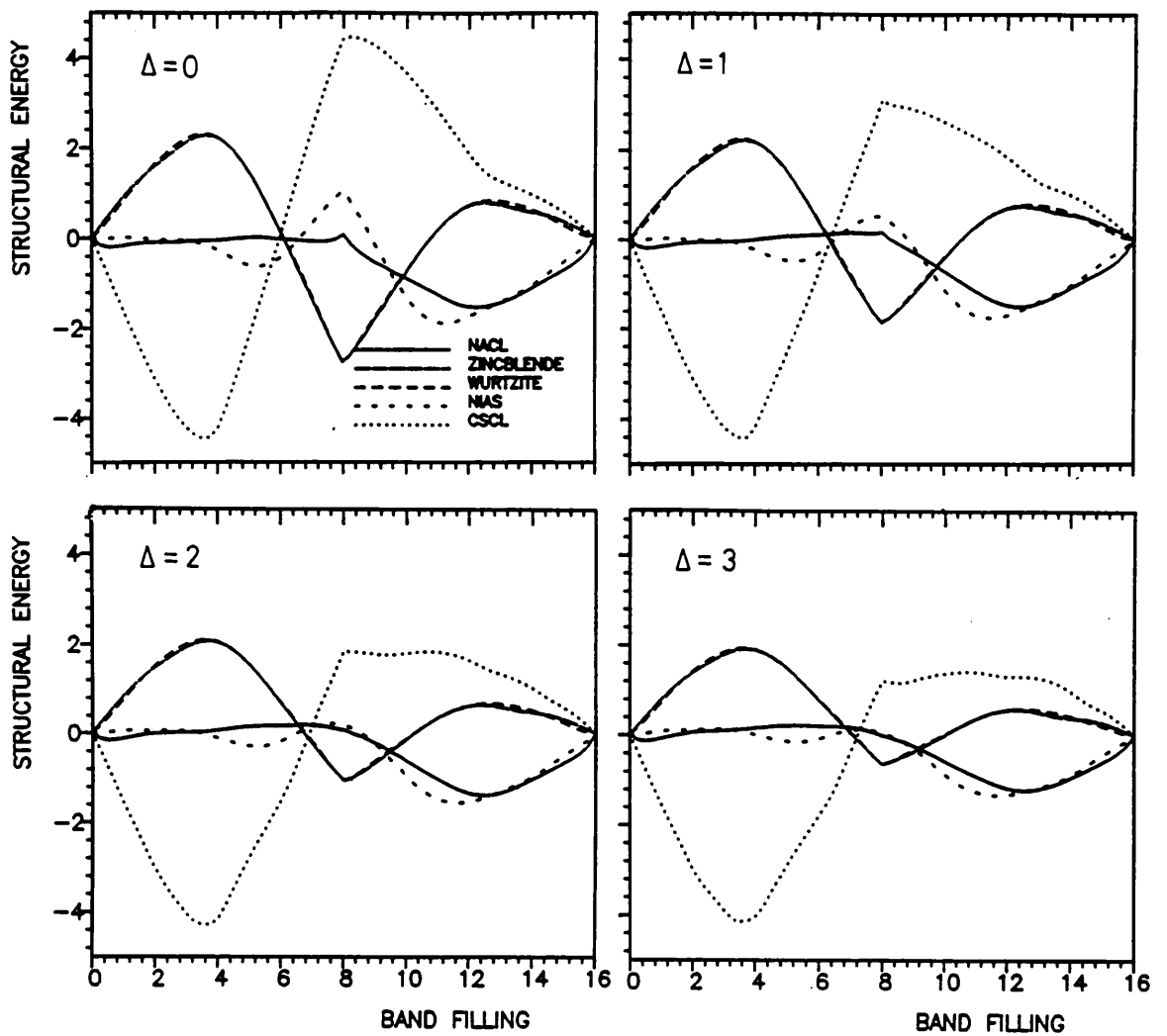


Figure 6.8

Structure energy versus band filling curves ( $\epsilon_{sp}^A = \epsilon_{sp}^B = 0$  and  $h_{pp} \propto h_{bond}^2$ ) used for drawing the map in figure 6.6. Second neighbours were left out of the calculations for the NiAs structure. The reference is a cubic spline with nine knots, namely, 2, 4, 6, 8, 8, 8, 10, 12 and 14. The corresponding DOS are shown in appendix XI.

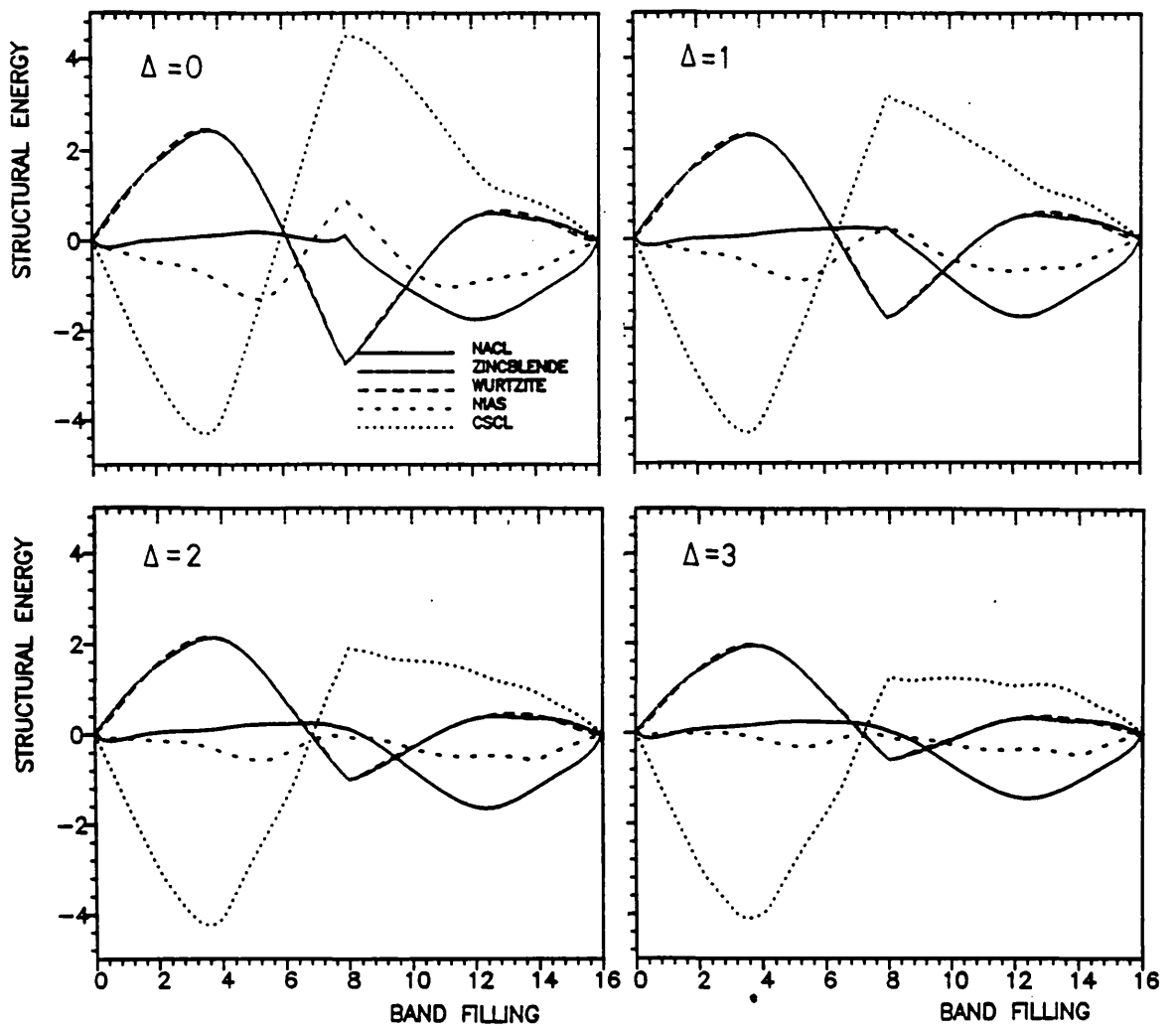


Figure 6.9  
 The same as figure 6.8 but now with the second neighbours included in NiAs.  
 These curves were used for drawing the map shown in figure 6.7.

Since this is the first time that an AB structure map is shown we will take this opportunity to discuss some general features associated with them. In these maps the occupancy of site A (B) is taken as the horizontal (vertical) axis. The atom sitting at site A is taken as the one with the highest center of gravity (which in NiAs is the nickel site as explained above). Site B being occupied by the atom with the lowest band has always a higher occupancy than site A which explains why the  $\Delta = \text{constant}$  curves are situated in the upper part of the figure relative to the diagonal passing through the origin.

Since  $\epsilon_{sp}^A = \epsilon_{sp}^B$ ,  $\Delta = 0$  corresponds to having the same type of atoms occupying the A and B sites in the compound. This situation is described in the diagonal curve in the structure map and corresponds to the elemental case considered in chapter 4. As  $\Delta$  departs from 0 the other curves are obtained thus describing the situation in which the A and B atomic sites are occupied by different types of atoms. The octets ( $N_A + N_B = 8$ ) lie on the diagonal line (not shown in the maps) linking the upper left and bottom right corners of the structure maps. Typical examples are I-VII and II-VI compounds like CsCl ( $N_A = 1$  and  $N_B = 7$ ) and NaCl ( $N_A = 2$  and  $N_B = 6$ ) respectively. We see from the maps in figures 6.6 and 6.7 that the theoretical model places tetrahedrally coordinated structures in the positions where these compounds should be (see also the experimental map in figure 6.5). This failure of the model can be amended by making the repulsion harder, i.e., instead of assuming that  $h_{pp} \propto h_{\text{bond}}^2$  (which in Harrison's (1980)  $h_{\text{bond}} \propto 1/R^2$  model corresponds to  $h_{pp} \propto 1/R^4$ ) one can assume that  $h_{pp} \propto 1/R^5$  (Majewski and Vogl 1986, 1987). This is done in the next section. A stronger repulsive potential is known to favour stability towards more closely packed arrangements as for example in the closed shell noble systems formed by Ne, Ar and the other noble gases (except He).

Before we leave this section we would like to remark on the differences

between these first two theoretical maps due to the second neighbours in NiAs. From figure 6.6 (first neighbours only) one notices that a large NiAs stability region develops in the super-octets ( $N_A + N_B > 8$ ) region. This region does not exist in the experimental map shown in figure 6.5 and given its size it is not likely to disappear as  $\epsilon_{sp}$  changes. On the other hand in the sub-octets region ( $N_A + N_B < 8$ ) a small NiAs stability area pointing to the upper left corner is developed in figure 6.7 (second neighbours included). This is more in accordance with the position of the sole representative of the nickel arsenide structure (namely, MgPo) in the experimental map. Therefore we will keep the second neighbours in this structure in all the forthcoming calculations.

## §6.4 Results for $h_{pp} \propto 1/R^5$ .

In this section we set a harder repulsive potential in order to attempt to improve the results along the upper part of the octets line. Details on the implementation of  $h_{pp} \propto 1/R^5$  are given in appendix III. In particular we notice that use of the structural energy difference theorem does not lead anymore to  $\Delta\mu_2 = 0$  (see appendix III). Also done in this section is the inclusion of the sodium thallium structure in the calculations. As for CsCl and NiAs the second neighbours in NaTl will be taken into account with the ratio between the second to first neighbours being given by  $ss\sigma_2/ss\sigma_1 = 0.33$ .

The resulting theoretical structure maps are shown in figures 6.10, ( $\epsilon_{sp}^A = \epsilon_{sp}^B = 0$ ), 6.11 ( $\epsilon_{sp}^A = \epsilon_{sp}^B = -0.5$ ) and 6.12 ( $\epsilon_{sp}^A = \epsilon_{sp}^B = -1$ ) with the corresponding structural energy versus band filling curves being shown in figures 6.13, 6.14 and 6.15 respectively. The number of exact moments kept for each case varies because Beer's (1985) procedure for the calculation of band and gap edges does not work, in general, for any number of levels as explained before. In appendices XIII and XIV we list the number of exact moments used for each case and present some densities of states. Not all DOS are shown for  $\epsilon_{sp}^A \neq \epsilon_{sp}^B$  because as the  $sp$ -splitting and  $\Delta$  are increased more than one gap may develop in the spectrum and a reliable calculation for the band and gap edges would require, typically, more than fifteen exact levels of recursion (Turchi et al 1982 and chapter 2 this work). In such cases the continued fraction was terminated with Beer and Pettifor's optimized square root terminator (Beer and Pettifor 1984, Beer 1985), with eleven exact levels of recursion, for the calculation of integrated quantities. As shown in chapter 2 (see also Turchi et al op. cit.) the resulting

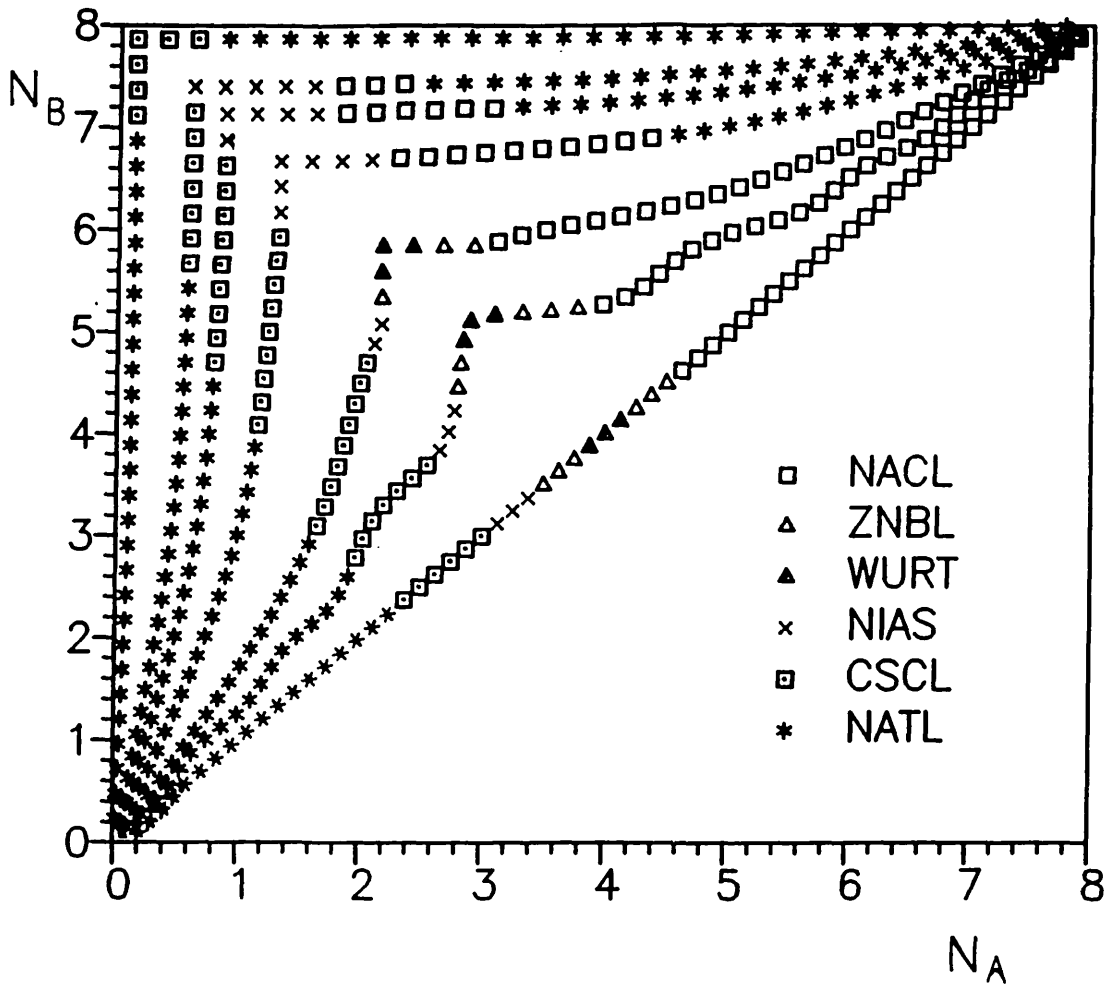


Figure 6.10

Theoretical structure map for  $h_{pp} \propto 1/R^5$ ,  $\epsilon_{sp}^A = \epsilon_{sp}^B = 0$  and  $\Delta = 0, 0.5, 1, 2, 3, 4$  and  $10$ . Structure energy versus band filling curves and DOS are shown in figure 6.13 and appendix XII respectively.

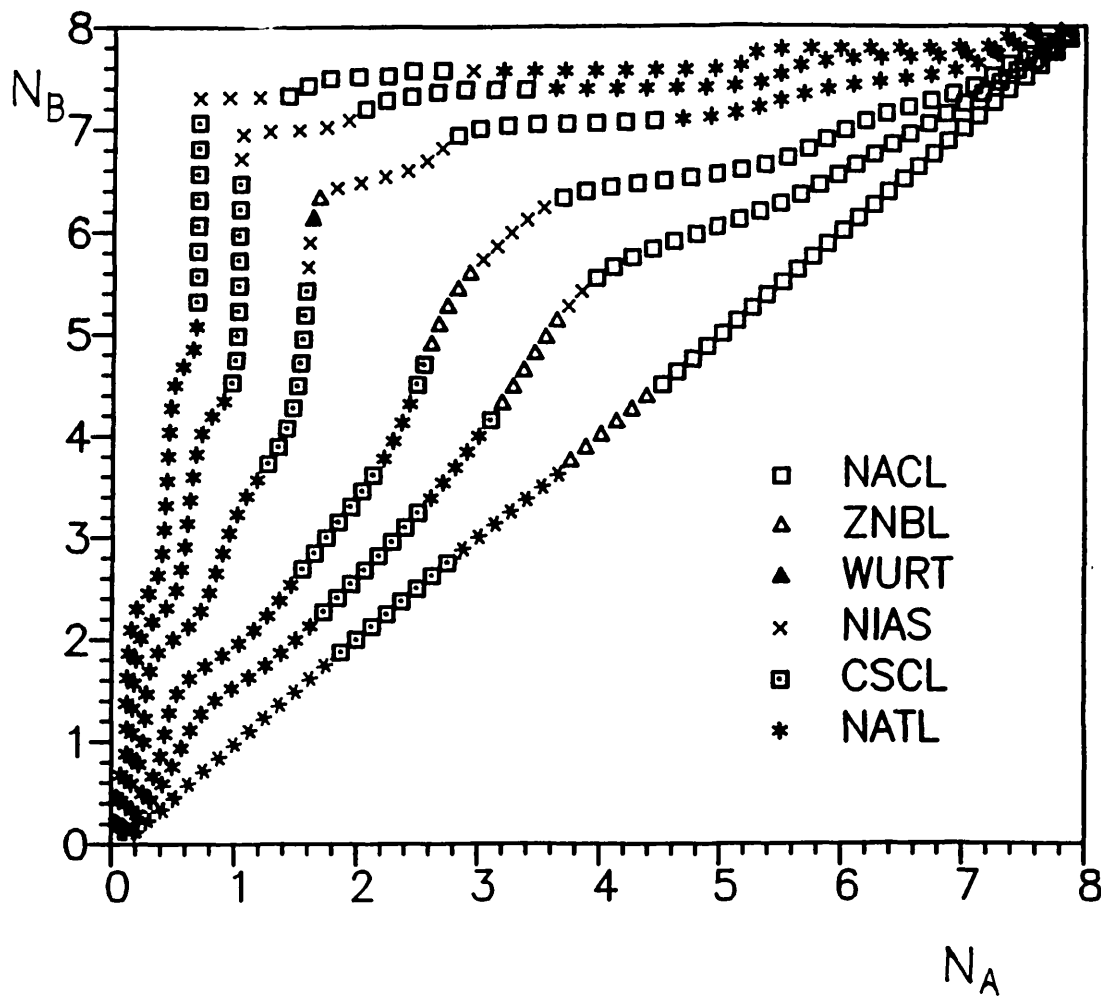


Figure 6.11

Theoretical structure map for  $h_{pp} \propto 1/R^5$ ,  $\epsilon_{sp}^A = \epsilon_{sp}^B = -0.5$  and  $\Delta = 0, 0.5, 1, 2, 3$  and  $4$ . Structure energy versus band filling curves are shown in figure 6.14. DOS are shown in appendix XIII.

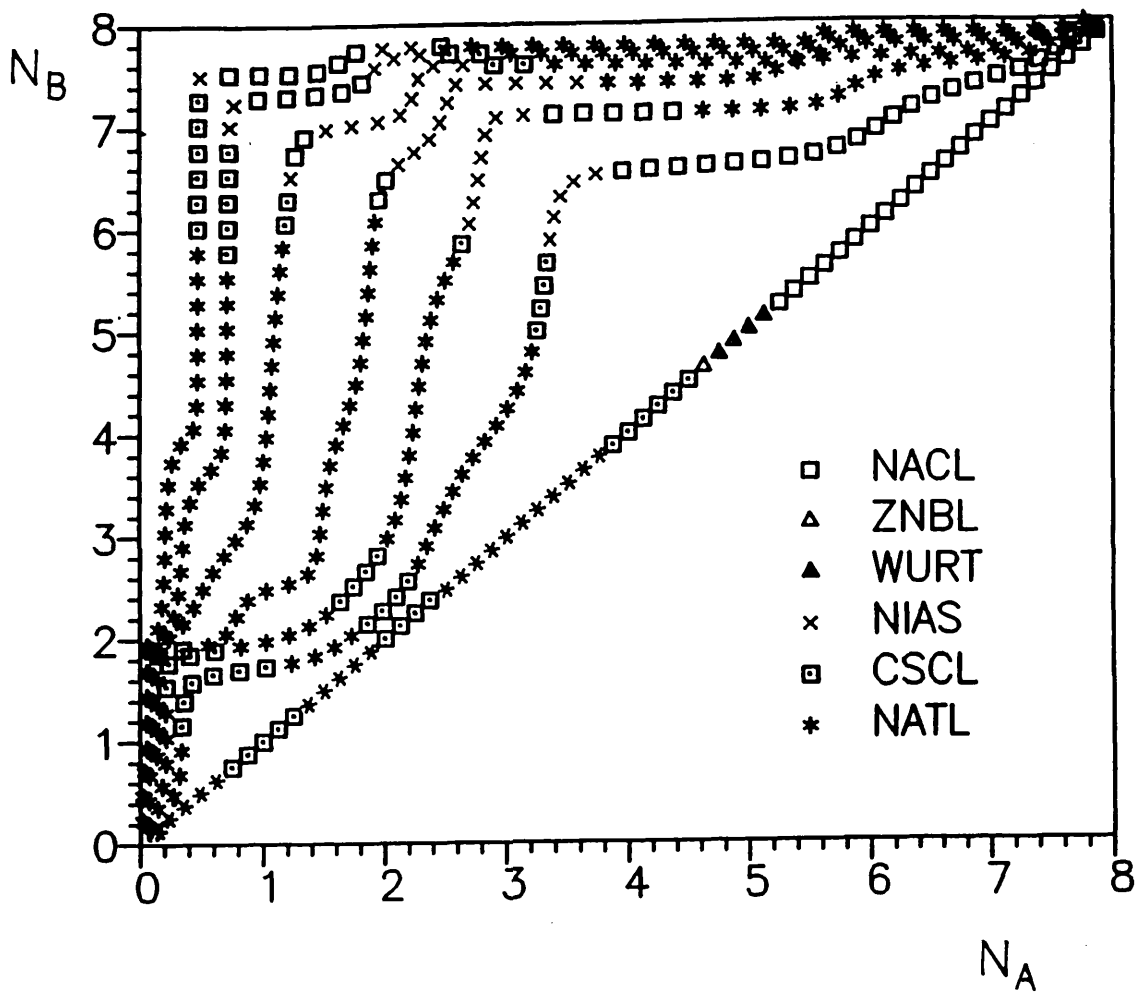


Figure 6.12

Theoretical structure map for  $h_{pp} \propto 1/R^5$ .  $\epsilon_{sp}^A = \epsilon_{sp}^B = -1$  and  $\Delta = 0, 1, 2, 3, 4, 5$  and  $6$ . Structure energy versus band filling curves are shown in figure 6.15.



integrated quantities are accurate enough to predict structural energy differences reliably.

Let us now compare the theoretical results with the experimental map in figure 6.5. Notice that this map is symmetric with respect to the dashed line across its diagonal. We will therefore only pay attention to that part of the map above that line.

The first thing to notice in the  $h_{pp} \propto 1/R^5$  structure maps is the improvement obtained in the I-VII and II-VI regions which are now dominated by NiAs (the hexagonal analog of NaCl) and CsCl arrangements (see figure 6.10,  $\epsilon_{sp}^A = \epsilon_{sp}^B = 0$ ) as opposed to tetrahedrally coordinated structures as in the  $h_{pp} \propto h_{bond}^2$  case. Notice the similarity between the NiAs and NaCl densities of states shown in appendix XIII. If NiAs were left out those regions would be occupied by the NaCl structure (see structural energy versus band filling curves in figure 6.13. The stability region obtained for NiAs is not in disagreement with the position of MgPo in the experimental map in figure 6.5.

The stability region of NaCl at the top left corner of the experimental map is reproduced well by the theoretical maps shown in figures 6.11 and 6.12 ( $\epsilon_{sp}^A = \epsilon_{sp}^B = -0.5$  and  $-1$  respectively). The small CsCl island there is also obtained with all three theoretical maps. Another region in the experimental map that is reproduced by the theoretical results is the one in its bottom left corner which is shared by NaTl and CsCl structures. In the upper right corner of the experimental map there is a region of NaCl stability which is very well defined in all three theoretical maps. Finally the islands of tetrahedrally coordinated stability in the experimental map is obtained in the theoretical maps in figures 6.10 and 6.11.

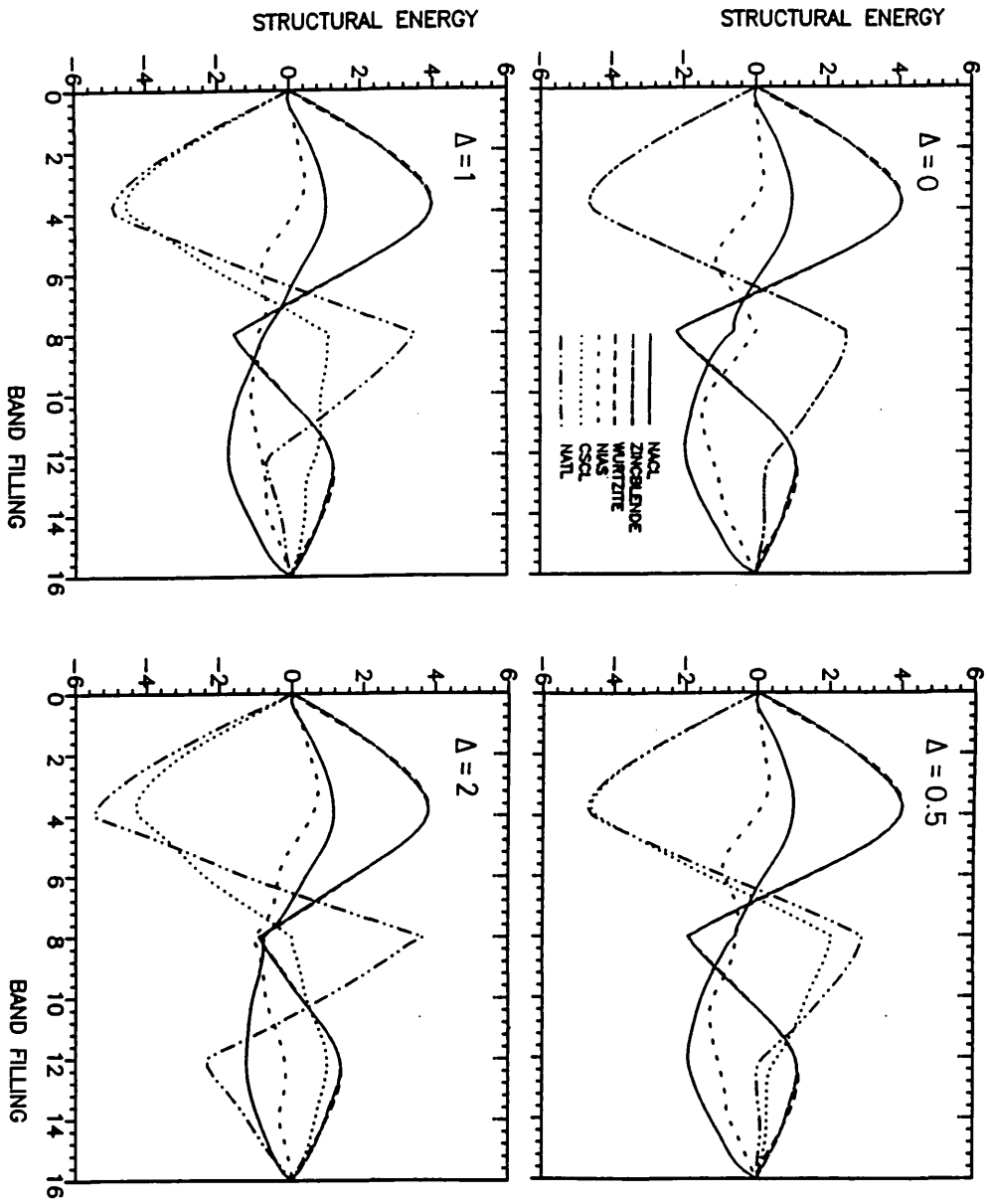


Figure 6.13 (continue)

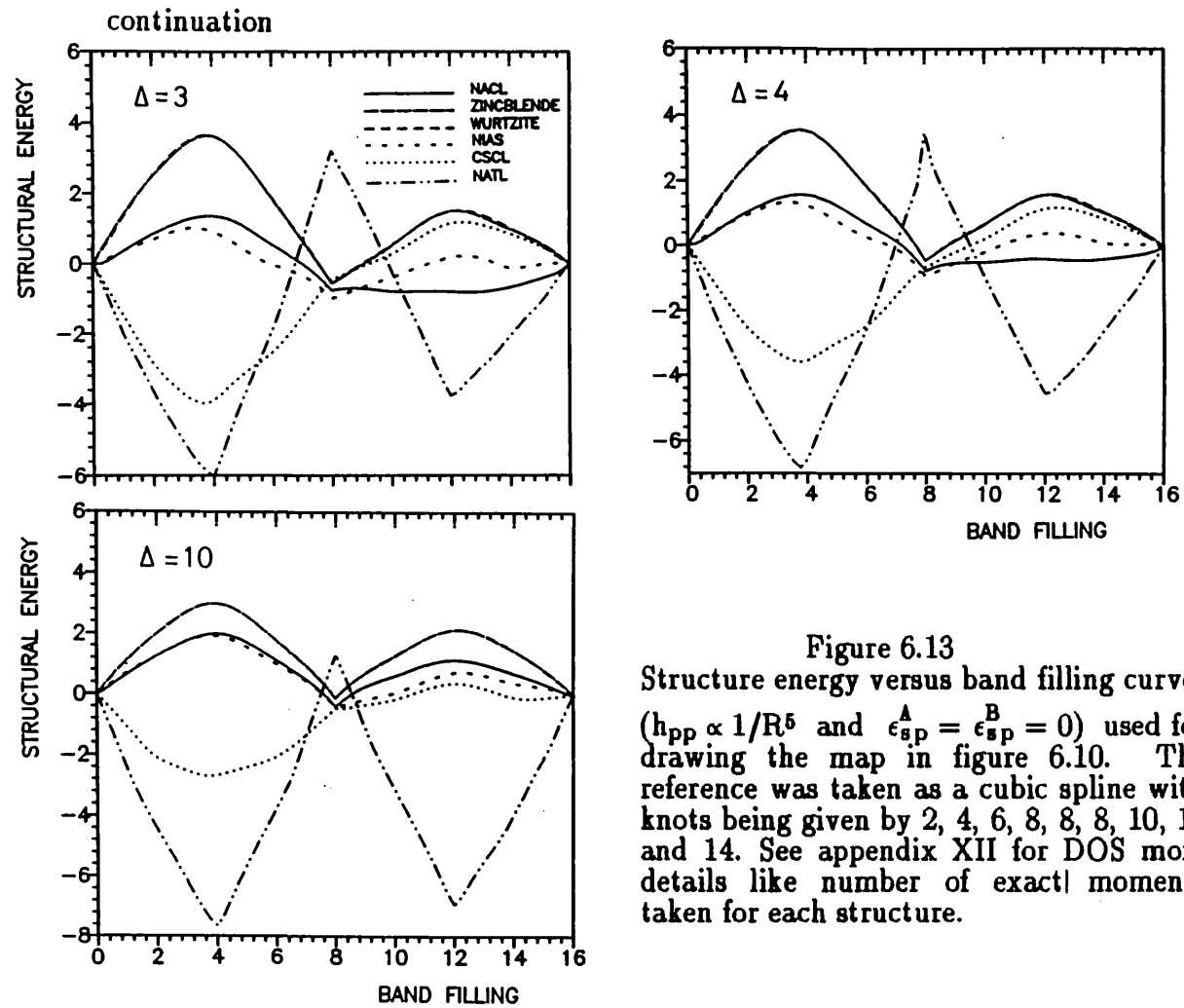


Figure 6.13  
 Structure energy versus band filling curves  
 ( $h_{pp} \propto 1/R^5$  and  $\epsilon_{sp}^A = \epsilon_{sp}^B = 0$ ) used for  
 drawing the map in figure 6.10. The  
 reference was taken as a cubic spline with  
 knots being given by 2, 4, 6, 8, 8, 8, 10, 12  
 and 14. See appendix XII for DOS more  
 details like number of exact moments  
 taken for each structure.

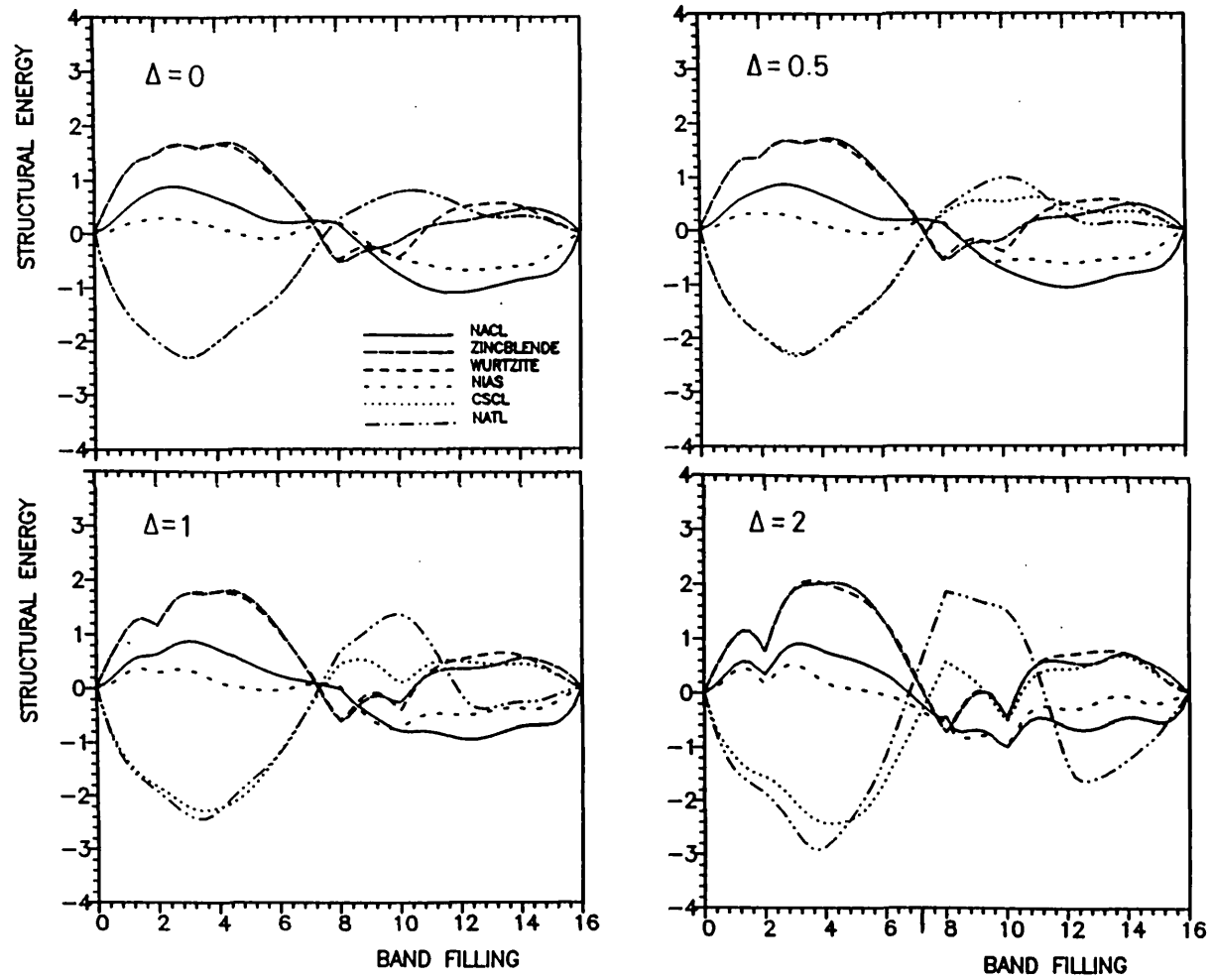


Figure 6.14 (continue)

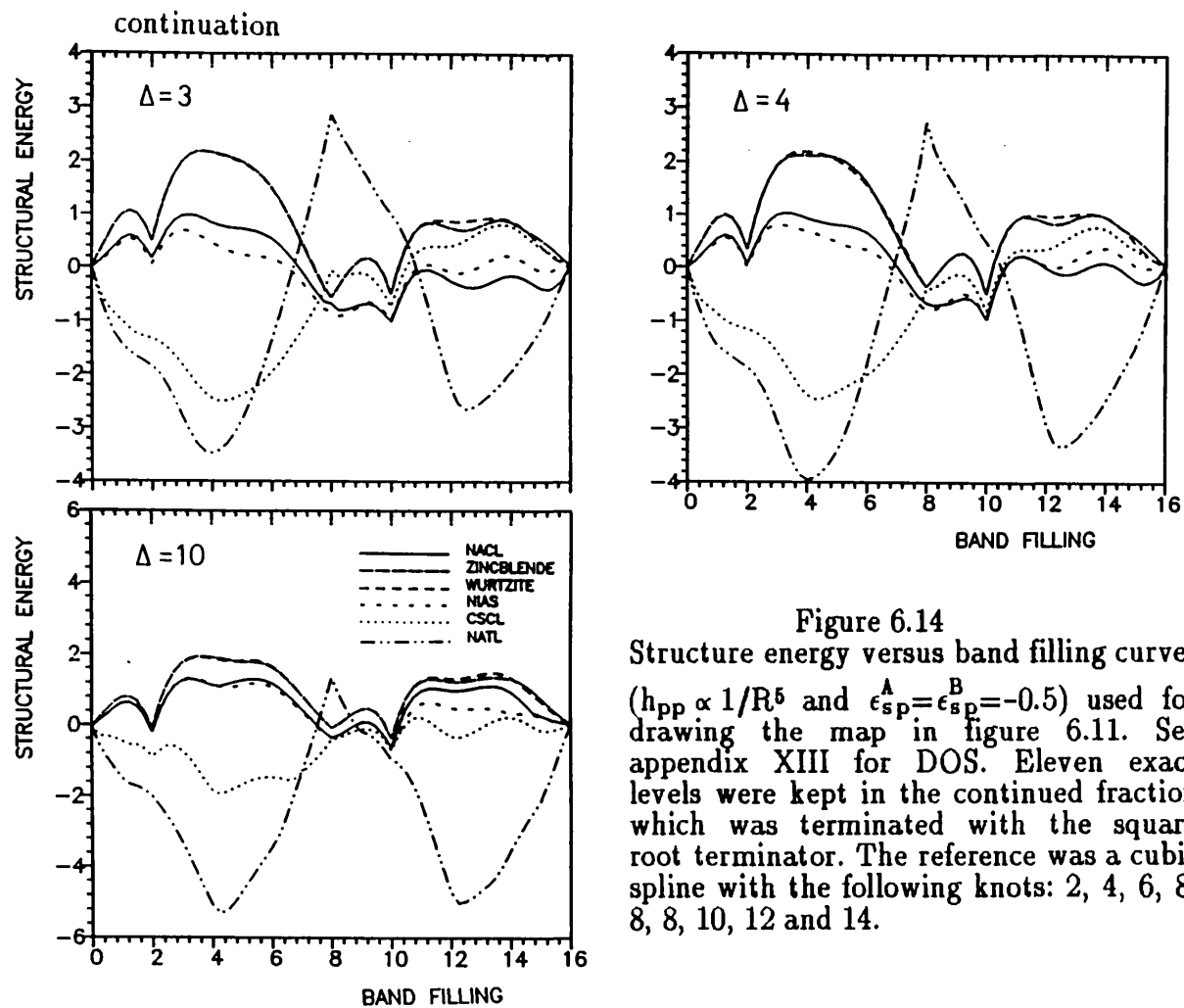


Figure 6.14  
Structure energy versus band filling curves  
( $h_{pp} \propto 1/R^5$  and  $\epsilon_{sp}^A = \epsilon_{sp}^B = -0.5$ ) used for drawing the map in figure 6.11. See appendix XIII for DOS. Eleven exact levels were kept in the continued fraction which was terminated with the square root terminator. The reference was a cubic spline with the following knots: 2, 4, 6, 8, 8, 8, 10, 12 and 14.

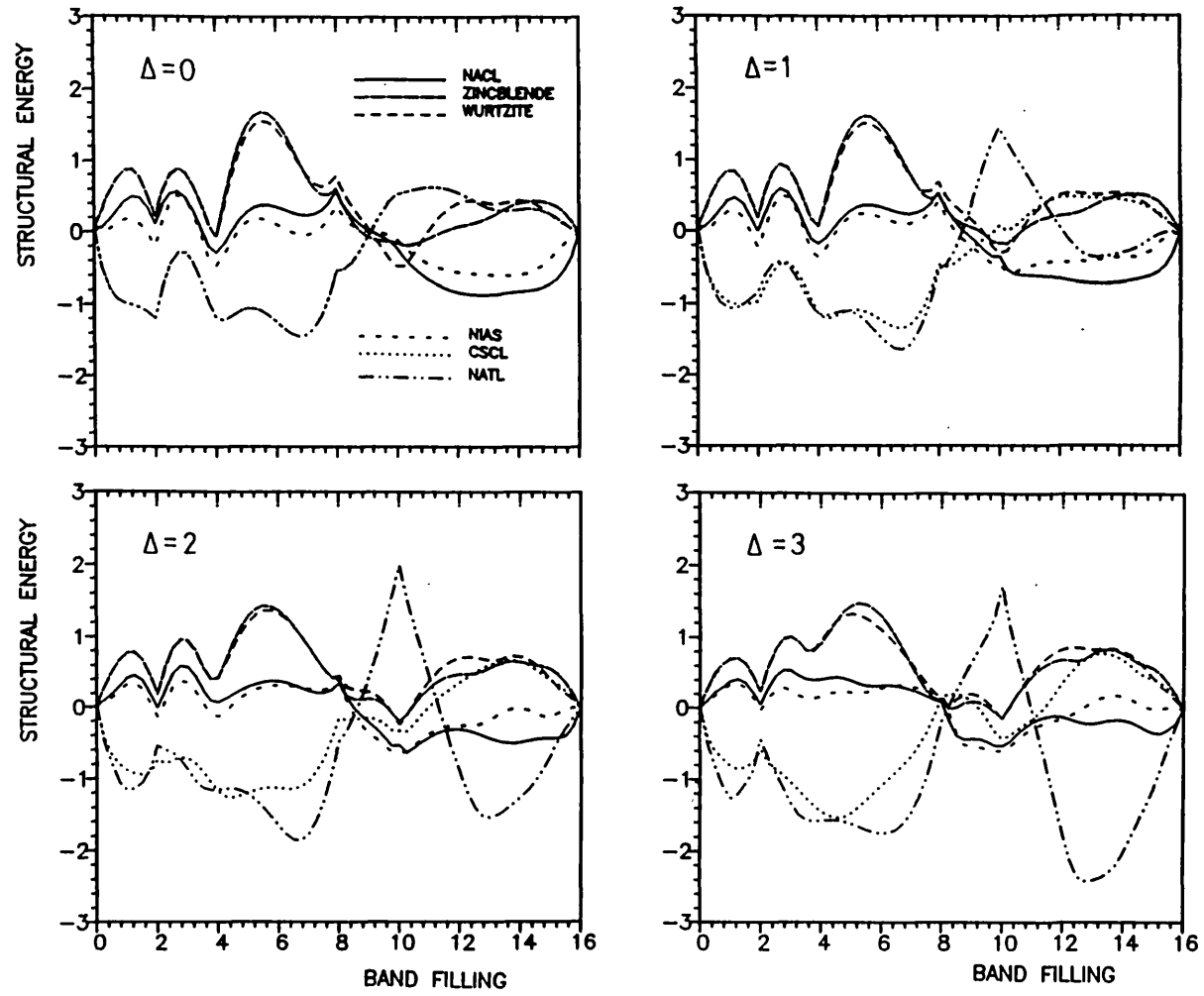


Figure 6.15 (continue)

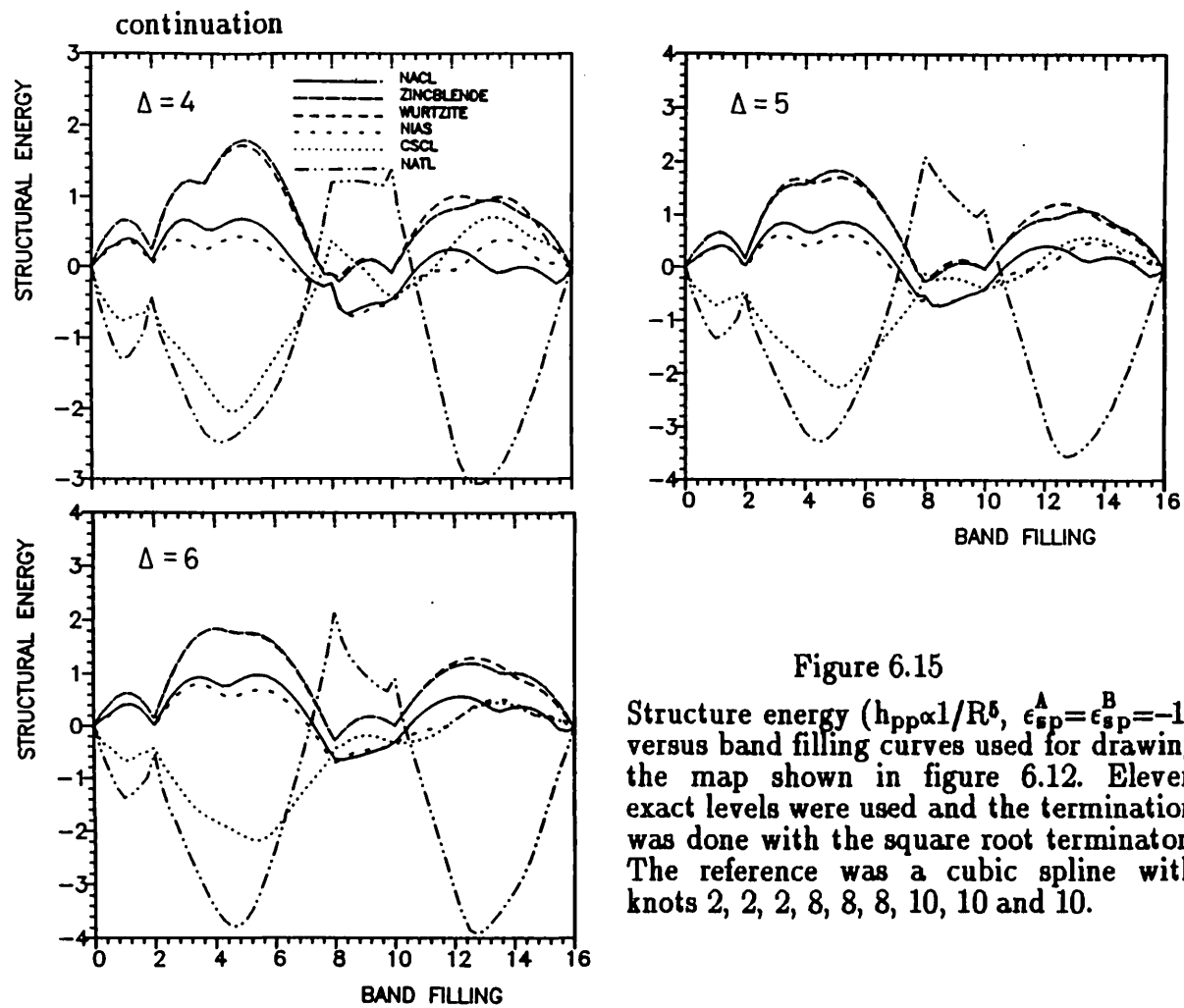


Figure 6.15  
 Structure energy ( $h_{pp} \propto 1/R^5$ ,  $\epsilon_{sp}^A = \epsilon_{sp}^B = -1$ ) versus band filling curves used for drawing the map shown in figure 6.12. Eleven exact levels were used and the termination was done with the square root terminator. The reference was a cubic spline with knots 2, 2, 2, 8, 8, 8, 10, 10 and 10.

Let us show some results for  $\epsilon_{sp}^A \neq \epsilon_{sp}^B$ . In figure 6.16 we show a theoretical map corresponding to  $\epsilon_{sp}^A = 0$  and  $\epsilon_{sp}^B = -1$  with the structural energy versus band filling curves being shown in figure 6.17. In the nickel arsenide calculations A is the nickel site and B is the arsenic site just as what happens in MgPo (magnesium is in the nickel site, has a smaller sp-splitting than polonium and the center of gravity of its band is above that for polonium). We see that the stability regions defined by this map are very similar to those displayed by the map in figure 6.10, i.e., the one for which  $\epsilon_{sp}^A = \epsilon_{sp}^B = 0$  (apart from the fact that the CsCl stability in this new map extends a bit further down towards the bottom left corner of the figure and the NiAs stability region for low values of  $\Delta$  has disappeared in favour of NaTl). Figure 6.18 presents the structural energy versus band filling curves for the case  $\epsilon_{sp}^A = 0$  and  $\epsilon_{sp}^B = -0.25$ , with  $\Delta = 0$  and  $\Delta = 3$ . Comparison of these curves with the corresponding ones for  $\epsilon_{sp}^A = \epsilon_{sp}^B = 0$  (figure 6.13) shows no major difference between them. We see no reason to believe that anything different will come out from other values of  $\Delta$ . The regions of structure stability seem to be insensitive to this small (0.25) change in the scale of this parameter.



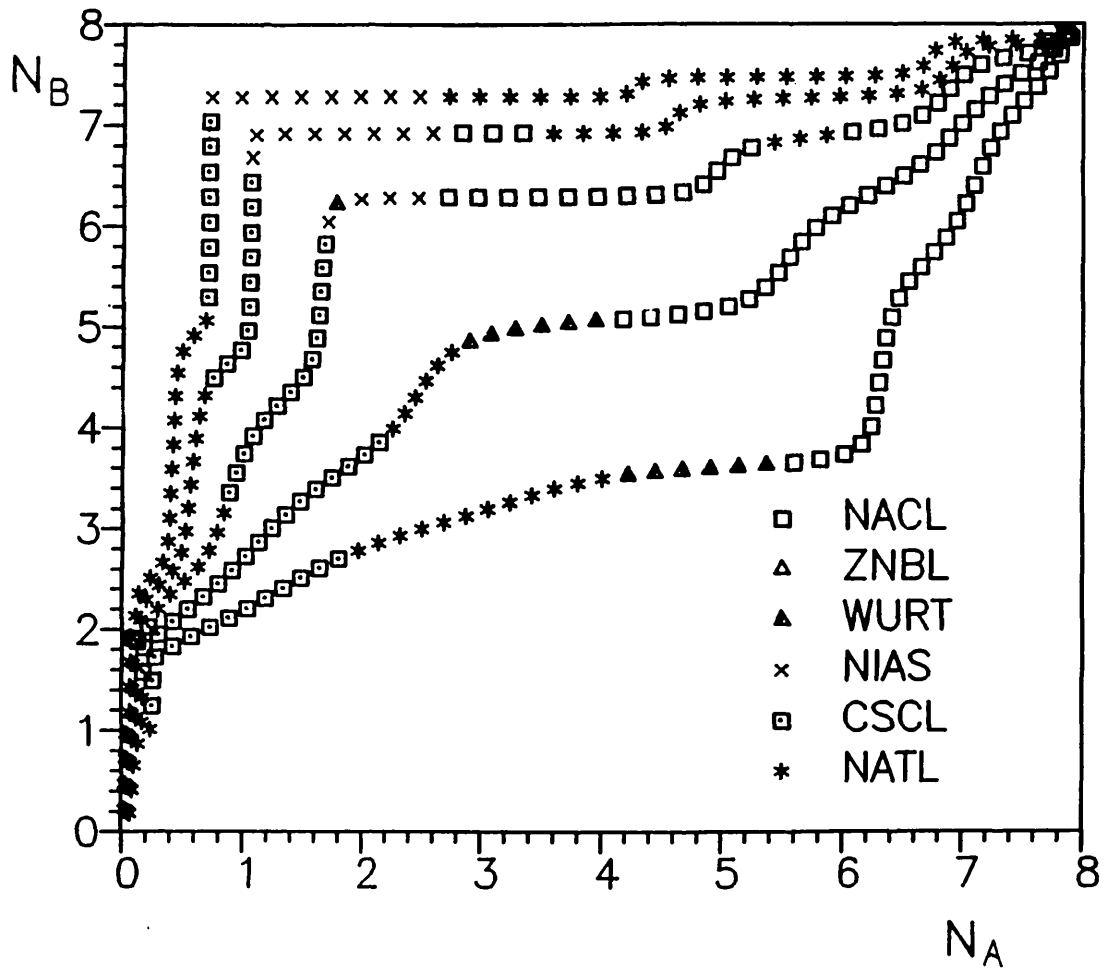


Figure 6.16

Theoretical structure map for  $h_{pp} \propto 1/R^5$ ,  $\epsilon_{sp}^A = 0$ ,  $\epsilon_{sp}^B = -1$  and  $\Delta = 0, 1, 2, 3$  and  $4$ . Structure energy versus band filling curves are shown in figure 6.17.

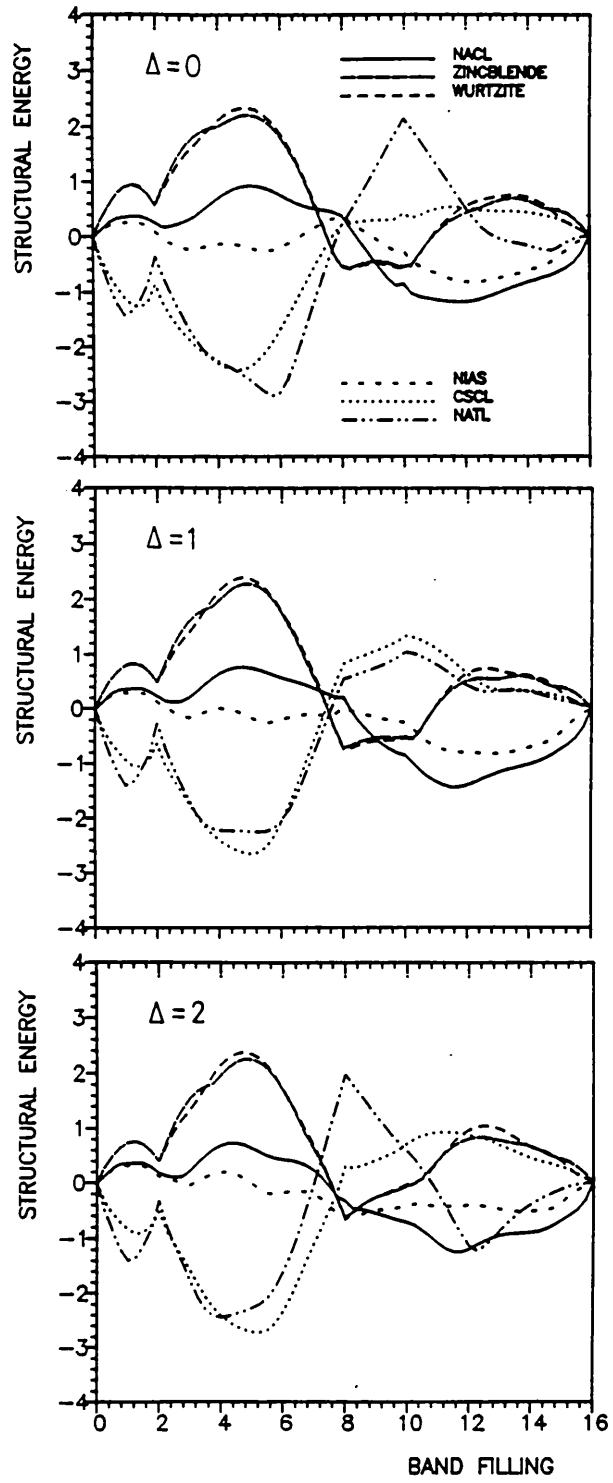


Figure 6.17 (continue)

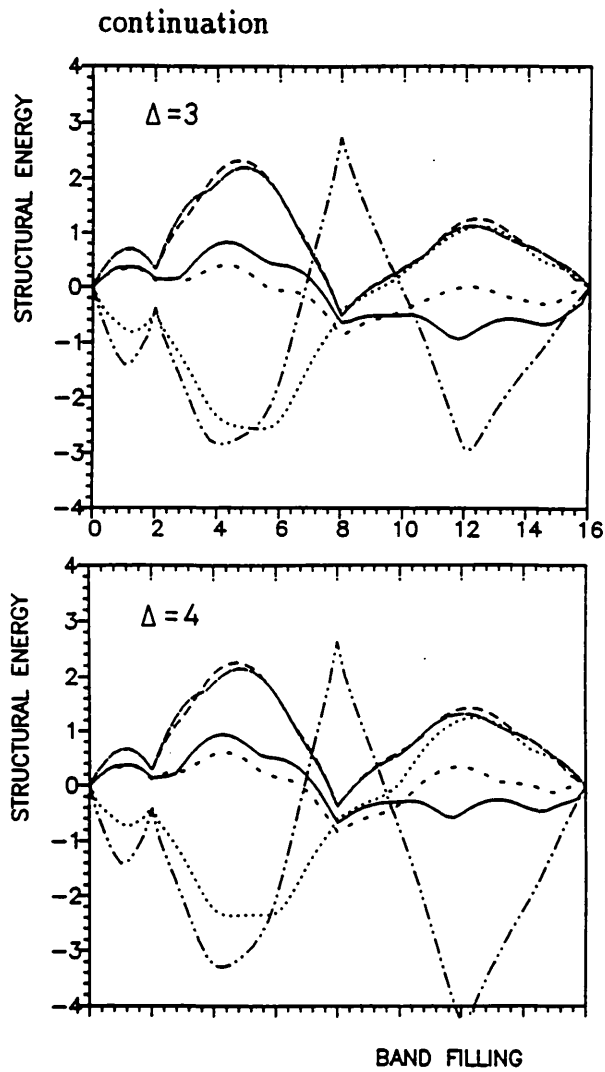


Figure 6.17

Structure energy versus band filling curves ( $h_{pp} \propto 1/R^5$ ,  $\epsilon_{sp}^A = 0$ ,  $\epsilon_{sp}^B = -1$ ) used for drawing the map shown in figure 6.16. Eleven exact levels were used and the termination was done with the square root terminator. The reference was taken as a cubic spline with knots 2, 2, 2, 8, 8, 8, 10, 10 and 10.

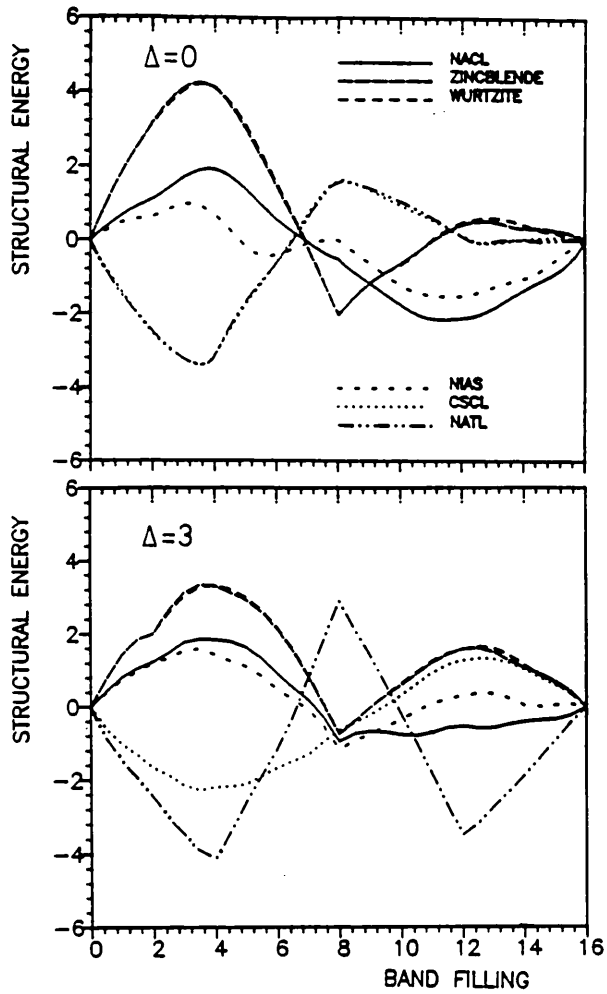


Figure 6.18

Structure energy ( $h_{pp} \propto 1/R^5$ ,  $\epsilon_{sp}^A = 0$ ,  $\epsilon_{sp}^B = -0.25$ ) versus band filling curves with  $\Delta = 3$  and  $\Delta = 4$ . Eleven exact levels were used and the termination was done with the square root terminator. The reference was taken as a cubic spline with knots 2, 2, 2, 8, 8, 8, 10, 10 and 10.

## §6.5 Conclusions

A harder repulsive potential was postulated in order that the model could be able to account satisfactorily for the structural trends observed amongst the AB compounds. Use of the structural energy difference theorem then provided the means to proceed to the comparison among six common AB structure types, namely NaCl, CsCl, ZnS (cubic), ZnS (hexagonal), NiAs and NaTl. The non-interchangeable sites in NiAs were set up as observed in MgPo. The results were then expressed in terms of structure maps drawn for different values of  $\epsilon_{sp}^A = \epsilon_{sp}^B$ . The model was shown to be able to reproduce the main trends observed in the experimental structure map drawn with the use of the Mendeleev number. However, different values of the sp-splitting had to be used to achieve this, leading to more than one different theoretical map. This result should be contrasted with the simplicity of the result obtained for the elements in which a single map was shown to be sufficient to reproduce the observed structural trends.

## Appendix I: Levels, Moments and Notation

The notation used to label the coefficients in the recursion method has not been uniform in the literature. Let us define the one we shall use throughout this work. The matrix element of the Green function relevant to the calculation of the local density of states will be written as

$$G_{00}(E) = \frac{b_0^2}{E - a_0 - \frac{b_1^2}{E - a_1 - \dots}} \quad (\text{I.1})$$

and this is all one needs to specify the notation. The correspondence with the tight-binding matrix elements in the chain model is as shown in figure 2.1. The first few moments can therefore be written as (remember that  $\mu_0 = \langle u_0 | u_0 \rangle = b_0^2$ )

$$\begin{aligned} \mu_0 &= b_0^2 \\ \mu_1 &= a_0 \\ \mu_2 &= a_0^2 + b_1^2 \\ \mu_3 &= a_0^3 + 2a_0b_1^2 + a_1b_1^2 \end{aligned} \quad (\text{I.2})$$

The relationship between number of coefficients and correspondent number of exact moments is then easily figured out. We list the coefficients inside squares and in the upper-left corner of each square we place the corresponding number of exact moments as if only the coefficients up to that particular one were known.

Coefficients		No. of pairs	No. of exact moments	No. of levels
2	$a_0$	1	2	0
4	$a_1$	2	4	1
6	$a_2$	3	6	2
8	$a_3$	4	8	3
$\vdots$	$\vdots$	$\vdots$	$\vdots$	$\vdots$

We see that for  $N$  known pairs of coefficients, a corresponding number of  $2N$  moments is implicitly known. Notice that the 0th moment has been included in this counting. We will also be counting the number of levels. The  $n$ th level is the set of atoms that can be reached with a minimum of  $n$  hops from the origin. Therefore with only one level one can compute (exactly) all the moments up to  $\mu_2$  and with the inclusion of self-tracing (on-site) paths also  $\mu_3$  can be evaluated. The fourth moment is the first to require a path that reaches the 2nd level and with the reasoning above, two levels allows us to compute all the moments up to  $\mu_5$ . In general, given  $n$  levels all the moments up to  $\mu_{2n+1}$  can be computed exactly.

The continued fraction in the form of (I.1) is a rather lengthy kind of notation. In most situations we shall instead prefer to adopt the following compact form

$$\mathcal{K}_{i=0}^N \left[ \frac{\alpha_i}{\beta_i} \right] = \frac{\alpha_0^2}{\beta_0 + \frac{\alpha_1^2}{\beta_1 + \frac{\alpha_2^2}{\beta_2 + \dots + \frac{\alpha_N^2}{\beta_N}}}} \quad (I.3)$$

for a finite (truncated) continued fraction. Therefore (I.1) can be written as

$$G_{00}(E) = (-1) \mathcal{K}_{i=0}^{\infty} \left[ \frac{-b_i^2}{E - a_i} \right]. \quad (\text{I.4})$$

We will also be defining a terminator  $t(E)$  in the continued fraction by

$$G_{00} = \frac{b_0^2}{E - a_0 - \frac{b_1^2}{E - a_1 - \frac{b_2^2}{E - a_2 - \dots - \frac{b_N^2}{E - a_N - t(E)}}}} \quad (\text{I.5})$$

in which we see that  $N$  levels (i.e.,  $2N + 1$  moments) are being used.



## Appendix II: Turchi's Termination

Let us summarize some of Turchi's results (Turchi et al 1982) for the spectrum with a single gap. We will try to keep the notation as close as possible to Turchi's original notation. We will be mostly interested in writing explicitly the recursion relations for the coefficients and commenting about them. Such relations were already obtained in Turchi's work but we will derive them here again because it is instructive and illuminating for the comments. It is also interesting to see them being obtained straight from the terminating function.

Let us write the continued fraction first:

$$G_{00} = \frac{b_0^2}{E - a_0 - \frac{b_1^2}{E - a_1 - \frac{b_2^2}{E - a_2 - \dots - \frac{b_{n-1}^2}{E - a_{n-1} - g_n(E)}}}} \quad (II.1)$$

Notice that Turchi's notation does not include  $b_n^2$  in  $g_n(E)$  as we do. Notice also that, from the way we are defining our continued fraction,  $b_{i-1}^2$  in Turchi's notation corresponds to  $b_i^2$  in our notation. The band and gap edges are represented by  $E_1 < E_2 < E_3 < E_4$  and some useful parameters are defined by

$$W = \frac{1}{2}(E_4 - E_1) \quad G = \frac{1}{2}(E_3 - E_2) \quad (II.2a)$$

$$a = \frac{1}{2}(E_4 + E_1) \quad g = \frac{1}{2}(E_3 + E_2) \quad (II.2b)$$

Turchi et al (1982) have provided two equivalent analytic forms for the terminating function  $g_n(E)$ . The starting point is an ordered tight-binding infinite linear chain in which the coefficients play the role of tight-binding matrix

elements. The semi-infinite linear chain is then obtained by suppressing the site  $n-1$  or eliminating the bond between  $n-1$  and  $n$ . The terminating function generated with the starting point at site  $n$  was then found to be

$$g_n(E) = \frac{E^2 + A_1 E + A_2 + 2b_n^2 - [X(E)]^{\frac{1}{2}}}{2(E + A_1 + a_{n-1})} \quad (\text{II.3})$$

$$= \frac{2b_n^2 (E + A_1 + a_n)}{E^2 + A_1 E + A_2 + 2b_n^2 + [X(E)]^{\frac{1}{2}}}$$

where

$$X(E) = (E - E_1)(E - E_2)(E - E_3)(E - E_4) \quad (\text{II.4a})$$

$$A_1 = -(g + a) \quad (\text{II.4b})$$

$$A_2 = ga - \frac{1}{2}(W^2 + G^2) \quad (\text{II.4c})$$

The asymptotic coefficients were found to be bounded, i.e.,

$$a - G \leq a_n \leq a + G \quad (\text{II.5a})$$

and

$$\frac{W - G}{2} \leq b_n \leq \frac{W + G}{2} \quad (\text{II.5b})$$

The first of these inequalities can be obtained simply by imposing that the DOS be positive. Let's see this. First notice that  $\text{Im } g_n(E)$  must be negative in order that the DOS be greater than zero. Notice also that the complex square root in the denominator of  $g_n(E)$  must be dealt with care. It must be such that (see Turchi et al op.cit.)  $\sqrt{X(E)} / \sqrt{|X(E)|}$  takes the following values in the real energy axis

$$\begin{array}{ccccccccc} & & & \boxed{-i} & & \boxed{+i} & & & \\ +1 & & -1 & & +1 & & & & \\ \hline \end{array}$$

Therefore, in order that  $\text{Im } g_n(E) < 0$ , we see that the numerator must be negative in the lower band and positive in the upper band. If we write

$$E + A_1 + a_n = E - [(g + a) - a_n]$$

we see that this condition is fulfilled if  $(g + a) - a_n$  is inside the gap, i.e.,

$$g - G < (g + a) - a_n < g + G$$

which can easily be seen to lead straight back to (II.5a). This relation was obtained only for the last known coefficient  $a_n$ . But since  $a_n$  is assumed to be in the asymptotic region (Turchi et al 1982) it should hold for all asymptotic coefficients. For instance one could always generate one more pair of coefficients using the recurrence relations (see below) and choose to terminate the continued fraction one step later. Then the inequalities would hold for the next pair. With this reasoning one sees that it must hold for all coefficients provided that they are in the asymptotic region. An important consequence is that if the computed gap width is too small compared with the true gap width, and if the last known coefficient  $a_n$  is close to an extreme, then one can end up with a negative part in the DOS. This can be seen as a warning signal that tells us that something went wrong in the computation of the gap edges. This is a healthy check for the gap edges particularly important if one is working with only a few number (around ten)

levels. However it can always be switched of, if required, by simply imposing that  $\text{Im } g_n(E) < 0$  in the computing routines.

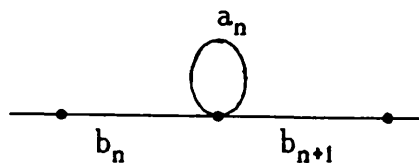
As mentioned, asymptotic coefficients are linked by recurrence relations. These can be obtained from the two forms given above for  $g_n(E)$ . From (II.3) one sees that

$$\begin{aligned} \left[ E^2 + A_1 E + A_2 + 2b_n^2 \right]^2 - X(E) &= \\ &= 4b_n^2 \left[ E - \alpha_n \right] \left[ E - \alpha_{n-1} \right] \end{aligned} \quad (\text{II.6})$$

where  $\alpha_n = (g + a) - a_n$ . Setting  $E = \alpha_n$  one gets

$$\begin{aligned} 2b_n^2 &= - \left[ \alpha_n^2 + A_1 \alpha_n + A_2 \right] \pm \left[ X(\alpha_n) \right]^{\frac{1}{2}} \\ &= - \left[ a_n^2 + A_1 a_n + A_2 \right] \pm \left[ X(g + a - a_n) \right]^{\frac{1}{2}} \end{aligned} \quad (\text{II.7})$$

Notice that in the tight-binding linear chain we have



for the neighbourhood of site  $n$ . Starting from this site, if one chooses to go to the right one gets  $(a_n, b_{n+1}^2)$  as one pair of asymptotic coefficients whereas the other direction gives  $(a_n, b_n^2)$ . In fact for a given value of  $\alpha_n$  in (II.7), one sign provides, say,  $b_{n+1}^2$  and the other  $b_n^2$ . We have the freedom to make the choice.

Notice also that if  $(a_n, b_{n+1}^2)$  satisfy (II.7) so does  $(a_{n-1}, b_n^2)$ , i.e., any pair of neighbouring coefficients in the linear chain satisfies (II.7). If one denotes one such pair by  $(x, y)$  one gets

$$\left[ x^2 + A_1 x + A_2 + 2y \right]^2 = X(g + a - x) \quad . \quad (II.8)$$

In what follows we write this equation more explicitly. For such we make use of the following equation which was introduced by Turchi et al (op.cit.)

$$\sqrt{X(E)} \xrightarrow{E \rightarrow \infty} E^2 \left[ 1 + A_1/E + \dots + A_m/E^m + \dots \right] .$$

and is used to define  $A_1, A_2, A_3$  and  $A_4$ . If we take the square of both sides we get

$$X(E) \xrightarrow{E \rightarrow \infty} E^4 + 2A_1 E^3 + (2A_2 + A_1^2) E^2 + (2A_3 + 2A_1 A_2) E + (2A_4 + 2A_1 A_3 + A_2^2) \quad . \quad (II.9)$$

Now using (II.4a) one can compare equal powers of  $E$  to arrive to an expression for the  $A$ 's.  $A_1$  and  $A_2$  have already been given in (II.4b) and (II.4c) respectively. The expressions for  $A_3$  and  $A_4$  were also obtained by Turchi et al (1982) and are given by

$$A_3 = (g - a) (W^2 - G^2) / 2$$

$$A_4 = \frac{1}{2} (g - a) (aW^2 - gG^2) - \frac{1}{8} [W^2 - G^2]^2$$

We can now write the right hand side of (II.8), i.e.,

$X(g+a-x) = X(-A_1-x)$  as

$$X(-A_1-x) = (-A_1-x)^4 + S_1(-A_1-x)^3 + S_2(-A_1-x)^2 + S_3(-A_1-x) + S_4$$

in which the  $S$ 's are the coefficients in (II.9). Collecting together the same powers of  $x$  gives

$$X(-A_1-x) = x^4 + 2A_1x^3 + (2A_2 + A_1^2)x^2 + (-2A_3 + 2A_1A_2)x + (2A_4 + A_2^2) \quad (\text{II.10})$$

The left-hand side of (II.8) can be expanded to give

$$4yx^2 + (4A_1y + 2A_3)x + (4y^2 + 4A_2y - 2A_4) = 0 \quad (\text{II.11})$$

which is of second order in either  $x$  or  $y$ , i.e.,

$$x^2 + \left(A_1 + \frac{A_3}{2y}\right)x + \left(A_2 + y - \frac{A_4}{2y}\right) = 0 \quad (\text{II.12a})$$

or

$$y^2 + (A_2 + A_1x + x^2)y + (A_3x - A_4)/2 = 0 \quad (\text{II.12b})$$

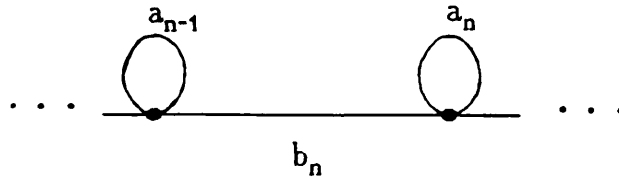
We can now write down the recurrence relations. For fixed  $y$ , say  $y = b_n^2$ , we have  $x = a_{n-1}$  or  $x = a_n$ . Therefore

$$a_{n-1} + a_n = -\left(A_1 + \frac{A_3}{2b_n^2}\right) \quad (\text{II.13a})$$

and

$$a_{n-1}a_n = A_2 + b_n^2 - \frac{A_4}{2b_n^2} \quad (\text{II.13b})$$

which corresponds to

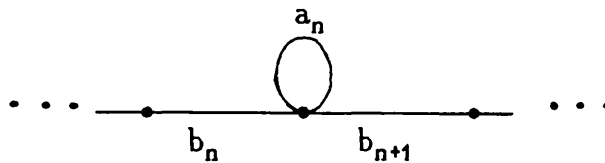


Similarly for fixed  $x$ , say  $a_n$ , we have either  $y = b_n^2$  or  $y = b_{n+1}^2$ , i.e.,

$$b_n^2 + b_{n+1}^2 = -(A_2 + A_1 a_n + a_n^2) \quad (\text{II.14a})$$

$$b_n^2 b_{n+1}^2 = (A_3 a_n - A_4)/2 \quad (\text{II.14b})$$

which corresponds to



Equations (II.13) or (II.14) can be used to evaluate  $A_1, A_2, A_3$  and  $A_4$  that enter into the terminating function, as explained in Turchi et al (1982). In (II.14) for example one can plot the left-hand-side as a function of  $a_n$ . Provided one is in the asymptotic regime a straight line is produced which gives estimates for the  $A$ 's. On the other hand if the band and gap edges are already

known then equations (II.13) and (II.14) may be used for generating coefficients. Suppose that the last known pair of coefficients is  $(a_n, b_n^2)$ . Then one may use (II.14a) to compute  $b_{n+1}^2$  and then (II.13a) with  $n \rightarrow n+1$ , i.e.,

$$a_n + a_{n+1} = -\left(A_1 + \frac{A_3}{2b_{n+1}^2}\right)$$

to compute  $a_{n+1}$  and so on and so forth.

One may also want to check that exact and asymptotic coefficients match at the boundary. Then with the known value of  $a_n$  one evaluates the (asymptotic) values of  $b_n^2$  and  $b_{n+1}^2$  – with the freedom of choosing which one is which – from (II.14) and compare the exact and asymptotic values of  $b_n^2$ .



### Appendix III: Assumptions for the sp Model

In this appendix we summarize the assumptions for the sp model presented in chapters 4 (elements) and 6 (binary compounds).

#### III.1 Elements

We consider first neighbours now and include second neighbours next. Let us write  $ss\sigma$  as a function of  $R$ , i.e.,

$$ss\sigma = \alpha F(R) \quad (\text{III.1})$$

where  $\alpha$  is a constant and the  $R$  dependence is carried out by  $F(R)$ . If we assume that the repulsive pair potentials  $h_{pp}$  are such that

$$h_{pp} = \beta [F(R)]^2 \quad (\text{III.2})$$

with  $\beta$  being a constant, then imposing  $E_{\text{rep}}^A = E_{\text{rep}}^B$  for two given sites in structures A and B, i.e.,

$$z_1^A \beta [F(R_1^A)]^2 = z_1^B \beta [F(R_1^B)]^2 \quad (\text{III.3})$$

we get

$$z_1^A [ss\sigma^A]^2 = z_1^B [ss\sigma^B]^2 \quad (\text{III.4})$$

Here  $z_1^A$  ( $z_1^B$ ) stands for the number of first neighbours of the selected site of structure A (B). If one takes structure A as the reference one can use this

equation to calculate  $ss\sigma$  for structure B. Therefore equation (III.4) fixes the bond lengths – or the volumes – at which the two structures are to be compared. Notice that the second moment of the local density of states at a given site is given by

$$\begin{aligned}\mu_2^i &= \mathcal{J}_1^i \left[ (ss\sigma^i)^2 + (sp\sigma^i)^2 + (pp\sigma^i)^2 + 2(pp\pi^i)^2 \right] \\ &= \mathcal{J}_1^i (ss\sigma^i)^2 \left[ 1 + \left[ \frac{(sp\sigma^i)^2}{(ss\sigma^i)^2} + \dots \right] \right]\end{aligned}$$

where  $i = A$  or  $B$ . Therefore we see that as long as the ratios appearing in this expression are kept the same for both structures, i.e.,

$$\frac{sp\sigma^A}{ss\sigma^A} = \frac{sp\sigma^B}{ss\sigma^B}$$

and so on, then equation (III.4) implies that the second moment of the local density of states is the same for structures A and B, i.e.,

$$\mu_2^A = \mu_2^B \quad . \quad (III.5)$$

Notice that the form of  $F(R)$  was not important for this result. The model is fairly general the only assumption being given by equation (III.2). We will see below that the explicit form of  $F(R)$  has to be given if second neighbours are to be considered.

If the second neighbours are to be taken into account for, say, structure B then equation (III.3) reads

$$\mathcal{J}_1^A \beta [F(R_1^A)]^2 = \mathcal{J}_1^B \beta [F(R_1^B)]^2 + \mathcal{J}_2^B \beta [F(R_2^B)]^2 \quad (\text{III.6})$$

in which we are assuming that (III.2) remains valid for the second neighbours with the same constant  $\beta$  and the same R dependence. One is then led to the generalization of (III.4) namely

$$\mathcal{J}_1^A [\text{ss}\sigma_1^A]^2 = \mathcal{J}_1^B [\text{ss}\sigma_1^B]^2 \left\{ 1 + \frac{\mathcal{J}_2^B / \mathcal{J}_1^B}{\frac{[\text{ss}\sigma_2^B]^2}{[\text{ss}\sigma_1^B]^2}} \right\} \quad (\text{III.7})$$

in which we have made use of equation (III.1). If we call  $\mathcal{R} = \text{ss}\sigma_2^B / \text{ss}\sigma_1^B$  for structure B we can write

$$\text{ss}\sigma_1^B = \left[ \frac{\mathcal{J}_1^A}{\mathcal{J}_1^B + \mathcal{J}_2^B \mathcal{R}^2} \right]^{1/2} \text{ss}\sigma_1^A \quad (\text{III.8})$$

As before we can recast this result in terms of the 2nd moments if we notice that  $\mu_2^B$  is written as

$$\begin{aligned} \mu_2^B &= \mathcal{J}_1^B (\text{ss}\sigma_1^B)^2 \left[ 1 + \left[ \frac{(\text{sp}\sigma)_1^B}{(\text{ss}\sigma)_1^B} \right]^2 + \dots \right] + \\ &+ \mathcal{J}_2^B (\text{ss}\sigma_2^B)^2 \left[ 1 + \left[ \frac{(\text{sp}\sigma)_2^B}{(\text{ss}\sigma)_2^B} \right]^2 + \dots \right] \end{aligned}$$

If the ratios among the hopping integrals for the 2nd neighbours are kept the same as for the 1st neighbours then

$$\mu_2^B = \left[ \mathcal{J}_1^B (\text{ss}\sigma_1^B)^2 + \mathcal{J}_2^B (\text{ss}\sigma_2^B)^2 \right] \left[ 1 + \left[ \frac{(\text{sp}\sigma)_1^B}{(\text{ss}\sigma)_1^B} \right]^2 + \dots \right]$$

and we see that (III.8) is the same as imposing  $\mu_1^A = \mu_2^B$  as before. However we now have another parameter, namely  $\mathcal{R}$ , that demands the knowledge of  $F(R)$  for its calculation. In Andersen and Jepsen's (1984) scheme the hopping integrals decay exponentially with distance which gives  $\mathcal{R} \approx 1/3$ .

### III.2 Binary Compounds

In order to get the NaCl stability region in the right place in the structure map a stronger  $R$  dependence for  $h_{pp}$  has to be assumed which replaces the one given in equation (III.2). We take

$$h_{pp} = \beta [F(R)]^{n/2} \quad (III.9)$$

We will keep this notation with general  $n$  but in the calculations (see text) it will be made equal to 5. Notice that in Harrison's scheme  $F(R) \sim 1/R^2$  and we have  $h_{pp} \sim 1/R^5$  which was Majewski & Vogl's (1986, 1987) choice for the repulsive non-orthogonality corrections in their total energy calculations.

Let's go straight to the second neighbours case. The generalization of equation (III.6) is

$$\mathcal{J}_1^A \beta [F(R_1^A)]^{n/2} = \mathcal{J}_1^B \beta [F(R_1^B)]^{n/2} + \mathcal{J}_2^B \beta [F(R_2^B)]^{n/2} \quad (III.10)$$

which leads to

$$ss\sigma_1^B = \left[ \frac{\xi_1^A}{\xi_1^B + \xi_2^B \mathcal{R}^{n/2}} \right]^{2/n} ss\sigma_1^A$$

and is no longer expressed simply in terms of the second moment of the density of states.

## Appendix IV: LCAO Solution for the Dimer (Pure s, Pure p and sp)

In this appendix we calculate the structural energy of a dimer, i.e., a homopolar molecule, using a linear combination of atomic orbitals (LCAO). This is a simple task but since the results are used elsewhere in this work we show here how they have been obtained. The general reference is Harrison (1980).

### IV.1 One s-orbital per site

Let us calculate the recursion coefficients corresponding to this structure. We take the zero of energy as the energy of the s-orbital of the isolated atom, i.e.,  $\epsilon_s = 0$ . There are two atoms, 1 and 2, and we choose the starting vector (see chapter 2) as an s-orbital on site 1, i.e.,  $|s^{(1)}\rangle$ . The recurrence relation writes

$$H|v_n\rangle = b_n|v_{n-1}\rangle + a_n|v_n\rangle + b_{n+1}|v_{n+1}\rangle \quad (\text{IV.1})$$

where  $|v_{-1}\rangle = 0$ . Due to the orthonormality of the basis vectors  $|v_n\rangle$  this expression gives

$$a_n = \langle v_n | H | v_n \rangle \quad (\text{IV.2})$$

Choosing  $|v_0\rangle = |s^{(1)}\rangle$  the first iteration gives

$$\begin{aligned} H|v_0\rangle &= H|s^{(1)}\rangle \\ &= \sum_m \langle s^{(m)} | s^{(1)} \rangle |s^{(m)}\rangle \\ &= h_{m2} |s^{(m)}\rangle \end{aligned} \quad (\text{IV.3})$$

where  $h = ss\sigma$ . From (IV.2) and (IV.3) we have  $a_0 = 0$ . Since (IV.1) with  $n = 0$ , gives  $H|v_0\rangle = a_0|v_0\rangle + b_1|v_1\rangle = b_1|v_1\rangle$  we can write

$$b_1|v_1\rangle = h |s^{(2)}\rangle$$

or, assuming  $b_1$  real,

$$\langle v_1|b_1b_1|v_1\rangle = \langle s^{(2)}|h h|s^{(2)}\rangle$$

which gives

$$b_1^2 = h^2 \tag{IV.4a}$$

and

$$|v_1\rangle = |s^{(2)}\rangle \tag{IV.4b}$$

The second iteration gives

$$\begin{aligned} H|v_1\rangle &= H|s^{(2)}\rangle \\ &= h|s^{(1)}\rangle \end{aligned} \tag{IV.5}$$

and as before from (IV.2) and (IV.5)  $a_1 = 0$ . From (IV.1) now with  $n=1$  we have  $H|v_1\rangle = b_1|v_0\rangle + b_2|v_2\rangle$ . Using (IV.5) for the left hand side and  $b_1|v_0\rangle = h|s^{(1)}\rangle$  we see that  $b_2|v_2\rangle = 0$  or  $b_2 = 0$ . This gives for the resolvent  $G(E)$  the following expression

$$G(E) = \frac{1}{E - \frac{h^2}{E}} \tag{IV.6}$$

i.e., a truncated continued fraction. This result was expected because the Hamiltonian being a  $2 \times 2$  matrix could be tridiagonalized by a basis containing only two state vectors. Actually the Hamiltonian matrix is given by

$$H = \begin{bmatrix} 0 & ss\sigma \\ ss\sigma & 0 \end{bmatrix} \quad (IV.7)$$

which is already tridiagonal with  $a_0 = a_1 = 0$  and  $b_1 = ss\sigma$  and so the calculation above was unnecessary. It is however the simplest possible application of Haydock's recursion, but enough to illustrate the operational details of the method. Continuing from (IV.6) we see that it can be written as

$$\begin{aligned} G(E) &= \frac{E}{E^2 - h^2} \\ &= \frac{1/2}{E + h} + \frac{1/2}{E - h} \end{aligned}$$

Therefore the "density of states"  $n(E) = (-2/\pi)\lim_{\eta \rightarrow 0} \text{Im } G(E+i\eta)$  where the factor 2 is due to spin degeneracy, is given by

$$n(E) = \delta(E - h) + \delta(E + h) \quad (IV.8)$$

where we have used  $\lim_{\eta \rightarrow 0} (x-a+i\eta) = -\pi\delta(x-a)$ . The bonding and antibonding combinations ( $\epsilon_s - |ss\sigma|$  and  $\epsilon_s + |ss\sigma|$ , respectively, if we had taken  $\epsilon_s \neq 0$ ) are very clear in this expression. The structural (or band) energy as a function of band filling  $N \leq 2$  is then given by

$$E_{\text{band}} = \begin{cases} N(-|h|) & \text{for } N < 1 \\ (-|h|) + (N-1)|h| & \text{for } N > 1 \end{cases} \quad (IV.9)$$



## IV.2 Pure p-orbitals case

As before we fix the atomic p-orbital to zero, i.e.,  $\epsilon_p = 0$ . We could follow the same lines as in the previous case, now in three parts one for each of the three possible orbitals  $p_x$ ,  $p_y$  and  $p_z$ . Since there are no matrix elements of the Hamiltonian between any of these orbitals the results will be just like before with  $h$  representing the adequate matrix element. The Hamiltonian matrix is tridiagonal as before with  $b_1 = pp\sigma$ ,  $b_2 = b_3 = pp\pi$ . The  $\pi$ -orbitals are degenerate sharing the same eigenvalue  $pp\pi$ . Choosing the molecular axis in the  $z$ -direction, the final result is

$$G_z(E) = \frac{E}{E^2 - pp\sigma^2} \quad (\text{IV.10a})$$

$$G_x(E) = G_y(E) = \frac{E}{E^2 - pp\pi^2} \quad (\text{IV.10b})$$

Taken into account the spin degeneracy, the density of states becomes

$$\begin{aligned} n(E) = & \delta(E - |pp\sigma|) + \delta(E + |pp\sigma|) \\ & + \delta(E - |pp\pi|) + \delta(E + |pp\pi|) \\ & + \delta(E - |pp\pi|) + \delta(E + |pp\pi|) \end{aligned} \quad (\text{IV.11})$$

which gives the structural energy (note that  $|pp\pi| < |pp\sigma|$ )

$$E_{\text{band}} =$$

$$\begin{cases} -N|pp\sigma| & N < 1 \\ -(N-1)|pp\pi| - |pp\sigma| & 1 < N < 3 \\ (N-3)|pp\pi| - |pp\sigma| - 2|pp\pi| & 3 < N < 5 \\ (N-5)|pp\sigma| - |pp\sigma| - 2|pp\pi| + 2|pp\pi| & 5 < N < 6 \end{cases} \quad (\text{IV.12})$$

## IV.2 sp-orbitals case

In this case there are four valence states for each atom and s and p states are hybridized in the molecule. With the molecular axis in the z-direction the  $p_x$  and  $p_y$  orbitals are coupled only to themselves and form bonding ( $\epsilon_p - |pp\pi|$ ) and antibonding ( $\epsilon_p + |pp\pi|$ ) combinations just as the s-orbitals in the pure s case. The  $\sigma$ -states resulting from the s and  $p_z$  combinations give a 4x4 block that looks like

$$H_{sp_z} = \begin{pmatrix} \epsilon_s & ss\sigma & 0 & sp\sigma \\ ss\sigma & \epsilon_s & -sp\sigma & 0 \\ 0 & -sp\sigma & \epsilon_p & pp\sigma \\ sp\sigma & 0 & pp\sigma & \epsilon_p \end{pmatrix} \quad (\text{IV.13})$$

where the hybridization is carried out by  $sp\sigma$  which connects the otherwise independent s and  $p_z$  blocks. Diagonalizing this block is easy if we write bonding and antibonding combinations of s and  $p_z$  orbitals. The bonding combinations are

$$\begin{cases} (|s^{(1)}\rangle + |s^{(2)}\rangle) + (|p_z^{(1)}\rangle - |p_z^{(2)}\rangle) \\ (|s^{(1)}\rangle + |s^{(2)}\rangle) - (|p_z^{(1)}\rangle - |p_z^{(2)}\rangle) \end{cases} \quad (\text{IV.14a})$$

and the antibonding are

$$\begin{cases} (|s^{(1)}\rangle - |s^{(2)}\rangle) + (|p_z^{(1)}\rangle + |p_z^{(2)}\rangle) \\ -( |s^{(1)}\rangle - |s^{(2)}\rangle) + (|p_z^{(1)}\rangle + |p_z^{(2)}\rangle) \end{cases} \quad (\text{IV.14b})$$

Since there are no matrix elements between these bonding and antibonding combinations (Harrison 1980), the matrix  $U$  whose columns are the coefficients of these combinations block diagonalizes  $H_{sp_z}$  through the transformation  $U^{-1}H_{sp_z}U$ . More specifically the matrix  $U$  is given by

$$U = \frac{1}{2} \begin{pmatrix} 1 & 1 & 1 & -1 \\ 1 & 1 & -1 & 1 \\ 1 & -1 & 1 & 1 \\ -1 & 1 & 1 & 1 \end{pmatrix} \quad (\text{IV.15})$$

and its inverse is easily found to be  $U^{-1} = \frac{1}{2} U$ . Let us call  $E_b^s$  and  $E_b^p$  the bonding energies  $\epsilon_s - |ss\sigma|$  and  $\epsilon_p - |pp\sigma|$  respectively, and  $E_a^s$  and  $E_a^p$  the antibonding energies  $\epsilon_s + |ss\sigma|$  and  $\epsilon_p + |pp\sigma|$ . Despite  $pp\sigma > 0$  we are using the absolute value so that no confusion may arise. It is then easy to see that

$$U^{-1}H_{sp_z}U = \quad (\text{IV.16})$$

$$\frac{1}{2} \begin{pmatrix} E_b^s + E_b^p - 2(sp\sigma) & E_b^s - E_b^p & & 0 \\ E_b^s - E_b^p & E_b^s + E_b^p + 2(sp\sigma) & & 0 \\ & & E_a^s + E_a^p + 2(sp\sigma) & -E_a^s + E_a^p \\ 0 & & -E_a^s + E_a^p & E_a^s + E_a^p - 2(sp\sigma) \end{pmatrix}.$$

The resultant quadratic equations can then be solved and the final eigenvalues are

of the molecular Hamiltonian are

$$\frac{E_b^s + E_b^p}{2} \pm \sqrt{sp\sigma^2 + \left[ \frac{E_b^s - E_b^p}{2} \right]^2}$$
$$\frac{E_a^s + E_a^p}{2} \pm \sqrt{sp\sigma^2 + \left[ \frac{E_a^s - E_a^p}{2} \right]^2}$$

(IV.17)

$$\epsilon_p \pm pp\pi$$

and

$$\epsilon_p \pm pp\pi$$

where the last two sets correspond to bonding and antibonding combinations of the  $p_x$  and  $p_y$  orbitals. With these eigenvalues which give the position of the  $\delta$ -functions one can easily write an expression for the structural energy as we did in the pure cases.

## Appendix V: LCAO Solution for the Dimer (Pure d and sd)

The LCAO molecular Hamiltonian of a homopolar molecule with s and d atomic orbitals per site is considered in this appendix. The 5 d-orbitals have the following symmetry (Pettifor 1983)

Orbital	Symmetry	
1	xy	
2	yz	
3	zx	(V.1)
4	$(x^2 - y^2)/2$	
5	$(3z^2 - r^2)/(2 \cdot 3^{1/2})$	

The procedure follows the same lines as in appendix IV for the sp-molecule. We start with d-orbitals only (the pure d case) and later allow sd hybridization to occur. The pure s case has already been considered in appendix IV.

### IV.1 The pure d case

Taking the z-axis along the molecular bond the Hamiltonian matrix elements are of the form (Slater and Koster 1954):  $H_{11} = H_{44} = dd\delta$ ,  $H_{22} = H_{33} = dd\pi$ , and  $H_{55} = dd\sigma$ . There are no matrix elements between any other combination and therefore the molecular Hamiltonian is block diagonal with five independent 2x2 blocks of the form

$$\begin{pmatrix} \epsilon_d & h_i \\ h_i & \epsilon_d \end{pmatrix} \quad (V.2)$$

where  $h_i = ddi$  and  $i = \sigma, \pi, \text{ or } \delta$ . The  $\delta$  and  $\pi$  blocks are seen to be doubly degenerate. The eigenvalues are then easily found to be  $E_i = \epsilon_d \pm h_i$  which immediately leads to the band energy (see appendix IV).

## V.2 sd-orbitals case

There are now six valence states for each atom and a finite  $\epsilon_{sd}$  separation allows for sd hybridization. Fortunately only the  $\sigma$ -states are coupled, the  $\delta$  and  $\pi$  states forming again 2x2 blocks as in the pure case. The coupled  $\sigma$ -states form a 4x4 block as in the sp case, i.e.,

$$H_{sd_5} = \begin{pmatrix} \epsilon_s & ss\sigma & 0 & sd\sigma \\ ss\sigma & \epsilon_s & sd\sigma & 0 \\ 0 & sd\sigma & \epsilon_d & dd\sigma \\ sd\sigma & 0 & dd\sigma & \epsilon_d \end{pmatrix} \quad (V.3)$$

where  $|d_5\rangle = |3(z^2 - r^2)\rangle$ . In order to block diagonalise  $H_{sd_5}$  we write the following bonding combinations (notice the difference in sign compared with the sp combinations)

$$\begin{cases} (|s^{(1)}\rangle + |s^{(2)}\rangle) + (|d_5^{(1)}\rangle + |d_5^{(2)}\rangle) \\ (|s^{(1)}\rangle + |s^{(2)}\rangle) - (|d_5^{(1)}\rangle + |d_5^{(2)}\rangle) \end{cases} \quad (V.4a)$$

and antibonding combinations

$$\begin{cases} (|s^{(1)}\rangle - |s^{(2)}\rangle) + (|d_5^{(1)}\rangle - |d_5^{(2)}\rangle) \\ (|s^{(1)}\rangle - |s^{(2)}\rangle) - (|d_5^{(1)}\rangle - |d_5^{(2)}\rangle) \end{cases} \quad (V.4b)$$

As in the  $sp$ -case there are no matrix combinations between these combinations and therefore the  $4 \times 4$  block above is reduced to two  $2 \times 2$  blocks through the transformation  $U^{-1}H_{sd_5}U$  where

$$U = \frac{1}{2} \begin{pmatrix} 1 & 1 & 1 & 1 \\ 1 & 1 & -1 & -1 \\ 1 & -1 & 1 & -1 \\ 1 & -1 & -1 & 1 \end{pmatrix} \quad (V.5)$$

It is easy to check that  $U^{-1} = \frac{1}{2}U$ . As we did in appendix IV let us call  $E_b^s$  and  $E_b^d$  the bonding energies  $\epsilon_s - |ss\sigma|$  and  $\epsilon_d - |dd\sigma|$  respectively, and  $E_a^s$  and  $E_a^d$  the antibonding energies  $\epsilon_s + |ss\sigma|$  and  $\epsilon_d + |dd\sigma|$ . It is then easy to see that

$$U^{-1}H_{sp_z}U = \quad (V.6)$$

$$\frac{1}{2} \begin{pmatrix} E_b^s + E_b^p + 2sp\sigma & E_b^s - E_b^p & & 0 \\ E_b^s - E_b^p & E_b^s + E_b^p - 2sp\sigma & & \\ & 0 & E_a^s + E_a^p - 2sp\sigma & E_a^s - E_a^p \\ & & E_a^s - E_a^p & E_a^s + E_a^p + 2sp\sigma \end{pmatrix}$$

One can now solve the quadratic equations for the two blocks to get energy

eigenvalues with the same form as in the sp case, i.e.,

$$\frac{E_b^s + E_b^d}{2} \pm \sqrt{(sd\sigma)^2 + \left[ \frac{E_b^s - E_b^d}{2} \right]^2} \quad (\text{V.7a})$$

$$\frac{E_a^s + E_a^d}{2} \pm \sqrt{(sd\sigma)^2 + \left[ \frac{E_a^s - E_a^d}{2} \right]^2} \quad (\text{V.7b})$$

$$\epsilon_d \pm dd\pi \quad (\text{doubly degenerate}) \quad (\text{V.7c})$$

and

$$\epsilon_d \pm dd\pi \quad (\text{doubly degenerate}) \quad (\text{V.7d})$$

where the last two sets correspond to bonding and antibonding combinations of the other orbitals. These molecular levels can now be filled with electrons and the band energy evaluation carried out as done in appendix IV for the sp molecule.



## Appendix VI: LCAO Solution for the Linear Chain (Pure cases: s, p and d)

In this appendix we show how to calculate the structural energy of a linear chain for a single s-orbital on each site. The 1D type of structure we consider is actually a zig-zag chain (see text) with bond angles equal to 90 degrees. Nevertheless since the interaction between s-states is angle independent these two structures are energetically equivalent if only s-orbitals are present. The generalization to the pure p and pure d cases is trivial and we indicate how this is done.

### VI.1 The pure s case

In the linear chain the equally spaced sites lie along a straight line like

$$\begin{array}{cccccccc} \dots & \bullet & & \bullet & & \bullet & & \bullet & & \bullet & & \bullet & & \dots \\ & -3 & -2 & -1 & 0 & 1 & 2 & 3 & & & & & & \end{array}$$

where we label 0 the central site of interest. Let us recall the basic recurrence relation

$$H|v_n\rangle = b_n|v_{n-1}\rangle + a_n|v_n\rangle + b_{n+1}|v_{n+1}\rangle \quad (VI.1)$$

We shall be taking the zero of energy as the energy of the s-orbital of the isolated atom, i.e.,  $\epsilon_s = 0$  and the notation for a orbital on site n will be  $|s^{(n)}\rangle$ .

Starting with  $n = 0$  (first iteration) equation (VI.1) becomes

$$H|v_0\rangle = a_0|v_0\rangle + b_1|v_1\rangle \quad (VI.2)$$

and we define the initial vector as

$$|v_0\rangle = |s^{(0)}\rangle \quad (\text{VI.3})$$

which gives

$$H|v_0\rangle = \sum \langle s^{(m)} | H | s^{(0)} \rangle |s^{(m)}\rangle$$

and since

$$\langle s^{(m)} | H | s^{(0)} \rangle = \begin{cases} h & \text{for } m = 1 \text{ or } m = -1 \\ 0 & \text{otherwise} \end{cases}$$

where  $h = \sigma \sigma$  we have

$$H|v_0\rangle = h (|s^{(-1)}\rangle + |s^{(1)}\rangle) \quad (\text{VI.4})$$

Since  $a_n = \langle v_n | H | v_n \rangle$  we have, from (VI.3) and (VI.4),  $a_0 = 0$  and from (VI.2)

$$H|v_0\rangle = b_1 |v_1\rangle \quad (\text{VI.5})$$

Therefore  $\langle v_0 | H \cdot H | v_0 \rangle = b_1^2 \langle v_1 | v_1 \rangle = b_1^2$  and using (VI.4) assuming  $\langle s^{(m)} | s^{(n)} \rangle = \delta_{mn}$  we get

$$b_1^2 = 2 \cdot h^2 \quad (\text{VI.6})$$

and from (VI.4) and (VI.5)

$$|v_1\rangle = \frac{h}{b_1} (|s^{(-1)}\rangle + |s^{(1)}\rangle) \quad (VI.7)$$

For the next iteration ( $n = 1$ ) we have to calculate  $H|v_1\rangle$ . This gives

$$H|v_1\rangle = \frac{1}{2h} (h|s^{(-2)}\rangle + 2h|s^{(0)}\rangle + h|s^{(2)}\rangle) \quad (VI.8)$$

and therefore we get  $a_1 = \langle v_1|H|v_1\rangle = 0$ . But, from (VI.1) with  $n = 1$ ,

$$H|v_1\rangle - b_1|v_0\rangle = b_2|v_2\rangle \quad (VI.9)$$

and then, using (VI.8), (VI.6) and (VI.3) we have

$$b_2^2 = h^2 \quad (VI.10)$$

and

$$|v_2\rangle = \frac{h^2}{b_1 b_2} (|s^{(-2)}\rangle + |s^{(2)}\rangle) \quad (VI.11)$$

A third iteration is easily seen to give

$$b_3^2 = h^2 \quad (VI.12)$$

and

$$|v_3\rangle = \frac{h^3}{b_1 b_2 b_3} (|s^{(-3)}\rangle + |s^{(3)}\rangle) \quad (VI.13)$$

The symmetry of the problem then allows us to write

$$b_n^2 = h^2 \quad (\text{VI.14})$$

and

$$|v_n\rangle = \frac{h^n}{b_1 b_2 b_3 \cdots b_n} (|s^{(-n)}\rangle + |s^{(n)}\rangle) \quad (\text{VI.15})$$

Thus the resolvent  $G(E) = \langle v_0 | (E-H)^{-1} | v_0 \rangle$  is

$$G(E) = \frac{1}{E - \frac{2h^2}{E - \frac{h^2}{E - \frac{h^2}{\ddots}}}} \quad (\text{VI.16a})$$

$$= \frac{1}{E - 2t(E)} \quad (\text{VI.16b})$$

where

$$t(E) = \frac{h^2}{E - \frac{h^2}{E - \frac{h^2}{\ddots}}} \\ = \frac{h^2}{E - t(E)}$$

which gives a quadratic equation for  $t(E)$ . Rejecting the plus solution on the basis that the resolvent preserve its analytic character of the form  $E^{-1}$  when  $E \rightarrow \infty$  (see text) we have

$$t(E) = \frac{E - \sqrt{E^2 - 4h^2}}{2} \quad (\text{VI.17})$$

Therefore there is a band of allowed energies in the range  $-2|h| < E < 2|h|$  and inside this interval

$$G(E) = \frac{-i}{\sqrt{4h^2 - E^2}} \quad (VI.18)$$

Then local density of states  $n(E) = -(1/\pi) \text{Im } G(E)$  is

$$n(E) = \frac{2}{\pi} \frac{1}{\sqrt{4h^2 - E^2}} \quad -2|h| < E < 2|h| \quad (VI.19)$$

and the Fermi energy is determined by

$$\begin{aligned} N &= \int_{-2|h|}^{\epsilon_f} n(E) dE \\ &= \cos^{-1} \left[ \frac{\epsilon_f(N)}{2|h|} \right] + 2 \end{aligned}$$

which gives

$$\epsilon_f(N) = -2|h| \cos\left(\frac{N\pi}{2}\right) \quad (VI.20)$$

The band energy is easily determined from

$$\begin{aligned} E_{\text{band}} &= \int_{-2|h|}^{\epsilon_f} E n(E) d(E) \\ &= \frac{-2}{\pi} \sqrt{4h^2 - \epsilon_f^2} \end{aligned}$$

or, using (VI.20),

$$E_{\text{band}}(N) = \frac{-4|h|}{\pi} \text{sen}\left(\frac{N\pi}{2}\right) \quad (\text{VI.21})$$

which gives  $E_{\text{band}}$  as a function of band filling.

## VI.2 The pure p case

When only p orbitals are present there are no matrix elements between states with the same symmetry, i.e.,  $\langle i|H|j\rangle = 0$  if  $i \neq j$ ,  $i, j = x, y$  or  $z$ . Therefore it is only a matter of starting with  $|v_0\rangle = |i\rangle$  and follow the same steps as above for the pure s case. The local density of states is given by

$$n(E) = n_x(E) + n_y(E) + n_z(E) \quad (\text{VI.22})$$

where

$$\begin{aligned} n_x(E) &= n_y(E) \\ &= \frac{2}{\pi} \left[ 4 \cdot pp \pi^2 - E \right]^{-\frac{1}{2}} \end{aligned} \quad (\text{VI.23a})$$

and

$$n_z(E) = \frac{2}{\pi} \left[ 4 \cdot pp \sigma^2 - E \right]^{-\frac{1}{2}} \quad (\text{VI.23b})$$

where we assumed that the chain is parallel to the  $z$ -axis.

## VI.3 The pure d case

As in the previous case there are no matrix elements of the Hamiltonian between orbitals with different symmetry. Therefore

$$n(E) = \sum n_i(E) \quad (\text{VI.24})$$

where  $i = xy, yz, zx, (x^2-y^2)$  and  $(3z^2-r^2)$  (see appendix V). With the chain along the  $z$ -direction the partial densities of states are given by

$$\begin{aligned} n_{xy} &= n_{x^2-y^2} \\ &= \frac{2}{\pi} [4 \cdot dd \varrho^2 - E]^{-\frac{1}{2}} \end{aligned} \quad (\text{VI.25a})$$

$$\begin{aligned} n_{xz} &= n_{zy} \\ &= \frac{2}{\pi} [4 \cdot dd \pi^2 - E]^{-\frac{1}{2}} \end{aligned} \quad (\text{VI.25b})$$

and

$$n_{3z^2-r^2} = \frac{2}{\pi} [4 \cdot dd \sigma^2 - E]^{-\frac{1}{2}} \quad (\text{VI.25c})$$

## Appendix VII: Experimental Tables

In order to compare the theoretical structural map with experimental results, we must use the same sort of scale in both diagrams. This amounts to determining  $\epsilon_{sp}/(12 \cdot ss\sigma_{sc})$  for all the elements whose stability behaviour is expected to be described by the model. In this expression  $ss\sigma_{sc}$  is the value that this matrix element would take if the chemical element in question were crystallised in the simple cubic structure. In order to be consistent with the theoretical model we will calculate  $ss\sigma_{sc}$  by assuming that the second moments are the same for both the real lattice and the simple cubic lattice. This gives

$$6 \cdot ss\sigma_{sc}^2 = \zeta \cdot ss\sigma_{exp}^2$$

or

$$ss\sigma_{sc} = (\zeta/6)^{\frac{1}{2}} \cdot ss\sigma_{exp} \quad (\text{VII.1})$$

where  $\zeta$  is the coordination of the real structure. The value of  $ss\sigma_{exp}$  is calculated from the observed equilibrium bond length  $d$  using Harrison's  $R^{-2}$  (1980) scaling law, i.e.,

$$\begin{aligned} ss\sigma_{exp} &= -1.40 \frac{\hbar^2}{md^2} \\ &= -1.40 \frac{\hbar^2}{me^2} \frac{e^2}{2a_H} \frac{2a_H}{d^2} \end{aligned}$$

If we use atomic units i.e.,  $\hbar = 1$ , Bohr's radius  $a_H$  as the unit of length ( $a_H = \hbar^2/me^2 = 1\text{au}$ ) and the Rydberg as the unit of energy ( $1\text{Ryd} = e^2/2a_H$ ) we get



$$\begin{aligned}
ss\sigma_{\text{exp}} &= \frac{-2.80}{(d/a_H)^2} \text{Ryd} \\
&= \frac{-2.80}{d^2} \text{Ryd} \tag{VII.2}
\end{aligned}$$

where the equilibrium bond length  $d$  is measured in atomic units.

Expressions (VII.1) and (VII.2) allows us to determine  $\epsilon_{\text{sp}}/12 \cdot ss\sigma_{\text{sc}}$  from the equilibrium bond length and structure coordination. Another remark is about relativistic effects which are most important for the heavy elements and are known to increase  $sp$  separation (Christensen et al 1986). These enter into the  $\epsilon_{\text{sp}}$  calculation for the elements on the right hand side of the periodic table and are taken from Herman and Skillman (1968) tables. Those not listed by these tables are linearly interpolated within a given period. For example the increase in the  $sp$  separation for third period elements Ge and Se are 0.54 ev and 0.82 ev respectively. If we order the elements in this period from left to right as Ga, Ge, As, Se and Br a linear interpolation gives 0.4 ev, 0.68 ev and 0.96 ev for the  $sp$ -increase in Ga, As and Br respectively. We list below the relevant constants where only the  $sp$  elements with one of the structures considered in the theory are taken into account. In Groups IA and IIA only Li, Na, Be and Mg are taken because hybridization with  $d$ -bands may be too important for the other elements. The bond-lengths and stable structures are taken from Donohue (1974) and the  $\epsilon_s$  and  $\epsilon_p$  values come from Harrison (1980). Li and Na  $\epsilon_p$  values are not listed by Harrison and were therefore taken from Majewski and Vogl (1987). The value of  $ss\sigma$  for hydrogen was obtained from Slater (1963) table 4-2. Notice that our model seeks for a semi quantitative description of the relative structural trends and therefore the exact positioning of a given element in the structural map is not so important. In these tables  $Y = [(\epsilon_{\text{sp}} - \epsilon_{\text{rel}})/(12 \cdot ss\sigma_{\text{sc}})] \cdot 10/\pi$  and the energy is given in electrons volts.

	Group IA			Group IIA	
	H	Li	Na	Be	Mg
$-\epsilon_s$	13.6	5.48	5.13	8.17	6.86
$-\epsilon_p$	3.4	1.04	0.53	4.15	2.99
$\epsilon_{rel}$	0.0	0.0	0.0	0.0	0.0
$-\sigma_{sc}$	1.58	1.56	1.06	2.95	1.47
$-Y$	1.57	0.74	1.10	0.36	0.69

Table VII.1 - Constants for groups IA and IIA used to draw the sp-structural map. Energies given in electron-volts.

	Group IIIB		Group VB
	Al	Tl	N
$-\epsilon_s$	10.11	9.92	23.04
$-\epsilon_p$	4.86	4.61	11.47
$\epsilon_{rel}$	0.14	2.72	0.0
$-\sigma_{sc}$	1.84	1.28	3.80
$-Y$	0.76	1.53	0.79

Table VII.2 - Constants for groups IIIB and VB used in the sp-structural map. Energies given in electron-volts.

	Group IVB				
	C	Si	Ge	Sn	Pb
$-\epsilon_s$	17.52	13.55	14.38	12.50	12.07
$-\epsilon_p$	8.97	6.52	6.36	5.94	5.77
$\epsilon_{rel}$	0.0	0.14	0.54	1.09	3.13
$-\sigma_{sc}$	3.67	1.57	1.45	1.1	1.23
$-Y$	1.88	1.16	1.46	1.67	1.81

Table VII.3 - Constants for group IVB used in the sp-structural map. Energies given in electron-volts.

Group VIB

	O	S	Se	Te	Po
$-\epsilon_s$	29.14	20.80	20.32	17.11	16.21
$-\epsilon_p$	14.13	10.27	9.53	8.59	8.19
$\epsilon_{rel}$	0.0	0.140	0.82	1.63	3.94
$-\sigma_{sc}$	3.29	1.46	1.09	0.77	0.94
$-Y$	1.16	1.74	2.31	2.65	2.59

Table VII.4 - Constants for group VIB used in the sp-structural map. Energies given in electron-volts.

Group VIIB

	F	Cl	Br	I
$-\epsilon_s$	35.80	24.63	23.35	19.42
$-\epsilon_p$	16.99	12.31	11.20	9.97
$\epsilon_{rel}$	0.0	0.14	0.96	1.90
$\sigma_{sc}$	1.96	1.11	0.84	0.59
$-Y$	2.15	2.39	2.91	3.22

Table VII.5 - Constants for group VIIB used in the sp-structural map. Energies given in electron-volts.

## Appendix VIII: Dimer Approximated to a Fixed Number of Moments

In this appendix we show how to calculate the dimer levels approximated to a fixed number of exact moments of the density of states. We calculate the weights  $w_i$  and  $\delta$ -function positions  $\lambda_i$  in the expansion

$$n(E) = \sum_i w_i \delta(E - \lambda_i) \quad (\text{VIII.1})$$

from the tridiagonal hamiltonian suitably truncated to give only a fixed number of exact moments. The moments corresponding to  $n(E)$  are given by

$$\begin{aligned} \mu_n &= \int E^n n(E) dE \\ &= \sum w_i \lambda_i^n \end{aligned} \quad (\text{VIII.2})$$

where  $n = 0, 1, \dots$ , and the idea is to invert this linear system with respect of  $w_i$ . Notice that both the moments and the  $\delta$ -function positions are known from the tridiagonal matrix. The former are given by  $\mu_n = \text{Tr}[\mathcal{H}^n]$  and the later are the eigenvalues of the tridiagonal hamiltonian  $\mathcal{H}$ .

VIII.1 The solution for  $n = 4$ .

We consider the following system of equations

$$A + B + D + G = \mu_0 \quad (\text{VIII.3a})$$

$$Aa + Bb + Dd + Gg = \mu_1 \quad (\text{VIII.3b})$$

$$Aa^2 + Bb^2 + Dd^2 + Gg^2 = \mu_2 \quad (\text{VIII.3c})$$

$$Aa^3 + Bb^3 + Dd^3 + Gg^3 = \mu_3 \quad (\text{VIII.3d})$$

where the capital (lower) case play the role of the weights (eigenvalues). Multiplying the first of these equations by  $-a$ ,  $-a^2$  and  $-a^3$  and adding to (VIII.3b), (VIII.3c) and (VIII.3d) respectively we get

$$(b-a)B + (d-a)D + (g-a)G = \mu_1 - a\mu_0 \quad (\text{VIII.4a})$$

$$(b^2-a^2)B + (d^2-a^2)D + (g^2-a^2)G = \mu_2 - a^2\mu_0 \quad (\text{VIII.4b})$$

$$(b^3-a^3)B + (d^3-a^3)D + (g^3-a^3)G = \mu_3 - a^3\mu_0 \quad (\text{VIII.4c})$$

We now multiply (VIII.4a) first by  $-(b+a)$  and then by  $-(b^2+ab+a^2)$  and add to (VIII.4b) and (VIII.4c) respectively. After some algebraic manipulations we get

$$(d-a)(d-b)D + (g-a)(g-b)G = \mu_2 - a^2\mu_0 - [(\mu_1 - a\mu_0)(b+a)] \quad (\text{VIII.5a})$$

$$\begin{aligned} (d+b+a)(d-a)(d-b)D + (g+b+a)(g-b)(g-a)G \\ = \mu_3 - a^3\mu_0 - [(\mu_1 - a\mu_0)(b^2+ab+a^2)] \end{aligned} \quad (\text{VIII.5b})$$

Proceeding in the same manner we now eliminate D from these equations. The final result is

$$G = \frac{\mu_3 - (d+b+a)\mu_2 + (bd+ad+ab)\mu_1 - (abd)\mu_0}{(g-b)(g-a)(g-d)} \quad (\text{VIII.6})$$

and the expressions for the other weights can be obtained by symmetry. For example A is given by (VIII.6) with the substitution  $g \rightleftharpoons a$ , i.e.,

$$A = \frac{\mu_3 - (d+b+g)\mu_2 + (bd+gd+gb)\mu_1 - (gbd)\mu_0}{(a-b)(a-g)(a-d)} \quad (\text{VIII.7})$$

and similarly for B and D.

VIII.2 The dimer solution up to  $\mu_3$  for  $\epsilon_{sp} = 0$ .

Up to  $\mu_3$  the tridiagonal hamiltonian is the  $2 \times 2$  matrix (see appendix I)

$$\begin{bmatrix} a_0 & b_1 \\ b_1 & a_1 \end{bmatrix}$$

Since we fix the center of the gravity of the band to zero (i.e.,  $\epsilon_s + 3\epsilon_p = 0$ ) we have  $\epsilon_s = \epsilon_p = 0$ . Therefore, since there are no triangular paths in the dimer structure all the odd moments vanish which implies that  $a_i = 0$  for all  $i$ . The eigenvalues are then given by  $\pm b_1$  and the weights are determined by

$$A + B = \mu_0 \quad (\text{VIII.8a})$$

$$Aa + Bb = \mu_1 \quad (\text{VIII.8b})$$

which gives

$$A = \frac{\mu_1 - b\mu_0}{a - b} \quad (\text{VIII.9a})$$

and

$$B = \frac{\mu_1 - a\mu_0}{b - a} \quad (\text{VIII.9b})$$

which is a special case of the solution for the system (VIII.3). Since  $\mu_0 = 1$  and  $\mu_1 = a_0 = 0$ ,  $a = -b_1$  and  $b = b_1$  we have  $A = B = 1/2$ . Taking into account spin degeneracy we see the weights on each  $\delta$ -function are equal to one. In the sp dimer there are four partial densities of states (one s and three p states) with the following values for  $b_1$  (notice that  $\mu_2 = a_0^2 + b_1^2 = b_1^2$ ) :

$$\text{s-partial DOS} \quad b_1^2 = ss\sigma^2 + sp\sigma^2 \quad (\text{VIII.10a})$$

$$\text{z-partial DOS} \quad b_1^2 = pp\sigma^2 + sp\sigma^2 \quad (\text{VIII.10b})$$

$$\text{x-partial DOS} \quad b_1^2 = pp\pi^2 \quad (\text{VIII.10c})$$

$$\text{y-partial DOS} \quad b_1^2 = pp\pi^2 \quad (\text{VIII.10d})$$

all of which with unity weight. In these expressions the z-axis was defined in the direction of the molecular bond.

VIII.3 The dimer solution up to  $\mu_4$  and  $\mu_5$  for  $\epsilon_{sp} = 0$ .

The dimer approximate solution keeping only the moments up to  $\mu_4$  is the same as if we kept the moments up to  $\mu_5$ . This is so because the 3x3 tridiagonal hamiltonian, namely,

$$\begin{bmatrix} a_0 & b_1 & 0 \\ b_1 & a_1 & b_2 \\ 0 & b_2 & a_2 \end{bmatrix} \quad (\text{VIII.11})$$

involves  $a_2$  and the knowledge of this parameter implies the knowledge of  $\mu_5$ . The eigenvalues of this matrix with  $a_i = 0$  are given by

$$\lambda_1 = 0 \quad (\text{VIII.12a})$$

$$\lambda_2 = -\lambda_3 = [b_1^2 + b_2^2]^{\frac{1}{2}} \quad (\text{VIII.12b})$$

The weights can be calculated in the same spirit as in the previous case using the solution of (VIII.3) for  $n = 3$  which gives

$$w_1 = \frac{1}{2} \frac{b_2^2}{b_1^2 + b_2^2} \quad (\text{VIII.13a})$$

$$w_2 = w_3 = \frac{1}{2} \frac{b_1^2}{b_1^2 + b_2^2} \quad (\text{VIII.13b})$$

These expressions have to be multiplied by two for spin degeneracy. Notice that  $b_1^2$  is given by (VIII.10) and  $b_2^2$  is determined from  $\mu_4$  by noticing that

$$\mu_4 = b_1^4 + b_1^2 b_2^2$$

from the chain model with  $a_i = 0$ . Also notice that in the case of the non-hybridized  $x$  and  $y$  states  $\mu_4 = pp\pi^4$  and therefore  $b_2^2 = 0$  (see (VIII.10c,d) from which  $b_1^2 = pp\pi^2$ ) which implies that there is no occupancy of the  $E = 0$  level of the  $\pi$ -orbitals.



#### VIII.4 The dimer solution up to $\mu_6$ for $\epsilon_{sp} = 0$ .

Up to  $\mu_6$  we add  $b_3$  as part of our knowledge about the system and, in order to have all the elements of the resulting  $4 \times 4$  hamiltonian,  $a_3$  is also assumed to be known. Since, however,  $4 \times 4$  is the dimension of the biggest block (the  $sp$ -block) of the exact hamiltonian, we are now provided with the full information about the system. The solution at this level is therefore exact and is derived in detail in appendix V.

## Appendix IX: The Double Band Gap

In this appendix we give some details on how to compute the terminating function for a density of states with two gaps in the spectra, which will be used elsewhere in this work. The basic reference is Turchi et al (1982) to which we refer the interested reader for details. The fully specification of the terminator  $g_n(E)$  using Turchi's approach is not difficult but rather messy and this is the main reason why we devote this appendix to it. Another reason is that we do present a double band gap DOS, namely the one for a one dimensional zig-zag chain (see chapter 4).

Notice that the first step towards appending a terminator in the continued fraction is the determination of the band and gap edges, i.e.,  $E_i$  with  $i = 2 \cdot q + 2$ , where  $q$  is the number of gaps in the DOS. This can be done from the continued fraction coefficients provided that a sufficient number of pairs is given so that the asymptotic regime is well established. About ten exact levels are enough to describe a single gap but, as expected, a higher number is required to describe two gaps (typically more than 15 – Turchi et al 1982). Beer's approach can be extended to allow the computation of the edges in the double band gap case by imposing that the Green's function diverges simultaneously at all edges. However we decided not to undertake this task in the present work because it could get too involved and was not really necessary for our purposes.

Let's draw the general lines towards computing a double band gap DOS as suggested by Turchi et al (1982). We first define a set of parameters  $A_i$ ,  $i=1, 2, \dots, 6$ , which are linked to the gap edges  $E_i$ ,  $i=1, 2, \dots, 6$  in a nonlinear fashion (as in appendix II for the single band gap). The function in the terminator whose square root gives rise to the relevant cuts in the real axis is now generalized to

$$X(E) = \prod_i^{2q+2} (E - E_i) \quad (IX.1)$$

where  $q = \hat{2}$  is the number of gaps. The  $A_i$ 's are defined via

$$\sqrt{X(E)} \xrightarrow{E \rightarrow \infty} E^3(1 + A_1/E + \cdots + A_m/E^m + \cdots)$$

so that

$$\begin{aligned} X(E) &\xrightarrow{E \rightarrow \infty} E^6(1 + A_1/E + \cdots)(1 + A_1/E + \cdots) \\ &= E^6 \left( (1 + 2A_1/E + (2A_2 + A_1^2)/E^2 + (2A_3 + 2A_1A_2)/E^3 + \right. \\ &\quad (2A_4 + 2A_1A_3 + A_2^2)/E^4 + (2A_5 + 2A_1A_4 + 2A_2A_3)/E^5 + \\ &\quad \left. (2A_6 + 2A_1A_5 + 2A_2A_4 + A_3^2)/E^6 + O(1/E^7) \right) . \end{aligned}$$

On the other hand

$$\begin{aligned} X(E) &= (E - E_1)(E - E_2) \cdots (E - E_6) \\ &= E^6 + [-\sum E_i]E^5 + \left[ \sum_{i < j} E_i E_j \right] E^4 + \left[ -\sum_{i < j < k} E_i E_j E_k \right] E^3 + \\ &\quad \left[ \sum_{i < j < k < l} E_i E_j E_k E_l \right] E^2 + \left[ -\sum_{i < j < k < l < m} E_i E_j E_k E_l E_m \right] E^1 \\ &\quad + \left[ \sum_{i < j < k < l < m < n} E_i E_j E_k E_l E_m E_n \right] E^0 . \end{aligned}$$

Identification of terms of the same order in the last two expressions gives

$$A_1 = (-\sum E_i) / 2$$

$$A_2 = ( \sum_{i<j} E_i E_j - A_1^2 ) / 2$$

$$A_3 = (- \sum_{i<j<k} E_i E_j E_k - 2A_1 A_2) / 2$$

$$A_4 = ( \sum_{i<j<k<l} E_i E_j E_k E_l - 2A_1 A_3 - A_2^2 ) / 2 \quad (\text{IX.2})$$

$$A_5 = (- \sum_{i<j<k<l<m} E_i E_j E_k E_l E_m - 2A_1 A_4 - 2A_2 A_3) / 2$$

$$A_6 = ( \sum_{i<j<k<l<m<n} E_i E_j E_k E_l E_m E_n - 2A_1 A_5 - 2A_2 A_3 - A_3^2 )$$

which give the  $A$ 's as a function of the band and gap edges.

Let us now turn to the terminating function itself. The appropriate terminator when the last known pair of exact coefficients is  $(a_n, b_n)$  is given by

$$g_n(E) = \frac{2\alpha_n(E)}{\nu_{n-1}(E) + \sqrt{X(E)}} \quad (\text{IX.3})$$

where

$$\alpha_n(E) = (E - \alpha_n^1) \cdots (E - \alpha_n^n) \quad (\text{IX.4})$$

The parameters  $\alpha_n^1$  and  $\alpha_n^2$  are given as the solutions of a set of two coupled equations which here are put together into a single quadratic equation, i.e.,

$$x^2 + (A_1 + a_n)x + (a_n^2 + b_n^2 + b_{n+1}^2 + A_1 a_n + A_2) = 0 \quad (\text{IX.5})$$

whose roots are either  $\alpha_n^1$  or  $\alpha_n^2$ . In order to specify this equation completely one has to give  $A_1, A_2$  and  $b_{n+1}^2$ . These can be calculated from recurrence relations, i.e.,

$$\begin{aligned} a_n^3 + 2a_n(b_n^2 + b_{n+1}^2) + a_{n+1}b_{n+1}^2 + a_{n-1}b_n^2 + A_1(a_n^2 + b_n^2 + b_{n+1}^2) + A_2 a_n + A_3 &= 0 \\ 2b_{n-1}^2 b_n^2 b_{n+1}^2 + A_4(a_{n-1}a_n - b_n^2) - A_5(a_{n-1} + a_n) + A_6 &= 0 \end{aligned} \quad (\text{IX.6})$$

which involve exact coefficients in the asymptotic region. We still have to specify the polynomial  $\nu_{n-1}(E)$  appearing in the terminating function. This is given by

$$\nu_{n-1}(E) = E^3 + A_1 E^2 + A_2 E + A_3 + 2b_n^2(E + a_{n-1} + a_n + A_1) \quad (\text{IX.7})$$

The general idea for the computation of  $g_n(E)$  as suggested by Turchi et al (op.cit.) is then the following: given enough (exact) coefficients  $(a_i, b_i)$ ,  $i=0, 1, \dots, n$ , to characterize the asymptotic regime one can use (IX.6) to calculate the  $A$ 's and therefore the band edges by inverting (IX.2). Since  $b_{n+1}$  also follows from (IX.6) one can go back to (IX.5) and determine  $\alpha_n^1$  and  $\alpha_n^2$  which leads to the knowledge of  $\alpha_n(E)$  in (IX.4). Also, given the coefficients and the  $A$ 's,  $\nu_{n-1}(E)$  is completely specified by (IX.7). Thus the terminating function is fully known and can therefore be inserted into the corresponding level in the continued fraction (see appendix II) which then allows the computation of the DOS. Unfortunately the method is difficult to be carried out in practice, particularly for the determination of the edges, which is aggravated if not enough coefficients are available.

However, the difficulty here is the determination of the band and gap

edges, which is inaccurate when the number of coefficients available is not enough to characterize the asymptotic region. Thus, provided that the  $E_i$ 's are known a priori from some other source, there is no need to have a completely settled asymptotic regime and sensible densities of states can be computed with, say, 10 to 15 levels of exact recursion. In chapter 4 we will come across a linear structure with two gaps in the spectrum of energy. In order to exhibit the plot of the corresponding DOS we appealed to a very naive and simple method for determining the gap and band edges: we simply read them from the plot of the square root terminated DOS. From our experience with the recursion method we realized that the error involved in doing this is quite small and provided one is not particularly interested in an accurate determination of the band gaps, it makes no real difference either to the overall shape of the DOS or to the integrated quantities.

Assuming that the band and gaps edges are known one can go along the following steps towards computing a double band gap DOS. First determine the  $A$ 's from (IX.2) and  $b_{n+1}$  from the first of equations (IX.6), i.e.,

$$b_{n+1}^2 = - \frac{A_4(a_{n-1}a_n - b_n^2) - A_5(a_{n-1} + a_n) + A_6}{2b_{n-1}^2 b_n^2} \quad . \quad (\text{IX.8})$$

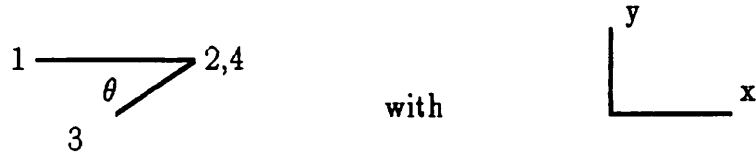
Therefore  $\alpha_n^1$  and  $\alpha_n^2$  can be calculated as the roots of (IX.5) which inserted in (IX.4) gives  $\alpha_n(E)$  for  $q=2$ , i.e.,

$$\alpha_n(E) = (E - \alpha_n^1)(E - \alpha_n^2) \quad . \quad (\text{IX.9})$$

Since  $\nu_{n-1}(E)$  is totally specified by giving the  $E_i$ 's and the  $A$ 's, the terminating function  $g_n(E)$  is therefore completely known.

## Appendix X: Fourth Moment for Zig-Zag type of Path

In this appendix we evaluate the fourth moment corresponding to the following path in the  $xy$ -plane



as a function of the bond angle  $\theta$ , for the case of pure  $p$  symmetry. The general form of the 4th moment is

$$\mu_4 = \sum_{\alpha, \beta, \gamma, \delta} \langle 1\alpha | H | 2\beta \rangle \langle 2\beta | H | 3\gamma \rangle \langle 3\gamma | H | 4\delta \rangle \langle 4\delta | H | 1\alpha \rangle \quad (\text{X.1})$$

where  $\alpha$ ,  $\beta$ ,  $\gamma$  and  $\delta$  represent the orbitals  $p_x$ ,  $p_y$  and  $p_z$ .

Since the sites are occupied only by  $p$  orbitals, we must have  $\beta = \alpha$  and  $\delta = \alpha$ , otherwise the first and/or the last matrix elements in this expression would be zero. This means that the orbitals at sites 1, 2 and 4 (this site happens to be the same as site 2 for this kind of path) must be the same. Therefore one can write (X.1) as

$$\mu_4 = \sum_{\alpha, \beta} \langle 1\alpha | H | 2\alpha \rangle^2 \langle 2\alpha | H | 3\gamma \rangle^2 \quad (\text{X.2})$$

We will now write the unity vector  $\hat{R}$  that points from site 3 to site 2 in terms of the bond angle, ie  $\hat{R} = l\hat{i} + m\hat{j}$  where  $l = \cos\theta$ ,  $m = \sin\theta$ , and  $\hat{i}$  and  $\hat{j}$  are the unity vectors in the direction of the x-axis and the y-axis respectively. If we now use Slater and Koster relations (Slater and Koster, 1954) or either simply decompose the orbitals in the directions parallel and perpendicular to  $\hat{R}$  we can write down the several terms appearing in (X.2). They are

$$\begin{array}{c} |x\rangle \\ \text{---} \\ |x\rangle \end{array} \begin{array}{c} |x\rangle \\ \text{---} \\ \diagup \\ |x\rangle \end{array} = pp\sigma^2 [l^2 pp\sigma + (1-l^2)pp\pi]^2$$

$$\begin{array}{c} |x\rangle \\ \text{---} \\ |y\rangle \end{array} \begin{array}{c} |x\rangle \\ \text{---} \\ \diagup \\ |y\rangle \end{array} = pp\sigma^2 [lm pp\sigma - lm pp\pi]^2$$

$$\begin{array}{c} |y\rangle \\ \text{---} \\ |y\rangle \end{array} \begin{array}{c} |y\rangle \\ \text{---} \\ \diagup \\ |y\rangle \end{array} = pp\pi^2 [m^2 pp\sigma + (1-m^2)pp\pi]^2$$

$$\begin{array}{c} |y\rangle \\ \text{---} \\ |x\rangle \end{array} \begin{array}{c} |y\rangle \\ \text{---} \\ \diagup \\ |x\rangle \end{array} = pp\pi^2 [lm pp\sigma - lm pp\pi]^2$$

and

$$\begin{array}{c} |z\rangle \\ \text{---} \\ |z\rangle \end{array} \begin{array}{c} |z\rangle \\ \text{---} \\ \diagup \\ |z\rangle \end{array} = pp\pi^4$$



Putting all together we get

$$\begin{aligned} \mu_4 &= \rho\rho\sigma^2 \left[ l^2\rho\rho\sigma^2 + (1-l^2)\rho\rho\pi^2 \right] + \\ &\quad \rho\rho\pi^2 \left[ (1-l^2)\rho\rho\sigma^2 + l^2\rho\rho\pi^2 \right] + \rho\rho\pi^4 \end{aligned} \tag{X.3}$$

which is the expression we have been looking for.

## Appendix XI: Moments of $\Delta E_{\text{band}}$ at Constant Band Filling

In this appendix we show how to derive a relation between the moments of the band energy difference between two structures at constant band filling and the moments of the difference in the density of states (see Turchi and Ducastelle 1985). One starts with the band energy for structure  $i$  which is written as

$$E_{b_i}(x) = \int^x t \rho_i(t) dt \quad . \quad (\text{XI.1})$$

and look for an expression for  $\Delta E_b(x_1, x_2) = E_{b_2}(x_2) - E_{b_1}(x_1)$  under the constraint that the band filling is the same for structures 1 and 2 at the Fermi energies  $x_1$  and  $x_2$  respectively, i.e.,

$$\int^{x_1} \rho_1(t) dt = \int^{x_2} \rho_2(t) dt \quad . \quad (\text{XI.2})$$

The band energy difference can be written as

$$\begin{aligned} \Delta E_b(x_1, x_2) &= \int^{x_2} t \rho_2(t) dt - \int^{x_1} t \rho_1(t) dt \\ &= \int^{x_2} t \Delta \rho(t) dt - \int_{x_2}^{x_1} t \rho_1(t) dt \end{aligned}$$

where  $\Delta \rho = \rho_2 - \rho_1$ . To first order in  $\Delta x = x_2 - x_1$  the second integral can be approximated by  $-x_2 \rho_1(x_2) \Delta x$  which gives

$$\Delta E_b(x_1, x_2) \simeq x_2 \rho_1(x_2) \Delta x + \int^{x_2} t \Delta \rho(t) dt \quad . \quad (\text{XI.3})$$

In the same way one can write an approximate expression for the charge conservation expressed in (XI.2), namely,

$$0 \simeq \rho_1(x_2)\Delta x + \int^{x_2} \Delta\rho(t) dt$$

which can be inserted in (XI.3) to give

$$\Delta E_b(x) \simeq \int^x t \Delta\rho(t) dt - x \int^x \Delta\rho(t) dt \quad (\text{XI.4})$$

where  $x = x_1$  or  $x_2$ . The first integral can be done by parts which leads to

$$\begin{aligned} \Delta E_b(x) &\simeq - \int^x d\epsilon \int^\epsilon \Delta\rho(t) dt \\ &\simeq - \int^x d\epsilon \Delta N(\epsilon) \end{aligned} \quad (\text{XI.5})$$

where  $\Delta N(\epsilon)$  is the difference in the number of electrons at energy  $\epsilon$ .

The moments of the band energy are defined by

$$\mu_n(E_b) = \int_{-\infty}^{+\infty} t^n E_b(t) dt$$

and then

$$\mu_n(\Delta E_b) = \int_{-\infty}^{+\infty} t^n \Delta E_b(t) dt$$

This expression can be integrated by parts giving

$$\begin{aligned}\mu_n(\Delta E_b) &= \frac{-1}{n+1} \int_{-\infty}^{+\infty} dt t^{n+1} \frac{d}{dt} [\Delta E_b(t)] \\ &\simeq \frac{1}{n+1} \int_{-\infty}^{+\infty} dt t^{n+1} \int^t \Delta \rho(x) dx\end{aligned}$$

where we used (XI.5) for  $\Delta E_b(t)$ , i.e., we are evaluating  $\mu_n(\Delta E_b)$  at constant band filling. After another integration by parts we get

$$\mu_n(\Delta E_b) \simeq \frac{-1}{(n+1)(n+2)} \int_{-\infty}^{+\infty} t^{n+2} \Delta \rho(t) dt$$

or

$$\mu_n(\Delta E_b) \simeq \frac{-1}{(n+1)(n+2)} \mu_n(\Delta \rho) \quad (\text{XI.6})$$

which is the expression we were looking for.

## Appendix XII: DOS for the AB Compounds ( $\epsilon_{sp}^A = \epsilon_{sp}^B = 0$ )

In this appendix we show the densities of states for the AB compounds corresponding to the case when the pair potentials are proportional to the square of the hopping integrals ( $h_{pp} \propto h_{bond}^2$ ) described in chapter 6. Here the parameters are given by  $\epsilon_{sp}^A = \epsilon_{sp}^B = 0$  and  $\Delta = 0, 1, 2$  and 3. Connected spectra are terminated with the square root terminator and for single band gap DOS the termination of Turchi et al is used. In both cases Beer and Pettifor (Beer 1985) optimized technique is used for the calculation of band edges. The band-widths (band-gaps) have been increased (decreased) by factors  $\alpha$  and  $\beta$  (see chapter 2). These parameters along with the number of exact moments are given below. Whenever the DOS for both sites are shown, the top one corresponds to the A site (highest band), the middle one to the B site (lowest band) and the bottom DOS is the DOS per formula unit (i.e., for both sites). In this case the integrated DOS is also shown, with the readings in the vertical axis having to be multiplied by a factor of eight. Notice that for  $\epsilon_{sp}^A = \epsilon_{sp}^B$  and  $\Delta = 0$  there is no need to show the DOS for each site as they are equal (except for NiAs).

Table XII.1 ( $\Delta = 0$ )

	NaCl	ZnS (cub)	ZnS (hex)	NiAs (1st)	NiAs (2nd)	CsCl
2L	18 (18)	18 (18)	18 (18)	18 (18)	18 (18)	18 (18)
$\alpha$	3 (3)	3 (3)	3 (3)	3 (3)	3 (3)	3 (3)
$\beta$	3 (3)	3 (3)	3 (3)	3 (3)	3 (3)	3 (3)

Data for figure XII.1. The number in brackets corresponds to the B site and 2L stands for the number of exact moments. For NiAs the parameters are shown both for first neighbours only (1st) and first plus second neighbours (2nd).

Table XII.2 ( $\Delta = 1$ )

	NaCl	ZnS (cub)	ZnS (hex)	NiAs (1st)	NiAs (2nd)	CsCl
2L	20 (20)	18 (18)	18 (18)	18 (18)	18 (20)	18 (18)
$\alpha$	3 (3)	3 (3)	3 (3)	2.9 (3)	3 (3)	3 (3)
$\beta$	3 (3)	3 (3)	3 (3)	3 (2.9)	3 (3)	3 (3)

Data for figure XII.2. Same remarks as for table XII.1.

Table XII.3 ( $\Delta = 2$ )

	NaCl	ZnS (cub)	ZnS (hex)	NiAs (1st)	NiAs (2nd)	CsCl
2L	20 (20)	18 (18)	18 (18)	18 (18)	18 (20)	20 (20)
$\alpha$	3 (1.8)	3 (3)	3 (3)	1.0 (3)	3 (3)	3 (3)
$\beta$	1.8 (3)	3 (3)	3 (3)	3 (1.0)	3 (3)	3 (3)

Data for figure XII.3. Same remarks as for table XII.1.

Table XII.4 ( $\Delta = 3$ )

	NaCl	ZnS (cub)	ZnS (hex)	NiAs (1st)	NiAs (2nd)	CsCl
2L	20 (20)	18 (18)	18 (18)	18 (18)	18 (20)	16 (20)
$\alpha$	3 (1.5)	3 (3)	3 (3)	0.8 (3)	3 (3)	3 (3)
$\beta$	1.5 (3)	3 (3)	3 (3)	3 (0.8)	3 (3)	3 (3)

Data for figure XII.4. Same remarks as for table XII.1.

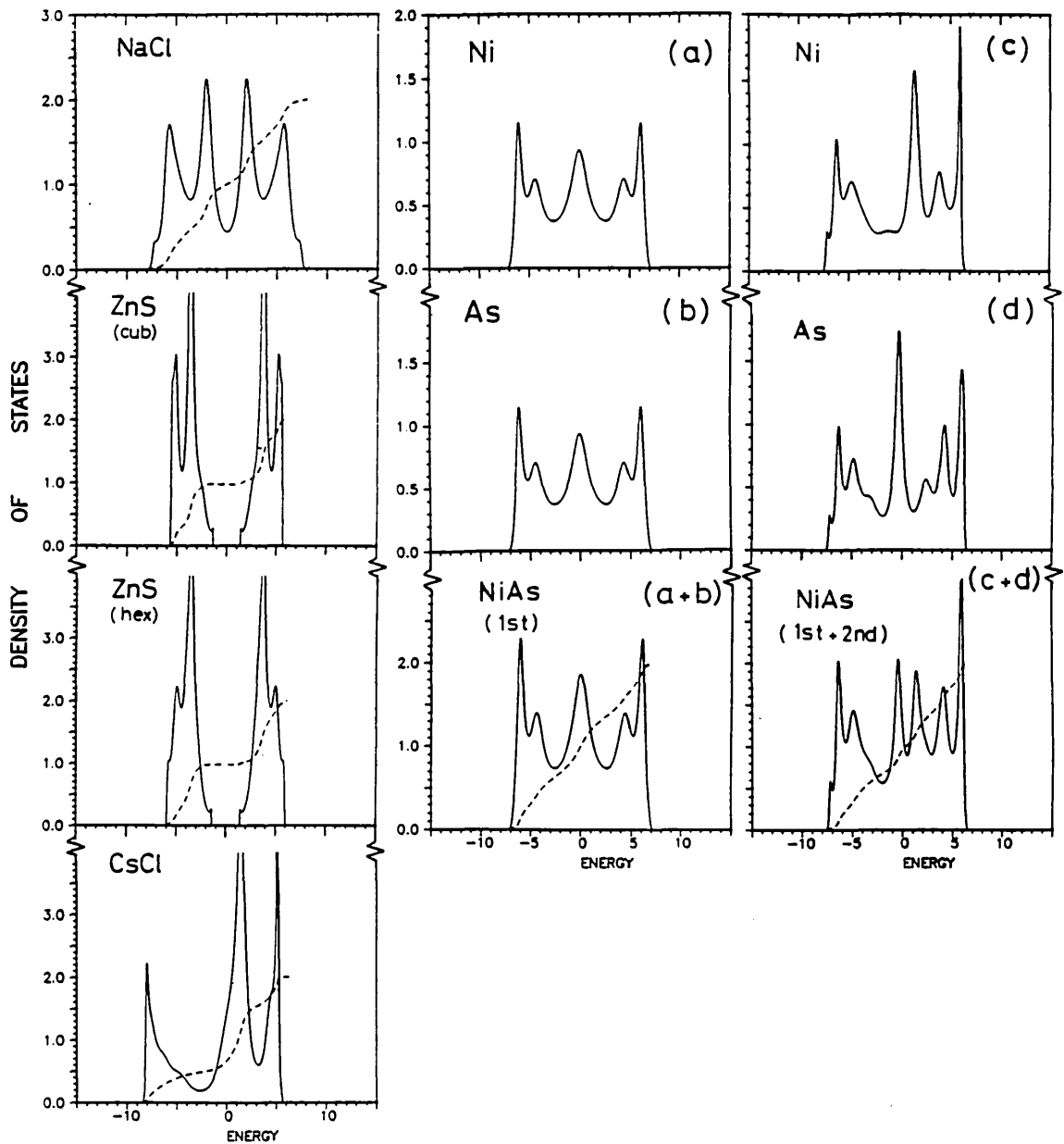


Figure XII.1

Densities of states for the AB compounds with  $\epsilon_{sp}^A = \epsilon_{sp}^B = 0$ ,  $\Delta = 0$  and  $h_{pp} \propto h_{bond}^2$ . Nickel arsenide is shown both with and without second neighbours in the hamiltonian. The integrated DOS (dashed line) has to be read with the vertical scale multiplied by 8. See table XII.1 in appendix XII for more details on the data used to draw these curves.



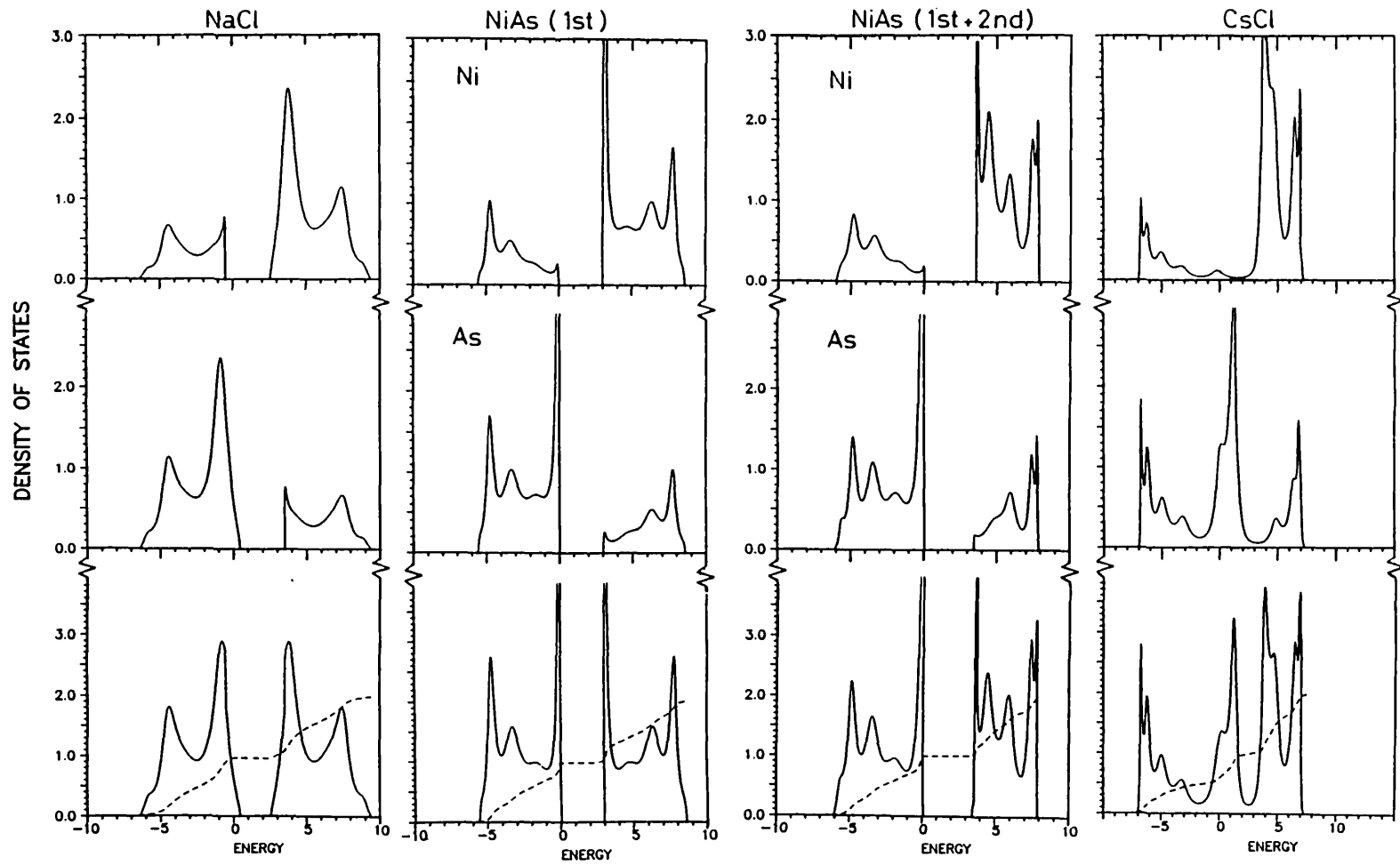


Figure XII.2 (continue)

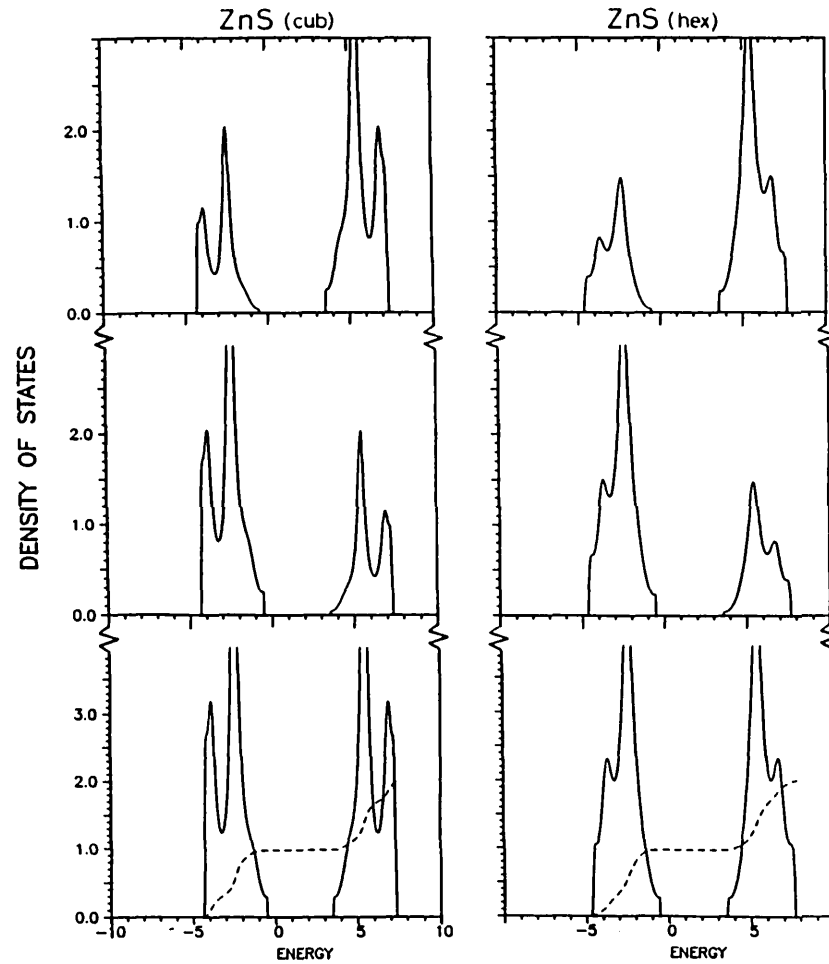


Figure XII.2 (continuation)

Densities of states for the AB compounds with  $\epsilon_{sp}^A = \epsilon_{sp}^B = 0$ ,  $\Delta = 1$  and  $h_{pp} \propto h_{bond}^2$ . Nickel arsenide is shown both with and without second neighbours in the hamiltonian. The integrated DOS (dashed line) has to be read with the vertical scale multiplied by 8. See table XII.2 in appendix XII for more details data used to draw these curves.

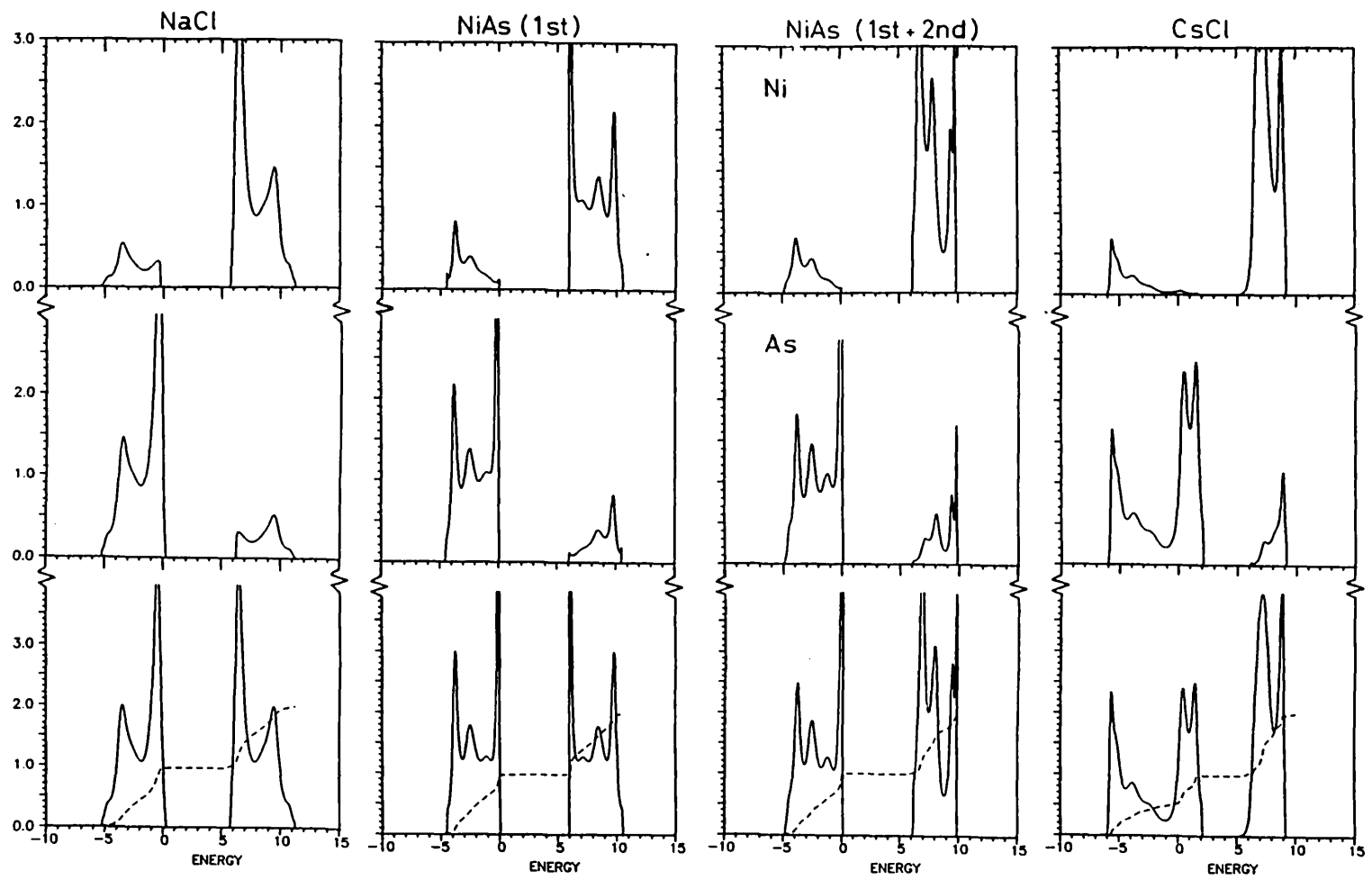


Figure XII.3 (continue)

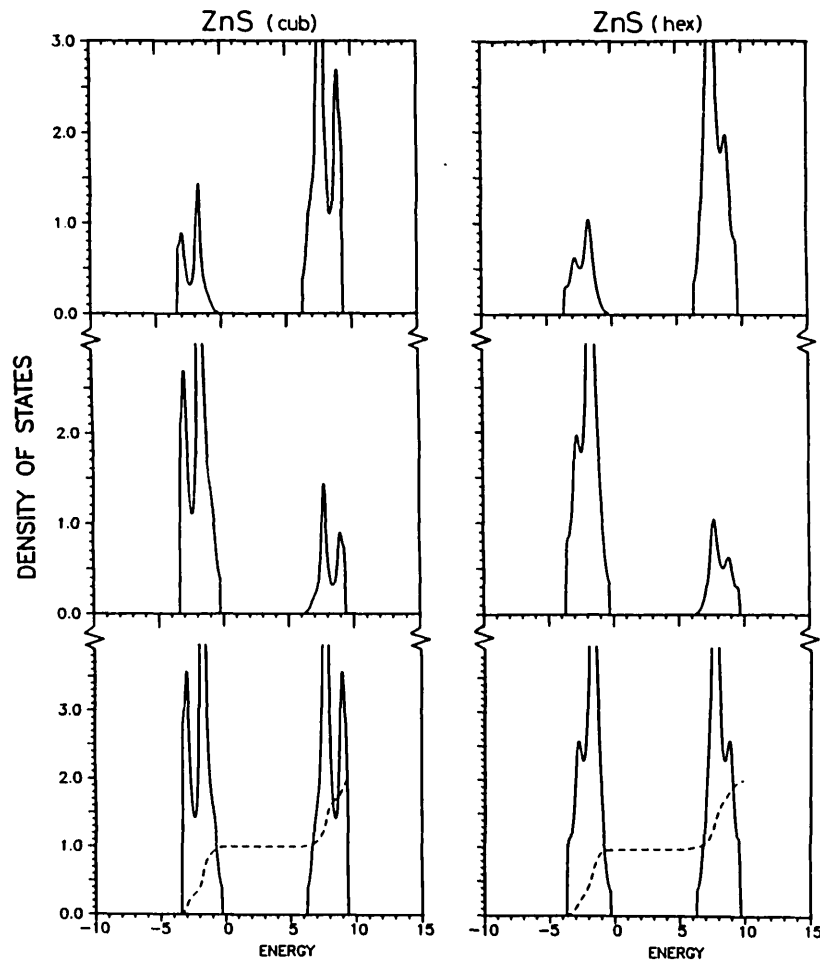


Figure XII.3 (continuation)

Densities of states for the AB compounds with  $\epsilon_{sp}^A = \epsilon_{sp}^B = 0$ ,  $\Delta = 2$  and  $h_{pp} \propto h_{bond}^2$ . Nickel arsenide is shown both with and without second neighbours in the hamiltonian. The integrated DOS (dashed line) has to be read with the vertical scale multiplied by 8. See table XII.3 in appendix XII for more details on the data used to draw these curves.

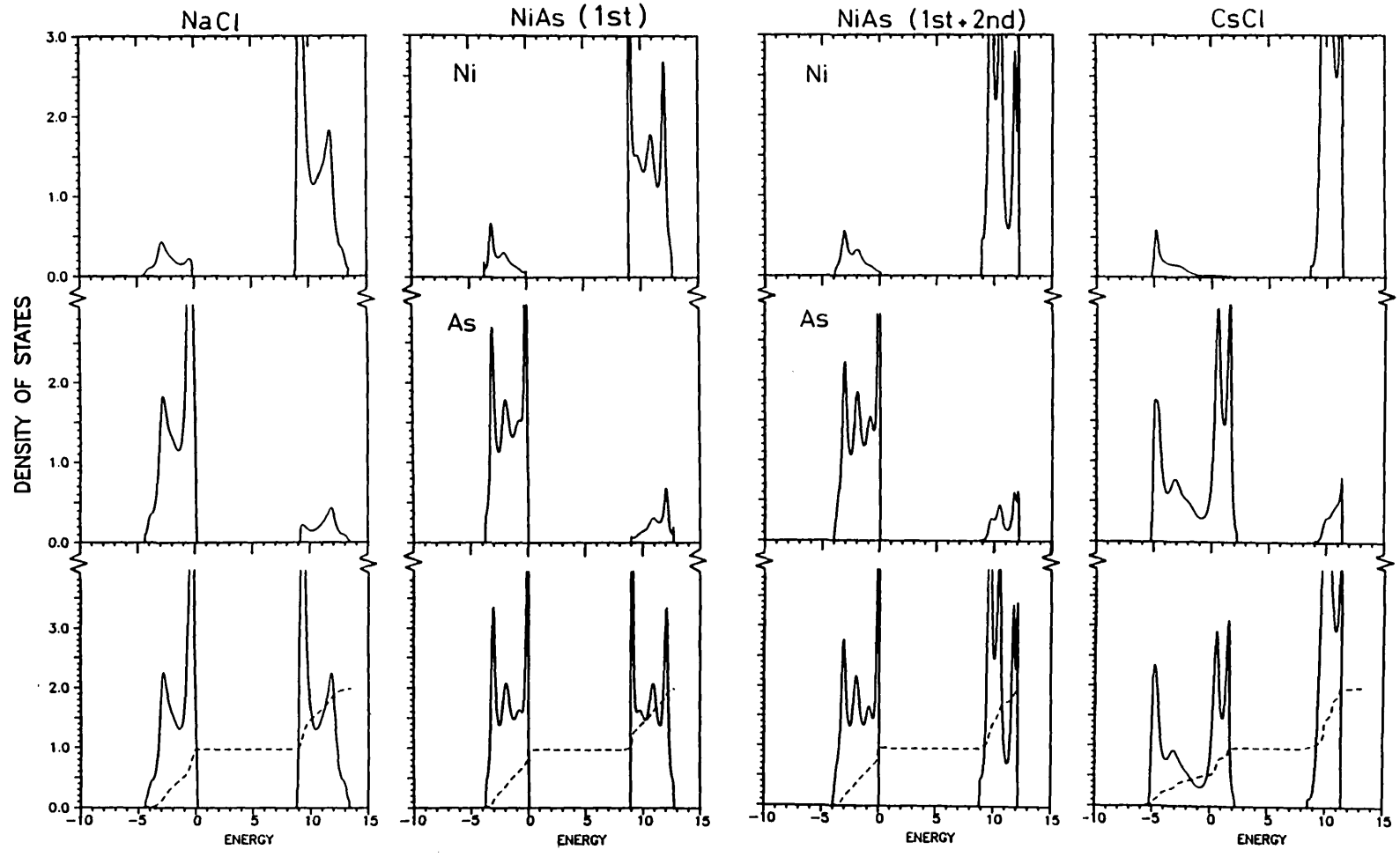


Figure XII.4 (continue)

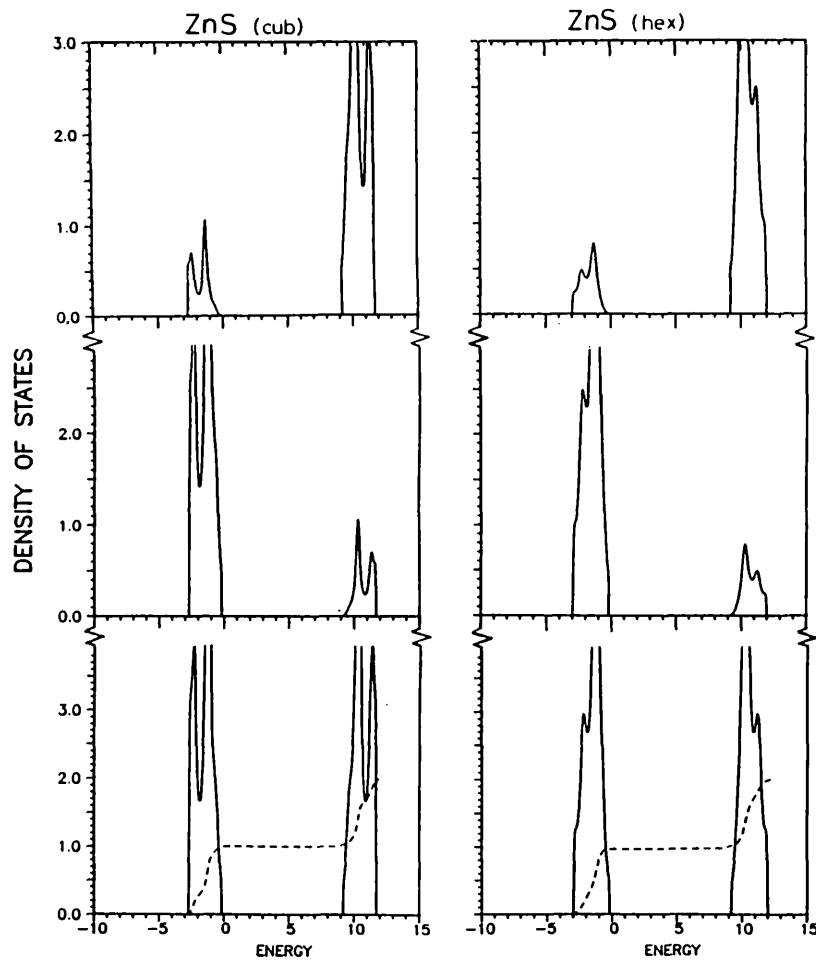


Figure XII.4 (continuation)

Densities of states for the AB compounds with  $\epsilon_{sp}^A = \epsilon_{sp}^B = 0$ ,  $\Delta = 3$  and  $h_{pp} \propto h_{bond}^2$ . Nickel arsenide is shown both with and without second neighbours in the hamiltonian. The integrated DOS (dashed line) has to be read with the vertical scale multiplied by 8. See table XII.4 in appendix XII for more details on the data used to draw these curves.

### Appendix XIII: DOS for the AB Compounds ( $\epsilon_{sp}^A = \epsilon_{sp}^B = -0.5$ )

In this appendix we show densities of states for the AB compounds corresponding to the case when the pair potentials are proportional to the inverse of the bond-length to the fifth power, i.e.,  $h_{pp} \propto 1/R^5$ , described in chapter 6. Here the parameters are given by  $\epsilon_{sp}^A = \epsilon_{sp}^B = 0$  and  $\Delta = 0, 0.5, 1, 2$  and  $3$ . Connected spectra are terminated with the square root terminator and for single band gap DOS the termination of Turchi et al is used. In both cases Beer and Pettifor (Beer 1985) optimized technique is used for the calculation of band edges. The band-widths (band-gaps) have been increased (decreased) by factors  $\alpha$  and  $\beta$  (see chapter 2). The values of these parameters along with the number of exact moments are given below. As explained in appendix XII whenever the DOS for both sites are shown, the top one corresponds to the A site (highest band), the middle one to the B site (lowest band) and the bottom DOS is the DOS per formula unit (i.e., for both sites). In this case the integrated DOS is also shown, with the readings in the vertical axis having to be multiplied by a factor of eight. Notice that for  $\epsilon_{sp}^A = \epsilon_{sp}^B$  and  $\Delta = 0$  there is no need to show the DOS for each site as they are equal (except for NiAs).

Table XIII.1 ( $\Delta = 0$ )

	NaCl	ZnS (cub)	ZnS (hex)	NiAs	CsCl	NaTl
2L	18 (18)	21 (21)	21 (21)	20 (20)	20 (20)	20 (20)
$\alpha$	3 (3)	3 (3)	3 (3)	3 (3)	3 (3)	3 (3)
$\beta$	3 (3)	3 (3)	3 (3)	3 (3)	3 (3)	3 (3)

Data for figure XIII.1 corresponding to the A and B sites in the AB compound. Here 2L stands for the number of exact moments and the number in brackets corresponds to the B site.

Table XIII.2 ( $\Delta = 0.5$ )

	NaCl	ZnS (cub)	ZnS (hex)	NiAs	CsCl	NaTl
2L	22 (22)	22 (22)	22 (22)	22 (22)	22 (22)	20 (20)
$\alpha$	3 (3)	3 (3)	3 (3)	3 (3)	3 (3)	3 (3)
$\beta$	3 (3)	3 (3)	3 (3)	3 (3)	3 (3)	3 (3)

Data for figure XIII.2 corresponding to the A and B sites in the AB compound. Here 2L stands for the number of exact moments and the number in brackets corresponds to the B site.



Table XIII.3 ( $\Delta = 1$ )

	NaCl	ZnS (cub)	ZnS (hex)	NiAs	CsCl	NaTl
2L	20 (20)	22 (22)	22 (22)	18 (20)	20 (20)	20 (20)
$\alpha$	3 (3)	3 (3)	3 (3)	3 (3)	3 (3)	3 (3)
$\beta$	3 (3)	3 (3)	3 (3)	3 (3)	3 (3)	3 (3)

Data for figure XIII.3 corresponding to the A and B sites in the AB compound. Here 2L stands for the number of exact moments and the number in brackets corresponds to the B site.

Table XIII.4 ( $\Delta = 2$ )

	NaCl	ZnS (cub)	ZnS (hex)	NiAs	CsCl	NaTl
2L	20 (20)	22 (22)	22 (22)	22 (20)	22 (20)	20 (20)
$\alpha$	3 (1.5)	3 (3)	3 (3)	3 (3)	3 (3)	3 (3)
$\beta$	1.5 (3)	3 (3)	3 (3)	1.5 (1.5)	3 (3)	3 (3)

Data for figure XIII.4 corresponding to the A and B sites in the AB compound. Here 2L stands for the number of exact moments and the number in brackets corresponds to the B site.

Table XIII.5 ( $\Delta = 3$ )

	NaCl	ZnS (cub)	ZnS (hex)	NiAs	CsCl	NaTl
2L	20 (20)	22 (22)	22 (22)	22 (20)	22 (20)	22 (22)
$\alpha$	3 (1.5)	3 (3)	3 (3)	3 (3)	3 (3)	3 (3)
$\beta$	1.5 (3)	3 (3)	3 (3)	3 (3)	3 (3)	3 (3)

Data for figure XIII.5 corresponding to the A and B sites in the AB compound. Here 2L stands for the number of exact moments and the number in brackets corresponds to the B site.

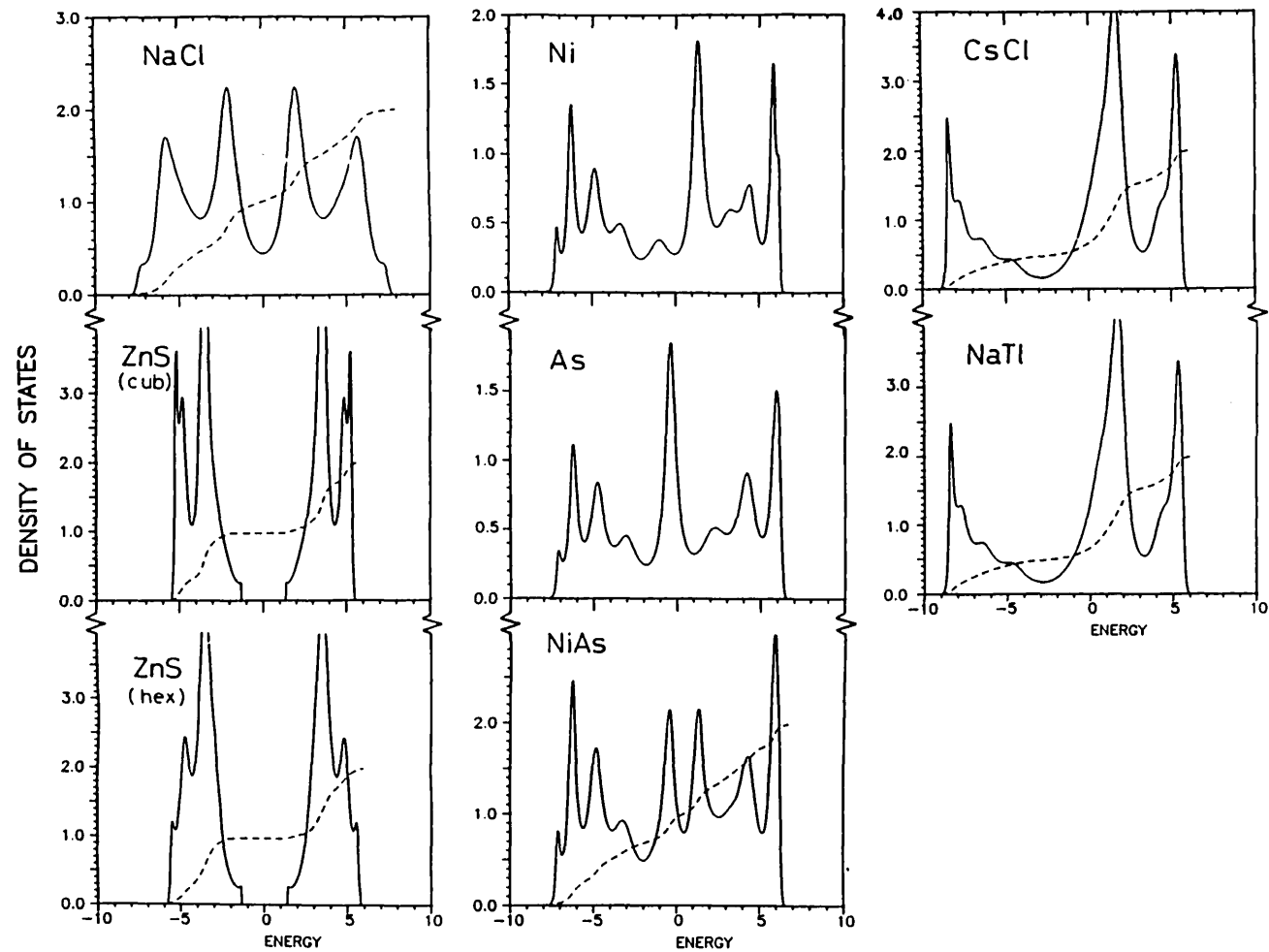


Figure XIII.1 DOS for the AB compounds with  $\epsilon_{sp}^A = \epsilon_{sp}^B = 0$ ,  $\Delta = 0$  and  $h_{pp} \propto 1/R^5$ . The DOS for each site are not shown (except for NiAs) because they are identical to each other. The integrated DOS (dashed line) has to be read with the vertical scale multiplied by 8. See table XIII.1 in appendix XIII for more details.

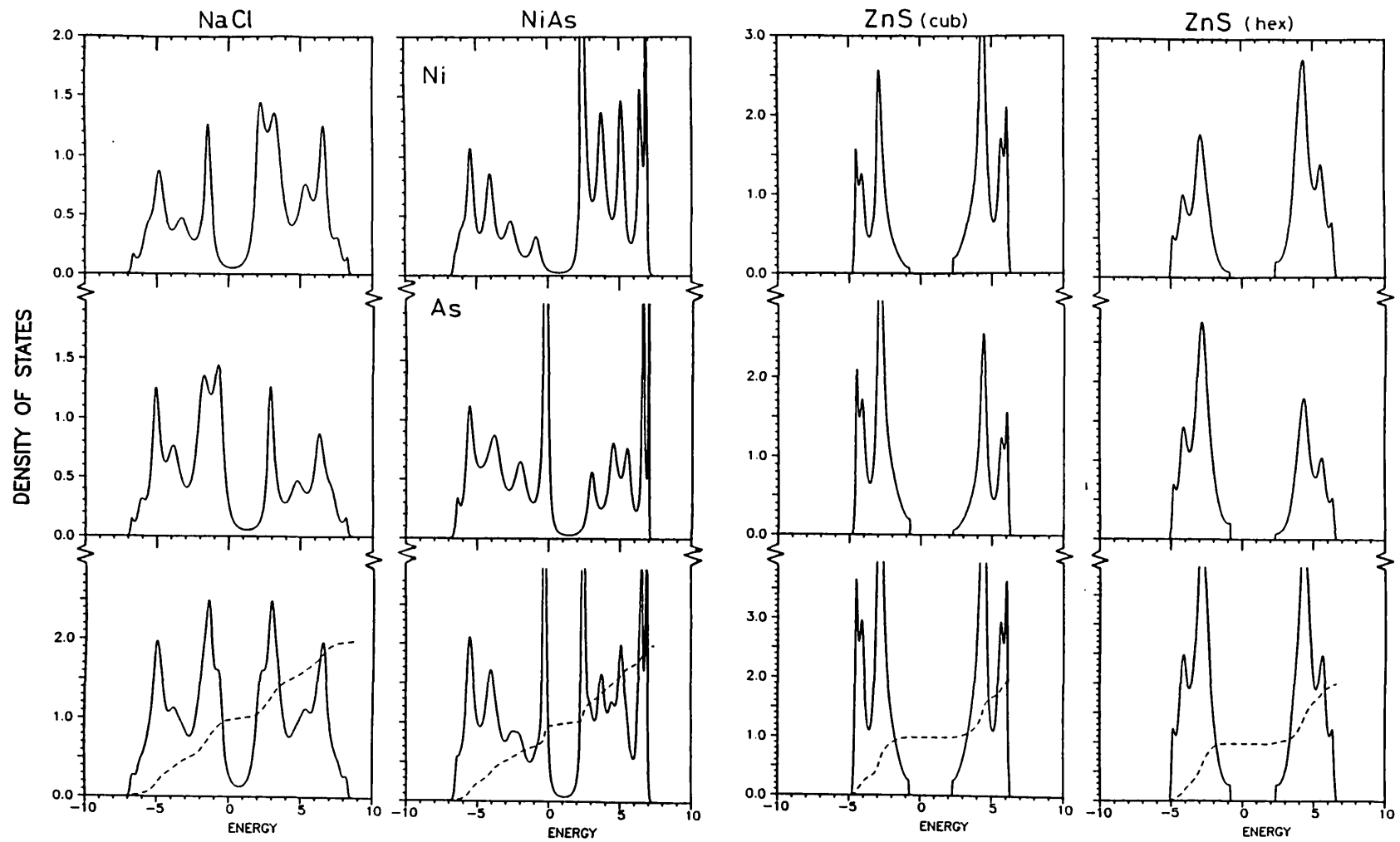


Figure XIII.2 (continue)

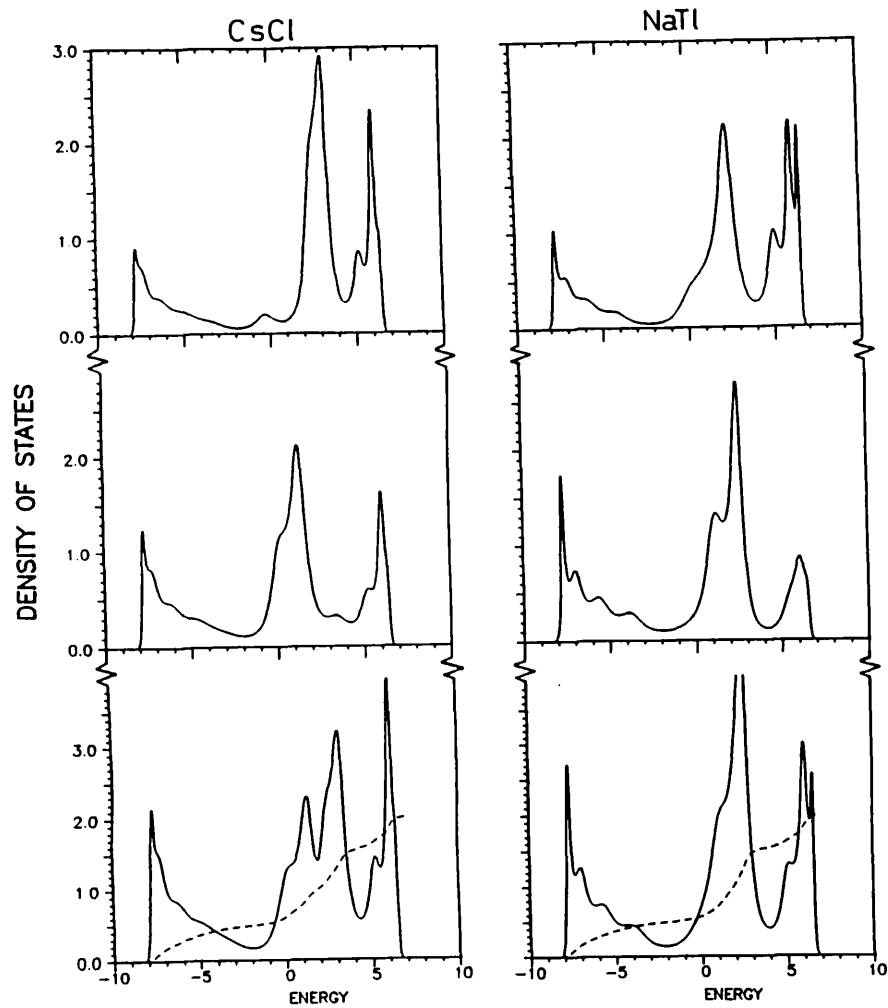


Figure XIII.2 (continuation)

Densities of states for the AB compounds with  $\epsilon_{sp}^A = \epsilon_{sp}^B = 0$ ,  $\Delta = 0.5$  and  $h_{pp} \propto 1/R^5$ . The integrated DOS (dashed line) has to be read with the vertical scale multiplied by 8. See table XIII.2 in appendix XIII for more details on the data used for these curves.

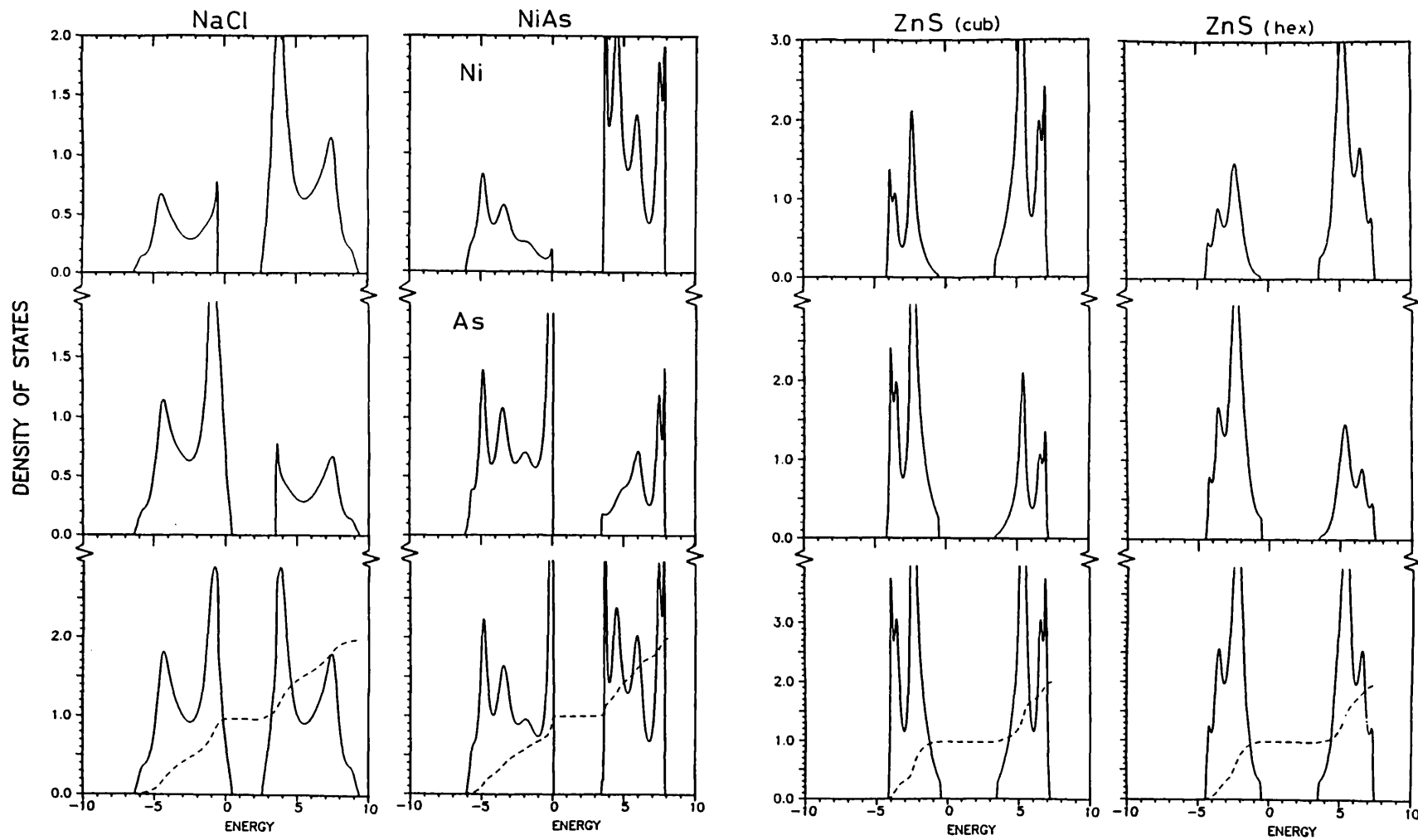


Figure XIII.3 (continue)

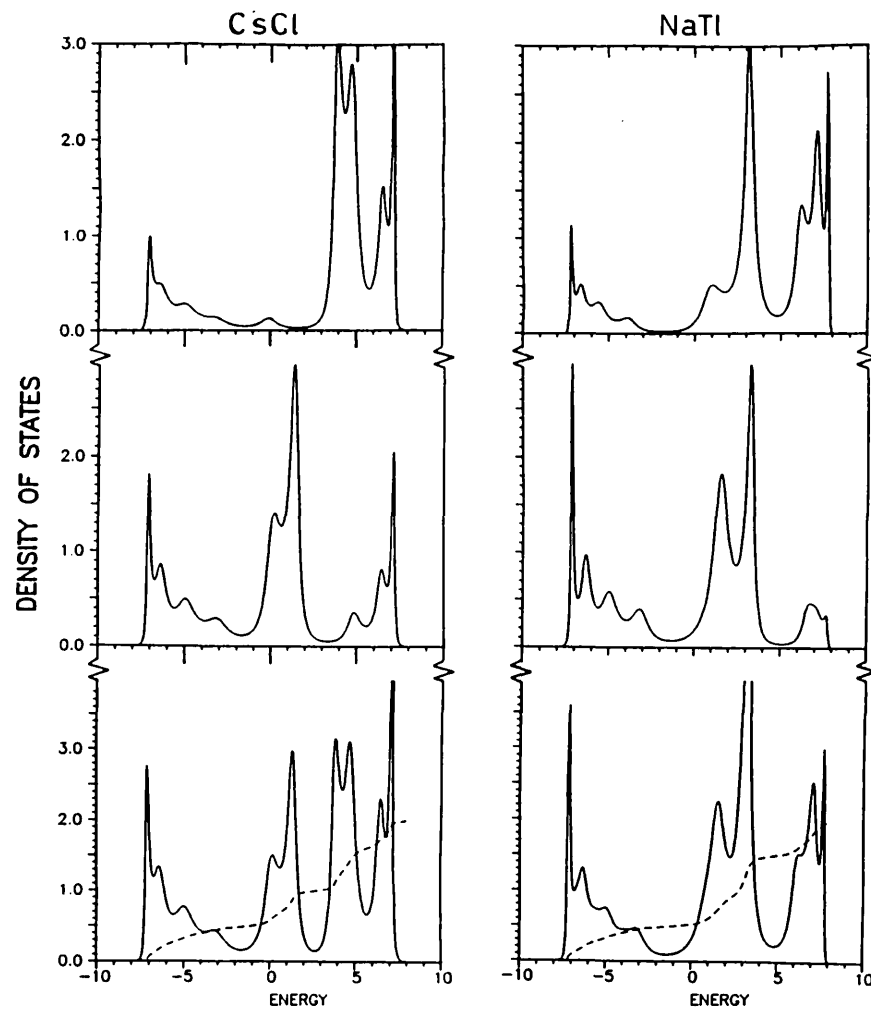


Figure XIII.3 (continuation)

Densities of states for the AB compounds with  $\epsilon_{sp}^A = \epsilon_{sp}^B = 0$ ,  $\Delta = 1$  and  $h_{pp} \propto 1/R^5$ . The integrated DOS (dashed line) has to be read with the vertical scale multiplied by 8. See table XIII.3 in appendix XIII for more details on the data used for these curves.

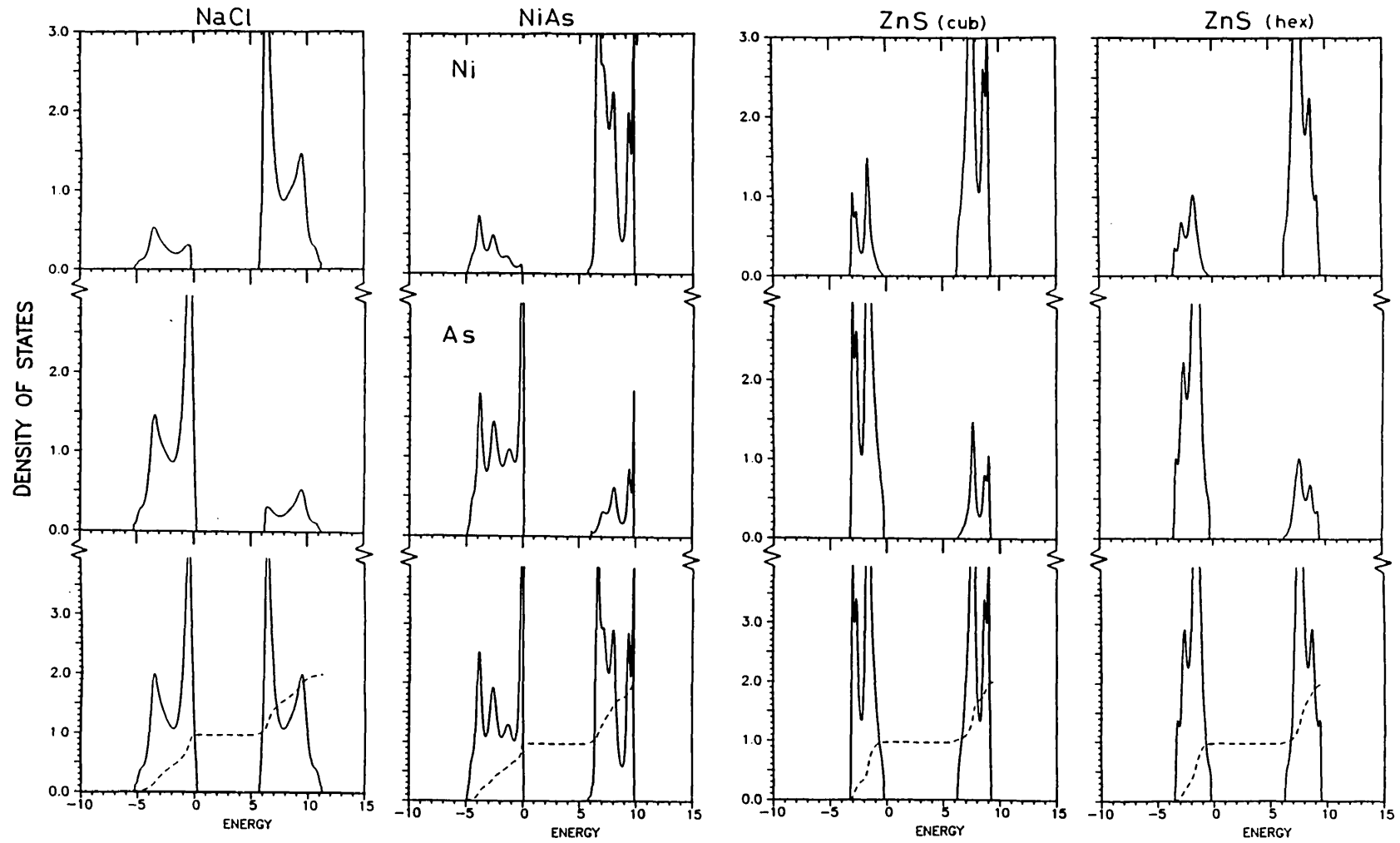


Figure XIII.4 (continue)



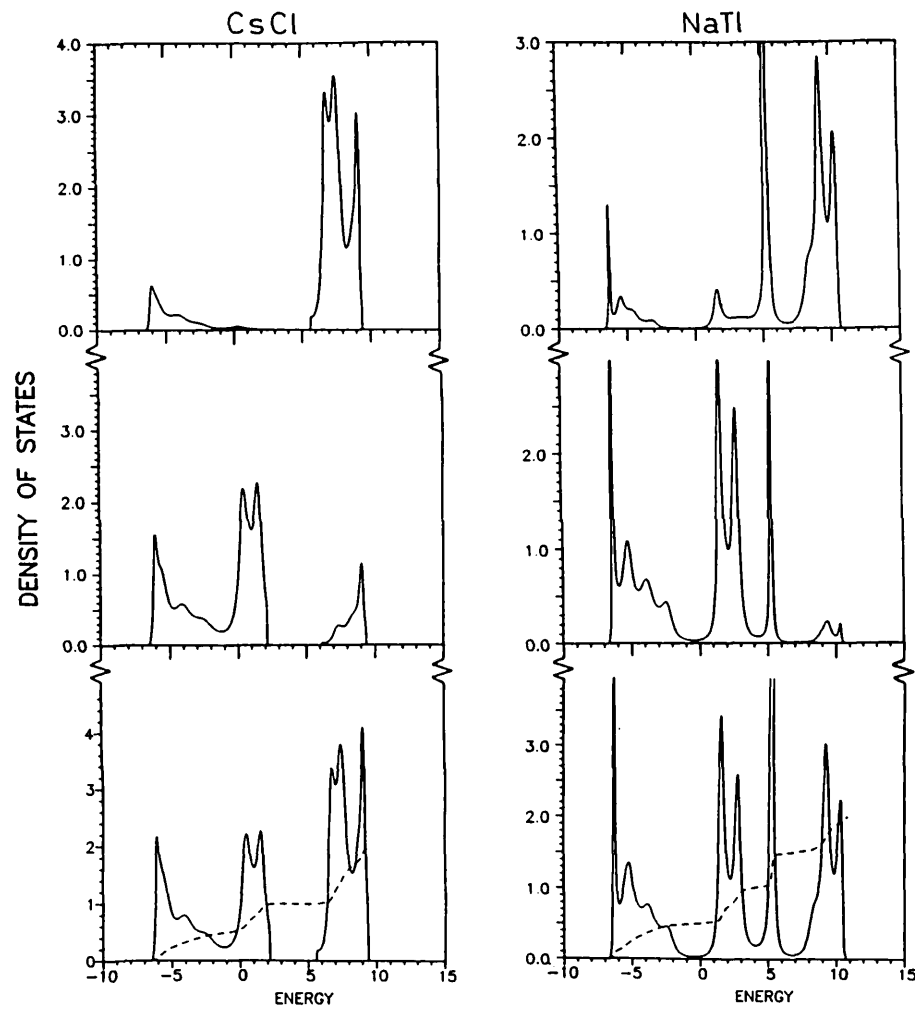


Figure XIII.4 (continuation)

Densities of states for the AB compounds with  $\epsilon_{sp}^A = \epsilon_{sp}^B = 0$ ,  $\Delta = 2$  and  $h_{pp} \propto 1/R^5$ . The integrated DOS (dashed line) has to be read with the vertical scale multiplied by 8. See table XIII.4 in appendix XIII for more details on the data used for these curves.

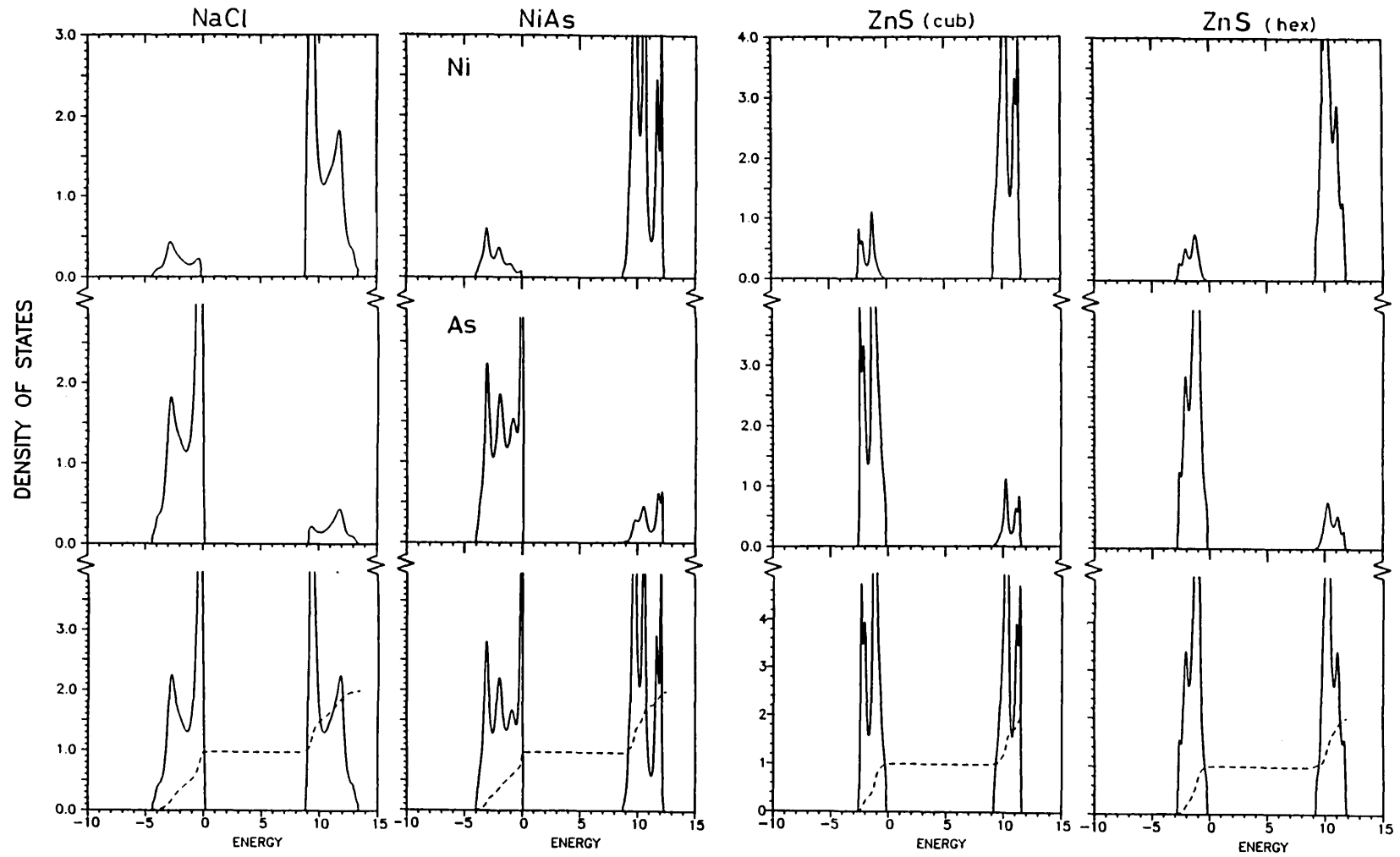


Figure XIII.5 (continue)

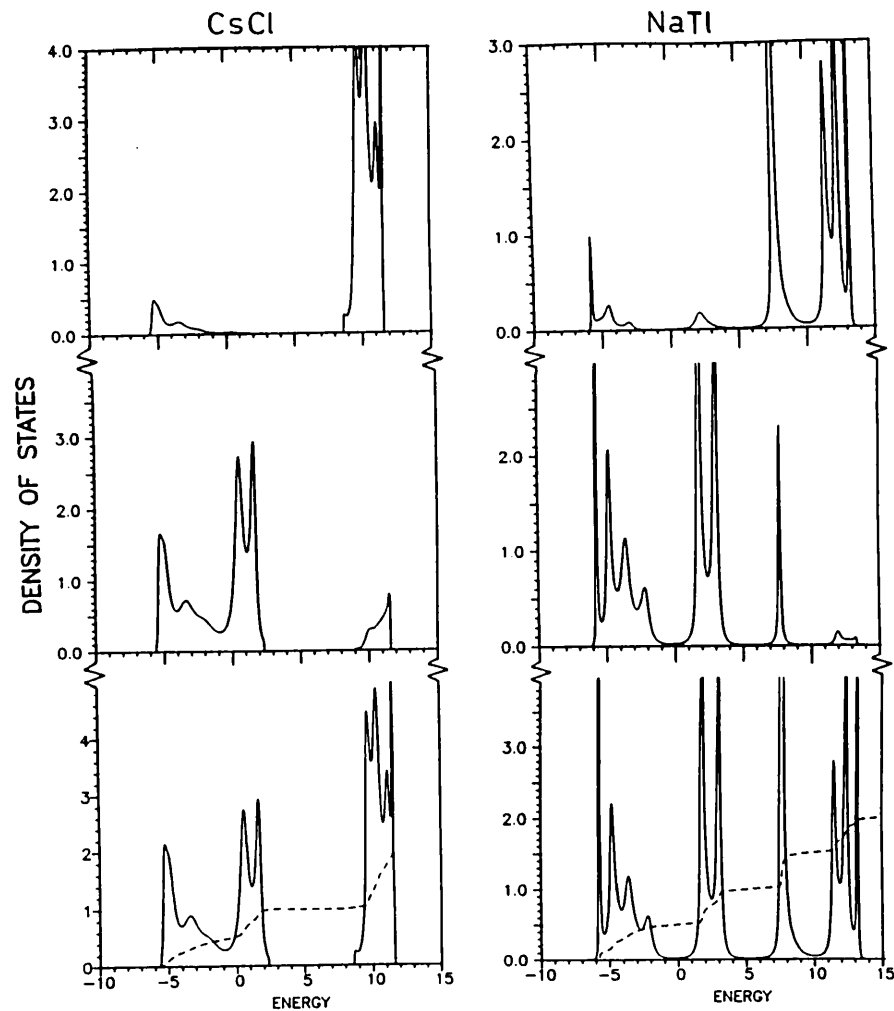


Figure XIII.5 (continuation)

Densities of states for the AB compounds with  $\epsilon_{sp}^A = \epsilon_{sp}^B = 0$ ,  $\Delta = 3$  and  $h_{pp} \propto 1/R^5$ . The integrated DOS (dashed line) has to be read with the vertical scale multiplied by 8. See table XIII.5 in appendix XIII for more details on the data used for these curves.

#### Appendix XIV: DOS for the AB Compounds ( $\epsilon_{sp}^A = \epsilon_{sp}^B = -1$ )

In this appendix we show densities of states for the AB compounds corresponding to the case  $h_{pp} \propto 1/R^5$  described in chapter 6. The sp-splittings are given by  $\epsilon_{sp}^A = \epsilon_{sp}^B = -0.5$  and only the cases  $\Delta = 0$  and  $\Delta = 0.5$  are shown. This is because as  $\Delta$  gets larger more than one gap starts to form in the DOS. The optimized square root termination of Beer and Pettifor (Beer 1985) was used and the band-widths have been increased by a factor  $\alpha = 3$  (see chapter 2). The number of exact moments kept in the continued fraction was equal to 22 for all six structures. As explained in appendix XII whenever the DOS for both sites are shown, the top one corresponds to the A site (highest band), the middle one to the B site (lowest band) and the bottom DOS is the DOS per formula unit (i.e., for both sites). In this case the integrated DOS is also shown, with the readings in the vertical axis having to be multiplied by a factor of eight. Notice that for  $\epsilon_{sp}^A = \epsilon_{sp}^B$  and  $\Delta = 0$  there is no need to show the DOS for each site as they are equal (except for NiAs).

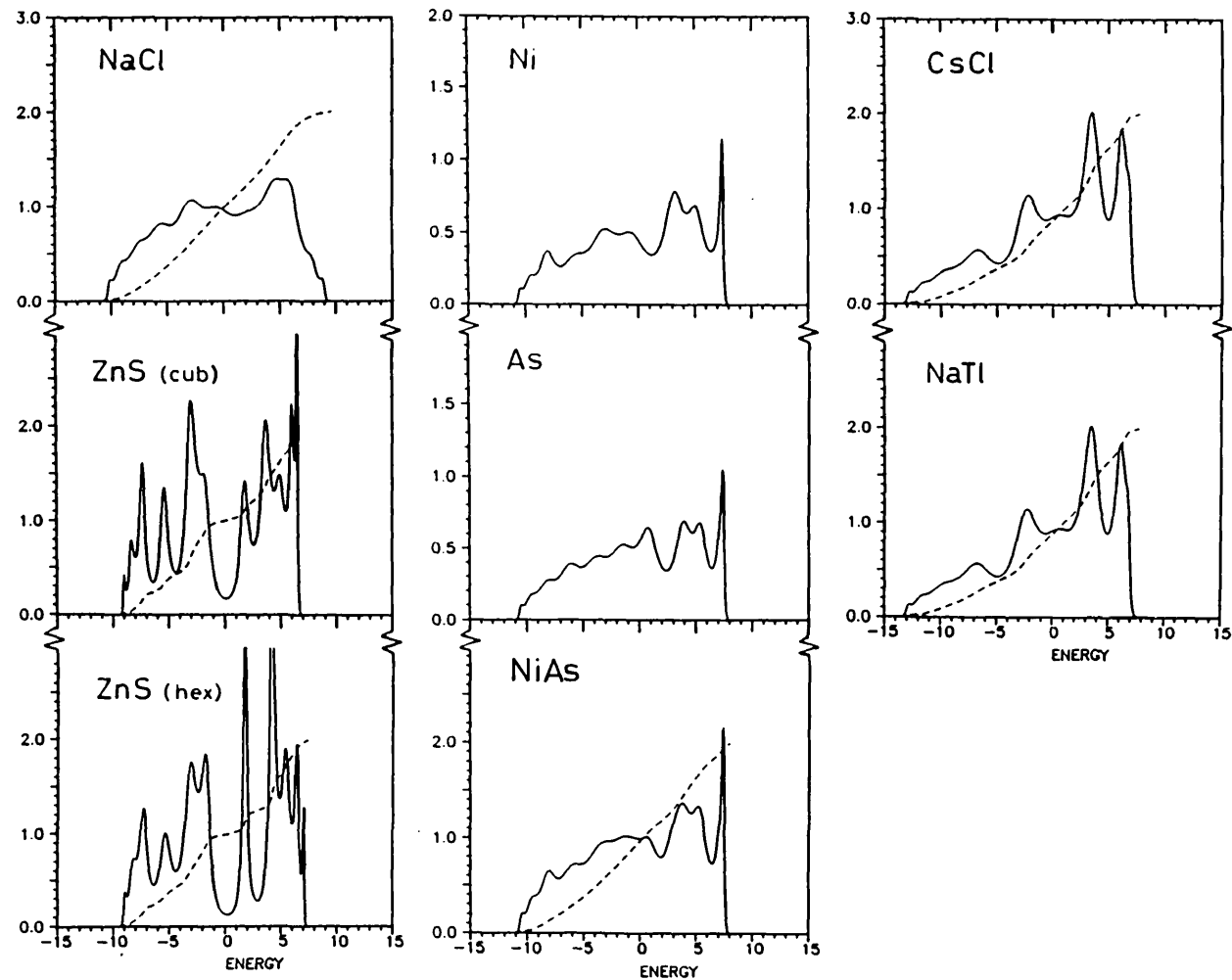


Figure XIV.1. DOS ( $\epsilon_{sp}^A = \epsilon_{sp}^B = -0.5$ ,  $\Delta = 0$  and  $h_{pp} \propto 1/R^5$ ) for the AB compounds. The DOS for each site is not shown (except for NiAs) because they are identical to each other. The integrated DOS (dashed line) has to be read with the vertical scale multiplied by 8. See appendix XIV for details.

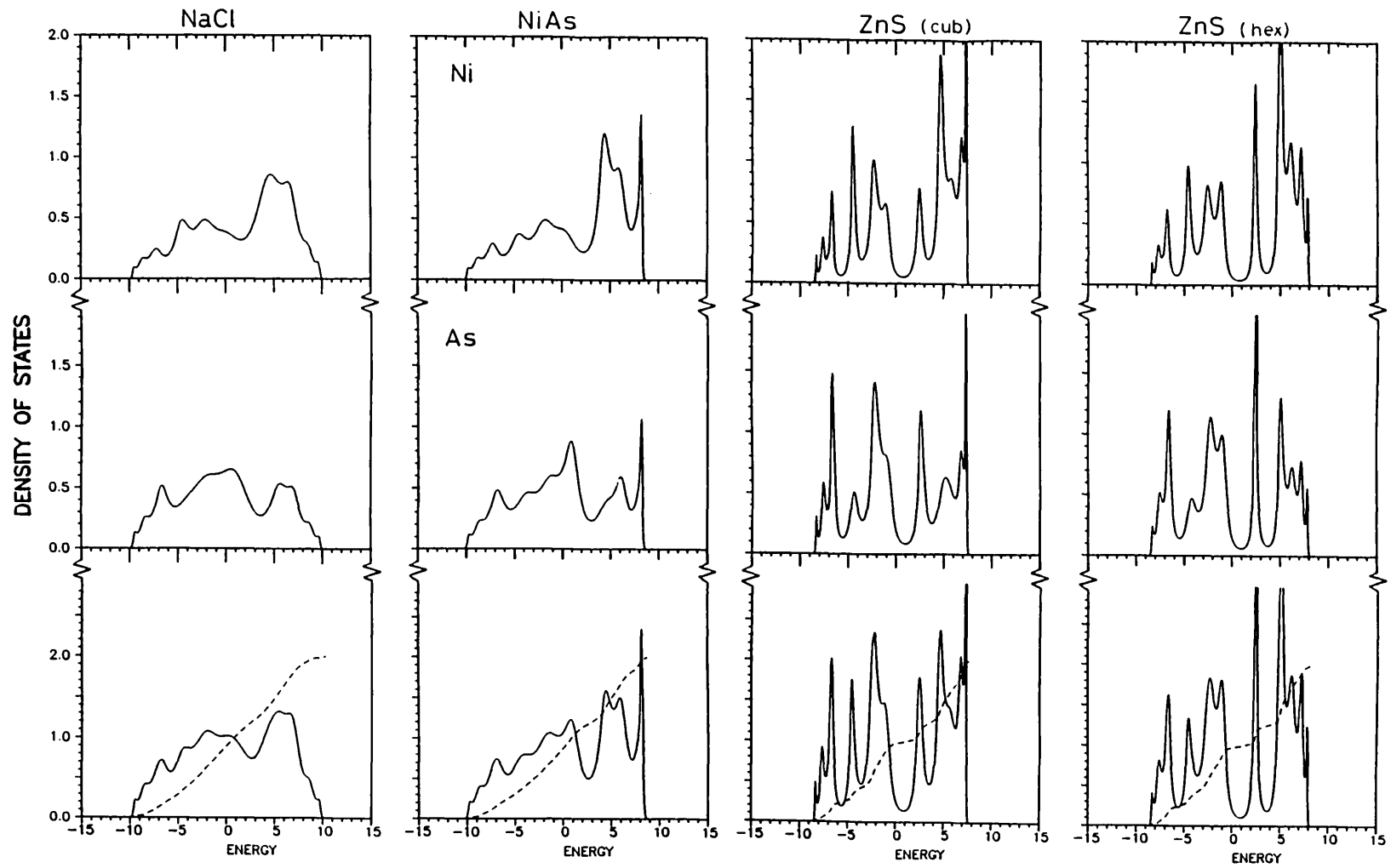


Figure XIV.2 (continue)

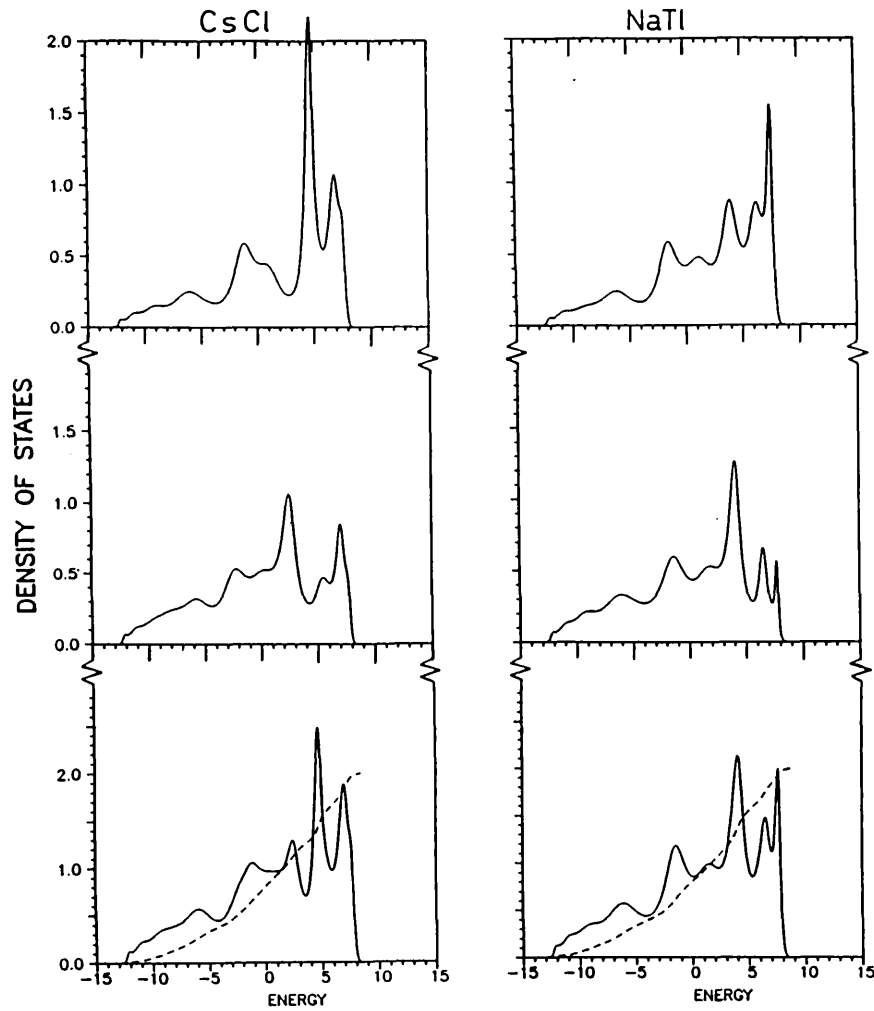


Figure XIV.2. (continuation)

Densities of states (22 exact moments) for the AB compounds with  $\epsilon_{sp}^A = \epsilon_{sp}^B = -0.5$ ,  $\Delta = 0.5$  and  $h_{pp} \propto 1/R^5$ . The integrated DOS (dashed line) has to be read with the vertical scale multiplied by 8. See appendix XIV for more details.

## Appendix XV: Results for the Transition Metals

In this appendix we report some results on the structural stability of the transition metal elements, obtained with the application of the theoretical model presented in chapter 3. The computation is done in the same way as for the sp elements, namely, using the recursion method for the calculation of the densities of states and with the different structures being compared at the volumes prepared in accordance with the structural energy difference theorem (see chapter 3). The number of exact moments kept in the calculations varies between 16 and 20 and the continued fractions were terminated with either the square root terminator (connected spectrum) or the termination of Turchi et al 1982 (single band gap). The calculations are exact for the dimer as shown in appendix V.

### XV.1 Hopping integrals

In the pure d case, there are five d-orbitals, one for each value of the magnetic quantum number  $m$ . Within the atomic sphere approximation of Andersen (1973) canonical d bands may be obtained which are dependent neither on the particular transition metal nor on the lattice constant. The hopping integrals then obey the following ratio

$$dd\sigma : dd\pi : dd\delta :: -6 : 4 : -1 \quad . \quad (XV.1)$$

If sd hybridization is introduced the ratio  $dd\sigma/ss\sigma$  has to be known in order to perform the calculations. If one takes Harrison's (1980) expression, namely,



$ss\sigma = (-2.8/R^2) \cdot 13.6 \text{ eV}$  along with Andersen's (op. cit.) canonical one, i.e.,  $dd\sigma = -6(4/R)^5 \text{ eV}$  (see Pettifor and Podloucky 1986) one can write

$$\frac{dd\sigma}{ss\sigma} = \frac{-6(4^5)}{(-2.8)13.6} \frac{1}{R^3} \quad . \quad (\text{XV.2})$$

In order to evaluate this ratio we take the bond length  $R$  as calculated from the Wigner-Seitz radius of fcc Molybdenum, i.e.,  $S = 2.92$  atomic units. In terms of the nearest neighbour distance  $R$ , the volume of the fcc primitive cell writes as  $\Omega_{\text{fcc}} = (2^{3/2}/2)R^3$ . Therefore since  $\Omega_{\text{fcc}} = (4/3)\pi S^3$  we can evaluate the ratio in (XV.2) which gives

$$\frac{dd\sigma}{ss\sigma} = 1.10 \quad . \quad (\text{XV.3})$$

Notice that had we evaluated this ratio using Harrison's expression for  $dd\sigma$ , namely  $dd\sigma = (-32.4 r_d^3/R^5) \text{ Ry}$  ( $r_d = 1.20/0.529 \text{ au}$ ), we would had got  $dd\sigma/ss\sigma = 0.92$  which is very close to (XV.3).

## XV.1 Results

Let us first present the results for the case when there is no hybridization with an s band (i.e., the pure d case). The repulsive pair potentials are chosen to depend on the bond length as  $h_{pp} \propto h_{\text{bond}}^2$  and since  $h_{\text{bond}} \propto 1/R^5$  we have  $h_{pp} \propto 1/R^{10}$ . We take  $dd\sigma = -1.10$  (the units are arbitrary since only relative stability is of interest) and use (XV.1) to evaluate  $dd\pi$  and  $dd\delta$ . The same ten structures considered in the study of the sp elements are taken into

account here. For the bcc Bravais lattice the second neighbours are included with  $ss\sigma_2/ss\sigma_1 = 1/3$  for the second to first neighbours hopping integrals ratio, just as we did for the sp elements. The structural energy against band filling curves are shown in figure XV.1 (top). We see that the predicted trend along the transition metal series is

fcc-hcp-fcc-bcc-h.comb-dia(hex)-dia(cub)-z.zag-dimer-s.cubic

where the honey comb stability starts for the band filling  $N$  around five. The stability of such open structures for  $N > 5$  is unexpected because the transition metal structures are known to be close packed.

In an attempt to account for this uncomfortable result we have included a hybridization with an s-band in which  $ss\sigma$  was taken as  $-1$ . Then we evaluated  $dd\sigma$  using the ratio in (XV.3) and took  $sd\sigma$  as  $sd\sigma = (ss\sigma \cdot dd\sigma)^{1/2}$ . The other hopping integrals were evaluated using (XV.1). The results for the structural energy are shown in figures XV.1 (bottom) and XV.2 where the sd-splitting is given by  $\epsilon_{sd} = 12 \cdot \tan(n\pi/10)$  for  $n = 0, -2$  and  $-3$  (this is the same kind of scale we used for  $\epsilon_{sp}$ ). We see no improvements at all, with the close packed stability region being even reduced in the cases  $n = -2$  and  $-3$ .

XV.3      Results for  $h_{pp} \propto h_{bond}^{5/2}$

Similarly as we did for the sp AB compounds we tried a harder repulsive potential for the transition metals in an attempt to stabilize the close

packed arrangements with respect to the open ones. Notice that in the sp case we took  $h_{pp} \propto h_{\text{bond}}^{5/2}$  which, due to the  $1/R^2$  dependence of the sp bond integrals (Harrison 1980), led to  $h_{pp} \propto 1/R^5$ . Here since the d hopping integrals vary as  $1/R^5$  we have  $h_{pp} \propto 1/R^{12.5}$ . The results are shown in figure XV.3 for the pure d and  $\epsilon_{sd} = 0$  cases. The structures considered are indicated in the figure. We see a great improvement in these results with the close packed arrangements being more stable than the diamond structure for all values of the band filling. However, at about  $N = 8$  and above the simple cubic structure takes over spoiling the result.

#### XV.4 Conclusion

The use of a harder repulsive potential improved the results by pushing up the cubic diamond stability curve relatively to the close packed ones. However the simple cubic lattice is still found as the most stable structure at the end of the series (figure XV.3). We have no major clue for these unexpected predictions as tight-binding calculations should give better results here than for the sp case, since the d-orbitals are more localized than these. Investigations towards understanding the source of these poor results and possible improvements are currently being carried out.

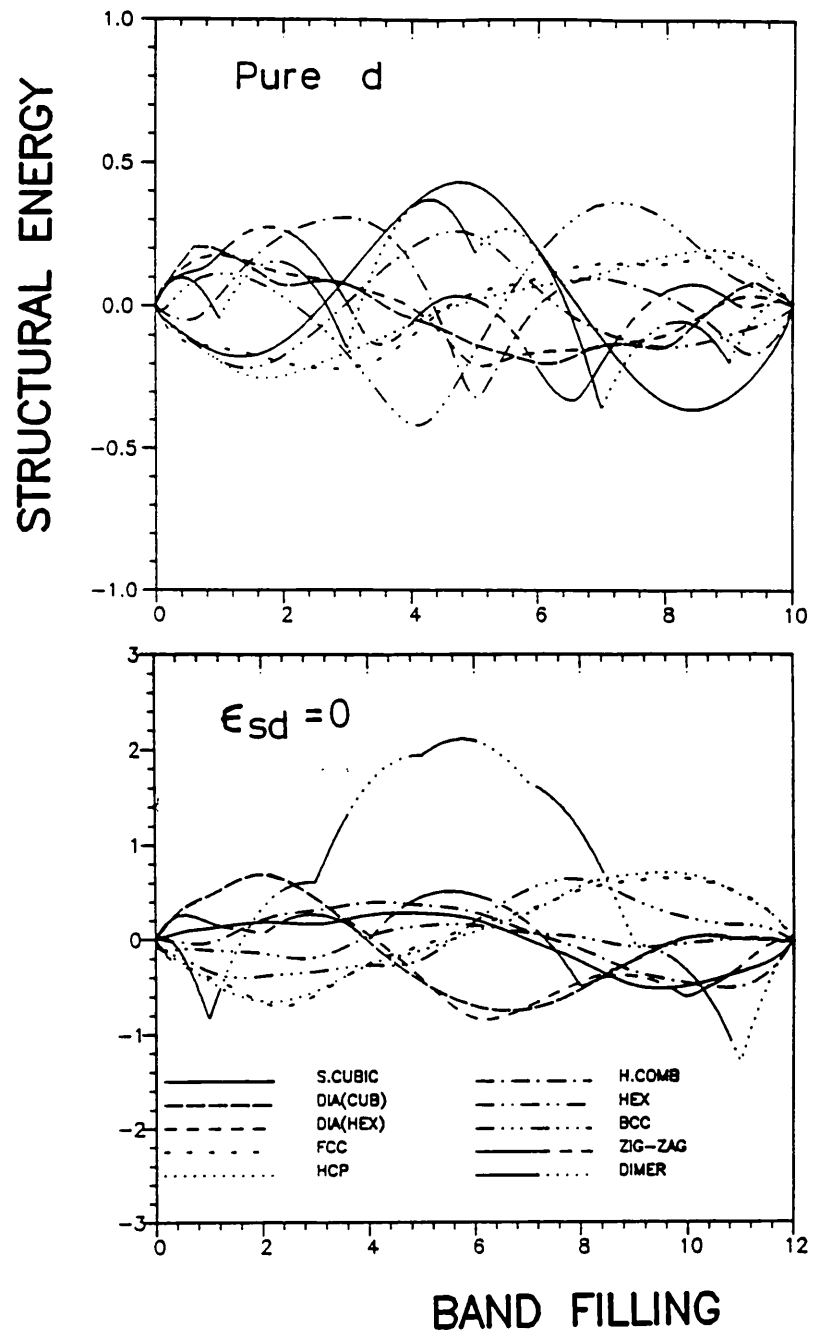


Figure XV.1

Structural energy versus band filling ( $h_{pp} \propto 1/R^{10}$ ) for the pure d case (top) and  $\epsilon_{sd} = 0$  (bottom). Andersen's (1975) canonical values are used for the hopping integrals, i.e.,  $dd\sigma:dd\pi:dd\delta:-6:4:-1$  and  $ss\sigma$  is fixed as for Molybdenum.

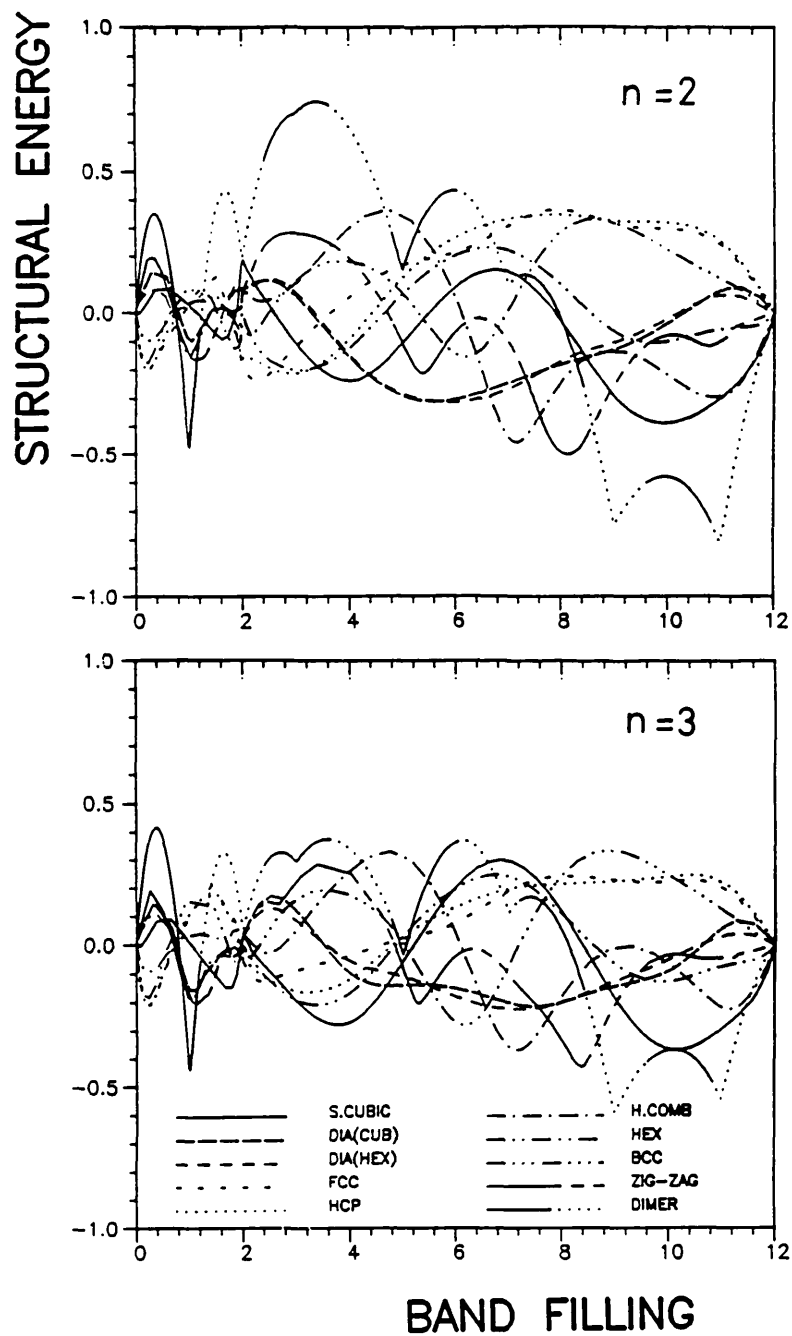


Figure XV.2

Structural energy versus band filling for the  $sd$  case. Here  $\epsilon_{sd} = -12 \cdot \tan(n\pi/10)$  with  $n = 2$  and  $3$  and  $h_{pp} \propto 1/R^{10}$ .

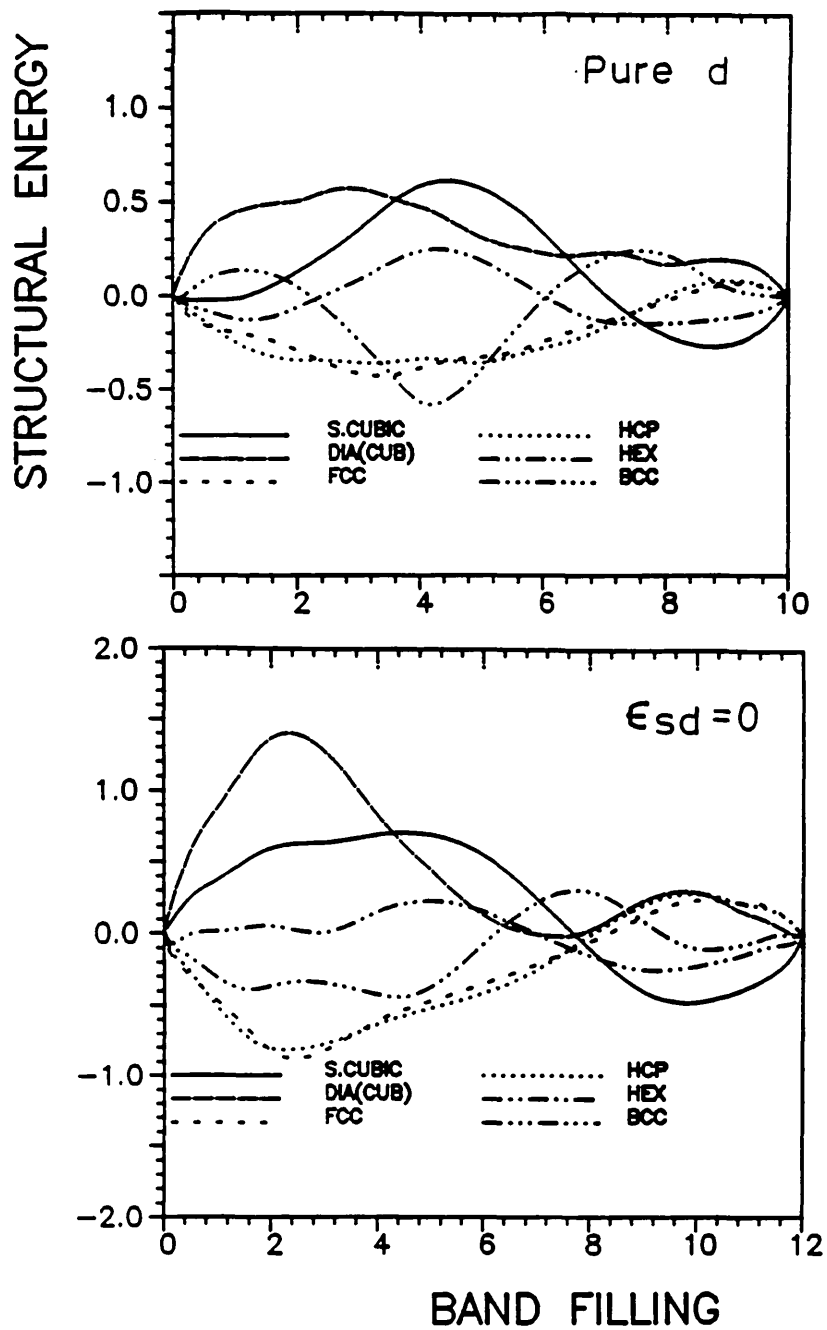


Figure XV.3

Structural energy versus band filling curves for the pure d (a) and  $\epsilon_{sd} = 0$  cases (b). In these cases  $h_{pp} \propto h_{\text{bond}}^{5/2}$  which leads to  $h_{pp} \propto 1/R^{12.5}$ .

## REFERENCES

- Allan G. 1970 *Ann. Phys., Paris* 5 169
- Andersen O.K. 1973 *Solid State Commun.* 13 133
- Andersen O.K. and Jepsen O. 1984 *Phys. Rev. Lett.* 53 2571
- Andersen O.K., Pawlowska Z. and Jepsen O. 1986 *Phys. Rev. B* 34 5253
- Anlage S.M. and Smith D.L. 1986 *Phys. Rev. B* 34 2336
- Aschcroft N.W. and Mermin D.N. 1976 *Solid State Physics* (New York: Holt, Rinehart and Winston)
- Beer N.R. 1985 *PhD Thesis* University of London
- Beer N.R. and Pettifor D.G. 1984 *Electronic Structure of Complex Systems* eds Phariseau P. and Temmerman W.: proc. NATO Adv. Study Inst. 1982 (New York: Plenum) p.769
- Blumstein C. and Wheeler J.C. 1973 *Phys. Rev. B* 8 1764
- Bullett D.W. 1975a *J.Phys.C: Solid State Phys.* 8 2695
- 1975b *J.Phys.C: Solid State Phys.* 8 2707
- 1980 *Solid State Phys.* Vol. 35 (New York: Academic)
- Burdett J.K. and Lee S. 1985a *J. Am. Chem. Soc.* 107 3051
- Burdett J.K. and Lee S. 1985b *J. Am. Chem. Soc.* 107 3063
- Callaway J. 1964 *Energy Band Theory* (New York: Academic)
- Callaway J. 1974 *Quantum Theory of the Solid State Part A* (New York: Academic) 1st ed.
- Chang K.J. and Cohen M.L. 1985 *Phys. Rev. B* 31 7819
- Christensen N.E., Satpathy S. and Pawlowska Z. 1986 *Phys. Rev. B* 34 5977
- Cohen Tannoudji C.C., Diu B. and Laloë F. 1977 *Quantum Mechanics Vol. I* (New York: Wiley)
- Coulson C.A. 1939 *Proc. Roy. Soc.* 169 A 413

- Cyrot Lackmann 1967 *Adv.Phys.* 16 393
- Donohue J. 1974 *The Structure of the Elements* (New York: Wiley)
- Ducastelle F. 1970 *J.Physique* 31
- Ducastelle F. and Cyrot-Lackmann F. 1970 *J.Phys.Chem.Solids* 31 1295  
 1971 *J.Phys.Chem.Solids* 32 285  
 1973 *J.Phys. C:Solid State Phys.* 6 3077
- Duthie J.C. and Pettifor D.G. 1977 38 564
- Evans R.C. 1966 *An Introduction to Crystal Chemistry* (Cambridge University Press: London)
- Finnis M.W. 1987 *Chemistry and Physics of Fracture* eds. Latanision R.M. and Jones R.H.: proc. NATO Adv. Study Inst. (New York: Plenum) p177
- Finnis M.W., Paxton A.T., Pettifor D.G., Sutton A.P. and Ohta Y. 1988 *Phil.Mag. A* 58 143
- Foulkes M. 1987 Ph.D. Thesis University of Cambridge
- Friedel J. 1954 *Adv. Phys.* 3 446
- Froyen S. and Cohen M.L. 1983 *Phys. Rev. B* 28 3258
- Froyen and Cohen 1984 *Phys. Rev. B* 29 3770
- Gaspard J.P. and Cyrot-Lackmann F. 1973 *J.Phys.C: Solid State Phys.* 6 3077
- Gaspard J.P. and Lambin P. 1985 *The Recursion Method and its Applications* eds: Pettifor D.G. and Weaire D.L. (Berlin: Springer) p72
- Glanville S., Paxton A.T., and Finnis M.W. 1988, *J. Phys. F: Met. Phys.* 18 693
- Gordon R.G. 1968 *J.Math.Phys.* 9 655
- Harris J. 1985 *Phys. Rev. B* 31 1770
- Harrison W.A. 1980 *Electronic Structure and the Properties of Solids* (San Francisco: W.A.Freeman)



- Haydock R., Heine V. and Kelly M.J. 1972 *J. Phys. C: Solid State Phys.* 5  
2845
- Haydock R., Heine V. and Kelly M.J. 1975 *J. Phys. C: Solid State Phys.* 8  
2591
- Haydock R., 1980 *Solid State Phys.* 35 (New York: Academic)
- Heine V. 1980 *Solid State Phys.* 35 (New York: Academic)
- Heine V. 1984 *Electronic Structure of Complex Systems*, eds P. Phariseau &  
Temmerman : proc NATO Adv. Study Inst. 1982 (New York: Plenum) p.761
- Hermann F. and Skilman S. 1968 *Atomic Structure Calculations* (New  
Jersey: Prentice Hall)
- Ho K.M., Tao H.J. and Zhu X.Y. 1984 *Phys. Rev. Lett.* 53 1586
- Hodges C.H. 1977 *J. Physique Lett.* 38 L187-9
- Hohenberg P. and Kohn W. 1964 *Phys. Rev. B* 136 864
- Jones H. *Proc. Phys. Soc. London* 49 250
- Jones R. and Lewis M.W. 1984 *Phil. Mag. B* 49 95
- Jones R. 1985 *The Recursion Method and its Applications* eds: Pettifor D.G.  
and Weaire D.L. (Berlin: Springer) p132
- Jones W.B. & Thron W.J. 1980 *Continued Fractions: Analytic Theory and  
Application Encyclopedia of Mathematics and its Applications* ed. Gian-Carlo  
Rota (Reading, Mass.: Addison-Wesley) vol. 11
- Kelly M.J. 1980 *Solid State Phys.* 35 (New York: Academic)
- Kittel C. 1987 *Quantum Theory of Solids* 2nd ed. (New York: Wiley)
- Kohn W. and Sham L.J. 1965 *Phys. Rev. A* 140 1133
- Magnus A. 1985 *The Recursion Method and its Applications*: eds Pettifor  
D.G. and Weaire D.L. (Berlin: Springer) p22
- Majewski J.A. and Vogl P. 1986 *Phys. Rev. Lett.* 57 1366  
1987 *Phys. Rev. B* 35 9666
- Merzbacher E. 1970 *Quantum Mechanics* 2nd ed. (New York: Wiley)

- McMahan A.K. and Moriarty J.A. 1982 Phys. Rev. B 27 3235
- Mooser E. and Pearson W.B. 1959 Acta Crystallogr. 12 1015
- Nex C.M.M. 1978 J.Phys. A: Math. and General 11 653
- Paxton A.T. 1987 PhD Thesis Oxford University
- Pearson W.B. 1972 *The crystal chemistry and physics of metals and alloys* (New York: Wiley)
- Pettifor D.G. and Varma C.M. 1979 J.Phys. C: Solid State Phys. 12 L253
- Pettifor D.G. 1983 *Physical Metallurgy* ed. by Cahn R.W. and Haasen P. (Elsevier-North Holland, Amsterdam) 3rd ed.
- Pettifor D.G. and Podloucky R. 1984 Phys. Rev. Lett. 53 1080
- 1986 J.Phys. C: Solid State Phys. 19 315
- Pettifor D.G. and Weaire D.L. (editors) 1985 *The Recursion Method and its Applications* (Berlin: Springer)
- Pettifor D.G. 1986a New Sci., 110 (1510) 48-53
- Pettifor D.G. 1986b J.Phys. C, Solid State Phys. 19 285
- Pettifor D.G. 1988 Mat.Sci. and Technology 4 675
- Shohat J.A. and Tamarkin J.D. 1943 *The Problem of Moments* (Providence, Rhode Island: American Mathematical Society)
- Simons G. and Bloch A.N. 1973 Phys. Rev. B 7 2754
- Singhal S.P. and Callaway J. 1977 Phys. Rev. B 16 1744
- Skinner A.J. and Pettifor D.G. (to be published)
- Slater J.C. 1963 *Quantum Theory of Molecules and Solids* Vol.1 (New York: McGraw Hill)
- Slater J.C. and Koster G.F. 1954 Phys.Rev. 94 1498
- Sutton A.P., Finnis M.W., Pettifor D.G. and Ohta Y. 1988 J.Phys.C: Solid State Phys. 21 35
- Turchi P., Ducastelle F. and Tréglià G. 1982 J.Phys.C: Solid State Phys. 15 2891

- Turchi P. and Ducastelle F. 1985 *The Recursion Method and its Applications* : eds Pettifor D.G. and Weaire D.L. (Berlin: Springer) p104
- Villars P. 1983 *J. Less-Common Met.* **92** 215
- 1984 *J. Less-Common Met.* **99** 33
- 1985 *J. Less-Common Met.* **102** 199
- Villars P. and Calvert L.D. 1985 *Pearsons handbook of crystallographic data for intermetallic phases* Vols 1-3, 1-3258 Metals Park, OH, ASM
- Yin M.T. and Cohen M.L. 1980 *Phys. Rev. Lett.* **45** 1004
- 1981 *Solid State Commun.* **38** 625
- Wall H.S. 1948 *Analytic Theory of Continued Fractions* (Van Nostrand: Princeton, New Jersey)
- Wyckoff R.W.G. 1963 *Crystal Structures* 2nd edn vol 1 (New York: Wiley)
- Williams A.R., Feibelman P.J. and Lang N.D. 1982 *Phys. Rev. B* **26** 5433
- Woodruff D.M., Anlage S.M. and Smith D.L. 1987 *Phys. Rev. B* **36**
- Zangwill A. and Bruinsma R. 1987 *Comments Cond. Mat. Phys.* **13** 1 pp.1-19
- Zunger A. 1980 *Phys. Rev. B* **22** 5839
- Zunger A. and Cohen M.L. 1978 *Phys. Rev. B* **18** 5449
- 1979 *Phys. Rev. B* **20** 4082